



Development of tubular perovskitefluorite oxygen transport membranes for biomass gasification

Martinez Aguilera, Lev

Publication date:
2020

Document Version
Publisher's PDF, also known as Version of record

[Link back to DTU Orbit](#)

Citation (APA):
Martinez Aguilera, L. (2020). *Development of tubular perovskitefluorite oxygen transport membranes for biomass gasification*. Technical University of Denmark.

General rights

Copyright and moral rights for the publications made accessible in the public portal are retained by the authors and/or other copyright owners and it is a condition of accessing publications that users recognise and abide by the legal requirements associated with these rights.

- Users may download and print one copy of any publication from the public portal for the purpose of private study or research.
- You may not further distribute the material or use it for any profit-making activity or commercial gain
- You may freely distribute the URL identifying the publication in the public portal

If you believe that this document breaches copyright please contact us providing details, and we will remove access to the work immediately and investigate your claim.



**Development of tubular perovskite-
fluorite oxygen transport membranes for
biomass gasification**

Ph.D. Dissertation

by

Lev Martinez Aguilera

Department of Energy Conversion and Storage

DTU Energy

Technical University of Denmark

March 2020

Preface

This thesis was the result of the PhD project “Development and characterization of tubular oxygen transport membranes” conducted from April 1st, 2017 to March 31st, 2020 at the Technical University of Denmark. This thesis has been submitted to fulfil the requirements for the degree of Doctor of Philosophy (PhD).

The performed studies are part of the project “Highly Flexible Energy Production by Oxy-Fired Biomass Gasification (HighFlex)”, financed by EUDP grant No.: 64018-0028 – before 12403–, “Highly Flexible Energy Production by Oxy-Fired Biomass Gasification (HighFlex)”. The aim of the HighFlex project was to demonstrate oxygen blown biomass gasification as a method to generate electricity, heat and synthetic fuels by the integration of highly efficient oxygen transport membranes in a state-of-the-art gasifier.

To achieve this objective, oxygen transport membranes based on dual-phase composites capable of withstanding high temperatures and reducing conditions, and highly mechanically stable tubular porous supports were developed and characterized. Oxygen permeability tests of tubular oxygen transport membranes were performed under controlled conditions and in a specially designed unit for partial oxidation of tars adjacent to a biomass gasifier, demonstrating the feasibility of using oxygen membranes in gasification and syngas applications.

The work presented in this thesis was performed in the facilities of DTU Energy under the supervision of Senior Researcher Ragnar Kiebach and the co-supervision of Researcher Astri Bjørnetun Haugen and Associate Professor Andreas Kaiser. The studies related to the partial oxidation of tars from biomass gasification were conducted at the facilities of DTU Chemical Engineering in close collaboration with Researcher Maria Puig Arnavat and Senior Scientist Jesper Ahrenfeldt.

Additional cooperation work was conducted with Postdoc Julio Garcia Fayos and Research Professor Jose Manuel Serra from Instituto de Tecnología Química of the Universitat Politècnica de València to develop and characterize the oxygen membranes materials.

Acknowledgements

I would like to express my gratitude to all the people involved through my PhD project, especially to my supervision team, Ragnar Kiebach, Astri Haugen and Andreas Kaiser for the scientific guidance, ideas, support and insightful advises that allowed me to take the right decisions and encourage me to go further, not only in my studies but also beyond.

Also to the magnificent researchers, scientists and technicians of DTU, Maria Puig Arnavat, Peter Vang Hendriksen, Christodoulos Chatzichristodoulou, Ebtisam Abdellahi, Jette Iversen, Jens Borchsenius, Jens Østergaard and Karen Brodersen, that also shared their expertise with me.

I am also grateful to all my DTU colleagues that were willing to back me up. To Steven Pirou for sharing all the knowledge and for his unconditional help. Also to Anastasiia Karabanova, Ilaria Ritucci, Martina Trini, Daniel Bøgh Drasbæk and Peyman Khajavi that besides their professional help they made of this journey something to be remembered.

Beyond the DTU walls, I really appreciate all the support that my family has given me from the other side of the Atlantic during my academic quest. I also want to thank my friends, Lana, Raul, Vignesh, Hillary, Mattia, Yan and Antonio, that always knew how to cheer me up through the PhD life.

Finally, I would also like to acknowledge DTU Energy and the HighFlex project, that gave me the opportunity to participate in this ambitious enterprise and allowed me meeting outstanding scientists in the field of ceramic processing and materials development.

Lev Martinez

Lyngby, Denmark, March 2020.

Abstract

Oxygen transport membranes (OTMs) are an attractive technology to be integrated in oxy-fuel and syngas applications to improve the efficiency of processes, such as carbon capture and storage (CCS) and oxy blown biomass gasification. Furthermore, the use of oxygen for combustion (instead of air) allows the use of the gases at the out-stream to generate electricity or fuel synthesis. However, these processes require temperatures above 800 °C and oxygen partial pressures (p_{O_2}) below 10^{-12} atm. Although efforts have been made to develop OTM materials capable of withstanding these conditions, the practical applications have been limited. By using dual-phase composites based on stable fluorite-type oxygen-ion conducting ceramics and electronic conducting perovskites, these limitations could be sorted out, allowing the development of this technology for industrial applications.

This thesis deals with the development of asymmetric tubular multilayer OTMs for their integration in gasification systems. To achieve the objectives, different tasks have been performed, including the selection of materials and the definition of the fabrication steps to produce defect-free OTMs with the desired microstructure. Thermoplastic extrusion and dip coating were chosen as the shaping techniques to produce a porous 3YSZ-based support tube, the catalytic layers and the active membrane. The test of the membranes under relevant conditions for syngas applications are highlighted.

In the first part of the thesis, $Ce_{0.9}Gd_{0.1}O_{1.95} - La_{0.6}Sr_{0.4}FeO_{3-\delta}$ (CGO-LSF) composite membranes supported on porous MgO supports, previously developed by DTU Energy, were tested in both controlled lab-scale conditions and a special unit for partial oxidation of tars, adjacent to a low temperature circulating fluidized bed (LT-CFB) gasifier, operated by DTU Chemical Engineering. The function of this partial oxidation unit was to treat a stream of producer gas (PG) generated in the LT-CFB gasifier at the operation temperature of the membrane at 850 °C.

Oxygen fluxes of $0.5 \text{ Nml}\cdot\text{cm}^{-2}\cdot\text{min}^{-1}$ and $1.5 \text{ Nml}\cdot\text{cm}^{-2}\cdot\text{min}^{-1}$ were obtained when operating the membrane unit in gradients of PG/Air and H_2 /Air, respectively. In lab-scale tests, the same kind of membrane provided an oxygen flux of $4.4 \text{ Nml}\cdot\text{cm}^{-2}\cdot\text{min}^{-1}$ when using an H_2 /Air gradient. This difference might be related to a reduction of the driving

force along the membrane or a potentially lower accuracy linked to the setup and instrumentation being used.

Analysis of the gas and tar composition at the output of the membrane demonstrated that the combination of heat and oxygen provided by the membrane led to 65% less tertiary tars and additional 50% and 20% more H₂ and CH₄ when comparing with the conversion related to the pure thermal conversion processes. Although the CGO-LSF oxygen transport membranes did not stand thermal cycling, the concept for the integration of OTMs in gasification systems was successfully proved.

For further progress, alternative and more resistant membrane materials were evaluated for the operation in syngas conditions. To improve the stability of dual phase membranes at 1000 °C and under low pO₂ of down to 10⁻²¹ atm, chromite based perovskites were selected as the electronic-conducting phase, while, Zr-based and Ce-based materials were used as high-performance oxygen-ion conductors. The MgO support tube was replaced by 3YSZ tubes due to significantly better mechanical and chemical stability of 3YSZ compared to MgO.

Two dual-phase phase composites fulfilled this requirement and were selected: (Sc₂O₃)_{0.10}(Y₂O₃)_{0.01}(ZrO₂)_{0.89} – LaCr_{0.85}Cu_{0.10}Ni_{0.05}O_{3-δ}, (ScYSZ-LCCN), which was previously studied as an OTM membrane in planar architectures, and Ce_{0.9}Gd_{0.1}O_{1.95} – Y_{0.8}Ca_{0.2}Cr_{0.8}Co_{0.2}O_{3-δ}, (CGO-YCCC). Based on literature review and experimental results of this work, the preferred volume ratio of the electronic and ionic conducting phase for both of these compositions (ScYSZ-LCCN and CGO-YCCC) was 70:30. (Y₂O₃)_{0.03}(ZrO₂)_{0.97} – 3YSZ – porous tubes were used as supports for the dual-phase OTM, due to their mechanical properties, high chemical stability and good permeability. Tubular supports with a permeability larger than 1x10⁻¹⁴ m⁻² and a flexural strength of ≥50 MPa have been achieved to ensure mechanical stability and sufficient gas permeability through the structure of the porous 3YSZ support.

The ScYSZ-LCCN membranes were fabricated in a multilayer architecture with two membrane architectures . In the first set-up, functional layers, including the ScYSZ-LCCN based membrane, were deposited on the 3YSZ porous supports. Several severe challenges were faced during the manufacturing of these tubular membranes, such as

extensively high processing temperatures of more than 1450 °C to densify the membrane layer, accompanied by Cr vaporization and the formation of La(OH)₃. This was leading to longitudinal fractures of the membranes. A thermal expansion coefficient mismatch ($\Delta\alpha = 1 \times 10^{-6} \text{K}^{-1}$) and a sintering onset temperature mismatch (126 °C) between the membrane and the porous support layers led to transversal cracks. Evaluation of cross sections by SEM and EDX revealed a membrane thickness of about 5 μm did not lead to cracks; nevertheless, a lack of gas tightness was observed and the formation of La₂Zr₂O₇ at the interface between the membrane layer and the outer catalytic layer was identified.

In the second set-up, a modification of the membrane architecture was done by adding 1 mol% and 3 mol% Fe₂O₃ to the porous supports and the thin film membrane layer as a sintering aid to reduce the stresses in the multilayer membrane caused by the sintering mismatches. It was possible to decrease the sintering temperature of the membrane to 1250 °C. Furthermore, the addition of iron to the 3YSZ supports allowed obtaining flexural strengths larger than 138 MPa and a gas permeability of $2.2 \times 10^{-14} \text{m}^2$. A sintering onset temperature mismatch of 10 °C and a $\Delta\alpha$ of $0.4 \times 10^{-6} \text{K}^{-1}$ between the active membrane and the porous support was obtained.

The 26% total shrinkage of the porous support was found to be the main driver for the densification of the membrane. Nevertheless, it was found that the system is highly sensitive to composition and to thickness variations of the functional layers. The total thickness of the functional layers, including catalytic layers and the active membrane, must not exceed 15 μm . Additionally, the LCCN in the ScYSZ-LCCN inner porous activation layer was reduced to less than 20 vol%, because LCCN phase higher fractions restricted the densification of the active membrane layer. A methodology for the fabrication of the tubes to obtain integer gas-tight oxygen membranes with outstanding mechanical and thermal stability was developed. It consists of depositions of the functional layers on calcined 3YSZ+3 mol% Fe₂O₃. An ScYSZ-LCCN 90:10 inner catalytic layer was deposited and calcined at 950 °C. Then the ScYSZ-LCCN 70:30 active membrane was deposited and sintered at 1250 °C for 4h with a ramp of 200 °C·h⁻¹. Finally, the ScYSZ-LCCN 70:30 outer catalytic layer was deposited and calcined at 1200 °C.

Formation of La₂Zr₂O₇, reduced percolation of the electronic-conducting phase (LCCN) or reaction of Fe with the LCCN phase have most likely reduced the oxygen flux in this

membranes. For the 8 μm thick composite membranes, an oxygen flux of $0.28 \text{ ml}\cdot\text{min}^{-1}\cdot\text{cm}^{-2}$ was obtained in a gradient of Air/ N_2 at $950 \text{ }^\circ\text{C}$. Further studies are required to exactly identify the mechanism that are responsible for the reduced oxygen fluxes, as well as to confirm the outstanding stability of the membrane materials after exposure to different oxygen gradients, including operation in Air/ H_2 for longer periods.

Another membrane generation, consisting of a CGO-YCCC composite as OTM material, was selected and investigated in this thesis as a result of compatibility tests between different material candidates for composite membranes. The CGO-YCCC composite could be fully densified after sintering in air at $1250 \text{ }^\circ\text{C}$ after 2 hours, probably due to an auto-sintering effect caused by the formation of a Co-liquid phase from the YCCC material that acted as sintering aid for the CGO-phase. The composite revealed oxygen fluxes of $0.3 \text{ ml}\cdot\text{min}^{-1}\cdot\text{cm}^{-2}$ and $0.25 \text{ ml}\cdot\text{min}^{-1}\cdot\text{cm}^{-2}$ in gradients of Air/Ar and Air/ CO_2 , respectively, at $900 \text{ }^\circ\text{C}$ when using a self-supported 1.3 mm thick membrane architecture. The composite membrane showed high stability over a period of 30 h in Air/ CO_2 at $900 \text{ }^\circ\text{C}$. However, under highly reducing conditions ($p\text{O}_2 \sim 10^{-20}$), formation of cracks on the composite membrane was observed. It is known that CGO shows a significant chemical expansion that can lead to crack formation along the CGO grain boundaries. Attempts to develop thin CGO-YCCC membranes supported on 3YSZ-based supports were carried out. However, the large TEC and the sintering temperature mismatch between the membrane composite and the porous supports led to transversal cracks and delamination in all the tested cases.

Finally, an alternative approach to overcome the challenges with the processing of multilayer membranes was investigated in this thesis. For this purpose, the development of flexible archetype capillaries with a diameter of 4 mm and a wall thickness of 0.5 mm were fabricated by thermoplastic extrusion. Within the time frame of this thesis, in a first proof of concept, dense CGO and ScYSZ capillaries were fabricated. This approach can be further extended for the fabrication of self-supported dual-phase composite membranes, such as CGO-LSF and CGO-YCCC. Although bulk diffusion limitations (depending on the wall thickness of the tube) and high pressure drops (depending on the length of the capillaries) need to be considered, larger surface area per volume unit could compensate these disadvantages.

Papers included in this thesis

Paper 1. Partial oxidation of biomass gasification tars with oxygen transport membranes.

Authors: Lev Martinez Aguilera, Maria Puig Arnavat, Simona Ovtar, Astri Bjørnetun Haugen, Andreas Kaiser, Jesper Ahrenfeldt, Ulrik Birk Henriksen, Peter Vang Hendriksen, Jonas Gurauskis, Wolff-Ragnar Kiebach.

Manuscript to be submitted. First Author.

Contribution of the PhD student: Coordination, performance and analysis of experimental results carried out in the partial oxidation unit for tars. Structuring of the paper, writing of the introduction and the experimental and analysis sections related to the gasifier unit.

Paper 2. Exploring the processing of tubular chromite- and zirconia-based oxygen transport membranes.

Authors: Astri Bjørnetun Haugen, Lev Martinez Aguilera, Kawai Kwok, Tesfaye Molla, Kjeld Bøhm Andersen, Steven Pirou, Andreas Kaiser, Peter Vang Hendriksen and Ragnar Kiebach.

Published. **Ceramics** — 2018, Volume 1, Issue 2, pp. 229-245.

Contribution of the PhD student: Definition of conditions of parameters for the study of the selected $(Y_2O_3)_{0.01}(Sc_2O_3)_{0.10}(ZrO_2)_{0.89} - LaCr_{0.85}Cu_{0.10}Ni_{0.05}O_{3-\delta}$ composite. Fabrication and characterization of the tubular oxygen membranes. Partial characterization of tubular supports. Writing of experimental section and results section related to manufacturing and characterization of the membranes.

Paper 3. $Y_{0.8}Ca_{0.2}Cr_{0.8}Co_{0.2}O_{3-\delta}$ – based dual phase membranes for O_2 separation for oxy-fuel and syngas applications.

Authors: Julio Garcia Fayos, Lev Martinez Aguilera, Astri Bjørnetun Haugen, Wolff-Ragnar Kiebach, Jose Manuel Serra.

Manuscript to be submitted.

Contribution of the PhD student: Selection of the materials based on literature review. Preparation and characterization of $Y_{0.8}Ca_{0.2}Cr_{0.8}Co_{0.2}O_{3-\delta}$ – fluorite-type ionic conductor composites with volumetric proportions 30:70. Development of HT-XRD, dilatometry and SEM-EDS studies. Writing of the experimental section related to the performed analysis. Review of the paper.

Paper 4. Interaction of $Y_{0.8}Ca_{0.2}Cr_{0.8}Co_{0.2}O_{3-\delta}$ – $Ce_{0.9}Gd_{0.1}O_{2-\delta}$ dual phase oxygen transport membranes on tubular $Zr_{0.97}Y_{0.6}O_{2-\delta}$.

Authors: Lev Martinez Aguilera, Astri Bjørnetun Haugen, Peter Vang Hendriksen, Andreas Kaiser, Wolff-Ragnar Kiebach.

Manuscript to be submitted. First Author.

Contribution of the PhD student: Fabrication and characterization of the tubular oxygen transport membranes. Structuration of the paper content, writing of the full paper.

Paper 5. Effective method to manufacture stable $(Sc_2O_3)_{0.10}(Y_2O_3)_{0.01}(ZrO_2)_{0.89}$ – $LaCr_{0.85}Cu_{0.10}Ni_{0.05}O_{3-\delta}$ asymmetric tubular ceramic oxygen transport membranes.

Authors: Lev Martinez Aguilera, Astri Bjørnetun Haugen, Peter Vang Hendriksen, Andreas Kaiser, Steven Pirou, Peyman Khajavi, Henrik Lund Frandsen, Julio Garcia Fayos, Jose Manuel Serra, Wolff-Ragnar Kiebach.

Manuscript to be submitted. First Author.

Contribution of the PhD student: Fabrication and characterization of the tubular oxygen transport membranes. Structuration of the paper content, writing of the full paper.

Paper 6. Development and fabrication of flexible ion-conductor ceramic capillaries via thermoplastic extrusion.

Authors: Lev Martinez Aguilera, Astri Bjørnetun Haugen, Wolff-Ragnar Kiebach.

Manuscript to be submitted. First Author.

Contribution of the PhD student: Fabrication and characterization of the capillaries. Structuration of the paper content, writing of the full paper.

Participation in disseminating activities

Martinez, L.; Haugen, A.B.; Kiebach, R. *Manufacturing of highly stable ScYSZ-LCCN tubular oxygen transport membranes*. Oral presentation. DTU Energy's PhD Symposium. Denmark, 2020.

Martinez, L.; Haugen, A.B.; Kiebach, R. *Tubular oxygen transport membranes based on dual phase composites*. Poster presentation. The 22nd International Conference on Solid State Ionics (SSI-22). Republic of Korea, 2019.

Martinez, L.; Haugen, A.B.; Kiebach, R. *Development of oxygen tubular oxygen transport membranes based on dual-phase chromites and ion-conductors*. Oral presentation. 2nd Nordic Conference on Ceramic and Glass Technology. Denmark, 2018.

Martinez, L.; Haugen, A.B.; Kiebach, R. *Compatibility Analysis of Chromites in Dual-Phase Composites for Oxygen Transport Membranes*. Poster presentation. The Electrochemical Society. Americas International Meeting on Electrochemistry and Solid State Science (AiMES). Mexico, 2018.

Martinez, L.; Pirou, S.; Haugen, A.B.; Kiebach, R. *Stability analysis of chromite-based dual-phase composites for oxygen transport membranes*. Poster presentation. Fraunhofer, 15th International Conference on Inorganic Membranes. (ICIM). Germany, 2018.

Martinez, L.; Haugen, A.B.; Kiebach, R. *Dual phase composites for tubular oxygen transport membranes*. Poster presentation. Sustain DTU Summit. Denmark, 2017.

Martinez, L.; Haugen, A.B.; Kiebach, R. *Dual phase composites for oxygen transport membranes*. Poster presentation. DTU Energy's PhD Symposium. Denmark, 2017.

Table of contents

Preface	3
Acknowledgements.....	5
Abstract.....	7
Papers included in this thesis	11
Participation in disseminating activities	13
Table of contents.....	15
List of figures.....	17
List of tables	23
List of acronyms	25
Chapter 1. Introduction	27
1.1 Oxygen generation and applications of oxygen-conducting membranes.....	27
1.2 Biomass gasification: an opportunity for oxygen transport membranes.....	29
Chapter 2. Objectives and content of the thesis	35
Chapter 3. Working principles	39
3.1 Working principle of oxygen transport membranes.	39
3.2 Oxygen transport mechanisms.....	40
3.2.1 Bulk mechanism limitation.	41
3.2.2 Surface exchange reactions.	42
3.2.3 Gas diffusion.....	43
3.3 Membrane geometry.....	45
3.4 Materials for oxygen transport membranes.	46
3.4.1 Mixed ion-electronic conductors.	47
3.4.2 Fluorite-perovskite dual-phase composites.....	48
Chapter 4. Fabrication and characterization of OTMs.....	65
4.1. Processing and fabrication of asymmetric tubular oxygen transport membranes.....	65
4.1.1 Thermoplastic extrusion.....	66
4.1.2 Sintering.....	73
4.1.3 Dip coating.....	77
4.2. Materials and membranes characterisation techniques	83
4.2.1 X-ray diffraction	83
4.2.2 Particle size distribution.....	84
4.2.3 Dilatometry	84
4.2.4 Scanning electron microscopy	86
4.2.5 Viscosity	87
4.2.6 Hg-porosimetry	88
4.2.7 Flexural strength of porous supports.....	88

4.2.8	Gas permeability of porous supports.....	90
4.2.9	Oxygen permeability	91
Chapter 5. Results		101
5.1	Partial oxidation of biomass gasification tars with oxygen transport membranes.	103
5.2	Exploring the processing of tubular chromite- and zirconia-based oxygen transport membranes.	131
5.3	$Y_{0.8}Ca_{0.2}Cr_{0.8}Co_{0.2}O_{3-\delta}$ -based dual phase membranes for oxyfuel and syngas applications.	157
5.4	Co-sintering and interaction of $Y_{0.8}Ca_{0.2}Cr_{0.8}Co_{0.2}O_{3-\delta} - Ce_{0.9}Gd_{0.1}O_{2-\delta}$ dual phase oxygen transport membranes with tubular $Zr_{0.97}Y_{0.6}O_{2.03}$ supports.....	185
5.5	Effective method to manufacture stable $(Sc_2O_3)_{0.10}(Y_2O_3)_{0.01}(ZrO_2)_{0.89} - LaCr_{0.85}Cu_{0.10}Ni_{0.05}O_{3-\delta}$ asymmetric tubular ceramic oxygen transport membranes.....	203
5.6	Development of thermoplastic extrusion for the fabrication of single-phase ion-conducting ceramic capillaries.....	253
Chapter 6. Summary and future work		263

List of figures

<i>Fig. 1.1. OTM Combined Reformer for IGCC Power Systems concept developed by Praxair.....</i>	<i>28</i>
<i>Fig. 1.2. Use of solid biomass in the Danish energy system in 2015.....</i>	<i>29</i>
<i>Fig. 1.3. Concept of LT-CFB gasifier.....</i>	<i>30</i>
<i>Fig. 3.1. Schematics of architecture and operations of an asymmetric dual-phase oxygen transport membrane.....</i>	<i>40</i>
<i>Fig. 3.2. Schematic of the mechanism of O₂ permeation through an oxygen membrane.....</i>	<i>41</i>
<i>Fig. 3.3. Schematics of asymmetric oxygen membranes in a) tubular and b) planar configurations.....</i>	<i>45</i>
<i>Fig. 3.4. Ideal perovskite crystal structure, ABO₃.....</i>	<i>47</i>
<i>Fig. 3.5. Schematics of a single-phase mixed oxygen ion/electronic conducting material, MIEC (left) and a dual phase membrane of an oxygen ion and electron conducting phase (right).....</i>	<i>48</i>
<i>Fig. 3.6. Ideal cubic fluorite structure, AO₂.....</i>	<i>49</i>
<i>Fig. 3.7. Oxygen loss upon heating or exposure to reducing atmosphere typically (fluorite structured metal oxide, MO₂) results in a lattice dilatation known as chemical expansion.....</i>	<i>50</i>
<i>Fig. 3.8. Crystal transitions of the ZrO₂ at different temperatures.....</i>	<i>51</i>
<i>Fig. 4.1. Schematic diagram of a single screw extruder.....</i>	<i>66</i>
<i>Fig. 4.2. Main components and processing of the binder system.....</i>	<i>67</i>
<i>Fig. 4.3. Brabender KE19 – 19/20DN single screw extruder: a) General setup, b) detail of the extruder's screw and c) green-state capillaries and porous supports.....</i>	<i>72</i>
<i>Fig. 4.4. Debinding profiles showing the steps where components are burnt out in a) 3YSZ-based porous supports and b) CGO and ScYSZ dense capillaries.....</i>	<i>73</i>
<i>Fig. 4.5. Mass transport mechanisms involved in the sintering process in a two-particle model.....</i>	<i>74</i>
<i>Fig. 4.6. Illustration of the sintering stages in two-spheres sintering model and multi-particle sketch. 1) green-state or loose powder, 2) initial neck growth, 3) onset of the grain growth and 4) grain growth and densification.....</i>	<i>75</i>
<i>Fig. 4.7. Solid state and liquid-phase sintering. a) phase-diagram of a binary system showing solid-state and liquid-phase sintering fields; b) liquid phase sintering concept; c) solid-state sintering process.....</i>	<i>76</i>
<i>Fig. 4.8. Sintering profile of the thin oxygen membranes supported on 3YSZ-based tubes.....</i>	<i>77</i>
<i>Fig. 4.9. Basic steps in sol-gel and slurry dip-coating.....</i>	<i>78</i>
<i>Fig. 4.10. Principles of dip coating a) Flow patterns during the dip-coating process b) Sequential structural development resulting from drying and evaporation of the solvent c) drying front and capillary regime.....</i>	<i>79</i>
<i>Fig. 4.11. Film thickness in relation with the withdrawal speed.....</i>	<i>81</i>
<i>Fig. 4.12. In house built dip-coater used for the development of the oxygen transport membranes.....</i>	<i>82</i>
<i>Fig. 4.13. Diagram showing the components of the dilatometer DIL402C.....</i>	<i>85</i>

Fig. 4.14. 4-point bending testing. a) Test configuration of 4-point bending of a semi-cylindrical specimen, 2) finite element mesh of a quarter of specimen, c) mounting of a 3YSZ sample in the testing rig	89
Fig. 4.15. Schematics of the Darcy's gas permeation setup	90
Fig. 4.16. Open flow oxygen-flux rig a) a schematic diagram showing the gas flow and the components; b) a picture of the sample after mounting in the rig, c) the entire rig with a detail of the sample mounted along the alumina tubes.	92
Fig. 4.17. Process diagram of the membrane unit for partial oxidation of tars. F: flowmeter, T: thermocouple, pO ₂ : Zirconia pO ₂ sensor.	93
Fig. 4.18. a) detail of the Kanthal® holders and the alumina spacers, b) picture of the membrane mounted in the unit, c) Main components of the membrane unit for partial oxidation.	94

Chapter 5.1

Fig. 1. LT-CFB gasifier flow diagram with the operating principle of a dense ceramic membrane for the partial oxidation of tars	105
Fig. 2. Designed set-up for the oxygen membrane testing: a) alumina spacers pre-sealed on the Kanthal holder with Inconel fittings; b-c) application of the NAS glass paste to the contact area between membranes and alumina spacers; d) oxygen membrane in place in the set-up unit	111
Fig. 3. Designed set-up for the oxygen membrane testing on a side stream of the LT-CFB gasifier: a) oxygen membrane placed in the set-up unit. Pulley and counterweight system to keep the membrane under a load is observed on the top of the unit. b) detail of the stainless steel cylinder covering the membrane with the air preheating section; c) overall view of the all set-up placed inside the furnace; d) set-up with of the furnace close and insulated.....	112
Fig. 4. Oxygen permeation flux of an infiltrated Ce _{0.9} Gd _{0.1} O _{1.95} – La _{0.6} Sr _{0.4} FeO _{3-d} membrane in the experimental test rig in a) nitrogen, b) hydrogen with a membrane area of 5 cm ²	115
Fig. 5. a) Oxygen permeation flux Ce _{0.9} Gd _{0.1} O _{1.95} – La _{0.6} Sr _{0.4} FeO _{3-d} membrane in producer gas for a) a 80 hour test and b) oxygen permeation flux and conversion rate as a function of hydrogen for a membrane surface area of 35 cm ²	116
Fig. 6. Oxygen permeation flux measurements of a CGO-LSF membrane in the experimental test rig as a function of time a) for a H ₂ :N ₂ mixture of 1:8.9 at 850 °C and b) for different H ₂ :N ₂ ratios and the simulated producer gas at 822 °C and 850 °C (membrane area in both tests was 5 cm ²).	118
Fig. 7. a) Oxygen permeation flux measurement as a function of time of a 35 cm ² CGO-LSF membrane tested in the partial oxidation test unit adjacent to a LT-CFB gasifier at 850 °C. b) White producer gas at the output of the membrane indicating the partial oxidation of the tars.	119
Fig. 8. Tars composition after treatment in a partial oxidation unit i) using an alumina blank and b) using a CGO-LSF membrane. Tests were carried out at 850 °C using air in the feed side.....	120
Fig. 9. Oxygen membrane after producer gas testing with carbon deposition (black colour) on the permeate side.....	121

Fig. 10. a) Optical microscopy images of longitudinal sections of the membrane: inlet side, middle and outlet side, b) SEM micrographs of fractured cross section of the inlet side (permeate) of the inlet side of the MgO support tested with producer gas.	122
Fig. 11. Micrographs of the CGO-LSF membrane tube and the membrane layer after testing in the gasifier test unit with the producer gas of a) inlet, b) middle, c) outlet.	123
Fig. 12. a/b) Micrographs of post-mortem samples showing needle-alike structures on the permeate side of the MgO support. c/d) EDS mapping of the needles and nearby components.	123

Chapter 5.2

Fig. 1. Flexural strength of tubular, porous 3YSZ supports plotted vs. (a) sintering temperature and (b) porosity. (c) Weibull plot of room temperature strength of specimens with 61.5 vol% pore former and sintered at 1300 °C.	138
Fig. 2. Micrographs of the porous 3YSZ support tubes with 61.5 vol% pore formers after sintering for 2 h at different temperatures. (a) and (b) 1250 °C, (c) 1300 °C, and (d) 1400 °C.	139
Fig. 3. Dilatometry of 3YSZ and 30/70 vol% LCCN/10Sc1YSZ as pellets and as the actual thermoplastic feedstock with 61.5 vol% pore formers for the support as a tube, and the 30/70 vol% LCCN/10Sc1YSZ as a casted tape rolled up to a cylinder.	140
Fig. 4. Photographs of (a) as-extruded support tubes, (b) tubes coated with inner activation layer and membrane layer after calcination and pre-sintering (the white parts on the ends are uncoated support), and (c) tubes after application of all layers (the white parts on the ends are uncoated support, the white part in the middle is the outer 10Sc1YSZ activation layer. The ruler shows length in millimeters).	141
Fig. 5. SEM micrographs of the tubular OTM layers, from top to bottom outer activation layer, composite membrane, inner activation layer and porous support, after sintering at (a) 1400 °C, 2 h (leaks), (b) 1425 °C, 2 h (leaks), (c) 1425 °C, 6 h (tight) and (d) 1450 °C, 6 h (tight, with some leaky spots).	141
Fig. 6. Effect of thickness on crack formation in the tubular OTMs. a) Transversal crack in thick membranes. b) longitudinal cracks and c) thin membrane without cracks, but severe loss of electronic conducting phase.	142
Fig. 7. Leakage dependence on thickness and density of the LCCN/10Sc1YSZ asymmetric membranes, with a qualitative estimate of regimes where the membrane leaks or is leak tight.	142
Fig. 8. Micrograph of the top surface of a tubular OTM (without outer porous activation layer) showing decomposition of the LCCN phase into Cr and La rich regions.	143
Fig. 9. SEM image (left) and EDS signals of La and Cr from a close-up of the tubular OTMs, showing evaporation of Cr and coarsening of the nominal LCCN grains (red circle) from the outer side from the crack (above the red line).	144
Fig. 10. SEM image (left) and EDS signals from Cr, Zr and La from the same area of a cross-section of the tubular OTMs with outer porous activation layer containing 60/40 vol% LCCN/10Sc1YSZ. The yellow line is a guide for the eye.	145

Chapter 5.3

Figure 1. FE-SEM images corresponding to YCCC composites cross sections and XRD patterns of the depicted samples.	164
Figure 2. SEM micrographs of the CGO-YCCC composite after (a) sintering in air at 1300°C and (b) after sintering and applying reducing conditions 5% H ₂ -Ar for 24h at 900°C.	165
Figure 3. Dilatometry curves of CGO, YCCC and CGO-YCCC composite. Onset point in brackets.	168
Figure 4. XRD diffractograms of CGO-YCCC composite taken at 500°C during heating (red) and cooling (blue) before and after sintering in air at 1100°C. (A) Relevant 2θ range, (B) and (C) YCCC peaks at 33.5° and 60.5° respectively. c: CGO, y: YCCC.	169
Figure 5. a) Arrhenius plot of the total electrical conductivity in air for the single phase YCCC, CGO, and the composite phase YCCC-CGO. b) total electrical conductivity in dependence of pO ₂ at 800 °C of the YCCC, CGO and YCCC-CGO composite.	170
Figure 6. a) BODE plot of YCCC-CGO at 850 °C. b) Nyquist plot of YCCC-CGO at 850 °C. c) Polarization resistance values of various composites at 850 °C.	171
Figure 7. a) Oxygen permeation of YCCC-CGO membrane in dependence of temperature when exposed to different gradients. Q _{feed} and Q _{sweep} = 300 ml·min ⁻¹ . b) Oxygen permeation as function of sweep gas flow for different temperatures and feeding modes. Q _{feed} = 300 ml·min ⁻¹	173
Figure 8. a) Oxygen permeation dependence of the CO ₂ content in the sweep at different temperatures. b) Oxygen permeation evolution with time at 900 °C under different sweep gas atmospheres. Q _{feed} , Q _{sweep} = 300 ml·min ⁻¹ . Air feeding in both tests.	174
Figure 9. (left) XRD measurements of YCCC-CGO membranes before (no BSCF activation) and after oxygen permeation tests. Au peaks belong to membranes sealing. (right) SE and BSD FE-SEM images of YCCC-CGO membrane after testing.	175

Chapter 5.4

Fig. 1. Schematics of the different components of the studied oxygen transport membrane.	188
Fig. 2. Fabrication process of the asymmetric tubular oxygen transport membranes. Thermal processes are outlined in red.	189
Fig. 3. Dilatometry analysis of the membrane and porous support materials CGO-YCCC, 3YSZ and 3YSZ-Fe ₃ (a) sintering curves and (b) thermal expansion coefficients.	191
Fig. 4. SEM micrographs of CGO-YCCC sintered at 1250 °C in air. a) pressed pellet, b) surface of thin membrane on 3YSZ support, and c) cross section of thin membrane on 3YSZ support,	192
Fig. 5. SEM-micrographs of CY7030 membranes on 1) 3YSZ PS, 2) CGO-Co IL/3YSZ PS and 3) CGO-Co IL/3YSZ-Fe ₃ PS.	193
Fig. 6. Possible observation of failure during the co-sintering of CY7030 membranes and 3YSZ-based porous support.	194
Fig. 7. EDS mapping of Zr and Ca of the CY7030 membrane – 3YSZ support interface.	196

Fig. 8. Interaction of Fe on the membranes CY7030 using 3YSZ tubular supports using a) CGO-Co inner activation layer and b) CGO-Fe inner activation layer. Lack of densification is observed within 1 μm of the membrane when Fe is used as dopant. 196

Chapter 5.5

Fig. 1. Schematic of the studied oxygen transport membrane's architecture and materials analysed in this study.....	208
Fig. 2. Manufacturing steps of the asymmetric tubular oxygen transport membranes: a) 3-step route and b) 4-step route. Thermal processes are outlined in red.	208
Fig. 3. Thermal profiles for (a) green tubes debinding at 950 °C, (b) inner activation layer / 1 st activation membrane layer calcination at 950 °C, (c) sintering of active membrane at 1250 °C, and (d) firing of outer activation layer at 1200 °C.	212
Fig. 4. XRD analysis of LCCN as a) untreated raw powder, b) sintered LCCN pellet in air at 1300 °C/2 h and c) sintered LCCN pellet exposed to reducing conditions 5% H_2N_2 at 900 °C for 24 hours.....	217
Fig. 5. Sintering curves of a) ScYSZ-LCCN 7030 components using a sintering rate of 1 °C $\cdot\text{min}^{-1}$, and b) a SEM micrograph of the composite surface after sintering at 1300 °C in air.....	219
Fig. 6. a) Sintering curves of the ScYSZ-LCCC composites with 60, 70 and 80 vol% LCCN using a heating rate of 1 °C $\cdot\text{min}^{-1}$. b) XRD analysis of ScYSZ-LCCN 7030 composite sintered in air at 1300 °C showing the ScYSZ, LCCN and LZO phases.....	220
Fig. 7. a) Sintering curves of porous support materials. 3YSZ, 3YSZFe1 (1 mol% Fe_2O_3) and 3YSZFe3 (3 mol% doped Fe_2O_3), b) Sintering curves of Fe-doped 3YSZ and Fe-doped active membrane composite materials.	224
Fig. 8. Cross sectional SEM micrographs of Fe_2O_3 -doped 3YSZ tubular supports after sintering at 1250 °C. (a) Single phase 3YSZ, (b) 1 mol% doped Fe_2O_3 and (c) 3 mol% doped Fe_2O_3	225
Fig. 9. TEC analyses of 3YSZ-based porous supports and ScYSZ-LCCN active membrane materials with different Fe_2O_3 concentrations as sintering aid.	228
Fig. 10. Top-view of dual-phase membranes doped with 3 mol% Fe_2O_3 supported on 3YSZ+3 mol% Fe_2O_3 tubes using different heating rates and sintered at 1250 °C/4hours: a) ScYSZ-LCCN 70:30 at 60 °C $\cdot\text{h}^{-1}$, b) ScYSZ-LCCN 70:30 at 200 °C $\cdot\text{h}^{-1}$ c) ScYSZ-LCCN 60:40 at 60 °C $\cdot\text{h}^{-1}$, b) ScYSZ-LCCN 60:40 at 200 °C $\cdot\text{h}^{-1}$	230
Fig. 11. SEM micrographs of membranes a) 3YSZFe3/SL7030Fe3 and 3YSZFe3/SL6040Fe3 after sintering at 1250 °C. Outer activation layer SL7030Fe3 is observed on the membrane.	231
Fig. 12. SEM cross section micrographs of 3YSZFe3 (PS)/ScYSZ (IL)/SL6040Fe3 (AM) a) IL original formula, b) IL with double pore former quantity.	232
Fig. 13. SEM cross section images of membranes containing different amount of LCCN in the inner activation layer. : a) SL9010Fe3, b) SL8020Fe3 and c) SL7030Fe3. Porous support: 3YSZFe3 supports, active membrane: SL6040Fe3	233

Fig. 14. EDS-map of the active membrane (AM), the inner activation layer (IL) and the porous support (PS).....	233
Fig. 15. Cross section micrographs of a) Skin layer formation in the activation layer-support interface when using a pre-sintered support. b) skin layer is diminished when using simultaneous debinding-calcination of the two components. System 3YSZFe3 (PS)/SL9010Fe3 (IL)//SL6040Fe3 (PS).....	234
Fig. 16. Effect of the Fe-content on the 3YSZ porous support on the densification of SL6040Fe3 active membranes after sintering at 1250 °C: a) 3YSZ porous support, b) 3YSZFe1 and c) 3YSZFe3. SL9010Fe3 was used as inner activation layer.	235
Fig. 17. SEM images of a) Full tubular OTM using 3YSZFe3 (PS), SL9010Fe3 (IL) , SL7030 (AM) and SL7030Fe3 (OL); and b) zoom in of the SL7030Fe3 (AM).....	238
Fig. 18. SEM micrographs of SL7030Fe1 active membranes after cyclic treatment at 1000 °C in a) air, b) 5%H ₂ -N ₂ and c) re-oxidised sample, d) picture of the samples.	239
Fig. 19. Oxygen flux of tubular OTM based on SL7030Fe1 active membrane a) Oxygen flux using Air/N ₂ gradient and varying the sweep gas flow, b) Reference measurements in Air/N ₂ gradient at 850 °C after using different gradients.	240

Chapter 5.6

Fig. 1. Different stages of the manufactured capillaries: a) Extrusion process of the ScYSZ capillary, b) comparison of 1 m long 5 mm green-state CGO capillary with a 14 mm green-state YSZ-based porous support, c) sintered ScYSZ and a CGO capillaries, d) CGO capillaries sintered at 1325, 1400 and 1575 °C.	257
Fig. 2. Fractured crossed section SEM micrographs of: a/b) ScYSZ sintered at 1325 °C, c/d) CGO sintered at 1325 °C, e/f) CGO sintered at 1400 °C, g/h) CGO sintered at 1575 °C.....	258
Fig. 3. Tests of U-turn in capillaries a) U-shape in CGO and ScYSZ green capillaries, b) SEM cross section of CGO capillary sintered at 1400 °C, c) SEM cross section of the U-turn in CGO capillary sintered at 1400 °C.....	259
Fig. 4. End-capping of capillaries. a) Capping tests of ScYSZ and CGO capillaries, b) optical microscope view of the capping in ScYSZ capillary, c) optical microscope view of the capping in CGO capillary...	259

List of tables

<i>Table 3.1 Performance of chromite-based oxygen transport membranes</i>	54
<i>Table 4.1. Compositions of the 3YSZ porous support feedstock.</i>	69
<i>Table 4.2. Melting and decomposition temperatures of the organic-phase components.</i>	70
<i>Table 4.3. Formulation of the active membrane and porous activation layers slurries</i>	82
 Chapter 5.1	
<i>Table 1: Composition of wheat straw crushed pellets</i>	108
<i>Table 2. Composition of tars of producer gas during stable operation of a LT-CFB gasifier.</i>	114
<i>Table 3. Producer gas composition during stable operation of the LT-CFB gasifier.</i>	114
<i>Table 4. Composition of the producer gas in oxidation unit using a membrane and an inner blank.</i>	121
 Chapter 5.2	
<i>Table 1. Components of the slurries for dip coating the functional layers.</i>	137
<i>Table 2. Properties of the porous 3YSZ support with 61.5 vol% pore formers.</i>	139
<i>Table 3. Thermal expansion coefficients of each layer of the asymmetric membrane.</i>	146
 Chapter 5.3	
<i>Table 1. Atomic composition of YCCC in different samples using EDS (Normalized data to Y = 0.80).</i> 165	
 Chapter 5.4	
<i>Table 1. Formulation of the active membrane and porous activation layers slurries</i>	189
<i>Table 2. Configurations of CY7030 membranes fabricated during this study.</i>	190
<i>Table 3. Thermal expansion coefficient mismatch ($\Delta\alpha$) between the CY7030 membrane and the YSZ-based porous supports</i>	191
<i>Table 4. EDS analysis of YCCC in the sintered dual-phase membrane.</i>	195
 Chapter 5.5	
<i>Table 1. Matrix of tested components in the ScYSZ-LCCN multilayer tubular systems.</i>	209
<i>Table 2. Formulation of the active membrane and porous activation layers slurries</i>	210
<i>Table 3. Thermal expansion coefficients and sintering onsets of Fe-doped membrane's components.</i>	223
<i>Table 4. Main features of the Fe₂O₃-doped 3YSZ porous supports</i>	224
<i>Table 5. EDS elemental composition of the studied active membranes</i>	236
<i>Table 6. EDS analysis of the SL7030Fe3 dual-phase dense membrane in different testing stages.</i>	239

Chapter 5.6

Table 1. Composition of the used thermoplastic extrusion feedstocks for capillary fabrication. 256

List of acronyms

Acronym	Meaning
ScYSZ	$(\text{Sc}_2\text{O}_3)_{0.10}(\text{Y}_2\text{O}_3)_{0.01}(\text{ZrO}_2)_{0.89}$
3YSZ	$(\text{Y}_2\text{O}_3)_{0.03}(\text{ZrO}_2)_{0.97}$
8YSZ	$(\text{Y}_2\text{O}_3)_{0.08}(\text{ZrO}_2)_{0.92}$
CGO	$\text{Ce}_{0.9}\text{Gd}_{0.1}\text{O}_{1.95}$
CGO-Co	$\text{Ce}_{0.9}\text{Gd}_{0.1}\text{O}_{1.95} + 1 \text{ mol\% } \text{Co}_3\text{O}_4$
CGO-Fe	$\text{Ce}_{0.9}\text{Gd}_{0.1}\text{O}_{1.95} + 1 \text{ mol\% } \text{Fe}_2\text{O}_3$
LCCN	$\text{LaCr}_{0.85}\text{Cu}_{0.10}\text{Ni}_{0.05}\text{O}_{3-\delta}$
YCCC	$\text{Y}_{0.8}\text{Ca}_{0.2}\text{Cr}_{0.8}\text{Co}_{0.2}\text{O}_{3-\delta}$
LSF	$\text{La}_{0.6}\text{Sr}_{0.4}\text{FeO}_{3-\delta}$
SL6040	$(\text{Sc}_2\text{O}_3)_{0.10}(\text{Y}_2\text{O}_3)_{0.01}(\text{ZrO}_2)_{0.89} - \text{LaCr}_{0.85}\text{Cu}_{0.10}\text{Ni}_{0.05}\text{O}_{3-\delta}$ 60:40 vol%
SL7030	$(\text{Sc}_2\text{O}_3)_{0.10}(\text{Y}_2\text{O}_3)_{0.01}(\text{ZrO}_2)_{0.89} - \text{LaCr}_{0.85}\text{Cu}_{0.10}\text{Ni}_{0.05}\text{O}_{3-\delta}$ 70:30 vol%
SL8010	$(\text{Sc}_2\text{O}_3)_{0.10}(\text{Y}_2\text{O}_3)_{0.01}(\text{ZrO}_2)_{0.89} - \text{LaCr}_{0.85}\text{Cu}_{0.10}\text{Ni}_{0.05}\text{O}_{3-\delta}$ 80:20 vol%
SL9010	$(\text{Sc}_2\text{O}_3)_{0.10}(\text{Y}_2\text{O}_3)_{0.01}(\text{ZrO}_2)_{0.89} - \text{LaCr}_{0.85}\text{Cu}_{0.10}\text{Ni}_{0.05}\text{O}_{3-\delta}$ 90:10 vol%
CY7030	$\text{Ce}_{0.9}\text{Gd}_{0.1}\text{O}_{1.95} - \text{Y}_{0.8}\text{Ca}_{0.2}\text{Cr}_{0.8}\text{Co}_{0.2}\text{O}_{3-\delta}$ 70:30 vol%
Fe1	+ 1 mol% Fe_2O_3
Fe3	+ 3 mol% Fe_2O_3
ScYZ	$(\text{Sc}_2\text{O}_3)_{0.10}(\text{Y}_2\text{O}_3)_{0.01}(\text{ZrO}_2)_{0.89}$
10Sc1YSZ	$(\text{Sc}_2\text{O}_3)_{0.10}(\text{Y}_2\text{O}_3)_{0.01}(\text{ZrO}_2)_{0.89}$
LZO	$\text{La}_2\text{Zr}_2\text{O}_7$
BSCF	$\text{Ba}_{0.5}\text{Sr}_{0.5}\text{Co}_{0.8}\text{Fe}_{0.2}\text{O}_{3-\delta}$
OTM	Oxygen transport membrane
MIEC	Mixed ionic-electronic conductor
PS	Porous support
IL	Inner activation layer
AM	Dense active membrane
OL	Outer activation layer
FE-SEM	Field emission scanning electron microscope
SEM	Scanning electron microscope

EDS/EDX	Energy dispersive spectroscopy
BSD	backscattered electrons detector
XRD	X-ray diffraction
HT-XRD	High temperature X-ray diffraction
TEC	Thermal expansion coefficient
pO ₂	Partial oxygen pressure
EC	Electrical conductivity
EIS	Electrochemical impedance spectroscopy
PVA	Polyvinyl alcohol
PVP	Polyvinylpyrrolidone
PMMA	Polymethyl methacrylate
DSB	Dibutyl sebacate
PSA	Pressure swing adsorption
VPSA	Vacuum pressure swing adsorption
CCS	Carbon capture and storage
ASU	Air separation unit
SMR	Steam methane reforming
ATR	Auto-thermal reforming
LT-CFB	Low Temperature Circulating Fluidised Bed gasification
jO ₂	Oxygen permeability / Oxygen flux
HighFlex	Highly Flexible Energy Production by Oxy-Fired Biomass Gasification
DTU	Technical University of Denmark
ITQ	Instituto de Tecnologia Quimica

Chapter 1. Introduction

1.1 Oxygen generation and applications of oxygen-conducting membranes

Oxygen is an important worldwide high-value commodity for the production of consumables and industrial applications, such as steel production, power generation and chemical industry processes. It is expected that the global industrial oxygen market size will increase by almost 60 % by 2025, boosted by the demand expected from the implementation of cleaner technologies for energy generation. [1,2,3]

Oxygen is mainly produced through atmospheric gas separation, where fractional distillation of liquefied air (also known as cryogenic distillation) and pressure swing adsorption (PSA) are the two main used industrial separation technologies. Cryogenic distillation is a well-developed technology for oxygen production with capacities larger than $30,000 \text{ Nm}^3\text{h}^{-1}$ and a purity of 99 %. Since it works with sub-zero temperatures at $-185 \text{ }^\circ\text{C}$ and 8-5 bar, it requires a high investment and an energy demand of ca. $225 \text{ kWh}\cdot\text{ton}^{-1}$. PSA is a batch process usually designed for capacities of up to $10,000 \text{ Nm}^3\text{h}^{-1}$. It uses zeolites and pressurized systems to adsorb N_2 and CO_2 from the air and can generate oxygen with a purity of ca. 95%. Its energy demand varies from 245 – $525 \text{ kWh}\cdot\text{ton}^{-1}$ depending on the use of vacuum (VPSA) to improve the absorption of the oxygen. Other emergent technologies for oxygen production have been used in practical applications, such as electrochemical water splitting, which generates high purity oxygen ($> 99.99\%$), but at high capital cost and with a high energy demand (ca. $1320 \text{ kWh}\cdot\text{ton}^{-1}$). [1,4,5]

A novel approach consists in the use of ion-conducting membranes that can be integrated in high temperature processes that require high purity oxygen, such as oxy-fuel combustion process for carbon capture and storage (CCS) and oxygen-blown gasification for conversion of carbon-based fuels (natural gas, biomass, coal) to syngas. [1,2]

By using pure O_2 instead of air, the efficiency of the combustion process increases since it is not necessary to heat up the inert N_2 , which after the process conforms ca. 60 vol.% of the product gases. In the case of CCS, CO_2 and H_2O are obtained, where H_2O can be easily condensed to obtain high purity CO_2 . In gasification, a mixture of H_2 , CO , CH_4 and

CO₂ (syngas or producer gas) is obtained. Syngas mixtures with proper H₂/CO ratio can be subsequently used in catalytic reactions to generate liquid fuels for power generation, as well as oxygenated organic compounds, such as methanol, acetic acid, dimethyl ether, among others. [1,6-8]

The state of the art industry-applied OTM is a pilot-scaled system developed by Praxair® to convert CH₄ into higher value fuels. The system's concept is shown in Fig. 1.1 and it is based on the arrangement of steam methane reforming (SMR), auto-thermal reforming (ATR) and air separation (ASU) in a single system working between 900 °C and 1050 °C and 27.5 bar. [9]

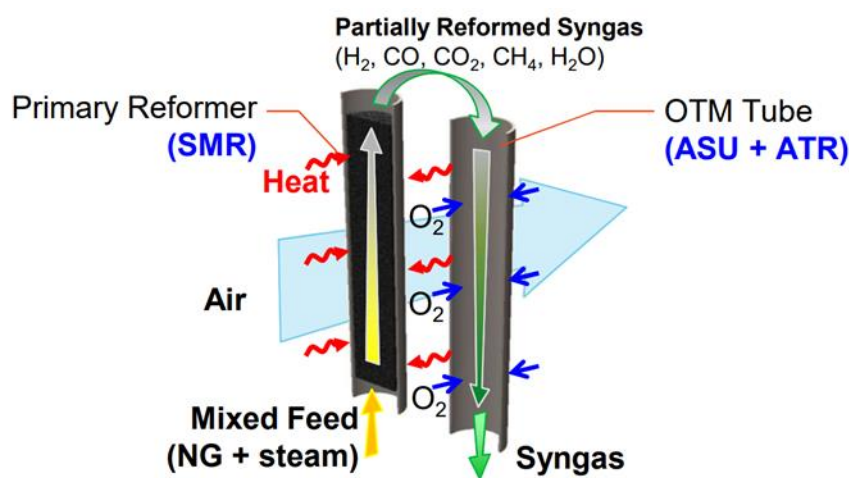


Fig. 1.1. OTM Combined Reformer for IGCC Power Systems concept developed by Praxair®. [9]

The combination of the units increases the thermal efficiency by combining endothermic (SMR) and exothermic (ATR) processes, as well as increasing the yield formation of H₂ and CO in the obtained syngas. The steam reforming step partially converts the CH₄ into synthesis gas, as well as converting heavier hydrocarbons into CH₄, H₂ and carbon oxides. This concept allows using other fuels, such as coal, as primary fuel. When working with CH₄, conversion rates >99 %, 70 vol.% H₂ content in the syngas and a H₂/CO ratio of 3.4 were obtained, demonstrating that integration of OTM in high temperature processes for oxyfuel and syngas applications is a feasible concept. [9-11]

1.2 Biomass gasification: an opportunity for oxygen transport membranes

The rise of global energy demand, expected to increase 1 % - 1.3 % each year up to 2040, and the efforts to meet international climate obligations, as well as national targets to become a fossil-fuel free and low emission society by 2050 are the main drivers to use low-carbon technologies for power generation. Biomass sources have been seen as CO₂-neutral sources that can help achieve these targets due to its potential refinement to obtained high-quality end-products, its flexibility regarding feedstock, and spread conversion technologies. Biomass is the major renewable energy source in Denmark. Although the largest share is for heating purposes and only about 10% is used for electricity generation, conversion of plants to consume solid biomass will increase biomass for the generation of power in the next years. [3,12-15]

Fig. 1.2 shows the use of solid biomass for energy production in Denmark, as well as its share among the renewable energy sources used in 2015. As it can be seen, only about 20% of the energy is produced from waste biomass (straw and biodegradable waste). Nevertheless, it has been estimated that by using the available waste- and straw-biomass in Denmark, ca. 32% of the Danish electricity demand could be covered. [16,17]

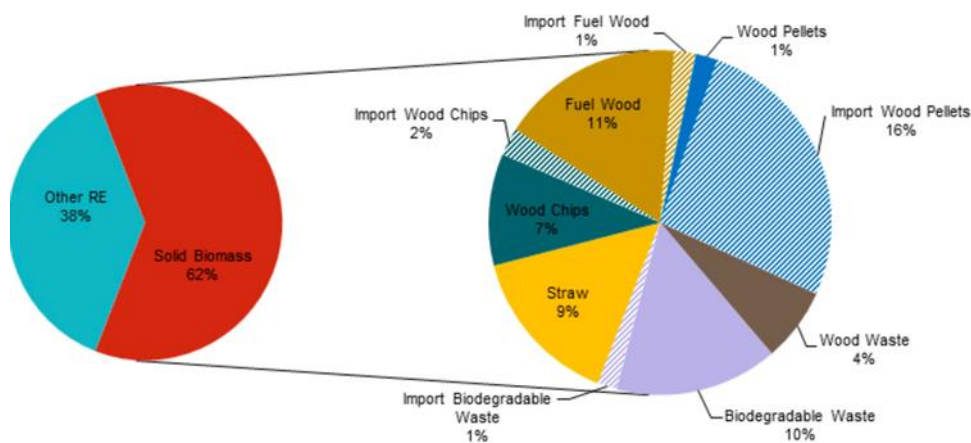


Fig. 1.2. Use of solid biomass in the Danish energy system in 2015. [16]

Biomass gasification is a promising thermochemical method where the reaction between the solid biomass and the gasification agent (air, oxygen, steam, steam-oxygen, etc.) produces syngas. Some gasifier concepts, such as the low temperature circulating fluidized bed (LT-CFB), are capable to treat marginal and residual biomass resources with high contents of low melting ash compounds such as straw, manure fibres, sewage

sludge, organic waste etc. By using waste biomass, the utilization of high-quality resources such as wood could be avoided, thus allowing their use for other purposes, such as construction material and carbon capture. [6,18]

The LT-CFB process is based on separate pyrolysis and gasification reactors with an inner stream of circulating particles that act as heat exchange media between the gasifier and the pyrolysis reactor. Temperature is kept below the melting point of the ashes, avoiding its agglomeration, subsequent fouling with alkalis (e.g. potassium) or corrosion (e.g. from chlorine) of the plant, as these compounds leave the process in solid form deposited on ash particles. The alkalis can thus be separated with the ash particles without including a raw gas cooler and potential related problems. By using this concept, old gas efficiencies of 87-93 % have been achieved on various feedstocks in the LT-CFB.

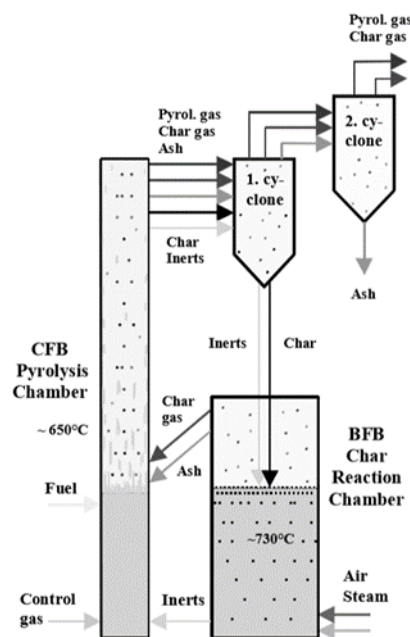


Fig. 1.3. Concept of LT-CFB gasifier. [17]

The initial application of the LT-CFB concept was the production of heat and power by using the syngas as fuel in an adjacent power plant with a boiler and a steam cycle. However, the primary limit in the applicability of low temperature gasification is the relatively high tar level in the producer gas. Among the different methods for tar-removal, thermal treatment by external heating or by partial combustion of the fuel gasses has been the most effective. [19-24]

As mentioned above, gasification is a thermochemical process between a fuel and the gasification agent, being the last one of important influence in the quality of the final syngas. Air gasification is widely used due to the simplicity of the technology and the abundance of air; however, syngas with a low calorific value $\sim 5 \text{ MJ}\cdot\text{m}^{-3}$ is obtained due to the dilution of the gases with N_2 . Steam gasification can produce syngas with a calorific value of $10 - 14 \text{ MJ}\cdot\text{m}^{-3}$ but the reaction is highly endothermic, decreasing the efficiency of the system because of the need of an external heat source. Other systems can produce syngas with even higher calorific values; however, the complexity of the system considerably increases both capital and operating costs. By using oxygen-blown gasification (pure O_2), the calorific value of the syngas can be increased to $7.7-9.5 \text{ MJ}\cdot\text{m}^{-3}$, enhancing the thermal efficiency of the system and keeping a relatively simple design. [6,8,18]

Thus, in-situ oxygen generation for LT-CFB gasification purposes is a niche where OTM can play an important role, as well as the partial oxidation treatment of the obtained tars to increase the conversion efficiency of the biomass by formation of additional H_2 , CH_4 and CO during the decomposition of tars. The application of OTMs for syngas production has been demonstrated and their integration in experimental coal gasifiers has been reported. Thus, development of materials with high oxygen permeability and resistant to the harsh reducing atmospheres is required to expand the application of OTM in this field. [9,25,26]

References.

- [1] Smart, S.; Diniz Da Costa, J.C. Oxygen transport membranes for power plant applications. Advanced membrane science and technology for sustainable energy and environmental applications, Chapter 9. Woodhead Publishing Limited, 2011. United Kingdom. DOI: 10.1533/9780857093790
- [2] Riaz, M.; Abdullah Butt, M. Oxygen Transport Membranes and their Role in CO_2 Capture and Syngas Production. Journal of Membrane Science and Technology — 2018, Volume 08, Issue 02. DOI: 10.4172/2155-9589.1000181

- [3] QYResearch Group. Global industrial oxygen market insights, forecast to 2025. November 2019. USA.
- [4] Banaszkiwicz, T.; Chorowski, M.; Gizicki, W. Comparative analysis of cryogenic and PTSA technologies for systems of oxygen production. *Aip Conference Proceedings* — 2014, Volume 1573, Issue 1, pp. 1373-1378. DOI: 10.1063/1.4860866
- [5] COSIA, GHG Working Group. Gas Technology Institute. Emerging and existing oxygen production technology scan and evaluation. April 2018, USA.
- [6] Puig-Arnavat, M.; Soprani, S.; Søgaaard, M.; Engelbrecht, K.; Ahrenfeldt, J.; Henriksen, U.B.; Hendriksen, P.V. Integration of mixed conducting membranes in an oxygen–steam biomass gasification process. *Rsc Advances* — 2013, Volume 3, Issue 43, pp. 20843-20854. 10.1039/c3ra44509g
- [7] Stadler, H.; Beggel, F.; Habermehl, M.; Persigehl, B.; Kneer, R.; Modigell, M.; Jeschke, P. Oxyfuel coal combustion by efficient integration of oxygen transport membranes. *International Journal of Greenhouse Gas Control* — 2011, Volume 5, Issue 1, pp. 7-15. 10.1016/j.ijggc.2010.03.004
- [8] Bathia, S.C. Biomass gasification. *Advanced renewable energy systems – 2014*, pp. 473-489. Elsevier.
- [9] OTM combined reformer for IGCC power systems. DOE/NETL Gasification systems and coal & coal-biomass to liquids project. Praxair. April 2018. USA.
- [10] Nataraj, S.; Moore, R.B.; Russek, S.L. Production of synthesis gas by mixed conducting membranes. Air Products and Chemicals, Inc. US Patent 6048472. April 2000. US6048472A
- [11] Speight, J.G. Gasification processes for syngas and hydrogen production. *Gasification for Synthetic Fuel Production: Fundamentals, Processes and Applications*. Elsevier — 2015, pp. 119-146. 10.1016/B978-0-85709-802-3.00006-0

- [12] World Energy Outlook 2019 Executive Summary. International Energy Agency. November 2019.
- [13] Kirkels, A.F. Discursive shifts in energy from biomass: A 30 year European overview. *Renewable and Sustainable Energy Reviews* — 2012, Volume 16, Issue 6, pp. 4105-4115.
- [14] System Plan 2018 – Electricity and gas in Denmark. Energinet Doc. no. 18/04372-17. November 2018.
- [15] Renewable Energy Outlook 2019 – Renewable energy Perspectives to 2035. Danish Energy. February 2019.
- [16] Biomass. Danish Energy Agency. Danish Ministry of Climate, Energy and Utilities. <https://ens.dk/en/our-responsibilities/bioenergy/solid-biomass>
- [17] Nielsen, R.G.; Stoholm, P.; Nielsen, M.B.; Krogh, J.; Nørholm, N.; Antonsen, S.; Sander, B.; Henriksen, U.B.; Qvale, E.B. The LT-CFB gasifier: First test results from the 500 kW test plant – 2005. *Biomass for energy, industry and climate*.
- [18] Ruan, R.; Zhang, Y.; Chen, P.; Liu, S.; Fan, L.; Zhou, N.; Ding, K.; Peng, P.; Addy, M.; Cheng, Y.; Anderson, E.; Wang, Y.; Liu, Y.; Lei, H.; Li, B. Biofuels: Introduction. *Biofuels. Alternative feedstocks and conversion processes for the production of liquid and gaseous biofuels. Biomass, Biofuels, Biochemicals 2019*, Pages 3-43. DOI: 10.1016/B978-0-12-816856-1.00001-4
- [19] Ahrenfeldt, J.; Thomsen, T.; Henriksen, U.B., Clausen, L.R. Biomass gasification cogeneration – A review of state of the art technology and near future perspectives. *Applied Thermal Engineering* 2013, 50(2), 1407- 1417. 10.1016/j.applthermaleng.2011.12.040
- [20] Zwart, R.; van der Heijden, S.; Emmen, R.; Dall Bentzen, J.; Ahrenfeldt, J.; Stoholm, P.; Krogh, J. (2010). Tar removal from low-temperature gasifiers. Petten: Energy Research Centre of the Netherlands (ECN). ECN-E-10- 008.

- [21] Sansaniwal, S.K.; Rosen, M.A.; Tyagi, S.K. Global challenges in the sustainable development of biomass gasification: An overview. *Renew Sustain Energy Rev* 2017; 80:23–43. 10.1016/j.rser.2017.05.215
- [22] Ruiz JA, Juárez MC, Morales MP, Muñoz P, Mendivil MA. Biomass gasification for electricity generation: Review of current technology barriers. *Renew Sustain Energy Rev* 2013;18:174–83. 10.1016/j.rser.2012.10.021
- [23] Milne, T.A.; Evans, R.J.; Abatzoglou, N. Biomass Gasifier “Tars”: Their Nature, Formation, and Conversion. National Renewable Energy Laboratory. November 1998, NREL/TP-570-25357. nrel.gov/docs/fy99osti/25357.pdf
- [24] Fjellerup, J.; Ahrenfeldt, J.; Henriksen, U.; Gøbel, B. (2005). Formation, Decomposition and Cracking of Biomass Tars in Gasification. Kgs.Lyngby: Technical University of Denmark. Department of Mechanical Engineering. orbit.dtu.dk/pyrotar2.pdf
- [25] Bouwmeester, HJM. Dense ceramic membranes for methane conversion. *Catalysis Today*. Vol 82. (2003) 141-150. 10.1016/s0920-5861(03)00222-0
- [26] Gupta, S; Adams, J.J.; Wilson, J.R.; Eddings, E.G.; Mahapatra, M.K.; Singh, P. Performance and post-test characterization of an OTM system in an experimental coal gasifier. *Appl Energy*. 2016;165:72-80. 10.1016/j.apenergy.2015.12.077

Chapter 2. Objectives and content of the thesis

This thesis deals with the development and characterization of a multilayer asymmetric tubular oxygen transport membrane (OTM) for integration in gasification systems. The work in this thesis includes the identification of adequate and stable membrane materials, their processing into tubular multi-layer components and the investigation of the performance of the materials and membrane structures. This implicates the exposition of the membrane's components to high temperatures and reducing environments.

- 1) **Selection of materials.** Two main inherent requirements need to be fulfilled for a dense ceramic OTM to enable the transport of oxygen ions through the crystal lattice: working temperature above 700 °C and, in the case of gasification systems, operation at oxygen partial pressures as low as 10^{-20} atm. Thus, highly stable ionic and electronic conductors are necessary for the active dense membrane. In addition, the matching of thermomechanical properties and chemical stability of all the membrane components is required to allow their integration into a system – including porous support, porous activation layers, dense active membrane and catalyst. After literature review and initial compatibility tests, two dual-phase composites were selected to be studied as materials for the active membrane: $(\text{Sc}_2\text{O}_3)_{0.10}(\text{Y}_2\text{O}_3)_{0.01}(\text{ZrO}_2)_{0.89} - \text{LaCr}_{0.85}\text{Cu}_{0.10}\text{Ni}_{0.05}\text{O}_{3-\delta}$ (Section 5.2 and Section 5.5) and $\text{Ce}_{0.9}\text{Gd}_{0.1}\text{O}_{1.95} - \text{Y}_{0.8}\text{Ca}_{0.2}\text{Cr}_{0.8}\text{Co}_{0.2}\text{O}_{3-\delta}$ (Section 5.3 and Section 5.4). The tubular porous supports for all the experiments were based on $(\text{Y}_2\text{O}_3)_{0.03}(\text{ZrO}_2)_{0.97}$ due to the high mechanical strength and chemical stability of this material. Fe_2O_3 was used as sintering aid in the different components of the membrane and the impact on the sintering behaviour was analysed. (Section 5.5).
- 2) **Development of tubular asymmetric membranes.** Manufacturing of the membranes was based on two main processing techniques: thermoplastic extrusion for the tubular porous supports and dip-coating for the deposition of the inner and outer porous activation layers and the dense active membrane. During the manufacturing, several chemical and structural issues were faced – e.g. vaporization of species, secondary phase formation, fractures, insufficient densification of the

active membrane layer – making the manufacturing of the asymmetric membranes challenging. The thesis includes the identification and solution of these challenges.

- 3) **Characterising and testing of tubular OTMs.** In order to assess the performance of the developed asymmetric oxygen transport membranes, short-term oxygen flux measurements, with a duration between 2 h to 20 h, were carried out in ideal relevant conditions N_2/Air , CO_2/Air , CH_4/Air , $5\%\text{H}_2\text{-N}_2/\text{Air}$ and H_2/Air between 800 °C and 950 °C (Section 5.5). Additionally, a unit for partial oxidation of tars (section 5.1), which was attached to a low temperature circulating fluidized bed gasifier (DTU Kemiteknik), was used to test the $\text{Ce}_{0.9}\text{Gd}_{0.1}\text{O}_{1.95}$ – $\text{La}_{0.6}\text{Sr}_{0.4}\text{FeO}_{3.8}$ dual-phase composite membranes previously developed by DTU Energy (ForskEL project 12202 “Ceramic Membranes for Oxy-Fired Biomass Gasification” and The Danish Council for Strategic Research project "Enefox – Energy efficient oxygen production for a sustainable energy system" DSF, 0603-00456B, 11-116387).

The work in this thesis is divided in six chapters, which are briefly described below,

Chapter 1 provides a general introduction and an overview to oxygen transport membranes (OTM) and its use in industrial and gasification systems. **Chapter 2** establishes the objectives of this thesis and its content. **Chapter 3** summarizes the basic concepts and working principles of dense ceramic oxygen transport membranes (Section 3.1), transport mechanisms of the oxygen across the membrane (Section 3.2) and a summary of planar and tubular membrane geometries, as well as their limitations and advantages (Section 3.3).

Chapter 4 describes the processing methods used to fabricate the tubular membranes – extrusion and dip-coating –, as well as the features of sintering of tubular geometries (Section 4.1). Microstructural and thermo-mechanical characterization techniques used in this work are also summarized (Section 4.2), including the experimental set up used for the oxygen permeability characterization, along with the calculation sequence to obtain the oxygen flux in operational conditions relevant for syngas applications (Section 4.3).

Chapter 5 summarizes the results and discussions of the experiments developed in this thesis. It tackles the selection of materials, as well as the development, characterization and testing of oxygen transport membranes. The chapter is based on 6 manuscripts – 1 of them already published and 5 to be submitted. Section 5.1 details the manuscript “Partial oxidation of biomass gasification tars with oxygen transport membranes”, in which $\text{Ce}_{0.9}\text{Gd}_{0.1}\text{O}_{1.95}$ – $\text{La}_{0.6}\text{Sr}_{0.4}\text{FeO}_{3-\delta}$ oxygen transport membranes were mounted in a specially designed rig to partially oxidize the tars produced in a low temperature circulating fluidized bed gasifier. The low performance of these membranes resulted in the conclusion for this thesis that more stable materials for OTM in biomass gasification applications needed to be developed first.

Section 5.2 contains the paper “Exploring the Processing of Tubular Chromite- and Zirconia-Based Oxygen Transport Membranes” published in *Ceramics* (2018). It describes the initial selected membrane architecture based on $(\text{Sc}_2\text{O}_3)_{0.10}(\text{Y}_2\text{O}_3)_{0.01}(\text{ZrO}_2)_{0.89}$ and $\text{LaCr}_{0.85}\text{Cu}_{0.10}\text{Ni}_{0.05}\text{O}_{3-\delta}$ as materials for dual-phase membranes on $(\text{Y}_2\text{O}_3)_{0.03}(\text{ZrO}_2)_{0.97}$ porous tubular supports. Several severe challenges were faced during the manufacturing of these tubular membranes, such as high processing temperatures, active membrane fractures and formation of lanthanum zirconate. This led to the conclusion that it was not feasible to develop this type of membrane architecture in the frame of this thesis.

Alternatively, a dual-phase composite for oxygen transport membranes (Section 5.3) was fabricated in order to avoid fabrication issues described for the $(\text{Sc}_2\text{O}_3)_{0.10}(\text{Y}_2\text{O}_3)_{0.01}(\text{ZrO}_2)_{0.89}$ and $\text{LaCr}_{0.85}\text{Cu}_{0.10}\text{Ni}_{0.05}\text{O}_{3-\delta}$ membranes, such as the formation of insulating phases and high processing temperatures. This study is presented in the manuscript “ $\text{Y}_{0.8}\text{Ca}_{0.2}\text{Cr}_{0.8}\text{Co}_{0.2}\text{O}_{3-\delta}$ – $\text{Ce}_{0.9}\text{Gd}_{0.1}\text{O}_{1.95}$ based dual phase membranes for O_2 separation for oxyfuel and syngas applications”. Section 5.4 describes the processing methodology to attempt fabricating dense membranes using this alternative composite on $(\text{Y}_2\text{O}_3)_{0.03}(\text{ZrO}_2)_{0.97}$ porous tubular supports. Although the manufacturing of thin asymmetric membranes was unsuccessful, the obtained results led to ideas to be applied on ZrO_2 -based composites.

An alternative based on $(\text{Sc}_2\text{O}_3)_{0.10}(\text{Y}_2\text{O}_3)_{0.01}(\text{ZrO}_2)_{0.89}$ – $\text{LaCr}_{0.85}\text{Cu}_{0.10}\text{Ni}_{0.05}\text{O}_{3-\delta}$ membranes is given in Section 5.5. It contains the article “Effective method to

manufacture stable $(\text{Sc}_2\text{O}_3)_{0.10}(\text{Y}_2\text{O}_3)_{0.01}(\text{ZrO}_2)_{0.89} - \text{LaCr}_{0.85}\text{Cu}_{0.10}\text{Ni}_{0.05}\text{O}_{3-\delta}$ asymmetric tubular ceramic oxygen transport membranes” where the use of Fe_2O_3 as sintering aid to match the thermomechanical properties of the membrane’s components is studied and a route to manufacture gas tight membranes is described.

Section 5.6 shows a brief communication where the successful manufacturing of flexible dense $(\text{Sc}_2\text{O}_3)_{0.10}(\text{Y}_2\text{O}_3)_{0.01}(\text{ZrO}_2)_{0.89}$ and $\text{Ce}_{0.9}\text{Gd}_{0.1}\text{O}_{1.95}$ capillary tubes with a 3 mm diameter using thermoplastic extrusion as shaping technique is described. The use of capillaries could be an option in the fabrication of self-supported dual-phase composites OTM in the future.

Chapter 6 concludes the thesis work and gives an outlook of possible improvements in the experimental methodologies, as well as an outlook on future developments on dual phase membrane architectures, similar to those developed in this thesis.

Chapter 3. Working principles

This chapter describes the working principles of the oxygen transport membranes (OTMs), as well as the three main limiting mechanisms that affect the oxygen transport. Differences and limitations between mixed ionic-electronic conductors and dual phase composites as materials for OTMs are described, including planar and tubular OTM geometries and their fabrication. References from literature regarding experimental oxygen fluxes of chromite-based composites, the main materials used in this thesis, are also included in this section.

3.1 Working principle of oxygen transport membranes.

An oxygen transport membrane (OTM) is a gas-tight ceramic layer permeable to oxygen and electrons and tight to other species, allowing an oxygen selectivity of 100%. As seen in Fig. 3.1. Oxygen ions are mainly transported via oxygen vacancies in the crystal lattice. The total oxygen flux that crosses the membrane is determined by both the bulk permeability and the reaction rate of molecular oxygen at the membrane/gas-phase interface, where the splitting and recombination of oxygen molecules takes part, according to Eq. 3.1. [1,2]



The difference in partial oxygen pressure, p_{O_2} , between the feed (high p_{O_2} side, usually air) and the permeate side (low p_{O_2} side, also known as sweep side) of the membrane, provides the driving force for the process. The total driving force, μ_{O_2} , is distributed between the central bulk and the interfacial zones, as depicted in Fig. 3.2. In steady state, when oxygen flux is governed by bulk oxygen diffusion, the Wagner equation (Eq. 3.2) allows the calculation of the oxygen transport across the membrane. [1,2]

$$J_{O_2} = \frac{1}{16F^2L} \int_{\mu'_{O_2}}^{\mu''_{O_2}} t_{ion} t_{el} \sigma_{tot} d\mu_{O_2} \quad (\text{Eq. 3.2})$$

Where J_{O_2} is the oxygen flux [$\text{mol}\cdot\text{m}^{-2}\cdot\text{s}^{-1}$], F is Faraday's constant, L is the thickness of the oxygen membrane, t_{el} and t_{ion} are fractions of the total conductivity of the material. The limits of the integral are the chemical potentials of molecular oxygen, μ_{O_2} , at the gas phase boundaries. [3,4]

By analysing Eq. 3.2, it is deduced that the thinner the membrane, the higher the oxygen flux through the membrane. Thus, using 10-30 μm thin films would allow increasing the oxygen production rate through the membrane without compromising its gas tightness to other species. Nevertheless, in order to provide mechanical stability and strength, membranes are usually deposited on porous supports. This architecture is known as asymmetric oxygen transport membrane. It has been widely used in experimental and practical applications and it is also the target architecture pursued in this work. [5]

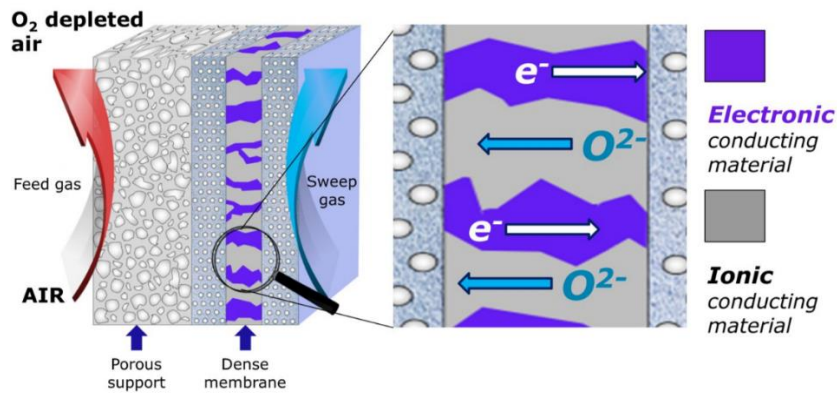


Fig. 3.1. Schematics of architecture and operations of an asymmetric dual-phase oxygen transport membrane. [6]

3.2 Oxygen transport mechanisms.

The transport of the oxygen through an OTM is carried out by oxygen vacancies in the crystal structure when a $p\text{O}_2$ gradient is the main driver of this transport. Five steps are involved in the transport of oxygen. An schematic of the cross section of a membrane and the equivalent resistances for the different transport mechanisms are depicted in Fig. 3.2. [7]

Zones 1, 2 and 6 represent the concentration limitations of the gas phases in the feed side, the porous support and the permeate side, which are processes related to gas diffusion. Zone 3 represents the surface exchange reaction at the feed side where dissociation of oxygen, electron transfer, reduction to oxygen ions and their incorporation into the active membrane layer at the interface to the catalytic active layer of the membrane take place. Zone 5 illustrates the oxygen associating reaction on the permeate side of the membrane, where oxygen ions recombine to form O_2 molecules which are then desorbed from the membrane surface.

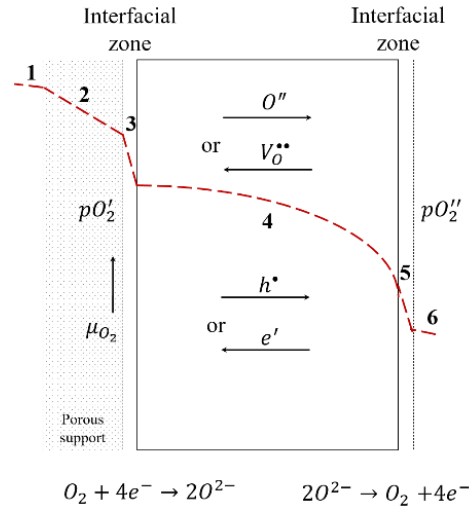


Fig. 3.2. Schematic of the mechanism of O_2 permeation through an oxygen membrane. [3,5,7]

Both processes 3 and 5, are controlled by the kinetics of the surface dissociation/association reaction. Zone 4 represent the bulk transport of the oxygen ions into the dense selective membrane. Oxygen ions diffuse through the vacancies in the crystal lattices driven by the pO_2 gradient along the membrane. Electrons are transported in opposite direction to keep the electric neutrality. The oxygen flux in Zone 4 is controlled by the membrane's intrinsic permeability and thickness. [6-8]

From the previous description, three main limiting factors for the oxygen transport can be defined: gas diffusion, bulk resistance and surface exchange reactions. In the following sections, the description of each transport limitation is elaborated. The description is based on mixed ionic-electronic conducting materials due to its simplicity; however, similar mechanisms would be present in dual-phase composites.

3.2.1 Bulk mechanism limitation.

The basic concept of bulk resistance is related to the fact that the lattice diffusion of the oxygen ions or the transport of electronic charges through the bulk oxide determines the rate of oxygen permeation. Bulk diffusion considers three regimes that can be limiting factors for the oxygen flux: oxygen vacancies, electrons and electron holes. [7,8] The Wagner equation that describes the bulk transport is given by:

$$J_{O_2} = \frac{RT}{16F^2L} \int_{\ln P'_{O_2}}^{\ln P''_{O_2}} \frac{\sigma_{el}\sigma_{ion}}{\sigma_{el} + \sigma_{ion}} d \ln P_{O_2} \quad (\text{Eq. 3.3})$$

Where J_{O_2} is the oxygen flux [$\text{mol}\cdot\text{m}^{-2}\cdot\text{s}^{-1}$], R the gas constant, T the temperature, F is Faraday's constant, L is the thickness of the oxygen membrane, σ_{el} and σ_{ion} are the electronic and the ionic conductivities of the material. Limits P_{O_2}' and P_{O_2}'' are the oxygen partial pressures at the high and low pressure sides, respectively. The relation $\frac{\sigma_{el}\sigma_{ion}}{\sigma_{el}+\sigma_{ion}}$ is known as ambipolar conductivity. [8]

Eq. 3.3 indicates that the bulk diffusion is strongly temperature activated, therefore operating at high temperatures would increase the oxygen flux. Additionally both ionic and electronic conductivity of the membrane material determine the oxygen flux rate through the membrane.

These properties are intrinsic of the used materials. The maximum ambipolar conductivity is obtained when the ionic and electronic conductivities are the same; however, in most of the perovskite-based single or dual-phase materials, the electronic conductivity is one order of magnitude higher than the ion conductivity, $\sigma_{el} \gg \sigma_{ion}$. [9] Thus, it is possible to simplify Eq. 3.3 to:

$$J_{O_2} = \frac{RT}{16F^2L} \int_{\ln P_{O_2}''}^{\ln P_{O_2}' } \sigma_{ion} d \ln P_{O_2} \quad (\text{Eq. 3.4})$$

3.2.2 Surface exchange reactions.

The Wagner equation is no longer applicable when oxygen is controlled by the surface exchange limitations. The formation of oxygen ions and oxygen molecules on the surface of the membrane is determined by the catalytic activity of the membrane material to carry out the dissociation and association reactions. Exchange reactions may occur in different steps according to the side where they take place; however, adsorption, dissociation, association charge transfer and diffusion of intermediate species may take place and any of these reactions might be rate determining. Due to the complexity of the reactions, it is difficult to define a general expression that describes the surface exchange reaction. In addition, factors as the used sweep gas and competitiveness of species may affect the exchange rates. [8] The exchange between oxygen in the gas phase and the oxygen ions in the crystal is described by Eq. 3.5:

$$J_{O_2} = -k \cdot p_{O_2}^n \left(\frac{\Delta\mu}{R_g T} \right) \quad (\text{Eq. 3.5})$$

Where k is the rate constant for surface oxygen exchange ($\text{mol}_{\text{O}_2} \cdot \text{m}^{-2} \cdot \text{s}^{-1}$), p_{O_2} is the oxygen partial pressure (Pa), n is the exponent for oxygen partial pressure dependence, $\Delta\mu$ is the oxygen chemical potential drop across the interface ($\text{J} \cdot \text{mol}^{-1}$). [10]

As pointed out above, the thickness of the membrane has an important influence on the oxygen flux when it is decreased. However, there is a critical length of the membrane where the surface exchange reactions and the bulk are equivalent. Decreasing the thickness of the membrane below this point will not increase the oxygen flux since this will be limited by the surface exchange reactions. [7,8] The equivalent and transition point from predominant bulk diffusion limitation to surface exchange limitation is called characteristic thickness, which is defined by:

$$L_c = \frac{D_s}{k_s} \quad (\text{Eq. 3.6})$$

Where D_s is the self-diffusion coefficient of oxygen and k_s the surface exchange coefficient. When the thickness of the membrane is smaller than L_c , the limiting mechanism will be related to surface exchange. Should the thickness of the membrane be larger than L_c , the limiting factor will be bulk diffusion. Considering the L_c , the oxygen flux can be described as: [6,8]

$$J_{\text{O}_2} = - \frac{1}{1 + \left(\frac{2L_c}{L}\right)} \cdot \frac{t_{\text{el}} t_{\text{ion}} \sigma_{\text{total}}}{16F^2} \cdot \frac{\Delta\mu_{\text{O}_2}^{\text{total}}}{L} \quad (\text{Eq. 3.7})$$

By comparing Eq. 3.2 and Eq.3.7 it can be noticed that the oxygen flux in 3.2 is reduced by the term $\left(1 + \frac{2L_c}{L}\right)^{-1}$, in the case of surface exchange limitations. The surface exchange rate will be different for different gradients of oxygen partial pressure along the membrane, and the interface with lower performance will determine the overall exchange behaviour. [8]

3.2.3 Gas diffusion.

The contribution of gas diffusion is limited by the transport of gases to the physical reaction interfaces on the membrane. This contribution can be substantial if the porous support or porous layers in contact with the membrane have features that can negatively affect the flow of gases, such as large thickness and high tortuosity, lack of porosity or

low percolation of the porous phase. However, gas transport in porous media is very complex to determine due to interactions of the gas with the pore structure, such as Knudsen diffusion, surface diffusion and viscous flow. [5,11].

When referred to oxygen flux, a simplified way to describe the diffusion of gas through the porous support is given by:

$$J_{O_2} = \frac{\left(\frac{1}{D_k} + \frac{1-x_{O_2s}}{D_{1m}}\right)^{-1} (C_{O_2s} - C'_{O_2s})}{t\left(\frac{-e}{\tau}\right)} \quad (\text{Eq. 3.8})$$

Where x_{O_2s} is the oxygen mole fraction, D_{1m} is the binary diffusion coefficient, which considers the diffusivity of the oxygen in the stream of the sweep side, C_{O_2s} and C'_{O_2s} are the oxygen concentrations at the two sides of the support, t is the support thickness, e the volume void fraction. The Knudsen diffusion coefficient, D_k is given by the expression:

$$D_k = \frac{2}{3} r_{pore} \sqrt{\frac{8RT}{\pi M_{O_2}}} \quad (\text{Eq. 3.9})$$

Where r_{pore} is the average radius of the support pores, R the constant of gases, T the temperature and M_{O_2} is the molar weight of O_2 .

Beneath the gas diffusion layer, a stagnant gas layer is formed around the reaction sites on the membrane's surface. The gas transport through this layer affects the concentration of the gases around the active zones and thereby the performance of the membrane. The oxygen flux through the stagnant gas layer is proportional to the concentration gradient through the layer according to: [12]

$$J_{O_2} = -D_{O_2-N_2} \frac{\Delta C_{O_2}}{\Delta x} \quad (\text{Eq. 3.10})$$

Where Δx is the thickness of the stagnant layer, $D_{O_2-N_2}$ is the binary diffusion coefficient of oxygen in nitrogen, and ΔC_{O_2} is the concentration difference along the layer. If fast diffusion of oxygen in air is observed, negligible loss of oxygen activity will occur. This can be achieved by increasing the flow rates of the gases, which would reduce the thickness of the boundary layer; e.g. by increasing the sweep gas flow to remove the oxygen produced in the permeate side of the membrane.

3.3 Membrane geometry

The selection of the oxygen transport membrane geometry is another important factor to be considered to ensure adequate membrane performance as part of the membrane integration into a module.

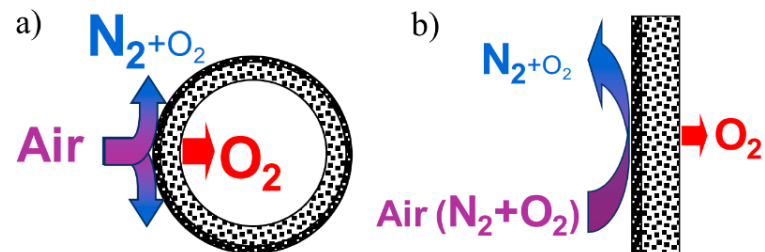


Fig. 3.3. Schematics of asymmetric oxygen membranes in a) tubular and b) planar configurations. [13]

Planar and tubular are the two main geometries used in ceramic oxygen membranes; however, an optimum configuration needs to be determined depending on membrane materials, microstructure, dimensions and exact integration of the membrane itself. Although each kind of geometry has specific advantages and shortcomings, it is aimed that the geometry and the module configuration of the membranes allow:

- High packing density (membrane surface per unit volume in modules)
- Low pressure drop
- Uniform velocity distribution (no “dead” regions)
- Low cost per unit membrane area.

Planar geometry has been widely used in solid oxide cells technology. Planar cells are fabricated on large scale using a tape-casting technique and applying the active membrane layer by tape-casting, dip-coating, spray coating or spin coating. One of the main advantages of planar systems is the easy stacking of the membranes to increase the membrane area, obtaining packing densities between 300–500 m²·m⁻³. Nevertheless, in this configuration pressure drops, a critical behaviour under thermal gradients may happen, and bending moments can lead to early failures. In addition, the large sealing areas are difficult to seal at high pressures. [13-17]

Tubular oxygen transport membranes are usually based on porous supports produced by extrusion or isostatic pressing. The active thin membrane is deposited using dip-coating

or spray-coating. Since these are widely known shaping techniques, low costs of production and operation are expected. Tubular geometries have a smaller sealing area per unit area of membrane compared to planar geometry and a packing density of approximately $300\text{--}1000\text{ m}^2\cdot\text{m}^{-3}$. During operation, they equally distribute the thermal gradients and, in a similar way, they have symmetrical distribution of the stresses when exposed to differential pressures, which set the ceramic under a state of compression. Creep buckling of tubes can occur if the support is not sufficiently robust to tolerate the combination of high temperature and pressure. Typically, the tubes have considerable thicknesses and large diameters, with typical values between 10-25 mm. [14,16-18]

To maximize the surface area per unit volume, the tube diameter should be reduced, which would provide the most cost-effective approach. In this context, hollow fibres and capillaries have attracted some attention due to a high packing density in the range of $6000\text{--}15000\text{ m}^2\cdot\text{m}^{-3}$. Hollow fibres with a wall thickness of 0.2 to 0.5 mm are usually produced by phase-inversion spinning/sintering techniques, and capillaries with a wall thickness of down to 0.5 mm can be produced by extrusion. This architecture provides a much larger gas/membrane interface; however, the main disadvantages of this configuration are the complex sealing, the pressure drop in small diameters, Euler buckling and the low mechanical strength of the materials at the operation conditions required to allow ion-conductivity, so the length of the tube must be kept relatively short. [14,16,17,19]

3.4 Materials for oxygen transport membranes.

From equations Eq. 3.2 – Eq. 3.10, it is clear that different factors need to be taken into account when designing an oxygen membrane. One of these factors is the selection of suitable materials with high ionic/electronic conductivities and resistant to the operation conditions.

Oxygen membrane materials for high temperatures can be separated in two main groups: single-phase mixed ion-electronic conductors and dual-phase composites that combine an ion-conducting ceramic with an electronic conductor. The main characteristics and drawbacks of the materials and their use in the two membrane concepts are described in the following chapters.

3.4.1 Mixed ion-electronic conductors.

Mixed ionic-electronic conductors (MIEC) are materials that can transport both ions and electronic charge carriers in a single phase. They have been studied for oxygen separation applications since the early 1970's. [20,21] MIEC materials can be classified in two groups according to their crystal structure: Ruddlesden-Popper phases ($A_{n+1}B_nO_{3n+1}$) and perovskites (ABO_3). [22,23] Most of mixed conductors with potential technological applications have the perovskite structure, which is able to accept cations and accommodate them in its crystal structure. When substituting the cation species, non-stoichiometry of the crystal structure occurs and leads to formation of oxygen vacancies and lattice disorder. This allows the relatively rapid and sustainable transport of oxygen ions under the appropriate conditions. [24-27]

Perovskites, ABO_3 .

The perovskite structure is defined by the formula ABO_3 , where A and B are cations with different sizes and radius of $A > B$. A-site cations are usually ions with low-charge of alkaline, alkaline-earth and rare-earth metals ($A^{2+}B^{4+}O_3$, $A^{1+}B^{5+}O_3$ or $A^{3+}B^{3+}O_3$). The B-site cations are usually transition metal ions with medium-size. The ideal cubic ABO_3 structure is illustrated in Fig. 3.4. The B-site cation is surrounded by an octahedron of oxygen ions, and the A-site cation is occupying a 12-fold coordination site formed in the middle of the cuboctahedron. [28,29]

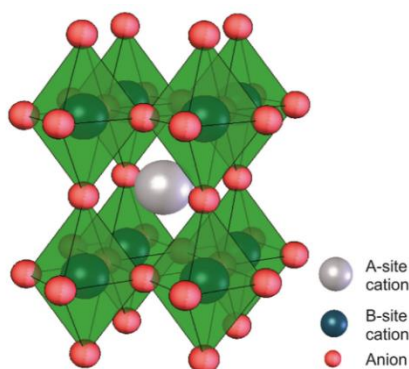


Fig. 3.4. Ideal perovskite crystal structure, ABO_3 . [28]

As mentioned above, perovskites can be easily doped by substituting A-site and B-site cations, which would modify their properties for a wide-range of applications as mixed ionic-electronic conductors. Ion-conductivity in a perovskite can be increased by

substituting lower valence cations in both A-site and B-site, since charge deficiency from the substitution creates oxide-ions vacancies. On the other hand, by adding aliovalent cations, the electronic conductivity can be increased, since the B-cation is oxidized, forming an electron hole. [6,30]

Typical perovskites with MIEC properties have Ba, Sr, La or Ca cations on the A-site, and Fe, Cr, Co, Ga cations on the B-site. The mixed conductivity and the stability of the perovskite structure will vary according to the composition and the type of doping. In this context, for the MIEC perovskite structure $\text{Ba}_{0.5}\text{Sr}_{0.5}\text{Co}_{0.8}\text{Fe}_{0.2}\text{O}_{3-\delta}$, $12.2 \text{ Nml}\cdot\text{min}^{-1}\cdot\text{cm}^{-2}$ was reported during operation at $1000 \text{ }^\circ\text{C}$ in an Air/Ar gradient. [31]

3.4.2 Fluorite-perovskite dual-phase composites.

Mixed ionic-electronic conductor materials show high performance as oxygen membranes but the stability of the perovskite is limited in reducing conditions. The reason is that these high performance MIEC perovskites usually have a limited pO_2 stability range, typically decomposing at pO_2 values below 10^{-12} atm , which limits the application of these materials under reducing conditions. [32] However, ionic-electronic conductors are not limited to single phase materials. For materials that show a good ionic but limited electronic conductivity, it is possible to add a second phase of a compatible electronic conducting material, obtaining a dual-phase composite. Fig. 3.5 shows the concept of a MIEC and a dual-phase composite, as well as the path for the charge carriers.

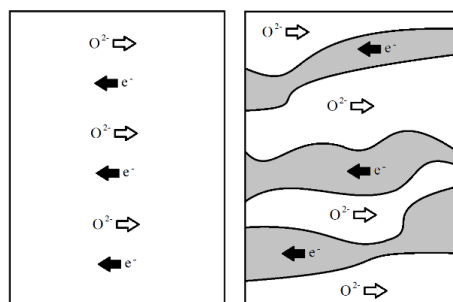


Fig. 3.5. Schematics of a single-phase mixed oxygen ion/electronic conducting material, MIEC (left) and a dual phase membrane of an oxygen ion and electron conducting phase (right). [33]

Materials are considered purely ionic conductors if the conduction is predominated by ions rather than by electrons and holes. Some fluorite type structures are among the highest ion-conducting materials, such as $(\text{Y}_2\text{O}_3)_{0.08}(\text{ZrO}_2)_{0.92}$ and $\text{Ce}_{0.9}\text{Gd}_{0.1}\text{O}_{2-\delta}$, which have been successfully used in high-temperature electrochemical devices. [6,7]

By using dual-phase composites based on fluorite-structure components with high ionic-conductivity and high-electronic conducting perovskites, it is possible to obtain an ionic-electronic conducting material that is stable under reducing conditions and high temperatures. However, it is necessary to select compatible materials for the manufacturing and operation conditions of the dual-phase oxygen membrane.

Fluorites, AO_2 .

Ideal fluorite structures are represented by AO_2 , where A refers to tetravalent cations, which occupy the eight tetrahedral interstitial sites, and O_2 represents the oxygen ions, which occupy the regular sites of a faced centered cubic crystal structure (Fig. 3.6). Fluorite-structured oxides based on ZrO_2 and CeO_2 have been widely studied as ionic conductors, due to their highly stable conductivity. [34,35] Following, some of the main features of ZrO_2 and CeO_2 are described, as well as the main doped-materials used as ion-conducting materials.

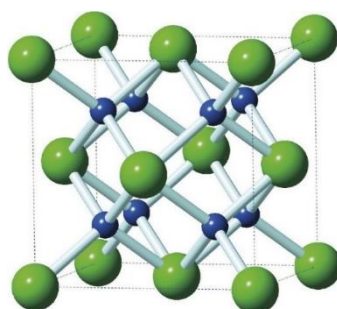
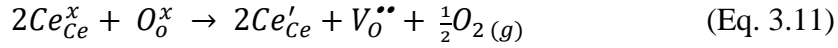


Fig. 3.6. Ideal cubic fluorite structure, AO_2 . [36]

Cerium Oxide, CeO_2 .

Cerium oxide (CeO_2), usually called ceria, is a highly stable, nontoxic, refractory ceramic material with a melting point of 2600°C . It does not undergo any crystallographic transition from room temperature to its melting point in air. Although the mechanical properties of pure ceria ceramics are usually rather poor, its ionic conductivity is outstanding. This can be increased by doping it with various rare earth elements, as Gadolinium (Gd^{3+}), whereby the negative charge of the acceptor with respect to the host cation (Ce^{4+}) is accommodated by the formation of oxygen vacancies, in order to keep the charge compensation. For each mole of Gd^{3+} incorporated into the ceria lattice, the charge neutrality is kept by forming $\frac{1}{2}$ mol of oxygen vacancies. [37-39]



The ionic conductivity occurs by the movement of oxygen ions through the crystal lattice as a result of thermally activated hopping of the oxygen ions moving from a crystal lattice site to a vacancy in another crystal lattice site. The ionic conductivity is consequently strongly temperature dependent. The highest ion-conductivity of CeO₂ is obtained when doping with 10-20 % Gd³⁺. Values of 0.22 S·cm⁻¹ at 750 °C in air have been reported for Ce_{0.8}Gd_{0.2}O_{2-δ}. [40]

It is important to point out that changes in temperature and oxygen partial pressure (pO₂) result in a reduction in the valence of the Ce from Ce⁴⁺ to Ce³⁺. In this process, electronic conductivity is given. Despite the loss of considerable amounts of oxygen from the crystal lattice, and the formation of a large number of oxygen vacancies, the CeO₂ fluorite structure is retained; however, as a result of the oxygen vacancy formation, ceria undergoes a so-called “chemical expansion”, which is a dilatation of the lattice [38,39].

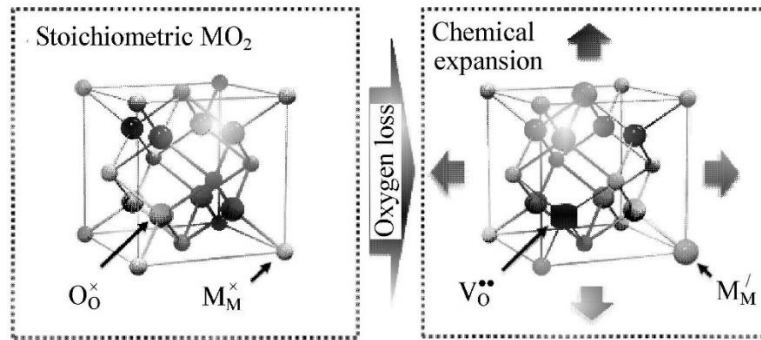


Fig. 3.7. Oxygen loss upon heating or exposure to reducing atmosphere typically (fluorite structured metal oxide, MO₂) results in a lattice dilatation known as chemical expansion. [39]

Chemical expansion has been shown to arise from two competing mechanisms: (1) an expansion due to reduction of multivalent cations with a corresponding increase in cation radii and (2) a contraction due to relaxation of ions around oxygen vacancies. Chemical expansion (ϵ_C) is proportional to the oxygen vacancy concentration (δ) by the chemical coefficient of expansion (α_C) according to Eq. 3.12 [39].

$$\epsilon_C = \alpha_C \delta \quad (\text{Eq. 3.12})$$

In ceria, the predicted cation expansion is about 15% and the anion relaxation is about -5%, yielding a chemical coefficient of expansion of about 10% per vacancy. In general,

ceria electrolytes are considered to be mechanically unstable at temperatures above 700°C, leading to mechanical failures when working at higher temperatures. In order to improve the mechanical stability of the CGO, variation in oxygen nonstoichiometry should be minimized, as this will reduce the stress in the membrane due to chemical expansion. This can be achieved by minimizing the thickness of the CGO layers, while at the same time increasing the oxygen flux delivered by the membrane. [38,39,41,42]

Zirconium oxide, ZrO_2 .

Zirconium oxide, ZrO_2 , is a ceramic that shows optical, thermal, electrical and mechanical properties. At temperatures below 1170 °C it has a monoclinic phase, which changes into a tetragonal phase between 1170 °C – 2370 °C and a cubic phase from 2370 °C to its melting point at 2706 °C. The cubic phase can be stabilized at room temperature by introducing divalent or trivalent cations in the ZrO_2 crystal structure, such as Ca^{2+} , Y^{3+} , Sc^{3+} or Mg^{2+} . [43]

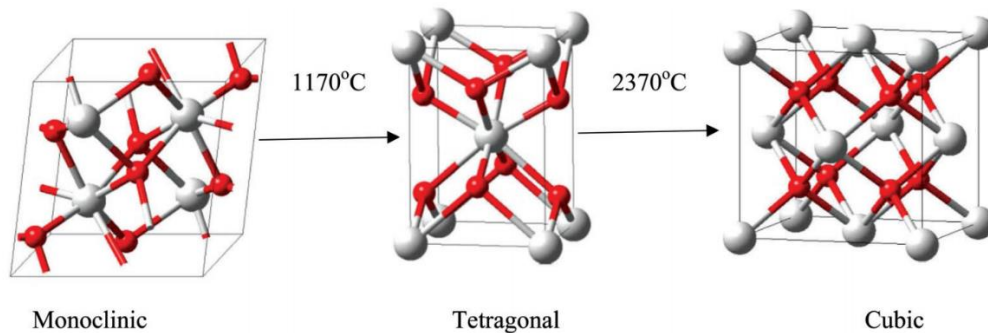


Fig. 3.8. Crystal transitions of the ZrO_2 at different temperatures. [44]

The substitution of cations of appropriate size, such as Y^{3+} , for the host lattice cation Zr^{4+} , not only stabilizes the cubic phase of the structure but also creates a large concentration of oxygen vacancies to maintain the charge neutrality in the lattice, which allows the oxygen ions to move through the crystal structure by using the oxygen vacancies. as described in Eq. 3.13. [43,45]



Several dopants have been studied in binary or ternary phases with the ZrO_2 . Ytria-stabilized zirconia, $(Y_2O_3)_x(ZrO_2)_{1-x}$, has been widely studied as ion-conductor in solid oxide cells due to its good physical and chemical properties, such as chemical, thermal

and mechanical stability and highly stable conductivity in the pO_2 range between $1 - 10^{-21}$ atm. [34,35] When substituted with 8 mol% Y_2O_3 , ZrO_2 shows a ionic conductivity of $0.05 S \cdot cm^{-1}$ and $0.18 S \cdot cm^{-1}$ in air at $750^\circ C$ and $1000^\circ C$ respectively. [46] Further addition of Y_2O_3 will decrease the ionic conductivity due to association of the oxygen vacancies and dopant cations, which results in defective complexes with low mobility [47] A 10 mol% Sc_2O_3 , 1 mol% Y_2O_3 and 89 mol% ZrO_2 non-transformable tetragonal phase provided an ionic conductivity of $0.12 S \cdot cm^{-1}$ at $850^\circ C$ in air [48,49]

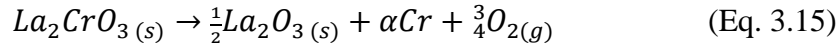
Chromite-based perovskites for oxygen membranes.

As previously discussed, perovskites, such as ferrites, cobaltites, and nickelates can provide high ionic and electronic properties, for example $Ba_{0.5}Sr_{0.5}Co_{0.8}Fe_{0.2}O_{3-\delta}$ (BSCF). However, this high performance perovskites usually show low stability in reducing conditions and high temperatures, limiting their application. Chromite-based perovskites have been widely studied as interconnect materials in solid oxide cells due to their high electronic conductivity, thermo-chemical stability at high temperatures ($\sim 1000^\circ C$) and reducing environments ($pO_2 \sim 10^{-20}$ atm). [31,32,50,51]

Lanthanum chromite, $LaCrO_3$ has been used as an interconnect material due to its p-type electronic conductivity in oxidizing conditions. However, the p-type conductivity decreases in reducing conditions as it becomes oxygen deficient and electron-holes are consumed through formation of oxygen vacancies. By doping $LaCrO_3$ with electron acceptors in the A-site, such as alkaline-earth elements, the p-type conduction is increased by small polaron mechanisms. Several studies have been focused in Sr and Ca-doped $LaCrO_3$, as well as in using Ni, Cu and Co as dopants for the B-site, such as $La_{1-x}A_xB_yCr_{1-y}O_{3-\delta}$ (A= Sr, Ca; B = Fe, Cu, Mn, Co). [50,52-56]

It has been demonstrated that Sr-containing perovskites can accelerate the oxygen exchange kinetics at the surface of the membrane. However, in $pO_2 < 10^{-7}$ and temperatures above $600^\circ C$, Sr segregates and a decrement of the electronic conductivity is observed. Thus, the use of Sr-free chromites, such as $LaCr_{0.85}Cu_{0.10}Ni_{0.05}O_{3-\delta}$, could offer significantly improved stability of the perovskite structure under reducing conditions [54,57-59]





One of the major drawback of the chromites is the vaporization of Cr^{6+} from the perovskite and the subsequent reaction of the La_2O_3 to form secondary phases that could affect the electronic conductivity, structural integrity or chemical stability of the perovskite, thus diminishing the performance of the OTM.

Cr^{6+} vaporization has been studied by different authors reporting the decomposition of chromite-based perovskites in oxidizing conditions above 900°C with an increase in the decomposition process above 1250°C . [51,60,61] Different Cr species are formed due to the reaction with oxygen and if water vapour is present in the air, decomposition increases significantly due to formation of hydroxide species. [62,63]

Additionally to lanthanum-based chromites, other ions can take the A-site position in the perovskite, such as Y. By replacing the La by Y, possible side-reactions due to vaporization of the chromium might be avoided, such as formation of $\text{La}(\text{OH})_3$ or $\text{La}_2\text{Zr}_2\text{O}_7$ when combined with ZrO_2 -based materials. Chromites, with the structure $\text{Y}_{0.8}\text{Ca}_{0.2}\text{Cr}_{0.9}\text{M}_{0.1}\text{O}_{3-\delta}$ ($\text{M}=\text{Co}, \text{Ni}, \text{Cu}, \text{Fe}, \text{Mn}$) have been studied, showing high stability and conductivities of up to $40 \text{ S}\cdot\text{cm}^{-1}$ and $20 \text{ S}\cdot\text{cm}^{-1}$ at 1000°C in $p\text{O}_2=0.21$ and $p\text{O}_2=10^{-17}$, respectively, which make them alternatives to be used in dual-phase OTMs. [65,66]

Performance of chromite-based dual-phase oxygen transport membranes.

Table 3.1 summarizes the oxygen fluxes of dual-phase composites containing chromite-based perovskites as electronic conductors in combination with ZrO_2 or CeO_2 -based ionic conductors. The table compiles information collected from literature considering geometry, membrane thickness, atmosphere gradients and operation temperatures. The oxygen flux values for the composites that were studied in this work are also shown.

Table 3.1 Performance of chromite-based oxygen transport membranes ^[6]

Dual-phase composite	Geom.*	Thick. [μm]	Temp. [°C]	Atm. pO _{2feed} /pO _{2perm}	O ₂ flux Nml·s ⁻¹ ·cm ⁻²
Ce _{0.9} Gd _{0.1} O _{1.95} – La _{0.75} Sr _{0.25} Cr _{0.97} V _{0.03} O _{3-δ} ^[67]	P	1000	800	Air/N ₂	0.21
Ce _{0.8} Sm _{0.2} O _{1.9} – La _{0.8} Sr _{0.2} CrO ₃ ^[68]	P	300	950	0.21/0.0092	0.19
Ce _{0.8} Sm _{0.2} O _{1.9} – La _{0.8} Sr _{0.2} CrO ₃ ^[69]	T	1100	950	Air/CO	1.16
Ce _{0.8} Sm _{0.2} O _{1.9} – Y _{0.8} Ca _{0.2} Cr _{0.8} Co _{0.2} O ₃ ^[70]	P	1300	950	Air/N ₂	0.31
Ce _{0.9} Gd _{0.1} O _{1.95} – Y _{0.8} Ca _{0.2} Cr _{0.8} Co _{0.2} O ₃ (This work)	P	1000		Air/N ₂	0.30
Ce _{0.9} Gd _{0.1} O _{1.95} – LaCr _{0.85} Cu _{0.10} Ni _{0.05} O _{3-δ} (This work)	P	1000		Air/N ₂	0.40
Zr _{0.8} Y _{0.2} O _{2-δ} – La _{0.8} Sr _{0.2} Cr _{0.5} Fe _{0.5} O _{3-δ} ^[71]	P	120	900	Air/Ar	0.06
				CO ₂ /H ₂	0.18
				Air/CO	1.20
Zr _{0.84} Y _{0.16} O _{2-δ} – La _{0.8} Sr _{0.2} Cr _{0.5} Fe _{0.5} O _{3-δ} ^[72]	C	270	950	Air/He	0.32
				Air/CO	4.53
Zr _{0.8} Y _{0.2} O _{2-δ} – La _{0.8} Sr _{0.2} CrO ₃ ^[73]	T	1230	950	Air/He	0.01
			930	Air/CO	0.04
Zr _{0.92} Y _{0.16} O _{2-δ} – La _{0.8} Sr _{0.2} CrO _{3-δ} ^[74]	P	115	800	Air/CO	0.04
Sc _{0.198} Ce _{0.012} Zr _{0.789} O _{2-δ} – (La _{0.8} Sr _{0.2}) _{0.95} Cr _{0.5} Fe _{0.5} O _{3-δ} ^[75]	P	20	900	Air/H ₂	3.54
		200			0.74
		300			0.53
Sc _{0.2} Y _{0.02} Zr _{0.89} O _{2-δ} – LaCr _{0.85} Cu _{0.10} Ni _{0.05} O _{3-δ} (This work)	P	1000	950	Air/N ₂	0.26
Sc _{0.2} Y _{0.02} Zr _{0.89} O _{2-δ} – LaCr _{0.85} Cu _{0.10} Ni _{0.05} O _{3-δ} ^[59]	P	1000	950	Air/N ₂	0.27
		1000		Air/CO ₂	0.25
		110		Air/N ₂	1.02
		110		AirCO ₂	1.00

* Geometry: P (Planar), T (Tubular), C (Capillary).

Although similar operating conditions and thicknesses would be needed to make a fair comparison of the performance of these materials, it is observed that thickness and driving force (atmosphere gradients) are the variables that significantly affect the oxygen flux.

When comparing the membranes with thicknesses ca. 1000 μm and working in an Air/N₂ gradient, it is noticed that Sc_{0.2}Y_{0.02}Zr_{0.89}O_{2-δ} – LaCr_{0.85}Cu_{0.10}Ni_{0.05}O_{3-δ} (ScYSZ-LCCN) and Ce_{0.9}Gd_{0.1}O_{1.95} – Y_{0.8}Ca_{0.2}Cr_{0.8}Co_{0.2}O₃ (CGO-YCCC) provide some of the highest oxygen fluxes, giving values of 0.26 and 0.30 Nml·s⁻¹·cm⁻², respectively. Other membranes showing higher oxygen fluxes have a fraction of the thickness or are working

with a larger driving force. By using thin membranes, e.g. of 20 μm , under the same conditions (Air/N₂ gradient at 950 °C), it would be expected to obtain oxygen fluxes with one order of magnitude higher, ca. 5.6 $\text{Nml}\cdot\text{s}^{-1}\cdot\text{cm}^{-2}$ and 6.4 $\text{Nml}\cdot\text{s}^{-1}\cdot\text{cm}^{-2}$ for the ScYSZ-LCCN and CGO-YCCC, respectively. This shows the potential of using thin membranes to increase the oxygen flux through the membranes and although studies to assess the stability of these composites in syngas conditions need to be done, both materials are promising candidates to develop thin asymmetric tubular OTM.

References

- [1] Julbe, A.; Farrusseng, D.; Guizard, C. Limitations and potentials of oxygen transport dense and porous ceramic membranes for oxidation reactions. IN *Catalysis Today* — 2005, Volume 104, Issue 2-4, pp. 102-113. DOI: 10.1016/j.cattod.2005.03.075
- [2] Den Exter, M.J.1; Haije, W.G.; Vente, J.F. Viability of ITM technology for oxygen production and oxidation processes: Material, system, and process aspects. *Inorganic Membranes for Energy and Environmental Applications* — 2009, pp. 27-51. DOI: 10.1007/978-0-387-34526-0_2
- [3] Gellings, P.J.; Bouwmeester, H.J.M. Ion and mixed conducting oxides as catalysts. *Catalysis Today* — 1992, volume 12, issue 1, pp. 1-105. DOI: 10.1016/0920-5861(92)80046-P
- [4] Bouwmeester, H.J.M.; Kruidhof, H; Burggraaf, A.J. Importance of the surface exchange kinetics as rate-limiting step in oxygen permeation through mixed-conducting oxides. *Solid State Ionics* — 1994, Volume 72, Issue pt 2, pp. 185-194. DOI: 10.1016/0167-2738(94)90145-7
- [5] Schulze-Küppers, F.; Baumann, S.; Meulenberg, W.A.; Bouwmeester, H.J.M. Influence of support layer resistance on oxygen fluxes through asymmetric membranes based on perovskite-type oxides SrTi_{1-x}FexO_{3- δ} . *Journal of Membrane Science* — 2020, Volume 596, pp. 117704. DOI: 10.1016/j.memsci.2019.117704

- [6] Pirou, S. Development of Dual-Phase Oxygen Transport Membranes for Carbon Capture Processes. Diss. Technical University of Denmark. 2017.
- [7] Smart, S.; Diniz Da Costa, J.C. Oxygen transport membranes for power plant applications. *Advanced membrane science and technology for sustainable energy and environmental applications*, Chapter 9. Woodhead Publishing Limited, 2011. United Kingdom. DOI: 10.1533/9780857093790
- [8] Bouwmeester, H.J.M.; Burggraaf, A.J. Dense ceramic membranes for oxygen separation. *Membrane Science and Technology* — 1996, Volume 4, Issue C, pp. 435-528. DOI: 10.1016/s0927-5193(96)80013-1
- [9] Cheng, S. Oxygen transport membranes for biomass gasification and cement industry. Diss. Technical University of Denmark. 2015.
- [10] Van Hassel, B.A. Oxygen transfer across composite oxygen transport membranes. *Solid State Ionics* — 2004, Volume 174, Issue 1-4, pp. 253-260. DOI: 10.1016/j.ssi.2004.07.034
- [11] Zhao, F.; Armstrong, T.J.; Virkar, A.V. Measurement of O₂-N₂ effective diffusivity in porous media at high temperatures using an electrochemical cell. *Journal of the Electrochemical Society* — 2003, Volume 150, Issue 3, pp. A249-A256. DOI: 10.1149/1.1540156
- [12] Qi, Y.; Huang, B.; Chuang, K.T. Dynamic modeling of solid oxide fuel cell: The effect of diffusion and inherent impedance. *Journal of Power Sources* — 2005, Volume 150, Issue 1-2, pp. 32-47. DOI: 10.1016/j.jpowsour.2005.02.080
- [13] Dahl, P.I.; Fontaine, M.L.; Peters, T.; Mei, S.; Larring, Y.; Henriksen, P.P.; Bredesen, R. Development and testing of membrane materials and modules for high temperature air separation. *Energy Procedia* — 2011, Volume 4, pp. 1243-1251. DOI: 10.1016/j.egypro.2011.01.180
- [14] Zhang, G.; Jin, W.; Xu, N. Design and Fabrication of Ceramic Catalytic Membrane Reactors for Green Chemical Engineering Applications. *Engineering* — 2018, Volume 4, Issue 6, pp. 848-860. DOI: 10.1016/j.eng.2017.05.001

- [15] Verda, V.; Ciano, C. Tubular Cells and Stacks. Modeling solid oxide fuel cells : methods, procedures and techniques — 2008, pp. 207-238. DOI: 10.1007/978-1-4020-6995-6_7
- [16] Sirman, J. The Evolution of Materials and Architecture for Oxygen Transport Membranes. Nonporous Inorganic Membranes: for Chemical Processing — 2006, pp. 165-184. 10.1002/3527608796.ch6
- [17] Doong, S. J. Advanced hydrogen (H₂) gas separation membrane development for power plants. Advanced Power Plant Materials, Design and Technology — 2010, pp. 111-142. DOI: 10.1533/9781845699468.2.111
- [18] Berk, Z. Chapter 10 - Membrane processes. Food Process Engineering and Technology — 2009, pp. 233-257. DOI: 10.1016/B978-0-12-373660-4.00010-7
- [19] Dong, X.; Jin, W. Mixed conducting ceramic membranes for high efficiency power generation with CO₂ capture. Current Opinion in Chemical Engineering — 2012, Volume 1, Issue 2, pp. 163-170. DOI: 10.1016/j.coche.2012.03.003
- [20] Takahashi, T.; Esaka, T.; Iwahara, H. Electrical conduction in the sintered oxides of the system Bi₂O₃-BaO. Journal of Solid State Chemistry — 1976, Volume 16, Issue 3-4, pp. 317-23. DOI: 10.1016/0022-4596(76)90047-5
- [21] Cales, B.; Baumard, J.F. Oxygen semi-permeability and electronic conductivity in calcia-stabilized zirconia. J Mater Sci — 1982, Volume V 71, pp. 3243-3248.
- [22] Kilner, J.A. Ion-conducting membranes: membrane separations. Encyclopedia of Separation Science — 2007, pp. 3187-3193. DOI: 10.1016/B0-12-226770-2/05571-X
- [23] Nikonov, A.V.; Kuterbekov, K.A.; Bekmyrza, K.Z.; Pavzderin, N.B. A brief review of conductivity and thermal expansion of perovskite-related oxides for SOFC cathode. Eurasian Journal of Physics and Functional Materials — 2018, Volume 2, Issue 3, pp. 274-292. DOI: 10.29317/ejpfm.2018020309

- [24] Riess, I. Mixed ionic-electronic conductors - material properties and applications. *Solid State Ionics* — 2003, Volume 157, Issue 1-4, pp. 1-17. DOI: 10.1016/S0167-2738(02)00182-0
- [25] Kilner, J.A. Ion-conducting membranes: Membrane separations. *Encyclopedia of Separation Science* — 2007, pp. 3187-3193. DOI: 10.1016/B0-12-226770-2/05571-X
- [26] Gopalan, S. Using ceramic mixed ionic and electronic conductors for gas separation. *Jom* — 2002, Volume 54, Issue 5, pp. 26-29. DOI: 10.1007/bf02701692
- [27] Leo, A.; Liu, S.; Costa, J.C.D. Development of mixed conducting membranes for clean coal energy delivery. *International Journal of Greenhouse Gas Control* — 2009, Volume 3, Issue 4, pp. 357-367. DOI: 10.1016/j.ijggc.2008.11.003
- [28] Nikonov, A.V.; Kuterbekov, K.A.; Bekmyrza, K.Zh.; Pavzderin, N.B. A brief review of conductivity and thermal expansion of perovskite-related oxides for SOFC cathode. *Eurasian Journal of Physics and Functional Materials* — 2018, Volume 2, Issue 3, pp. 274-292. DOI:10.29317/ejpfm.2018020309
- [29] Johnsson, M.; Lemmens, P. *Crystallography and Chemistry of Perovskites*. Cornell University, 2005.
- [30] Garcia Fayos, J. Development of ceramic MIEC membranes for oxygen separation: Application in catalytic industrial processes. PhD Diss. Instituto de Tecnologia Quimica. Universitat Politecnica de Valencia. 2017.
- [31] Baumann, S.; Serra, J.M.; Lobera, M.P.; Escolástico, S.; Schulze-Küppers, F.; Meulenbergh, W.A. Ultrahigh oxygen permeation flux through supported Ba_{0.5}Sr_{0.5}Co_{0.8}Fe_{0.2}O_{3-δ} membranes. *Journal of Membrane Science* — 2011, Volume 377, Issue 1-2, pp. 198-205. DOI: 10.1016/j.memsci.2011.04.050
- [32] Niedrig, C.; Menesklou, W.; Wagner, S.F.; Ivers-Tiffée, E. High-temperature pO₂ stability of metal oxides determined by amperometric oxygen titration. *Journal of the Electrochemical Society* — 2013, Volume 160, Issue 2, pp. F135-F140. DOI: 10.1149/2.063302jes

- [33] Dong, X.; Jin, W.; Xu, N.; Li, K. Dense ceramic catalytic membranes and membrane reactors for energy and environmental applications. *Chemical Communications* — 2011, Volume 47, Issue 39, pp. 10886-10902. DOI: 10.1039/c1cc13001c
- [34] Nasrallah, M.M.; Douglass, D.L. Ionic and electronic conductivity in Y₂O₃-doped monoclinic ZrO₂. *J Electrochem Soc* — 1974, Volume 121, Issue 2, pp. 255-262.
- [35] Ishihara, T. Oxide Ion-Conducting Materials for Electrolytes. *Materials for High-temperature Fuel Cells* — 2012, pp. 97-132. DOI: 10.1002/9783527644261.ch3
- [36] Suzuki, M.To.; Ikeda, H.; Oppeneer, P.M. First-principles Theory of Magnetic Multipoles in Condensed Matter Systems. *Journal of the Physical Society of Japan* — 2018, Volume 87, Issue 4, pp. 041008.
- [37] He, Z.; Yuan, H.; Glasscock, J.; Chatzichristodoulou, C.; Phair, J.; Kaiser, A.; Ramousse, S. Densification and Grain Growth during Early-stage Sintering of Ce_{0.9}Gd_{0.1}O_{1.95-δ} in Reducing Atmosphere. *Acta Materialia* — 2010, Volume 58, Issue 11, pp. 3860-3866. DOI: 10.1016/j.actamat.2010.03.046
- [38] Galusek, D.; Ghillányová, K. *Ceramic Oxides. Ceramics Science and Technology V2 - Materials and Properties*. Wiley-VCH, 2010.
- [39] Bishop, S.R. Chemical expansion of solid oxide fuel cell materials: A brief overview. *Acta Mechanica Sinica/lihue Xuebao* — 2013, Volume 29, Issue 3, pp. 312-317. DOI: 10.1007/s10409-013-0045-y
- [40] Sammes, N.M.; Zhihong, C. Ionic conductivity of ceria/yttria stabilized zirconia electrolyte materials. *Solid State Ionics* — 1997, Volume 100, Issue 1-2, pp. 39-44. DOI: 10.1016/S0167-2738(97)00306-8
- [41] Ni, D.W.; Glasscock, J.; Pons, A.; Zhang, W.5; Prasad, A.; Sanna, S.; Pryds, N.; Esposito, V. Densification of Highly Defective Ceria by High Temperature Controlled Re-Oxidation. *Journal of the Electrochemical Society* — 2014, Volume 161, Issue 11, pp. F3072-F3078. DOI: 10.1149/2.0121411jes

- [42] Chatzichristodoulou, C.; Sjøgaard, M.; Hendriksen, P.V. Oxygen permeation in thin, dense Ce_{0.9}Gd_{0.1}O_{1.95}- membranes I. Model study. *Journal of the Electrochemical Society* — 2011, Volume 158, Issue 5, pp. F61-F72. DOI: 10.1149/1.3556096
- [43] Zavodinsky, V.G. The Mechanism of Ionic Conductivity in Stabilized Cubic Zirconia. *Physics of the Solid State* — 2004, Volume 46, Issue 3, pp. 453-457. DOI:10.1134/1.1687859
- [44] Gautam, C.; Joyner, J.; Gautam, A.; Rao, J.; Vajtai, R. Zirconia based dental ceramics: structure, mechanical properties, biocompatibility and applications. *Dalton Transactions* — 2016, Volume 45, Issue 48, pp. 19194-19215. DOI: 10.1039/c6dt03484e
- [45] Guizard, C.G.; Julbe, A.C. Nanophase ceramic ion transport membranes for oxygen separation and gas stream enrichment. *Membrane Science and Technology* — 2000, Volume 6, Issue C, pp. 435-471. DOI: 10.1016/S0927-5193(00)80019-4
- [46] Chan, Y.H.; Lai, H.Y.; Chen, C.K. Enhancing oxygen ion conductivity of 8YSZ electrolytes in SOFC by doping with Fe₂O₃. *Computational Materials Science* — 2018, Volume 147, pp. 1-6. DOI: 10.1016/j.commatsci.2018.01.057
- [47] Kharton, V.V.; Naumovich, E.N.; Vecher, A.A. Research on the electrochemistry of oxygen ion conductors in the former Soviet Union. I. ZrO₂-based ceramic materials. *Journal of Solid State Electrochemistry* — 1999, Volume 3, Issue 2, pp. 61-81. DOI: 10.1007/s100080050131
- [48] Artemov, V.G.; Kuritsyna, I.E.; Lebedev, S.P.; Komandin, G.A.; Kapralov, P.O.; Spektor, I.E.; Kharton, V.V.; Bredikhin, S.I.; Volkov, A.A. Analysis of electric properties of ZrO₂-Y₂O₃ single crystals using terahertz IR and impedance spectroscopy techniques. *Russian Journal of Electrochemistry* — 2014, Volume 50, Issue 7, pp. 690-693. DOI: 10.1134/s1023193514070039

- [49] Liu, H.; Li, S.; Li, Q.; Li, Y. Investigation on the phase stability, sintering and thermal conductivity of Sc₂O₃-Y₂O₃-ZrO₂ for thermal barrier coating application. *Materials and Design* — 2010, Volume 31, Issue 6, pp. 2972-2977. DOI: 10.1016/j.matdes.2009.12.019
- [50] Gupta, S.; Mahapatra, M.K.; Singh, P. Lanthanum chromite based perovskites for oxygen transport membrane. *Materials Science and Engineering R: Reports* — 2015, Volume 90, pp. 1-36. 10.1016/j.mser.2015.01.001
- [51] Suvorov, S.A.; Shevchik, A.P. Chemical equilibria involving lanthanum chromite. *Refractories and Industrial Ceramics* — 2004, Volume 45, Issue 2, pp. 94-99. DOI: 10.1023/b:refr.0000029615.98571.67
- [52] Fergus, J.W. Lanthanum chromite-based materials for solid oxide fuel cell interconnects. *Solid State Ionics* — 2004, Volume 171, Issue 1-2, pp. 1-15. DOI: 10.1016/j.ssi.2004.04.010
- [53] Khandkar, A.C.; Milliken, C.E.; Elangovan, S.; Hartvigsen, J.J. Doped lanthanum chromite material for bipolar interconnects for solid oxide fuel cells. United States Patent number 5958304. September 28th, 1999. <https://patents.google.com/patent/US5958304>
- [54] Gupta, S.; Singh, P. Nickel and titanium doubly doped lanthanum strontium chromite for high temperature electrochemical devices. *Journal of Power Sources* — 2016, Volume 306, pp. 801-811. DOI: 10.1016/j.jpowsour.2015.11.111
- [55] Sarno, C.; Luisetto, I.; Zurlo, F.; Licoccia, S.; Di Bartolomeo, E. Lanthanum chromite based composite anodes for dry reforming of methane. *International Journal of Hydrogen Energy* — 2018, Volume 43, Issue 31, pp. 14742-14750. DOI: 10.1016/j.ijhydene.2018.06.021
- [56] Tanasescu, S.; Orasanu, A.; Berger, D.; Jitaru, I.; Schoonman, J. Electrical conductivity and thermodynamic properties of some alkaline earth-doped lanthanum chromites. *International Journal of Thermophysics* — 2005, Volume 26, Issue 2, pp. 543-557. DOI: 10.1007/s10765-005-4516-7

- [57] Oriyasa, Y.; Crumlin, E.J.; Sako, S.; Amezawa, K.; Uruga, T.; Biegalski, M.D.; Christen, H.M.; Uchimoto, Y.; Yang, S.H. Surface strontium segregation of solid oxide fuel cell cathodes proved by in situ depth-resolved x-ray absorption spectroscopy. *ECS Electrochemistry Letters* — 2014, Volume 3, Issue 4, pp. F23-F26. DOI: 10.1149/2.006404eel
- [58] Yasuda, I.; Hishinuma, M. Electrical-conductivity and chemical diffusion-coefficient of Sr-doped lanthanum chromites. *Solid State Ionics* — 1995, Volume 80, Issue 1-2, pp. 141-150. DOI: 10.1016/0167-2738(95)00136-T
- [59] Pirou, S.; Bermudez, J.M.; Tak Na, B.; Ovtar, S.; Yu, J.H.; Hendriksen, P.V.; Kaiser, A.; Ramirez Reina, T.; Millan, M.; Kiebach, R. Performance and stability of $(\text{ZrO}_2)_{0.89}(\text{Y}_2\text{O}_3)_{0.01}(\text{Sc}_2\text{O}_3)_{0.10}\text{-LaCr}_{0.85}\text{Cu}_{0.10}\text{Ni}_{0.05}\text{O}_{3-\delta}$ oxygen transport membranes under conditions relevant for oxy-fuel combustion. *Journal of Membrane Science* — 2018, Volume 552, pp. 115-123. DOI: 10.1016/j.memsci.2018.01.067
- [60] Povoden, E.; Chen, M.; Grundy, A.N.; Ivas, T.; Gauckler, L.J. Thermodynamic Assessment of the La-Cr-O System. *Journal of Phase Equilibria and Diffusion* — 2009, Volume 30, Issue 1, pp. 12-27. DOI: 10.1007/s11669-008-9463-0
- [61] Opila, E.J.; Myers, D.L.; Jacobson, N.S.; Nielsen, I.M.B.; Johnson, D.F.; Olminky, J.K.; Allendorf, M.D. Theoretical and Experimental Investigation of the Thermochemistry of $\text{CrO}_2(\text{OH})_2(\text{g})$. *Cheminform* — 2007, Volume 38, Issue 23. DOI: 10.1021/jp0647380
- [62] Hilpert, K.; Das, D.; Miller, M.; Peck, D.H.; Weiß, R. Chromium vapor species over solid oxide fuel cell interconnect materials and their potential for degradation processes. *Journal of the Electrochemical Society* — 1996, Volume 143, Issue 11, pp. 3642-3647. DOI: 10.1149/1.1837264
- [63] Badwal, S.P.S.; Deller, R.; Foger, K.; Ramprakash, Y.; Zhang, J.P. Interaction between chromia forming alloy interconnects and air electrode of solid oxide fuel cells. *Solid State Ionics* — 1997, Volume 99, Issue 3-4, pp. 297-310. DOI: 10.1016/S0167-2738(97)00247-6

- [65] Yoon, K.J.; Cramer, C.N.; Thomsen, E.C.; Coyle, C.A.; Coffey, G.W.; Marina, O.A. Calcium- and cobalt-doped yttrium chromites as an interconnect material for solid oxide fuel cells. *Journal of the Electrochemical Society* — 2010, Volume 157, Issue 6, pp. B856-B861. DOI: 10.1149/1.3337156
- [66] Yoon, K.J.; Cramer, C.N.; Stevenson, J.W.; Marina, O.A. Improvement of sintering, thermal behavior, and electrical properties of calcium- and transition metal-doped yttrium chromite. *Electrochemical and Solid-state Letters* — 2010, Volume 13, Issue 9, pp. B101-B105. DOI: 10.1149/1.3456525
- [67] Samson, A.J.; Søgaard, M.; Hendriksen, P.V. (Ce,Gd)O₂- δ -based dual phase membranes for oxygen separation. *Journal of Membrane Science* — 2014, Volume 470, pp. 178-188. DOI: 10.1016/j.memsci.2014.07.028
- [68] Yi, J.; Zuo, Y.; Liu, W.; Winnubst, L.; Chen, C. Oxygen permeation through a Ce_{0.8}Sm_{0.2}O₂- δ -La_{0.8}Sr_{0.2}CrO₃- δ dual-phase composite membrane. *Journal of Membrane Science* — 2006, Volume 280, Issue 1-2, pp. 849-855. DOI: 10.1016/j.memsci.2006.03.011
- [69] Wang, B.; Yi, J.; Winnubst, L.; Chen, C. Stability and oxygen permeation behavior of Ce_{0.8}Sm_{0.2}O₂- δ -La_{0.8}Sr_{0.2}CrO₃- δ composite membrane under large oxygen partial pressure gradients. *Journal of Membrane Science* — 2006, Volume 286, Issue 1-2, pp. 22-25. DOI: 10.1016/j.memsci.2006.06.009
- [70] Yoon, K.J.; Marina, O.A. Highly stable dual-phase Y_{0.8}Ca_{0.2}Cr_{0.8}Co_{0.2}O₃-Sm_{0.2}Ce_{0.8}O_{1.9} ceramic composite membrane for oxygen separation. *Journal of Membrane Science* — 2016, Volume 499, pp. 301-306. DOI: 10.1016/j.memsci.2015.10.064
- [71] Fang, W.; Zhang, Y.; Gao, J.; Chen, C. Oxygen permeability of asymmetric membrane of functional La_{0.8}Sr_{0.2}Cr_{0.5}Fe_{0.5}O₃- δ (LSCrF)-Zr_{0.8}Y_{0.2}O₂- δ (YSZ) supported on porous YSZ. *Ceramics International* — 2014, Volume 40, Issue 1, pp. 799-803. DOI: 10.1016/j.ceramint.2013.06.070

- [72] Liu, T.; Wang, Y.; Yuan, R.; Gao, J.; Chen, C.; Bouwmeester, H.J.M. Enhancing the oxygen permeation rate of $\text{Zr}_{0.84}\text{Y}_{0.16}\text{O}_{1.92}\text{-La}_{0.8}\text{Sr}_{0.2}\text{Cr}_{0.5}\text{Fe}_{0.5}\text{O}_{3-\delta}$ dual-phase hollow fiber membrane by coating with $\text{Ce}_{0.8}\text{Sm}_{0.2}\text{O}_{1.9}$ nanoparticles. *ACS Applied Materials and Interfaces* — 2013, Volume 5, Issue 19, pp. 9454-9460
- [73] Wang, B.; Zhan, M.C.; Zhu, D.C.; Liu, W.; Chen, C.S. Oxygen permeation and stability of $\text{Zr}_{0.8}\text{Y}_{0.2}\text{O}_{0.9}\text{-La}_{0.8}\text{Sr}_{0.2}\text{CrO}_{3-\delta}$ dual-phase composite. *Journal of Solid State Electrochemistry* — 2006, Volume 10, Issue 8, pp. 625-628. DOI: 10.1007/s10008-006-0136-9
- [74] Yu, A.S.; Oh, T.S.; Zhu, R.; Gallegos, A.; Gorte, R.J.; Vohs, J.M. Surface modification of $\text{La}_{0.8}\text{Sr}_{0.2}\text{CrO}_{3-\delta}\text{-YSZ}$ dual-phase membranes for syngas production. *Faraday Discussions* — 2015, Volume 182, pp. 213-225. DOI: 10.1039/c5fd00007f
- [75] Dehaney-Steven, Z.; Papargyriou, D.; Irvine, J.T.S. Flux investigations on composite $(\text{La}_{0.8}\text{Sr}_{0.2})_{0.95}\text{Cr}_{0.5}\text{Fe}_{0.5}\text{O}_{3-\delta}\text{-Sc}_{0.198}\text{Ce}_{0.012}\text{Zr}_{0.789}\text{O}_{1.90}$ oxygen transport membranes. *Solid State Ionics* — 2016, Volume 288, pp. 338-341. DOI: 10.1016/j.ssi.2016.01.017

Chapter 4. Fabrication and characterization of OTMs

Asymmetric tubular oxygen transport membranes (OTMs) are devices conformed by different thin layers, approximately 10 μm thick, supported on porous tubes. Tubular supports can be fabricated by extrusion or isostatic pressing and the thin layers can be deposited using spray coating, dip-coating or screen printing. All these shaping techniques are widely spread and can be used to reduce the fabrication costs of the membranes in scaling-up processes.

In this work, $(\text{Y}_2\text{O}_3)_{0.03}(\text{ZrO}_2)_{0.97}$ – herein referred to as 3YSZ – based porous supports were fabricated using thermoplastic extrusion, and thin layers of $(\text{Sc}_2\text{O}_3)_{0.10}(\text{Y}_2\text{O}_3)_{0.01}(\text{ZrO}_2)_{0.89}$ – $\text{LaCr}_{0.85}\text{Cu}_{0.10}\text{Ni}_{0.05}\text{O}_{3-\delta}$ (herein referred to as ScYSZ-LCCN) and $\text{Y}_{0.8}\text{Ca}_{0.2}\text{Cr}_{0.8}\text{Co}_{0.2}\text{O}_{3-\delta}$ – $\text{Ce}_{0.9}\text{Gd}_{0.1}\text{O}_{2-\delta}$ (herein referred to as CGO-YCCC) composites were deposited as OTMs using dip-coating. The selection of these shaping techniques was based on the availability of fabrication equipment and in-house know-how. In addition to the manufacturing process, different analysis techniques were performed on raw powders, porous supports and thin membranes to assess their characteristics with the purpose of defining different methods to develop the membranes.

This chapter consists of two sections. A brief introduction to the main shaping techniques, thermoplastic extrusion and dip-coating, is included in Section 4.1. Section 4.2 deals with the equipment and the experimental set-ups to characterize the studied materials: X-ray diffraction, particle size distribution, Hg-porosimetry, scanning electron microscopy – energy dispersing spectroscopy, dilatometry, measurement of Darcy permeability and oxygen flux.

4.1. Processing and fabrication of asymmetric tubular oxygen transport membranes

This section outlines the main fabrication techniques used along this study: thermoplastic extrusion and dip-coating. The principles of each shaping technique, the used equipment and the general settings are listed. Specific formulations and temperature conditions for each experiment are further described in specific sections of Chapter 5.

4.1.1 Thermoplastic extrusion

Thermoplastic extrusion is a technique where a mixture of fine, sinterable powders and molten polymers is forced through a die to shape continuous components of a fixed cross-sectional area, forming geometries such as tubes, rods, bars, etc. The obtained component is usually an unfinished article that requires additional processing to remove the sacrificial polymeric-phase through thermal debinding, solvent extraction or catalytic methods. Finally, a sintering step will bind the powder particles and densify them into a final product. [1,2] By using thermoplastic extrusion, it is possible to manufacture complex and thin-walled cross sections, provide high strength to the green extrudate and avoid a complex drying step. However, the high volume fraction of polymers in the mixture requires a complex and time consuming debinding process. [3]

4.1.1.1 Process principles.

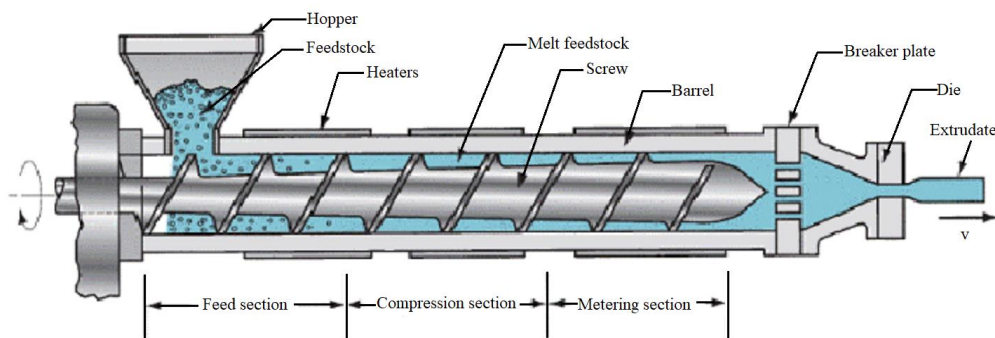


Fig. 4.1. Schematic diagram of a single screw extruder. [5]

The illustration of an extruder is shown in Fig. 4.1. A mix of polymers, powders and additives, so called feedstock, is fed in the extruder's hopper, which transfers the feedstock to the screw that continuously rotates in an axial fixed position within a heated barrel. The screw is divided in three parts: feed, compression and metering sections. The feedstock is pre-heated in the feeding section where melting of the material results from the external heating and the friction between the barrel and the bore. The melted feedstock is conveyed to the compression and metering sections. There, mixing and de-airing happens and the cross section of the screw depth is gradually reduced, which compresses the feedstock before it is pumped through the die to form an extrudate. [2,4] Later, the extrudate is thermally treated to remove the organic phase. Finally, a sintering process is carried out to obtain the final piece (Fig. 4.2).

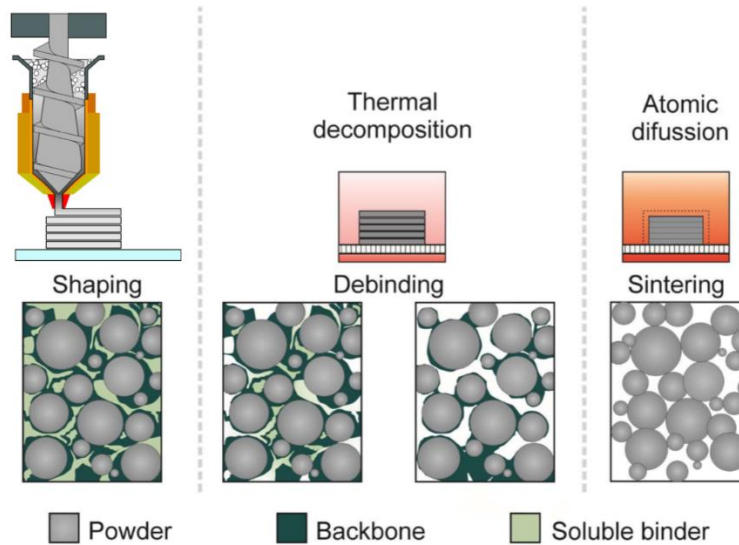


Fig. 4.2. Main components and processing of the binder system. [6]

4.1.1.2 Thermoplastic feedstock components.

The feedstock for thermoplastic extrusion is usually a mixture of components, consisting of a sinterable powder or powder mixture, additives and a polymeric blend, also called binder system. The thermoplastic feedstock in this study is based on an injection moulding formulation [7], which has been further optimized for thermoplastic extrusion by DTU Energy [8] (Energinet project 12202 “Ceramic membranes for oxy-fired biomass gasification”). This thermoplastic system allowed the fabrication of 3YSZ tubular porous supports with a flexural strength of more than 50 MPa and a permeability above $1 \times 10^{-14} \text{ m}^2$ for 3YSZ. [9] The components of the used feedstock, as well as some properties, can be found below in Table 4.1.

Binder system.

The binder system has an important role to increase the fluidity and retaining the shape of the extrudate. Although binder systems could consist of only one polymeric material, they are usually designed as multi-component systems that allow changing the rheological and debinding features of the system. [6,10] Three main components can be identified in a binder system:

1. Primary binder. They are usually low molecular weight components with low viscosity that allow the feedstock flowing adequately after being melted. It consists of 0–50 vol% of the binder system. It is removed during the first debinding step.
2. Backbone binder. These binding components hold the sinterable powder during the debinding stage and provide strength to the feedstock. They represent 50–90 vol% of the binder system. Backbones are usually polyolefin-based since they are materials resistant to a large variety of solvents and degrade into hydrocarbons before sintering.
3. Additives. They are mainly dispersants and stabilizers that allow the dispersion of the sinterable powder and prevent agglomeration and phase separation. They represent up to 10 vol% of the binder system.

Developing a binder system formulation is a complex task since different components and ratios can modify the rheological behaviour of the feedstock and this can impact the production process and the sintered final product. Thus, it is necessary to select the proper components based on the application, as well as on the process and sinterable powders to be used.

The binder system used in this thesis work for the 3YSZ-based porous supports consists of paraffin wax (melting point 53–57°C, Sigma-Aldrich, St. Louis, MO, USA) as main binder and ethylene-vinyl acetate copolymer (Elvax© 250, DuPont, Wilmington, DE, USA) as backbone. Stearic acid (Sigma-Aldrich, USA) was used as dispersant. [3]

Raw powder.

The main component of the feedstock is the powder that will be shaped and remain after the sintering process as a final product. The powder has an important influence on the mechanical properties and the rheological behaviour of the feedstock, since morphology and chemical composition will affect the interaction with the binder system at different shear conditions and determine the densification behaviour during the sintering process. Particle size and surface area are the main physical variables of the powders that can be controlled by thermal pre-treatment (calcination) or by milling of the powder. The required amount of binder, dispersant and other additives in the feedstock formulation is

proportional to (or increasing with) the surface area of the powder. The size and shape of the powder particles can influence the viscosity of the feedstock, e.g. large particles with moderate surface area might reduce the viscosity and flow behaviour of the feedstock at different shear rates and during the different phases of the extrusion process. Both, surface area and particle size will also influence the sintering process, as discussed below. [6,11]

3YSZ (TZ-3YS-E, Tosoh, Tokyo, Japan), was used as raw powder and Fe₂O₃ (Alfa Aesar, USA) was added, in 1 mol% and 3 mol% additions, as sintering aid. The surface area of the 3YSZ powder was previously measured as 16 m²·g⁻¹. The mean particle size of the 3YSZ powder for the different feedstocks was 40 nm. The Fe₂O₃ powder had a mean particle size ca. 250 nm.

Additives.

In order to modify the characteristics of the final morphology of the extrudate, some additional components are include in the feedstock formulation. It is important to point out that chemical interaction with other components and the surface area of additives needs to be considered for the tuning of the feedstock composition.

Table 4.1. Compositions of the 3YSZ porous support feedstock.

Component	Function	Specs/Provider	[wt.%]
Ceramic powder	Raw powder	TZ-3YS-E, Tosoh, Japan	50.8
Stearic acid	Dispersant	Sigma-Aldrich, USA	1.3
Ethylene-vinyl acetate	Backbone	Elvax© 250, DuPont, USA	9.7
Paraffin wax	Binder/plasticizer	Sigma-Aldrich, USA	4.8
Graphite	Pore former	FormulaBT SLA1518, Superior Graphite, USA	26.5
PMMA	Pore former	MR-10G, Esprix, USA	7.0

In the case of the 3YSZ-based porous supports, stearic acid (Sigma-Aldrich, USA) was added to the formulation as dispersant in 2.48 wt% to 3YSZ. Additionally, the use of pore formers was necessary to obtain tubular supports with sufficient open porosity to allow a permeability larger than 1x10⁻¹⁴ m² but at the same time the backbone should provide flexural strength larger than 50 MPa. The pore formers consisted of a combination of “spherical” graphite d_{V50} of 18 μm (FormulaBT SLA1518, Superior Graphite, USA) and polymethyl methacrylate (PMMA) d_{V50} of 9 μm (MR-10G, Esprix, USA). The proportion

of graphite to PMMA was 2:1, constituting 61.5 vol% of the total feedstock. The complete formulation of the 3YSZ porous support feedstock is shown in Table 4.1.

4.1.1.3 Mixing.

In order to obtain a high quality even extrudate, it is necessary to obtain a homogenous distribution of the binder system, pore formers and ceramic powders in the feedstock. A correct uniformity of the feedstock minimises the segregation of components during the shaping process, which would allow an isotropic shrinkage during sintering. This prevents deformation, undesired porosity, or formation of cracks and fractures. [6]

Mixing of the powders is a sequential process that initiates with the raw powder preparation. Since 3YSZ is a powder difficult to disperse, it is first coated with 2.5 % stearic acid using ball-milling in ethanol for 12 h in a step prior to the mixing of the components. Powders were dried and crushed in order to break the agglomerates formed during the drying process.

The mixing of the components was carried out using a BK20 mixer (Linden International, Germany). Fractions of the coated powder, wax and ethylene-vinyl-acetate were loaded to the mixer until all the components were added within a period of 90 minutes. Additional mixing of the feedstock was done for 120 min, changing the rotation of the mixer's blades to ensure the homogeneity of the feedstock.

Table 4.2. Melting and decomposition temperatures of the organic-phase components.

Component	Function	Melting point [°C]	Thermal degradation [°C]
Ethylene-vinyl acetate copolymer	Backbone	70 ^[12]	347 ^[13] 325-500 ^[14]
Paraffin wax	Main binder	57 ^[15]	210-450 ^[16]
Stearic acid	Dispersant	67 ^[12]	160-380 ^[16, 17]
Graphite	Pore former	-	650-900 ^[18,19]
PMMA	Pore former	160 ^[20]	307-450 ^[21] 375-438 ^[22]

The melting points of the components in the binder system and the viscosity of the feedstock determine the temperature for mixing and extrusion. It is expected that feedstocks with higher viscosities require higher mixing and processing temperatures;

however, it is necessary to consider that high temperatures may degrade the polymer-phase, which could change the rheological behaviour of the feedstock.

Melting and thermal decomposition points of the organic materials in the feedstock are shown in Table 4.2. It is important to mention that paraffin wax has a flashpoint of 113 °C [12], thus keeping the mixing and extrusion temperatures below 110 °C is important to avoid the degradation of the binder system and to maintain the rheological behaviour of the feedstock. The temperature for the kneading in the closed high shear mixer was set to 100 °C for all the feedstocks.

4.1.1.4 Extrusion.

The production of an extrudate is dependent not only on the feedstock composition, preparation and resulting flow properties of the feedstock but also on the processing conditions during and directly after the extrusion process. Temperature of the barrel, cooling conditions, die geometry and designs, length to diameter ratio of the extrusion screw (L/D), screw rotational speed, are some of the factors that play an important role in the quality of the final extrudate.

In thermoplastic extrusion, the operation temperature to melt of the polymer is a critical parameter to increase the yield of the extrusion process and to reduce the degradation of the binder system. Thus, it is necessary to select a temperature profile according to the feedstock rheology based on the screw limitations. In general, there are four temperature profiles that allow high yields [23]

- **Progressive:** Increasing the temperature from the feed to the die. This profile avoids premature melting and the formation of feedstock films on the barrel, which increases the friction coefficient in the system.
- **Inverted.** A decreasing temperature profile from the feeding to the die. This profile does not efficiently use the extruder friction to melt the feedstock in the compression and metering sections. The use of this profile is based on feedstock rheology and the screw design.
- **Straight.** Temperature all along the extruder is set at the same level. It does not provide good temperature control and does not promote the melting in the transition zone.

- Humped. The temperature is low in the feed section, increasing the temperature in the transition region and then decreasing the temperature towards the die. It promotes the melting process in the transition zone, and the lower temperature in the metering zone prevents the binder system from degrading.

3YSZ-based tubular porous supports were produced using an extruder Brabender KE19 – 19/20DN (Brabender, Germany) using a 14 mm external diameter die with wall thickness of 1 mm. The extruder is heated by electrical resistances along the barrel. This allows the control of the temperature. In this thesis work, the inverted thermal profile was used for the 3YSZ-based porous supports.

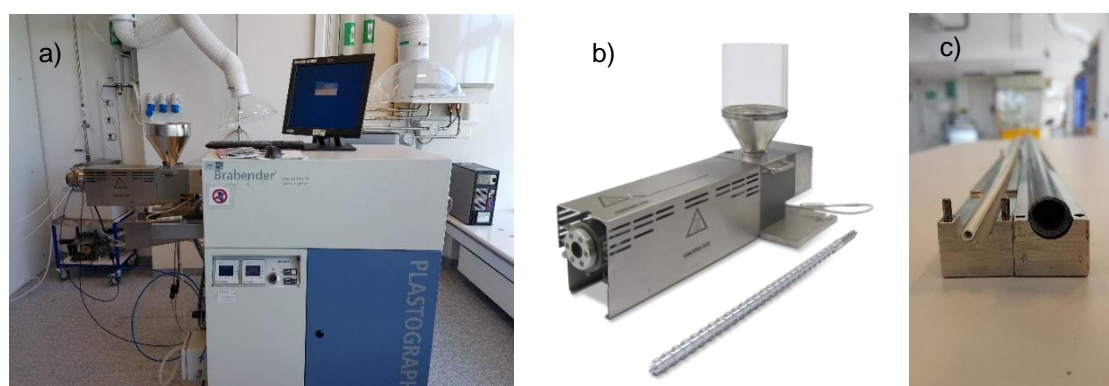


Fig. 4.3. Brabender KE19 – 19/20DN single screw extruder: a) General setup, b) detail of the extruder's screw and c) green-state capillaries and porous supports.

The temperature of the die was set ca. 10-15 °C lower than the rest of the barrel, in order to allow the gradual cooling of the feedstock and avoid its collapsing after leaving the die. Temperatures in the feeding, central and die zones were set at 105°C, 100 °C and 85 °C, respectively. Screw rotational speeds of 2 rpm, 5 rpm and 10 rpm were tested. By using low speeds, the extrudate have enough time to cool between the die and the support, which avoids bending of the tube due to thermal gradients. The support is a stainless steel bar shaped with a 14 mm-diameter semicircle, as seen in Fig. 4.3. By setting the rotational speed to 5 rpm and using a stream of compressed air at room temperature inside the extruded tubes, straight tubes were obtained.

4.1.1.5 Debinding

Debinding is the heat treatment process after extrusion that removes the binder system from the extrudate with the purpose of keeping the original shape. The most common way to remove the binder from a thermoplastic feedstock is by heating the components until

the binders melt down and flow out of the extrudate or until they are thermally degraded. The temperature profile to carry out the thermal debinding depends on the binder system formulation. Furnace setup, ventilation and distribution of parts inside the furnace, including features such as size and number, will also play a role on the definition of the temperature profile to be used. Dwells at specific temperatures are needed to burnout a specific fraction of the components. Slow heating rates are also required in order to control the decomposition of the binder composition to avoid excessive formation of gases that can alter the shape of the extrudate. [6]

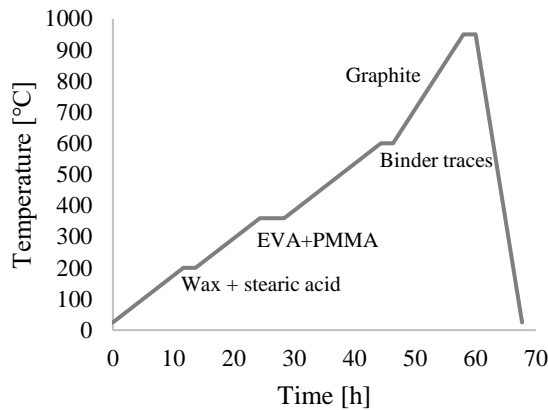


Fig. 4.4. Debinding profiles showing the steps where components are burnt out in a) 3YSZ-based porous supports and b) CGO and ScYSZ dense capillaries.

In this thesis work, a heating ramp of $15\text{ }^{\circ}\text{C}\cdot\text{h}^{-1}$ from room temperature to $600\text{ }^{\circ}\text{C}$ was used with three dwells of 2 hours, as shown in Fig. 4.4. In the first dwell at $200\text{ }^{\circ}\text{C}$, the paraffin wax and stearic acid start decomposing. During the second dwell at $360\text{ }^{\circ}\text{C}$, the ethylene-vinyl acetate copolymer and the PMMA initiate decomposition, paraffin wax and stearic acid having been totally removed from the structure. The decomposition of the ethylene-vinyl acetate copolymer continues during the ramp up to the third dwell at $600\text{ }^{\circ}\text{C}$, where all the traces of the binder components are removed. Between $600\text{ }^{\circ}\text{C}$ and $950\text{ }^{\circ}\text{C}$, a heating ramp of $30\text{ }^{\circ}\text{C}\cdot\text{h}^{-1}$ was used, in order to decompose the graphite. It is worth pointing out that $950\text{ }^{\circ}\text{C}$ was set as pre-sintering temperature for the extrusion tubes. The porous, pre-sintered supports were further sintered at higher temperatures after deposition of functional layers, including the active membrane for oxygen separation, as described further below.

4.1.2 Sintering

Sintering is the thermal process to obtain a final tube from raw powders. In this step, the final characteristics of the materials are tailored. Variables such as heating and cooling rates, sintering temperature and dwell at sintering temperature will affect the microstructure of the final material. Therefore, it is important to select the sintering conditions according to the powder properties, such as melting point, surface area and particle size.

“Sintering is a thermal treatment for bonding particles into a coherent, predominantly solid structure via mass transport events that often occur on the atomic scale. The bonding leads to improved strength and lower system energy” [24]

The main driving force of the sintering process is the reduction of the surface energy of the raw powder particles resulting in the bonding and re-arrangement and of adjacent particles and usually evolve towards a densified microstructure with lower free energy. As surface area is annihilated, the driving force of the particles declines and the sintering rate decreases. [6,25]

4.1.2.1 Mass transport mechanisms.

Different mass transfer mechanisms are involved in the sintering process. They can be broken down into two main groups: 1) Surface transport mechanisms: surface diffusion and evaporation-condensation. 2) Bulk transport mechanisms: grain boundary diffusion, plastic flow, viscous flow and lattice diffusion. The surface transport mechanisms contribute to a reduction of the surface area and the growth of the neck. The bulk transport mechanisms cause material migration from the inside of the particle (bulk) to the surface, leading to densification. [6,25]

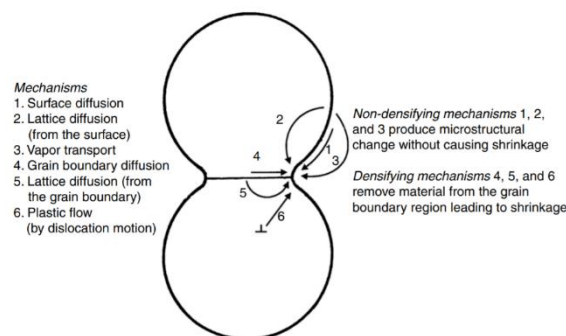


Fig. 4.5. Mass transport mechanisms involved in the sintering process in a two-particle model. [26]

4.1.2.2 Sintering stages.

The sintering process consists of three stages: Initial (neck growth), intermediate (grain growth onset) and final (densification). The three stages are described below [6,24,27,28] and illustrated in Fig. 4.6.

During the initial stage (2), an increase of the inter-particle contact area occurs, creating and growing necks and grain boundaries due to the different curvatures of the particles and the neck. Surface diffusion is the main mass transport mechanisms involved in the early neck growth, as well as in surface smoothing and particle joining. If the material has a high vapour pressure, sublimation and vapour transport produce the same effects as surface diffusion. An increase of the density from only ca. 60 to ca. 65% of the theoretical density of the powder is observed, thus this stage does not result in any dimensional change.

In the intermediate stage (3) the grain growth onsets, and the creation of isolated pore structures occurs due to neck growth. Pores remain interconnected; therefore, the structure is not dense. Shrinkage and densification of the material start happening.

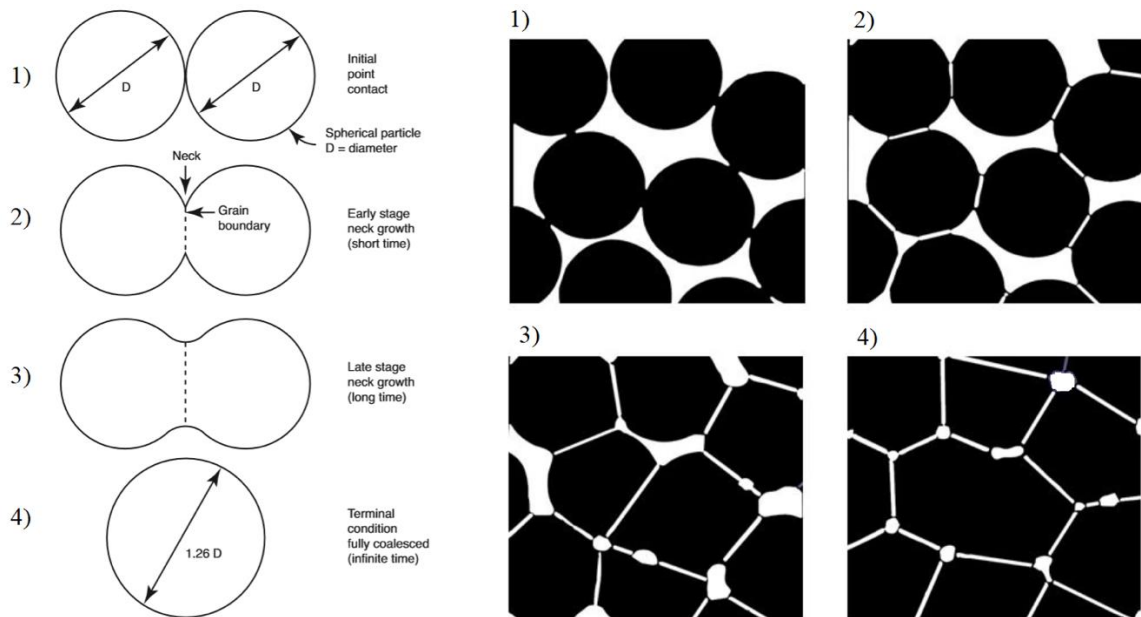


Fig. 4.6. Illustration of the sintering stages in two-spheres sintering model and multi-particle sketch. 1) green-state or loose powder, 2) initial neck growth, 3) onset of the grain growth and 4) grain growth and densification. [24]

In this stage, high green density could speed the sintering. Density increases up to ca. 90%. Bulk transport mechanisms, such as grain boundary diffusion, dominate this stage. Viscous flow has an important role if a liquid phase is present during the densification.

In the final stage (4) the pores collapse into closed spheres, generating grain growth. This stage usually leads to densification of the material, increasing the density from 95% to 99% of the theoretical density.

4.1.2.3 Sintering processes.

Solid-state sintering and liquid-phase sintering are two of the main sintering processes that can be usually found. Solid state sintering refers to the bonding and densification of a compact powder by the application of heat below the melting point of the material. Liquid-phase sintering involves a transient liquid phase that coexists with the solid-phase during the sintering. The liquid phase remains throughout all the sintering processes. The evolution of the sintering and microstructure is accelerated because of the fast material transport of the liquid. In the traditional liquid-phase sintering, the solid phase shows solubility in the liquid, but the reverse solubility of the liquid in the solid is low, which makes the liquid-phase not transient. [28,29]

Fig. 4.7. shows a binary phase-diagram where the composition and temperature associated to liquid-phase sintering corresponds to S_1+L and $L+S_2$ fields. S_1 and S_1+S_2 fields correspond to solid-state sintering processes. Fig. 4.7b and Fig. 4.7c shows the concept of liquid-phase sintering and solid-state sintering, respectively.

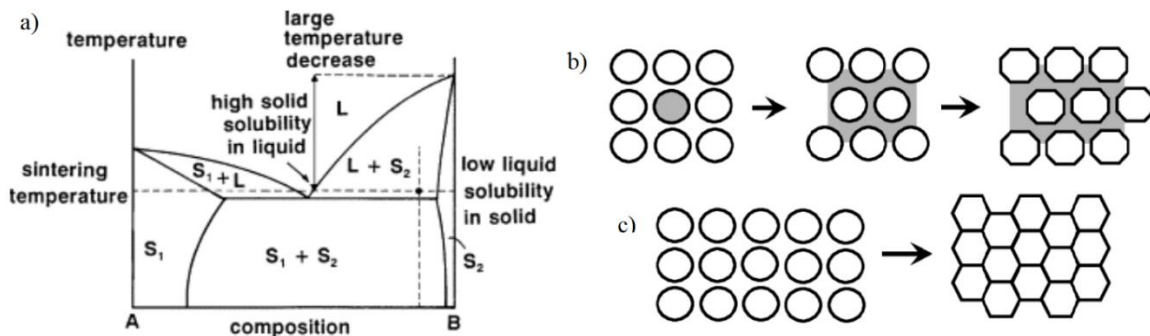


Fig. 4.7. Solid state and liquid-phase sintering. a) phase-diagram of a binary system showing solid-state and liquid-phase sintering fields; b) liquid phase sintering concept; c) solid-state sintering process. [30]

Additionally to solid-state and liquid-phase sintering, transient liquid phase and viscous flow sintering are other sintering categories. Viscous flow occurs when the volume of the liquid fraction is high enough to carry out the densification of a mixture without changing the grain shape. In the transient liquid phase sintering, a liquid phase forms in an early

stage of the sintering, but the liquid disappears during sintering processes. Then, the densification is completed by solid state sintering.

In this thesis, sintering of the tubular membranes was carried out after deposition of thin film membranes on the 3YSZ-based porous supports. Dwells of 2 hours at 360 °C and 600 °C were set to burn the organic phase of the dip-coated layers. After 600 °C, a single step up to sintering temperature was carried out using a heating rate of 60 °C·min⁻¹ or 200 °C·min⁻¹. Cooling rate of 120 °C·min⁻¹ was set in all the cases, as observed in Fig. 4.8.

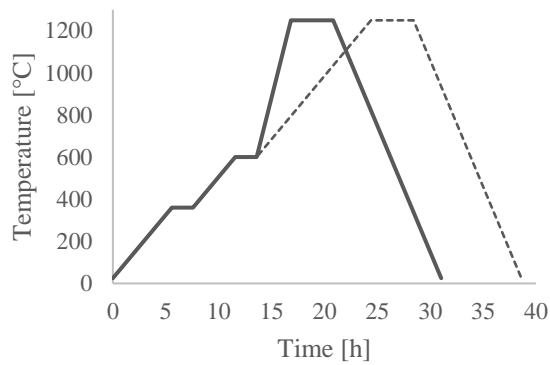


Fig. 4.8. Sintering profile of the thin oxygen membranes supported on 3YSZ-based tubes.

It is important to point out that this thesis work deals with co-sintering of different materials, which increases the degree of complexity since thermal expansion coefficients and reactivity among materials need to be taken into consideration. Thus, different sintering profiles and sintering temperatures were used, in order to obtain conditions that allows the fabrication of an unspoiled tubular membrane. The specific conditions are described in each section of Chapter 5.

4.1.3 Dip coating

Dip coating is a widely used thin-film deposition method due to its simple processing features, its low cost and its high coating quality. Practical applications can be found in fluorescent lights, circuit boards, biomedical equipment, as well as in nano-engineering of chemical conversion devices. Depending on the film precursor, thicknesses between 1 to 100 μm can be fabricated. This technique allows having good control of the film's thickness, and provides different microstructure features. [31,32]

4.1.3.1 Principle.

Dip-coating involves the deposition of a liquid film by immersion of a substrate in a precursor solution or a slurry and the subsequent withdrawal of the substrate from the coating media in a controlled way. After full withdrawal, the liquid-phase of the precursor is removed by evaporation to consolidate the film on the substrate. According to the nature of the deposited material, a further post-treatment, such as curing or sintering, might be performed, which implies a physical or chemical change of the film. Fig. 4.9 illustrates the dip-coating process. [33,34]

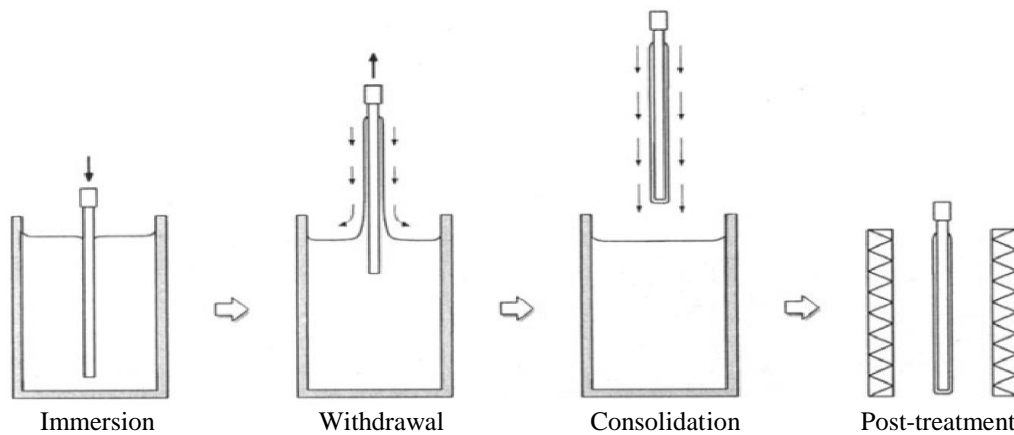


Fig. 4.9. Basic steps in sol-gel and slurry dip-coating. [34]

While the substrate is vertically withdrawn from the coating media at a constant speed, U_0 , two main forces interact and define the thickness of the wet film that is deposited on the substrate: the draining forces that drag the fluid from the substrate towards the coating media and the entering forces caused by the surface tension that retain the liquid on the substrate.

Fig. 4.10a shows the flow of the coating media on a moving substrate, where δ is the mechanical boundary layer of the coating media that interacts with the substrate. In the stagnation point, S , the draining and entering forces are in equilibrium. Below this point, the layers return back to the coating media. Above S , the entrained wet film remains on the substrate with a constant thickness, h_0 .

The wet film will show a dynamic drying above S , where solvent evaporates and drains to leave a gel-like layer behind in $x = 0$ (Fig. 4.10b). The simplest drying stage is the constant rate period, which is characterized by uniform evaporation of the solvent across

the entrained wet film. After most of the solvent is removed, the falling rate period occurs. In this stage the small amount of solvent trapped within the gel-alike is evaporated by diffusion of the solvent towards the surface.

The most complex processes in the drying stage occur at the drying front, at the interface between the wet film and the substrate interface. Here, the evaporation occurs at a higher rate, increasing the concentration of inorganic species of the film. As consequence, the solution is drawn from surrounding areas as result of the surface tension. This effect continues when the film dries, causing thickening of the film (Fig 4.10c)

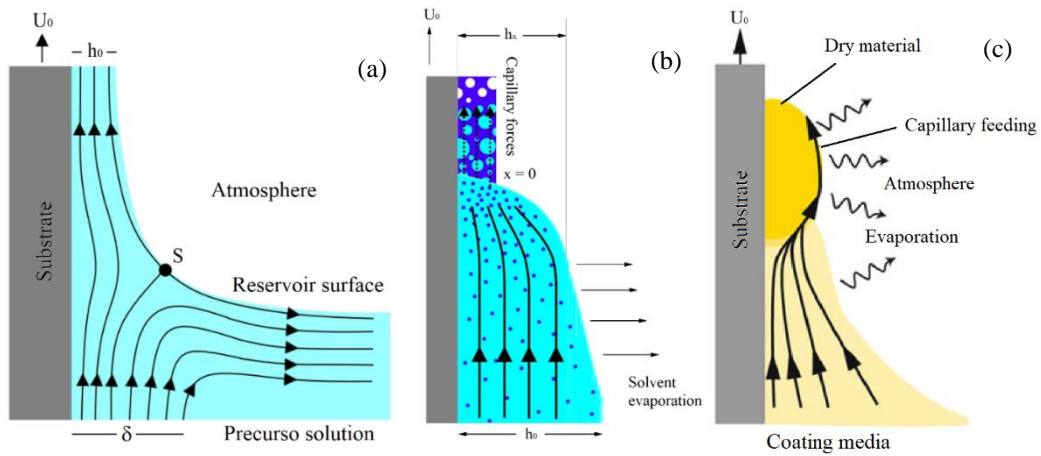


Fig. 4.10. Principles of dip coating a) Flow patterns during the dip-coating process b) Sequential structural development resulting from drying and evaporation of the solvent c) drying front and capillary regime. [33,34]

Three main regimens govern the thickness evolution of the film: Viscous flow, draining and capillary forces. In a viscous flow regime, high liquid viscosity, η , and high withdrawal speed U_0 , viscous drag (ηU_0) and gravity force (ρg) balance each other. The film thickness, h_0 , is given by:

$$h_0 = c \left(\frac{\eta U_0}{\rho g} \right)^{\frac{1}{2}} \quad \text{Eq. 4.1}$$

Where ρ is the density of the fluid, and the constant c is related to the rheological properties of the coating media. For most Newtonian fluids, this constant is approximately 0.8.

In situations when the viscosity of the coating media or the withdrawal speeds are not high enough, the viscous force becomes weaker and the balance between the entraining and draining forces is also dependant on the ratio of viscous drag to liquid-vapor surface

tension, γ_{LV} . This is called draining regime. In this case, the Landau-Levich equation for a Newtonian and non-evaporating fluid better describes the relation between the film thickness and the withdrawal speed by considering the surface tension,

$$h_0 = 0.94 \frac{(\eta U_0)^{\frac{2}{3}}}{\gamma_{LV}^{\frac{1}{6}} (\rho g)^{\frac{1}{2}}} \quad \text{Eq. 4.2}$$

This equation is usually applied when the withdrawal speeds are in the range 1-10 mm/s. However, when withdrawal speeds are even slower, below 0.1 mm/s, the capillary regime is used to describe the thickness of the film according to Eq. 4.3. In this case, additional factors need to be considered, such as the properties of the solution and the evaporation rate, E , of the solvent. A constant thickness of the wet film is not achieved in this regime, instead the dry film thickness after thermal treatment, h_f , is considered.

$$h_f = \frac{c_i M_i E}{\alpha_i \rho_i L U_0} \quad \text{Eq. 4.3}$$

Where c_i is the concentration of the inorganic phase in the coating media, M_i is the molar weight of the inorganic phase, ρ_i is the density of the inorganic material and α_i is the fraction of inorganic material in the film. L is the width of the film.

The dependence of film thickness on the withdrawal speed can be described by the combination of the drainage regime and the capillary regime equations, from which the minimum thickness can be obtained. Fig. 4.11 reveals that the two different coating regimes dominate and thickness of the film increases if the withdrawal speed is above or below the minimum.

Thus, the minimum thickness can be obtained from the overlap of the drainage and capillary regime equations. It is necessary to relate the wet film thickness of the Landau-Levich model (Draining regime) to the final dry thickness. This is done by including a material proportion constant, k_i , and a constant for the experimental physicochemical properties of the coating media, D .

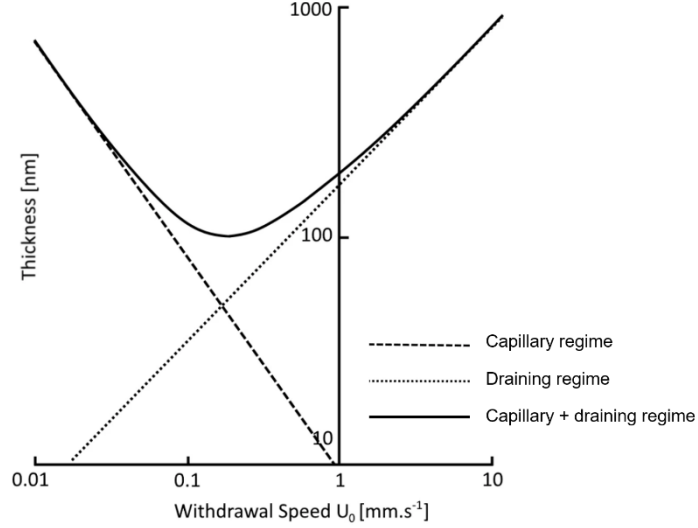


Fig. 4.11. Film thickness in relation with the withdrawal speed.

The obtained equation (Eq. 4.4) describes the final film thickness not considering the evaporation-dependant parameters, such as viscosity or surface tension.

$$h_f = k_i D U_0^{\frac{2}{3}} \quad \text{Eq. 4.4}$$

Summing up Eq.4.3 and 4.4,

$$h_f = k_i \left(\frac{E}{L U_0} + D U_0^{\frac{2}{3}} \right) \quad \text{Eq. 4.5}$$

By differentiating the thickness equation with respect to the withdrawal speed, U_0 , it is possible to obtain the minimum by setting $\frac{dh_f}{dU_0} = 0$, thus,

$$U_{min} = \left(\frac{2DL}{3E} \right)^{\frac{3}{5}} \quad \text{Eq. 4.6}$$

4.1.3.2 Equipment and settings used in this study.

Dip-coating of the functional layers was done using an in-house built dip-coater. [35] The withdrawal speed is controlled by a step engine, which allows a very precise control of the thickness and smoothness of the coatings. The maximum and minimum withdrawal rates are $2.5 \text{ cm}\cdot\text{s}^{-1}$ and $0.01 \text{ cm}\cdot\text{s}^{-1}$, respectively, with a maximum travel distance of 1 m. The software Faulhaber Motion Manager 5 was used to control the withdrawal rate.

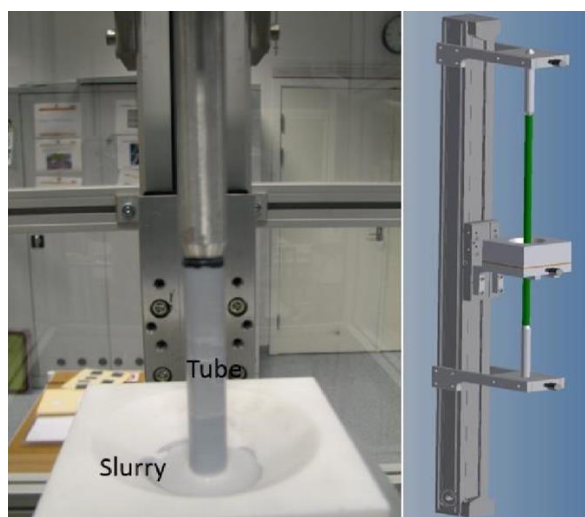


Fig. 4. 12. In house built dip-coater used for the development of the oxygen transport membranes.

The tubular porous supports were inserted through an opening using a silicon limb that conforms the basin or pool with the coating media (slurry). The porous support is held at the edges by rods. The slurry is poured in the pool before the start of the coating process. In this work, the withdrawal speed was set between 0.05 and $0.5 \text{ cm}\cdot\text{s}^{-1}$, in order to obtain films of a thickness of $4\text{-}10 \text{ }\mu\text{m}$ after drying.

4.1.3.3 Slurries composition.

The different dip coating slurries are made up of dispersants, binders, plasticizers, pore formers, a solvent and ceramic powders. The core components of dip-coating slurries for OTM layers are dispersed ceramic powder particles that will be homogeneously bound to the substrate by the binder, which will be removed during thermal treatment to form the porous or dense thin film layers on the support tube.

Table 4.3. Formulation of the active membrane and porous activation layers slurries

Function	Dense membrane	wt. %	Porous layer	wt. %
Solvent	Ethanol	67.5	Ethanol	61.8
Oxides	ScYSZ-LCCN (Fe)	28.6	ScYSZ, ScYSZ-LCCN, ScYSZ (Fe)	25.8
Dispersant	PVPK15	1.5	PVPK15	1.3
Binder	PVPK30	1.5	B30HH	3.1
Plasticiser	--		DBS	2.2
Pore former	--		Graphite UF-1	5.8

Table 4.3 shows the base compositions of the dense and porous slurries used in this work. More details on specific formulations for the experiments to produce different thin film catalytic and membrane layers are described in Chapter 5.

4.2. Materials and membranes characterisation techniques

This section lists and describes the experimental details of the characterization techniques to analyse raw materials, porous supports and the complete set of multilayer oxygen membranes. It also gives a brief description of relevant analysis techniques, such as oxygen flux measurements.

4.2.1 X-ray diffraction

X-ray diffraction analysis was mainly used for the identification of phase compositions in the pristine powders and in dual-phase composites after sintering in air. In some cases, Rietveld refinements were done. Two X-ray diffractometers were used:

- 1) D8 X-ray diffractometer (Bruker, Germany). XRD diffractograms were obtained varying 2θ in the interval $10^\circ - 90^\circ$ with a step width of 0.019° , a voltage of 40 kV and a current of 40 mA. This diffractometer was used for phase identification in pristine LCCN powder after sintering at 1300°C in air and after subsequent reduction at 900°C in $5\%\text{H}_2\text{-N}_2$. Rietveld refinements was done in these powders to identify changes in the lattice parameters. Phase identification of ScYSZ-LCCN, YCCC, and CGO-YCCC composites was also performed after sintering at 1300°C in air.
- 2) A high-Temperature XRD analysis was done, using a high resolution X-ray diffractometer Rigaku Smartlab varying 2θ in the interval 10° to 140° with a step width of 0.0152° , counting 8553 steps for the complete interval. The voltage was 40 kV at a current of 200 mA. 27 XRD measurements were taken in intervals between room temperature (RT) and 1100°C with steps of 100°C (RT – 600°C), 50°C (600°C – 900°C) and 25°C (900°C – 1100°C).

4.2.2 Particle size distribution

Particle size measurements of the powders for the porous supports and the dip-coating slurries were measured by a laser diffraction particle size analyser LS 13 320 (Beckman Coulter, USA), using ethanol as vehicle and a 5 mW laser diode with a wavelength of 750 nm (or 780 nm) as the main illumination source.

Laser diffraction measures particle size by scattering of the intensity of a monochromatic beam as function of scattering angle, wavelength, and polarization light when it interacts with the particles. Larger particles scatter light at small angles while smaller particles scatter light at larger angles. The unique angular scattering patterns are transformed into a special intensity pattern that is detected by a photo-detector array, and converted into a particle size distribution. The particle size is reported as a volume equivalent sphere diameter. [36,37]

Monitoring of the particle size was done during preparation of the powders or slurries after different ball milling times. For measuring the size of the ceramic particles in the slurries, the measurements were taken before final addition of pore formers to the formulation. A mean particle size of ca. 250 nm was set for the dual-phase composite. In the case of 3YSZ particles for the porous support, the particle size was adjusted for a $d_{V90} < 1 \mu\text{m}$ and a $d_{V50} < 0.3 \mu\text{m}$.

4.2.3 Dilatometry

Dilatometry is a thermo-analytical technique that consists in monitoring one dimension of the sample as a function of temperature or time (dilatation), under controlled conditions of temperature and atmosphere. The collected data will provide information regarding the thermal behaviour of the sample, such as thermal expansion, sintering shrinkage, softening point, etc. A sample, usually a rod of known length and section area, is inserted into a sample holder and brought into contact with a pushrod. The sample then is subjected to heating under controlled temperature and atmosphere conditions. The expansion or contraction of the sample is detected by the displacement transducer system that is connected to the pushrod, as visualized in Fig. 4.13. The parameters in a dilatometer measurement are the length change, the time and the temperature, which can then be subjected to analysis and interpretation. [38]

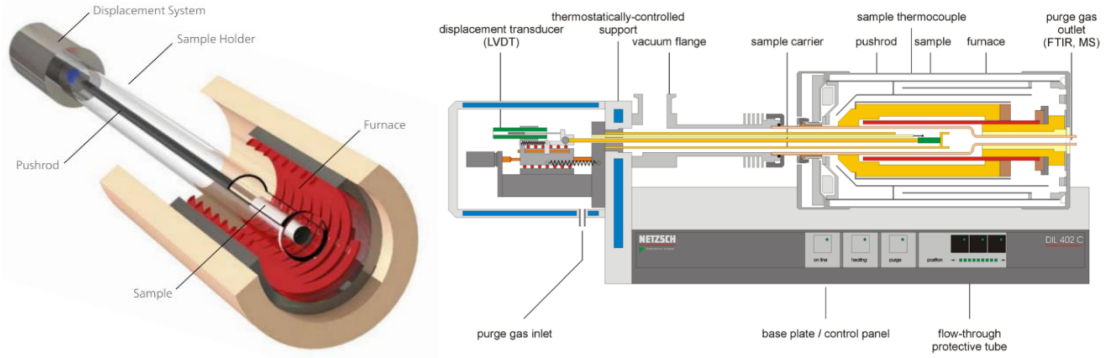


Fig. 4.13. Diagram showing the components of the dilatometer DIL402C. [38]

The length strain, ε_l , is calculated dividing the length change by the initial length, l_0 , according to:

$$\varepsilon_l = \frac{l - l_0}{l_0} = \frac{\Delta l}{l_0} \quad \text{Eq. 4.7}$$

Similarly, the diameter strain, ε_d , can be obtained:

$$\varepsilon_d = \frac{d - d_0}{d_0} = \frac{\Delta d}{d_0} \quad \text{Eq. 4.8}$$

When $\varepsilon_l = \varepsilon_d$, the material is called isotropic. In the case of an anisotropic material, the length and diameter strains are different, $\varepsilon_l \neq \varepsilon_d$. Anisotropic behaviour can occur due to inhomogeneous chemistry or due to preferred crystallographic orientations. [39]

The coefficient of thermal expansion (TEC), α , is a parameter used to express the dimensional change of a material in response to a specific change in temperature. [40] The strain is given by an initial strain, ε_0 , the TEC, α , and a reference temperature, T_0 , according to:

$$\varepsilon(T) = \varepsilon_0 + \int_{T_0}^T \alpha(T) dT \quad \text{Eq. 4.9}$$

In general, the TEC is given by,

$$\alpha(T) = \frac{d\varepsilon}{dT} = \frac{dl}{l_0 dT} \quad \text{Eq. 4.10}$$

This is called the physical coefficient of expansion, which denotes the change of length in an infinitesimal small temperature interval. However, in most of the cases the TEC is expressed as the change in a larger interval of temperature, which is called technical

coefficient of thermal expansion. Within a temperature interval T_1 and T_2 , the technical TEC is expressed as:

$$\alpha_{T_1}^{T_2} = \frac{\Delta l}{\Delta T} \cdot \frac{1}{l_0} \quad \text{Eq. 4.11}$$

Sintering curves and thermal expansion coefficients of the composites and single-phase powders were obtained using a dilatometer DIL402CD (Netzsch, Germany) in differential mode, using 4 mm long alumina rods as reference. Air at a constant flow rate of $20 \text{ ml}\cdot\text{min}^{-1}$ was used in all the tests.

The sample measurements were done using 1 cm long pellets prepared by cold uniaxial pressing using a 6 mm diameter die and a pressure of $1 \text{ ton}\cdot\text{cm}^{-2}$. For the sintering curves, as-prepared pellets were heated with a rate of $1 \text{ }^\circ\text{C}\cdot\text{min}^{-1}$ up to $1250 \text{ }^\circ\text{C}$ followed by cooling, using a ramp of $10 \text{ }^\circ\text{C}\cdot\text{min}^{-1}$.

For TEC measurements, as-prepared pellets were sintered in a chamber furnace in stagnant air at $1350 \text{ }^\circ\text{C}$ for 2 hours using heating and cooling ramps of $1 \text{ }^\circ\text{C}\cdot\text{min}^{-1}$ and of $2 \text{ }^\circ\text{C}\cdot\text{min}^{-1}$, respectively. TEC measurements were obtained using heating and cooling ramps of $2 \text{ }^\circ\text{C}\cdot\text{min}^{-1}$ with a 1 dwell at $1250 \text{ }^\circ\text{C}$. Analysis of the dilatometry data was done using Netzsch Proteus software.

4.2.4 Scanning electron microscopy

Microstructural analysis of the different components of the membrane, porous support, porous activation layers and active membrane, as well as the interaction between these layers during sintering, was done by using two different scanning electron microscopes (SEM):

A SEM TM3000 (Hitachi, Japan) was used, working with secondary electron detectors and accelerating voltage of 15 kV. An EDS (Quantax70) integrated to the SEM TM3000 was used for composition analysis. This SEM was mainly used to observe the microstructure of the support and the membranes.

A Zeiss Merlin field emission scanning electron microscope (FE-SEM), working with secondary and backscattered electron detectors and accelerating voltage of 15 kV, was used for the microstructural analysis of the samples. Elemental analysis of the fresh and

sintered powders was performed using a EDS X-Flash 6|60 working at 15 kV and 176 pA. This microscope was used for elemental composition analysis within the membrane. Image J (open source software) was used for all SEM data analyses to determine porosity of the porous supports.

4.2.5 Viscosity

One of the parameters that defines the characteristics of dip-coated films is viscosity. This was measured as a control parameter of the correct preparation of the dip-coating slurries and to determine their rheological behaviour.

The viscosity of a fluid, η , represents the fluid's resistance to a gradual deformation by the shear stress, τ . Shear stress can be defined as the force, F , applied in a shear area, A , according to,

$$\tau = \frac{F}{A} \quad (\text{Eq. 4.12})$$

If shear stress, τ , is applied to a liquid between two plates with area A separated by a distance, d , at a certain velocity, v , the deformation of the fluid will be given at a certain shear rate, $\dot{\gamma}$, according to,

$$\dot{\gamma} = \frac{v}{d} \quad (\text{Eq. 4.13})$$

Under shear stress, τ , the viscosity, η , will be related to the shear rate, $\dot{\gamma}$, according to,

$$\eta = \frac{\tau}{\dot{\gamma}} \quad (\text{Eq. 4.14})$$

If the viscosity is independent of the shear rate (i.e. the relation between the shear rate and the shear stress is linear), the flow of the fluid will be Newtonian. [41] The behaviour of Newtonian fluids is relatively simple and are easy to work with since they do not change with the shear rate, allowing good control of the thickness of thin films.

An MCR302 Rheometer (Anton Paar, Austria) with a 25 mm stainless steel parallel plate (PP25) was used to determine the viscosity and the rheological behaviour of the dip-coating slurries. The gap between the PP50 and the rheometer's fixed plate was set at 0.5

mm. Viscosity was measured in a shear rate interval between 1 s^{-1} and 100 s^{-1} . The used measuring method to determine the viscosity during the preparation of the solutions was the FFT (Fast Fourier Transformed) smoothing. Measurements were done by depositing ca. 1 ml of dip-coating slurry on the plates and using a chamber saturated with ethanol to minimize the evaporation of the slurry during the measurement. The powder slurries for the dense membranes and catalytic (activation) layers behaved as Newtonian fluids.

4.2.6 Hg-porosimetry

Porosimetry was used to determine the total porosity and the porosity-related characteristics of the sintered 3YSZ porous supports. Hg-porosimetry uses the non-wetting properties of mercury (Hg). Hg will not spontaneously penetrate into the pores of a material due to capillary action and it requires the application of an external pressure to be forced into the pores. [42] Given an specific pressure, P , the mercury will intrude the pores with larger diameter, D , according to,

$$D = -\frac{4\gamma\cos\theta}{P} \quad \text{Eq. 4.15}$$

Where γ is the surface tension of the Hg of 0.48 J.m^{-2} , and θ is the solid-liquid contact angle of the Hg with the substrate (140°). Then, the volume of the pores of each size class can be calculated by measuring the volume of Hg that intrudes into the pores at a determined pressure.

Samples of 3YSZ, 3YSZ+1 mol% Fe_2O_3 and + 3 mol% Fe_2O_3 were analysed through Hg-intrusion using an automatic pore size analyser PoreMaster 33 (Quantachrome Instruments, Boynton Beach, FL, USA).

4.2.7 Flexural strength of porous supports

Mechanical strength for an oxygen separation device (i.e. an OTM) is an important factor to be considered because the membranes need to withstand different stresses, such as pressure and thermal gradients. Flexural strength is the ability of a material to resist deformation under load. In the case of ceramic materials, which are brittle, this deformation usually leads to fractures. One of the methods to calculate the flexural strength is the 4-point bending technique. In this, a sample with known dimensions is placed on a span, then pushed down along the span to deform the material until failure.

[3,43] In 4-point bending tests 2 pins are used as supports and 2 pins to apply the load, as shown in Fig.4.14a. The maximum stress for a semi-circular tube can be calculated by,

$$\sigma_{max} = \frac{P a y_c}{I} \quad \text{Eq. 4.16}$$

Where P is the applied load, a is the distance between load and support pins, 12.5 mm, y_c is the distance between the support pin and the centroid of the specimen along the y-axis, I is the second moment of area of the cross section. I and y_c are given by the following equation, where R is the external radius and R_i the inner radius of the semi-circular tube.

$$I = \frac{\pi}{8} (R^4 - R_i^4) - \frac{8 (R^3 - R_i^3)^2}{9\pi (R^2 - R_i^2)} \quad \text{Eq. 4.17}$$

and

$$y_c = R - \frac{4}{3\pi} \frac{R^3 - R_i^3}{R^2 - R_i^2} \quad \text{Eq. 4.18}$$

Flexural strength of the porous supports was tested using four-point bending of a number of specially prepared samples. The test rig, the methodology and the peak stress data analysis is fully described by Kwok et al. [43].

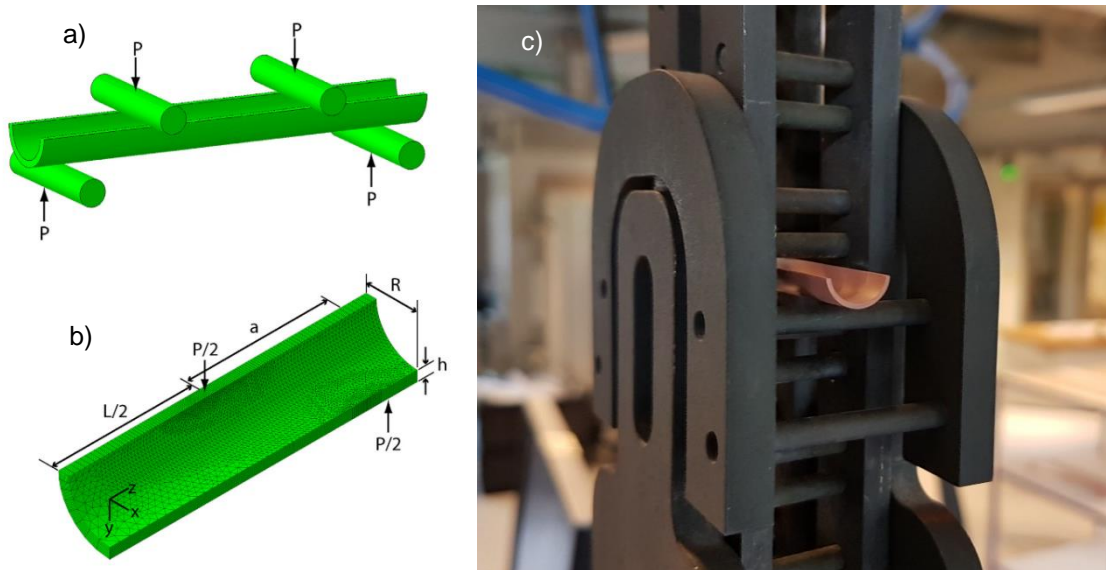


Fig. 4.14. 4-point bending testing. a) Test configuration of 4-point bending of a semi-cylindrical specimen, 2) finite element mesh of a quarter of specimen, c) mounting of a 3YSZ sample in the testing rig. [40]

6 cm long tubes were longitudinally diamond saw-cut by the half to obtain semi-cylindrical pieces. At least 6 pieces of each PS, 3YSZ, 3YSZ + 1 mol% Fe_2O_3 (3YSZ-Fe1) and 3YSZ + 3 mol% Fe_2O_3 (3YSZ-Fe3) were tested, in order to obtain representative data. A maximum load of 10 N was applied during the tests at room temperature. A

minimum flexural strength of 50 MPa was required for the tubular supports to be used in this thesis work.

4.2.8 Gas permeability of porous supports

Gas permeability tests were carried out to ensure that the 3YSZ-based porous supports do not limit the diffusion of the gases from the bulk gas to the active sites of the oxygen membranes. Permeability of the tubular porous supports was measured considering Darcy's law, which describes the flow of a fluid through permeable granular porous media. It states that the flow rate of a single phase fluid through a porous medium is proportional to the potential energy within the fluid according to Eq. 4.19:

$$Q = \frac{Ak\Delta P}{\mu\Delta L} \quad (\text{Eq. 4.19})$$

Where Q is the flow [$\text{m}^3\cdot\text{s}^{-1}$], A is the cross section area to flow [m^2], ΔP is the pressure drop [Pa], k is the intrinsic permeability of the medium [m^2], μ the viscosity of the fluid [$\text{Pa}\cdot\text{s}$], and ΔL is the length where the pressure drop occurs [m]. [44].

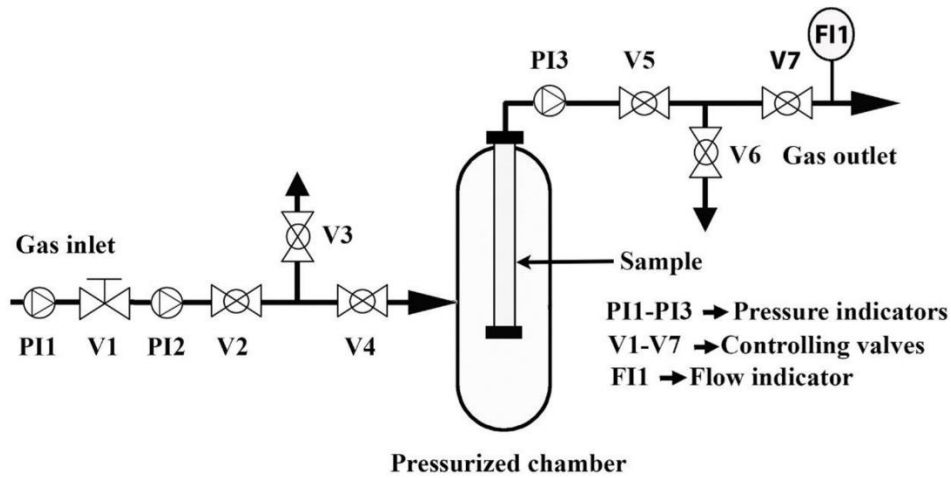


Fig. 4.15. Schematics of the Darcy's gas permeation setup. [42]

Measurements were performed in an in-house built rig with a process diagram as depicted in Fig. 4.15. It consists of a pressurised chamber where a capped section of the sample is set. Manometers indicate the inlet and outlet pressures. A pressure difference across the samples was created using an electro-pneumatic pressure controller (Tescom, ER3000, USA). A flowmeter (Agilent, USA) measures the permeated flow through the sample.

For the measurements, N₂ was used from 0.23 to 4 bars at room temperature in 1 cm and 0.7 cm sections of the 3YSZ-based porous supports. k values larger than 10^{-14} m² would provide sufficient gas permeability from the bulk to the membrane and avoid limitation in the gas supply to the membrane. [45].

4.2.9 Oxygen permeability

Two different setups were used for the oxygen flux characterization. The testing rigs are referred as “oxygen-flux rig” and “tars partial oxidation unit”.

4.2.9.1 Oxygen-flux rig

The oxygen flux rig is an in-house built open flow rig with high control of flows, pO₂ and temperatures. The feeding of the gases was controlled by individual Brooks mass flow controllers calibrated for each gas. A diagram of the rig is shown in Fig. 4.16. The rig consists of two alumina tubes that act as holders to set the sample in the hot zone of a vertical furnace. Temperature was monitored at the inlet and the outlet of the membrane in the sweep gas side by two thermocouples. Oxygen partial pressure, pO₂, was constantly monitored by two pO₂ sensors located at the inlet and outlet of the membrane. The membrane was sealed to the alumina holders using YS2B glass, with composition SiO₂, 67.94 wt.%, Al₂O₃, 14.91 wt.%, and Na₂O, 17.14 wt.%. For sealing, the glass was heated up to 1000 °C using a rate of 1 °C·min⁻¹. The glass sealing was kept for 2 hours at this temperature before the samples were cooled down to 850 °C.

In order to verify the gas tightness, N₂ was feed in the permeate side and the gas flow was monitored at the inlet and outlet of the membrane. At flow differences below 3% the membrane was considered to be gas tight. The air in the permeate side was set to 1 l·min⁻¹ for all the tests.

The gas flows of permeate N₂, CO₂, CH₄, 5% H₂N₂ and H₂ were set between 24 ml·min⁻¹ and 500 ml·min⁻¹ and the gases were fed to the rig at 850 °C, 900 °C and 950 °C. Between each change of gas, a measurement of the N₂/Air gradient at 850 °C was carried out, in order to compare the effect on the performance of the membrane.

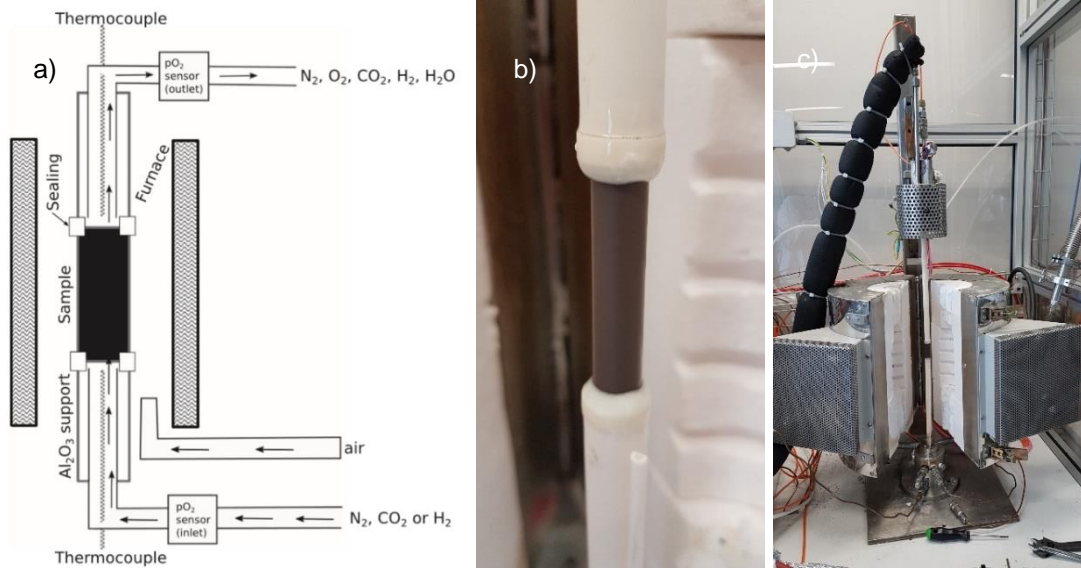


Fig. 4.16. Open flow oxygen-flux rig a) a schematic diagram showing the gas flow and the components [46]; b) a picture of the sample after mounting in the rig, c) the entire rig with a detail of the sample mounted along the alumina tubes.

The oxygen flux was calculated according to Eq. 20 [47],

$$J_{O_2} = \frac{\phi_{in}(pO_{2(out)} - pO_{2(in)})}{A} \quad (\text{Eq. 4.20})$$

Where J_{O_2} is the oxygen flux [$\text{ml} \cdot \text{min}^{-1} \cdot \text{cm}^{-2}$], A is the active surfaced area of the membrane [cm^2], ϕ_{in} is the total gas flow at the inlet of the membrane [$\text{ml} \cdot \text{min}^{-1}$], $pO_{2(out)}$ and $pO_{2(in)}$ are the oxygen partial pressures at the outlet and inlet of the membrane, respectively. The oxygen flux of the membrane under a H_2 /Air gradient was calculated using Eq. 3 [Ovtar], where $\phi_{H_2O}^{out}$ and $\phi_{H_2O}^{in}$ are the flow rates of produced water [$\text{ml} \cdot \text{min}^{-1}$], considering that the reaction $H_{2(g)} + O_{2(g)} \rightarrow H_2O_{(g)}$ is in equilibrium and can be described with a known equilibrium constant, $K_{eq}(T)$.

$$J_{O_2} = \frac{\phi_{H_2O}^{out} - \phi_{H_2O}^{in}}{A} \quad (\text{Eq. 4.21})$$

4.2.9.2 The unit for partial oxidation of tars.

The in-house-built tars partial oxidation unit consists of an open flow setup adjacent to a LT-CFB gasifier (DTU Chemical Engineering). The rig is capable of working with different sweep gases, such as producer gas, H_2 , 5% H_2 - N_2 , and H_2 . The change and regulation of the flow is done manually. A simplified process diagram of the tars partial oxidation unit with the main components is shown in Fig. 4.17.

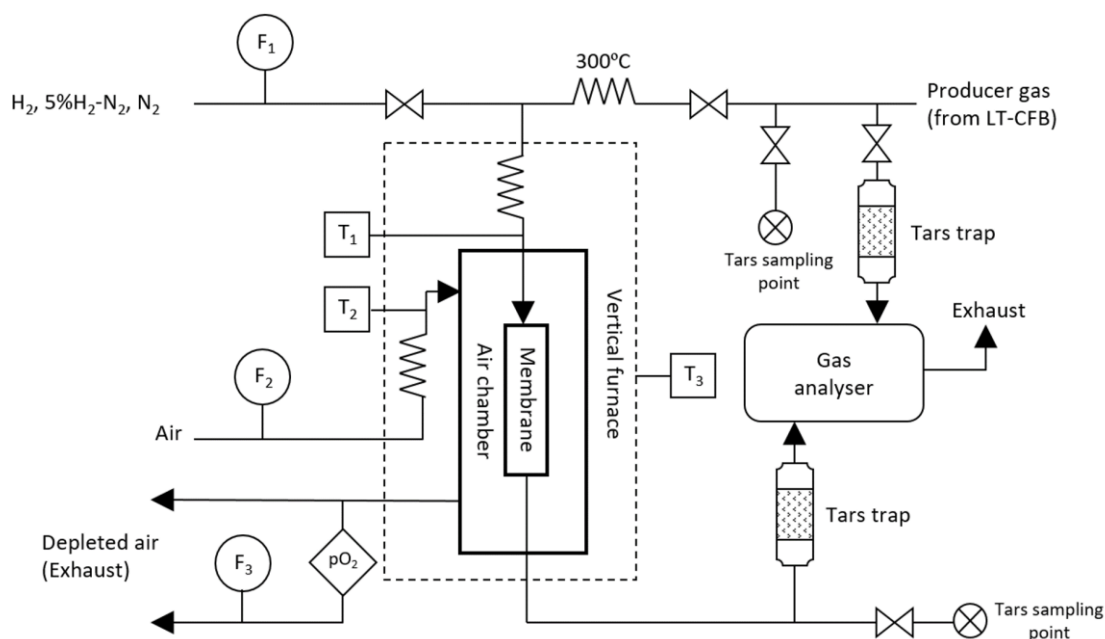


Fig. 4.17. Process diagram of the membrane unit for partial oxidation of tars. F: flowmeter, T: thermocouple, pO₂: Zirconia pO₂ sensor.

The rig consists of two alumina tubes that act as holders to set the sample in the hot zone of a vertical furnace, as seen in Fig. 4.18. Alumina spacers pre-sealed on Kanthal® holders are fixed to the Inconel fittings of the testing setup. The oxygen membrane is set between the alumina spacers and placed in the hot-zone of a vertical furnace. A YS2B glass powder was applied to the contact area between the membrane and the alumina spacers and sealed at 850°C with a heating rate of 5 °C·min⁻¹ and under compression, using a 1 kg load provided by a pulley and a counterweight system on the top of the system.

The membrane was covered by a stainless steel cylinder, where the feed gas flowed, the so-called “air chamber”. At the output of the air chamber, a sampling line for the measurement of the oxygen partial pressure was set, so the rest of the oxygen-depleted air could freely leave the unit. The lower part of the cylinder was open. The unit counts with two preheating systems for the feed gas (air) and the permeate gas (producer gas, H₂, N₂) that surround the air chamber using a spring-alike heat exchanger. Three gasometers were installed to measure the gas flow between 0.25 to 100 Nl·min⁻¹ for air (IGA Type AC-5M B733), H₂/N₂ (IGA Type AC-5M B733) and the depleted air into the pO₂ sensor (Gallus 2100 TCE – G4 T).

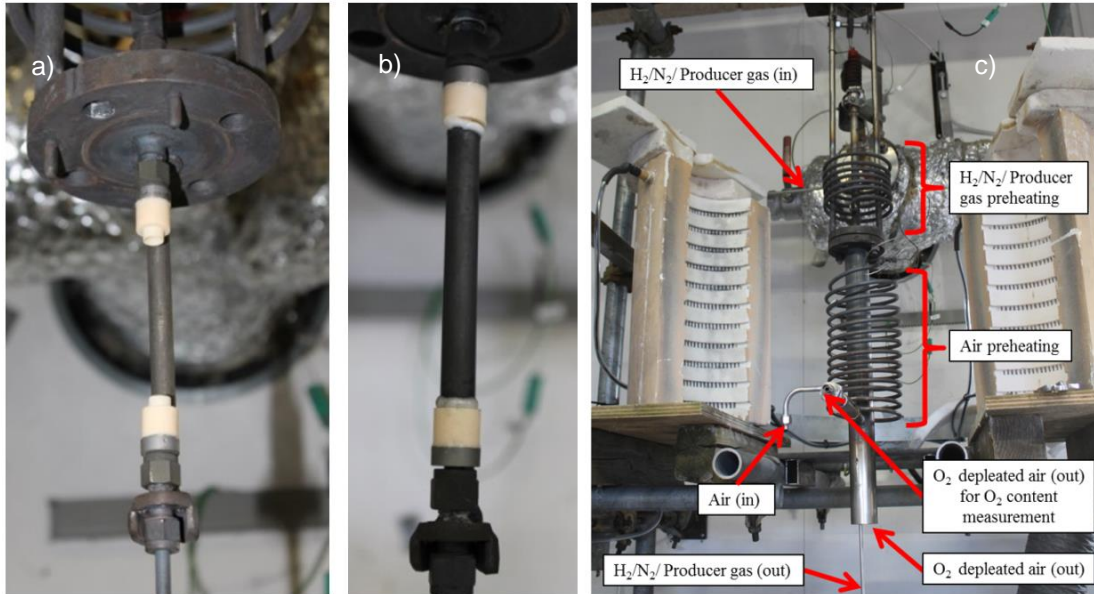


Fig. 4.18. a) detail of the Kanthal® holders and the alumina spacers, b) picture of the membrane mounted in the unit, c) Main components of the membrane unit for partial oxidation.

The system is equipped with three thermocouples to measure the inlet air temperature, the N₂/H₂/producer gas inlet temperature and the furnace temperature. Additionally, the temperature of the producer gas before and after the main valve of the side stream was measured. To prevent condensation of tars, the connecting part between the producer gas stream and the gasifier testing unit was heated to ca. 300 °C.

During the test, pre-heated air with a flowrate of 3 l·min⁻¹ was supplied to the feed side of the oxygen membrane. At the output of the air chamber, a sample of oxygen-depleted air (100 – 250 ml·min⁻¹) was pumped through an in-house built ZrO₂-based oxygen sensor to monitor the change of oxygen concentration in air. Different tests were conducted by feeding N₂, H₂ and producer gas in the sweep side of the membrane. The complete testing sequence and flows are described in the Section 5.1.

The oxygen permeation flux was calculated using the pO₂ at the output of the depleted air side, according to:

$$J(O_2) = \frac{pO_2(air) - pO_2(outlet)}{A} \quad (\text{Eq. 4.22})$$

pO₂(air) and pO₂(outlet) are the oxygen partial pressures of air (0.205 atm) and the oxygen-depleted air at the outlet, respectively. A is the area of the tube, which is estimated to be 35 cm².

References.

- [1] Hill, R.G. *Polymers in Biomaterials, Artificial Organs and Tissue Engineering* — 2005, pp. 37-47. DOI: 10.1533/9781845690861
- [2] Rosato, D.V.; Rosato, D.V.; Rosato, M.V. *Extrusion. Plastic Product Material and Process Selection Handbook* — 2004, pp. 227-281. DOI: 10.1016/b978-1-85617-431-2.x5000-2
- [3] Haugen, A.B.; Martinez Aguilera, L.; Kwok, K.; Molla, T.; Andersen, K.B.; Pirou, S.; Kaiser, A.; Hendriksen, P.V.; Kiebach, R. *Exploring the Processing of Tubular Chromite- and Zirconia-Based Oxygen Transport Membranes. Ceramics* — 2018, Volume 1, Issue 2, pp. 229-245. DOI: 10.3390/ceramics1020019
- [4] Crowley, M.M.; Zhang, F.; Repka, M.A.; Thumma, S.; Upadhye, S.B.; Battu, S.K.; McGinity, J.W.; Martin, C. *Pharmaceutical applications of hot-melt extrusion: Part I. Drug Development and Industrial Pharmacy* — 2007, Volume 33, Issue 9, pp. 909-926. DOI: 10.1080/03639040701498759
- [5] *Extrusion moulding process for plastic machining. Manufacturing Technology TechMiny. 2018.* <https://techminy.com/extrusion-moulding/>
- [6] Gonzalez-Gutierrez, J.; Cano, S.; Schuschnigg, S.; Kukla, C.; Sapkota, J.; Holzer, C. *Additive manufacturing of metallic and ceramic components by the material extrusion of highly-filled polymers: A review and future perspectives. Materials* — 2018, Volume 11, Issue 5, pp. 840. DOI: 10.3390/ma11050840
- [7] Trunec, M.; Cihlar, J. *Thermal removal of multicomponent binder from ceramic injection mouldings. Journal of the European Ceramic Society* — 2002, Volume 22, Issue 13, pp. 2231-2241. DOI: 10.1016/s0955-2219(02)00015-8
- [8] Kothanda Ramachandran, D.; Clemens, F.; Glasscock, J.; Søggaard, M.; Kaiser, A. *Tailoring the microstructure of porous MgO supports for asymmetric oxygen separation membranes: Optimization of thermoplastic feedstock systems. Ceramics International* — 2014, Volume 40, Issue 7, pp. 10465-10473. DOI: 10.1016/j.ceramint.2014.03.017

- [9] Haugen, B.A.; Gorauskis, J.; Kaiser, A.; Sjøgaard, M. Graphite and PMMA as pore formers for thermoplastic extrusion of porous 3Y-TZP oxygen transport membrane supports. *European Ceramic Society. Journal* — 2016, Volume 37, Issue 3, pp. 1039-1047. DOI: 10.1016/j.jeurceramsoc.2016.10.001
- [10] Zhou, J.C.; Huang, B.Y.; Wu, E.X. Extrusion moulding of hard-metal powder using a novel binder system. *Journal of Materials Processing Technology* — 2003, Volume 137, Issue 1-3, pp. 21-24. DOI: 10.1016/S0924-0136(02)01058-0
- [11] Clemens, F. thermoplastic extrusion for ceramic bodies. *Extrusion in ceramics. Engineering material and processes.* Springer — 2007, pp. 295-311.
- [12] Dupont Elvax 250 ®. Elvax Resin Data Sheet. DuPont Packaging & Industrial Polymers.
- [13] Marín, M.L.; Jiménez, A.; López, J.; Vilaplana, J. Thermal degradation of ethylene (vinyl acetate): Kinetic analysis of thermogravimetric data. *Journal of Thermal Analysis* — 1996, Volume 47, Issue 1, pp. 247-258. DOI: 10.1007/bf01982703
- [14] Costache, M.C.; Jiang, D.D.; Wilkie, C.A. Thermal degradation of ethylene-vinyl acetate copolymer nanocomposites. *Polymer* — 2005, Volume 46, Issue 18, pp. 6947-6958. DOI: 10.1016/j.polymer.2005.05.084
- [15] Paraffin wax, Product specification. Sigma-Aldrich, USA.
- [16] Jaw, K.S.; Hsu, C.K.; Lee, J.S. The thermal decomposition behaviors of stearic acid, paraffin wax and polyvinyl butyral. *Thermochimica Acta* — 2001, Volume 367, pp. 165-168. DOI: 10.1016/S0040-6031(00)00680-8
- [17] Ismael, M.R.; Clemens, F.; Graule, T.; Hoffmann, M.J. Effects of different thermoplastic binders on the processability of feedstocks for ceramic co-extrusion process. *Ceramics International* — 2011, Volume 37, Issue 8, pp. 3173-3182. DOI: 10.1016/j.ceramint.2011.05.084
- [18] Zhang, G.; Wen, M.; Wang, S.; Chen, J.; Wang, J. Insights into thermal reduction of the oxidized graphite from the electro-oxidation processing of nuclear graphite

- matrix. *Rsc Advances* — 2018, Volume 8, Issue 1, pp. 567-579. DOI: 10.1039/c7ra11578d
- [19] Crumpton, D.M.; Laitinen, R.A.; Smieja, J.; Cleary, D.A. Thermal analysis of carbon allotropes: An experiment for advanced undergraduates. *Journal of Chemical Education* — 1996, Volume 73, Issue 6, pp. 590-591. DOI: 10.1021/ed073p590
- [20] Poly(methyl methacrylate). Wikipedia.
- [21] Gałka, P.; Kowalonek, J.; Kaczmarek, H. Thermogravimetric analysis of thermal stability of poly(methyl methacrylate) films modified with photoinitiators. *Journal of Thermal Analysis and Calorimetry* — 2014, Volume 115, Issue 2, pp. 1387-1394. DOI: 10.1007/s10973-013-3446-z
- [22] Poomalai, P.; Varghese, T.O. Thermomechanical Behaviour of Poly(methyl methacrylate)/Copoly(ether-ester) Blends. *Isrn Materials Science* — 2011, Volume 2011, pp. 1-5. DOI: 10.5402/2011/921293
- [23] Giles, H.F.; Mount, E.M.; Wagner, J.R. *Extrusion: The Definitive Processing Guide and Handbook*. PDL Handbook Series — 2005, pp. 65 – 73.
- [24] Fang, Z.Z. *Sintering of Advanced Materials*. Woodhead Publishing — 2010, pp. 1-483. DOI: 10.1533/9781845699949
- [25] German, R.M. Sintering simplified: Surface area, density, and grain size relations. *Materials Science Forum* — 2016, Volume 835, pp. 50-75. DOI: 10.4028/www.scientific.net/msf.835.50
- [26] De Jonghe, L.C.; Rahaman, M.N. Chapter 4 - 4.1 Sintering of Ceramics. *Handbook of Advanced Ceramics*. Academic Press — 2003. DOI: 10.1016/B978-0-12-654640-8.X5000-7
- [27] Derlet, P.M. *Sintering theory*. Condensed Matter Theory. Paul Scherrer Institut. 2017.

- [28] German, R.M.; Liquid Phase Sintering: Metals. Encyclopedia of Materials: Science and Technology – 2001, pp. 4601-4603. DOI: 10.1016/B0-08-043152-6/00802-0
- [29] Kang, S.J.L. Sintering Processes. Sintering Densification, grain growth and microstructure — Elsevier, 2005, pp. 3-8. DOI: 10.1016/b978-075066385-4/50001-7
- [30] Halim, J. Synthesis and transport properties of 2D transition metal carbides (MXenes). Diss. Linköping University, 2018.
- [31] Puetz, J; Aegerter, M.A. Dip-coating technique. Sol-gel technologies for glass producers and users. Springer Science – 2004, pp. 37-48 DOI: 10.1007/978-0-387-88953-5_3
- [32] Cheng, S. (2015). Oxygen transport membranes for biomass gasification and cement industry. Roskilde: Department of Energy Conversion and Storage, Technical University of Denmark.
- [33] Brinker, C.J. Dip coating. Chemical Solution Deposition of Functional Oxide Thin Films. Springer — 2013, pp. 233-261. DOI: 10.1007/978-3-211-99311-8_10
- [34] Dip Coating Theory: Film Thickness. Ossila, Ltd. <https://www.ossila.com/pages/dip-coating-theory-film-thickness#Overview>
- [35] Kothanda Ramachandran, D. (2014). Experimental extrusion of tubular multilayer materials for Oxygen Transport Membranes. Diss. Department of Energy Conversion and Storage, Technical University of Denmark.
- [36] Pirou, S. Development of Dual-Phase Oxygen Transport Membranes for Carbon Capture Processes. Diss. Technical University of Denmark. 2017.
- [37] Laser Diffraction for Particle Size Analysis. Beckman Coulter, Inc. 2020
- [38] Dilatometer Series. DIL 402 Expedis® Select, Supreme and Supreme HT Method, Instruments, Applications. Netzsch Technologies, Germany.

- [39] Hunkel, M.; Surm, H.; Steinbacher, M. Dilatometry. Handbook of Thermal Analysis and Calorimetry — 2018, Volume 6, pp. 103-129. DOI: 10.1016/B978-0-444-64062-8.00019-X
- [40] Vengatesan, M.R.; Varghese, A.M.; Mittal, V.1. Thermal properties of thermoset polymers. Thermosets: Structure, Properties, and Applications: Second Edition — 2018, pp. 69-114. DOI: 10.1016/B978-0-08-101021-1.00003-4
- [41] Sahu, N.; Parija, B.; Panigrahi, S. Fundamental understanding and modeling of spin coating process: A review. Indian Journal of Physics — 2009, Volume 83, Issue 4, pp. 493-502
- [42] Mercury Intrusion Porosimetry Theory. Micrometrics Instrument Corporation. USA.
- [43] Kwok, K.; Kiesel, L.; Frandsen, H.L.; Søgaaard, M.; Hendriksen, P.V. Strength characterization of tubular ceramic materials by flexure of semi-cylindrical specimens. Journal of the European Ceramic Society — 2014, Volume 34, Issue 5, pp. 1423-1432. DOI: 10.1016/j.jeurceramsoc.2013.12.005
- [44] Bernabé, Y. Permeability and pore structure of rocks under pressure. Doctoral diss. Massachusetts Institute of Technology, Dept. of Earth, Atmospheric, and Planetary Sciences, 1986.
- [45] Haugen A.B.; Geffroy A.; Kaiser A.; Gil V. MgO as a non-pyrolyzable pore former in porous membrane supports. Journal of the European Ceramic Society — 2018, Volume 38, Issue 9, pp. 3279-3285. DOI: 10.1016/j.jeurceramsoc.2018.02.039
- [46] Ovtar, S.; Gorauski, J.; Haugen, A.B.; Chatzichristodoulou, C.; Kaiser, A.; Hendriksen, P.V. Oxygen transport properties of tubular Ce_{0.9}Gd_{0.1}O_{1.95}-La_{0.6}Sr_{0.4}FeO_{3-d} composite asymmetric oxygen permeation membranes supported on magnesium oxide. Journal of Membrane Science — 2017, Volume 523, pp. 576-587. DOI: 10.1016/j.memsci.2016.09.060
- [47] Pirou, S.; Bermudez, J.M.; Tak Na, B.; Ovtar, S.; Yu, J.H.; Hendriksen, P.V.; Kaiser, A.; Ramirez Reina, T.; Millan, M.; Kiebach, R. Performance and stability

of $(\text{ZrO}_2)_{0.89}(\text{Y}_2\text{O}_3)_{0.01}(\text{Sc}_2\text{O}_3)_{0.10}\text{-LaCr}_{0.85}\text{Cu}_{0.10}\text{Ni}_{0.05}\text{O}_{3-\delta}$ oxygen transport membranes under conditions relevant for oxy-fuel combustion. *Journal of Membrane Science* — 2018, Volume 552, pp. 115-123. DOI: 10.1016/j.memsci.2018.01.067

Chapter 5. Results

This chapter summarizes and discusses the experimental results carried out in this thesis work. It consists of six manuscripts, one of them already published and five to be submitted in peer reviewed journals. The manuscripts are included in each section of the chapter, which are briefly described below.

Section 5.1 describes the manuscript “*Partial oxidation of biomass gasification tars with oxygen transport membranes*”, in which $\text{Ce}_{0.9}\text{Gd}_{0.1}\text{O}_{1.95} - \text{La}_{0.6}\text{Sr}_{0.4}\text{FeO}_{3-\delta}$ oxygen membranes were integrated and tested in real biomass gasification conditions for the partial oxidation of tars in the producer gas. To the best of the authors’ knowledge, this is the first study that reports direct integration of oxygen transport membranes into the producer gas stream.

Section 5.2 includes the published paper “*Exploring the Processing of Tubular Chromite- and Zirconia-Based Oxygen Transport Membranes*” (Ceramics, 2018). This paper describes the faced challenges during the fabrication of oxygen membranes based on $(\text{Sc}_2\text{O}_3)_{0.10}(\text{Y}_2\text{O}_3)_{0.01}(\text{ZrO}_2)_{0.89}$ and $\text{LaCr}_{0.85}\text{Cu}_{0.10}\text{Ni}_{0.05}\text{O}_{3-\delta}$ composite using $(\text{Y}_2\text{O}_3)_{0.03}(\text{ZrO}_2)_{0.97}$ porous tubular supports.

Section 5.3. shows the manuscript “ *$\text{Y}_{0.8}\text{Ca}_{0.2}\text{Cr}_{0.8}\text{Co}_{0.2}\text{O}_{3-\delta}$ –based dual phase membranes for O_2 separation for oxyfuel and syngas applications*”, where different dual-phase composites using $\text{Y}_{0.8}\text{Ca}_{0.2}\text{Cr}_{0.8}\text{Co}_{0.2}\text{O}_{3-\delta}$ as electronic conductor and CeO_2 -based and ZrO_2 -based ion conductors were investigated. This manuscript was written in cooperation with the Instituto de Tecnología Química of the Universitat Politècnica de València, which is responsible to publish the manuscript.

Section 5.4 describes the manuscript “*Co-sintering and interaction of $\text{Y}_{0.8}\text{Ca}_{0.2}\text{Cr}_{0.8}\text{Co}_{0.2}\text{O}_{3-\delta} - \text{Ce}_{0.9}\text{Gd}_{0.1}\text{O}_{2-\delta}$ dual phase oxygen transport membranes with tubular $\text{Zr}_{0.97}\text{Y}_{0.06}\text{O}_{2.03}$ supports*”. In this study, the selected dual-phase composite investigated in Section 5.3 was used to fabricate tubular oxygen membranes. The manufacturing challenges are described, as well as the possibilities to use methodologies to tailor the thermal properties of ZrO_2 -based composites.

Section 5.5 includes and describes the manuscript “*Effective method to manufacture stable $(\text{Sc}_2\text{O}_3)_{0.10}(\text{Y}_2\text{O}_3)_{0.01}(\text{ZrO}_2)_{0.89} - \text{LaCr}_{0.85}\text{Cu}_{0.10}\text{Ni}_{0.05}\text{O}_{3-\delta}$ asymmetric tubular ceramic oxygen transport membranes*”. Fe_2O_3 was used to tailor the sintering onset temperature and the thermal expansion coefficient of the dual-phase membranes and $\text{Zr}_{0.97}\text{Y}_{0.06}\text{O}_{2.03}$ tubular supports to reduce the stresses during processing. This study line led to the development of robust oxygen membranes.

Section 5.6 shows the short study “Development and fabrication of flexible ion-conductor ceramic capillaries via thermoplastic extrusion”. The manuscript describes the fabrication of archetypes capillaries based on $\text{Ce}_{0.9}\text{Gd}_{0.1}\text{O}_{1.95}$ and $(\text{Sc}_2\text{O}_3)_{0.10}(\text{Y}_2\text{O}_3)_{0.01}(\text{ZrO}_2)_{0.89}$. The use of capillaries could be an alternative for the fabrication of self-supported dual-phase composites OTM and avoid the use of multilayer systems.

5.1 Partial oxidation of biomass gasification tars with oxygen transport membranes.

Biomass represents a renewable resource that can be used for energy production. Nevertheless, this resource is scarce and highly diverse, thus it is necessary to increase the efficiency of the conversion processes. Thermal gasification of biomass has been proven to be highly flexible and efficient if used optimally. Among the different gasification technologies, the low temperature circulating fluidized bed (LT-CFB) gasifier is capable to treat marginal and residual biomass resources with high contents of low melting ash compounds such as straw, manure fibres, sewage sludge, organic waste etc. However, the primary limit in the applicability of low temperature gasification is the relatively high tar level in the producer gas. Low tar content is conducive for multi-purpose utilization of producer gas including conversion in gas engines, fuel cells or in catalytic synthesis of synthetic fuels.

This section contains the manuscript “Partial oxidation of biomass gasification tars with oxygen transport membranes”. The objective of the work described in this section is to analyse the feasibility of using oxygen transport membranes (OTMs) for partial oxidation of tars directly in the producer gas stream of a LT-CFB gasifier. The oxygen membranes, previously developed at DTU Energy, are based on $\text{Ce}_{0.9}\text{Gd}_{0.1}\text{O}_{1.95} - \text{La}_{0.6}\text{Sr}_{0.4}\text{FeO}_{3-d}$ (CGO-LSF) composites supported on porous MgO tubes. The membranes were tested using a specially designed membrane partial oxidation unit attached to the LT-CFB “Pyroneer” gasifier, operated by DTU Chemical Engineering. Reference measurements were also obtained in lab-scale. Analysis of the producer gas streams and tars at the inlet and outlet of the unit and the oxygen flux registered by the membrane shows that the oxygen membranes contribute to increase by a factor of two the concentration of H_2 and CH_4 in the producer gas.

This study shows for the first time that oxygen membranes were directly integrated into a biomass gasifier system. Further work is required to improve the instrumentation of the gasifier unit, the development of more robust oxygen membranes towards reducing conditions and better integration of the membrane into the gasifier system.

Partial oxidation of biomass gasification tars with oxygen transport membranes

Lev Martinez Aguilera^a, Maria Puig Arnavat^b, Astri Bjørnetun Haugen^a, Jesper Ahrenfeldt^b, Ulrik Birk Henriksen^b, Peter Vang Hendriksen^a, Simona Ovtar^a, Jonas Gurauskis^a, Wolff-Ragnar Kiebach^{a*}

a Department of Energy, Technical University of Denmark, 2800 Kgs. Lyngby, Denmark

b Department of Chemical and Biochemical Engineering, Technical University of Denmark, 2800 Kgs. Lyngby, Denmark

** Corresponding author: woki@dtu.dk*

Abstract

Dual phase oxygen transport membranes were directly integrated into the producer gas stream of a low temperature circulating fluidized bed (LT-CFB) gasifier for partial oxidation of tars. The $\text{Ce}_{0.9}\text{Gd}_{0.1}\text{O}_{1.95} - \text{La}_{0.6}\text{Sr}_{0.4}\text{FeO}_{3-d}$ composite membranes were prepared by thermoplastic extrusion, dip-coating, co-sintered and infiltrated with electro-catalyst. Subsequently, they were investigated in two different set-ups: i) a membrane rig and ii) a partial oxidation testing unit of a gasifier. The stability and performance of the membrane was tested under two different gas configurations: i) in H_2 and ii) in producer gas. An oxygen flux of $1.5 \text{ Nm}^3 \cdot \text{cm}^{-2} \cdot \text{min}^{-1}$ was measured in air/ H_2 gradient at 850°C through a 10 cm long dense membrane with a diameter of 10 mm. A lower oxygen flux of $0.5 \text{ Nm}^3 \cdot \text{cm}^{-2} \cdot \text{min}^{-1}$ was measured for the air/producer gas configuration, which contained ca. $2000 \text{ mg} \cdot \text{Nm}^{-3}$ of primary tars. Analysis of the gas and the tar composition at the output of the membrane demonstrated that it contributed to the partial oxidation of the primary tars, resulting in a twofold increase of H_2 , CH_4 and CO in the producer gas. Despite challenges (such that the thermal cycling of the membrane in producer gas that leads to severe delamination), the successful integration of oxygen transport membranes in a gasifier unit demonstrated that these oxygen membranes can contribute to the reduction of tars in biomass gasification.

Introduction

Biomass represents a renewable resource that can be used for energy production. Nevertheless, this resource is scarce and it is necessary to increase the efficiency of the conversion processes. Thermal gasification of biomass has been proven to be highly flexible and efficient if used optimally. The LT-CFB Gasification process (Fig. 1) was

developed at DTU and subsequently scaled up and introduced to the market by DONG Energy under the name Pyroneer. [1,2,3]

This gasifier was designed specifically to gasify marginal and residual biomass resources with high contents of low melting ash compounds such as straw, manure fibres, sewage sludge, organic waste etc. that have proven difficult to convert efficiently in other processes and avoiding the utilization of high quality resources such as wood.

The process is based on separate pyrolysis and gasification reactors with sand and ash as inert particles circulating to transfer heat from the gasification process to the pyrolysis reactor. The maximum temperature in the char reactor is efficiently kept below the agglomeration temperature of the circulating particles. Due to slight cooling in the pyrolysis chamber and subsequently in the primary and secondary cyclones, even alkalis that may have been partly evaporated in the hot zones are solidified before leaving the system. The alkalis can be separated together with the ash particles without including a raw gas cooler. In this way, fouling and high temperature corrosion, mainly due to condensing potassium chloride [4], can be avoided and instead the valuable nutrients (potassium and phosphorus) are concentrated in the separated ashes. Avoiding the generation of toxic PAH (Polycyclic Aromatic Hydrocarbons) compounds in the ashes allows their use as fertilizer and soil enhancer. [5] At the Technical University of Denmark, cold gas efficiencies of 87-93 % have been achieved on various feedstocks in the LT-CFB. [6]

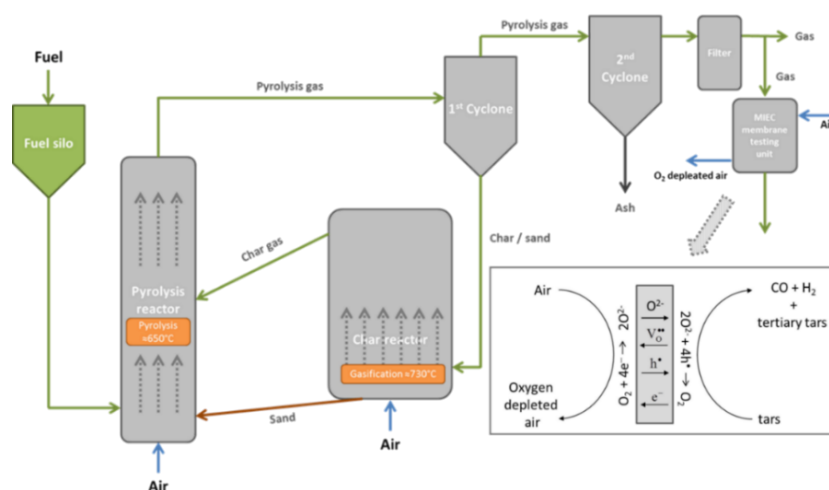


Fig. 1. LT-CFB gasifier flow diagram with the operating principle of a dense ceramic membrane for the partial oxidation of tars [7]

The application of the LT-CFB platform has so far been limited to production of heat and power if the gas is fed to an adjacent power plant with a boiler and a steam cycle. The primary limit in the applicability of low temperature gasification is the relatively high tar level in the producer gas. [8,9,10]

According to the International Energy Agency Bioenergy “all organics boiling at temperature above that of benzene should be considered as tar”. [11] Tar is a mixture of numerous aromatic organic compounds that are liquid at room temperature. There is no explicit definition on tars, but they may cause serious problems in downstream equipment such as fouling, corrosion, erosion and abrasion. As long as the gas temperature is above the tar dew-point, problems with the handling of the gas can be avoided. Nevertheless, if the gaseous tar condense, they can easily plug up equipment. [11,12] Tar is therefore a challenge in every biomass gasification concept.

The concentration and composition of tars depends on the design of the gasifier and the type of biomass used as fuel. The tar composition from a low temperature gasifier operating at 800-900 °C primarily consists of phenols, with only minor amounts of PAH. [13] Thus, the tars removal from the producer gas is necessary to make it utilizable directly in gas engines or fuel synthesis.

Several methods for tar removal are possible. Physical processes (e.g. filters), thermal methods and catalytic methods are the options that are mostly used. Most of these cleaning systems nowadays are too expensive or complex to be used in small-scale applications. The thermal methods seem to be the most appropriate. The thermal treatment of the fuel gas mixtures can be realized either by external heating or by partial combustion of the fuel gasses. [11,13] The partial oxidation of the gas results in a significant reduction of the tar. Primary and secondary tars are oxidized or converted to tertiary tars during this partial oxidation. The partial oxidation of the pyrolysis gas is one of the main reasons for the almost “tar-free” producer gas from a staged gasifier. [13]

The efficiency of the partial oxidation of tars can be controlled by the amount of oxygen in the fuel gas, as shown by Ahrenfeldt et al. [14]. The concept of controlling the oxygen concentration, proposed in this study, is based on the integration of dense ceramic membranes in the producer gas stream. Dense ceramic membranes made from mixed

oxide ionic and electronic conductive materials (MIEC) allow the separation of oxygen from the air supply at elevated temperatures (>550 °C). [15] The oxygen transport through the membrane occurs spontaneously via solid-state diffusion of oxide ions if the membrane is exposed to a gradient in the oxygen partial pressure, pO_2 , at high temperatures. The separation process is 100 % selective towards oxygen. [16]

The applicability of dense oxygen transport membranes for syngas production was experimentally shown by different groups. [17,18,19,20] Furthermore, the integration of oxygen transport membranes into an experimental coal gasifier was reported by Gupta et al. [18] Large research efforts for developing oxygen transport membranes are focused on two different groups of MIEC: i) acceptor-doped perovskite-type oxides $La_{1-x}A_xCo_{1-y}B_yO_{3-d}$ ($A = Sr, Ba$; $B = Fe, Mn, Cr$) and ii) doped fluorite-type oxides $Ce_{1-x}M_xO_{2-d}$ ($M = Gd, Sm, Pr$)³. Recently, composites of those materials draw large interest in the oxygen transport membrane research. [21,22,23]. Composites enable an easier tuning of the required properties, especially the oxide-ion and electronic conductivity.

For the partial oxidation of tars, membranes must be stable in a severe pO_2 gradient, with air on one side and producer gas on the other side of the membrane. Additionally, the membrane material must show the required performance in terms of oxygen flux, chemical stability and mechanical reliability. Based on earlier results [22] $Ce_{0.9}Gd_{0.1}O_{1.95} - La_{0.6}Sr_{0.4}FeO_{3-d}$ dual-phase composite membrane material was selected for the partial oxidation of tars in the producer gas.

The aim of this study is to demonstrate a proof of concept of the direct integration of an oxygen transport membrane into the producer gas stream of an LT-CFB gasifier for partial oxidation of tars. To the best of the authors' knowledge, this is the first study that reports the direct integration of an oxygen transport membrane into a producer gas stream.

Materials and methods

Feedstock for gasification tests

The biomass used in the LT-CFB gasifier during the test was wheat straw crushed pellets. The composition of the used biomass is listed in **Error! Reference source not found..**

Table 1: Composition of wheat straw crushed pellets

Parameter	Unit	as received	Parameter	Unit	Dry basis
Moisture content	%	10.6	Aluminium (Al)	mg/kg	150
Volatiles	%	61.1	Calcium (Ca)	mg/kg	6080
Fixed Carbon	%	21.2	Iron (Fe)	mg/kg	190
Ash	%	7	Potassium (K)	mg/kg	12000
Sulphur (S)	%	0.17	Magnesium (Mg)	mg/kg	750
Chlorine (Cl)	%	0.24	Sodium (Na)	mg/kg	370
Carbon (C)	%	43.8	Phosphorus (P)	mg/kg	680
Hydrogen (H)	%	5.5	Silicon (Si)	mg/kg	5900
Nitrogen (N)	%	0.6			
Oxygen (O)	%	38.3			

Fabrication of the oxygen transport membranes

A 10 cm tubular, asymmetric oxygen transport membrane was used for the partial oxidation of tars in this work. This component consists of a dual-phase $(La_{0.6}Sr_{0.4})_{0.98}FeO_{3-\delta}$ (LSF) and $Ce_{0.9}Gd_{0.1}O_{2-\delta}$ (CGO) 10 μm thin film as the active oxygen transport membrane. It is sandwiched between two 5-15 μm layers of porous CGO. These three thin films were deposited on MgO support tubes by dip coating and infiltrated with catalysts according to a previously developed procedure. [24]. For the currently used membrane, the sintering time was set to 4 h at 1250 °C, and only the outer porous layer was infiltrated with $LaCoO_{3-\delta}$ nanoparticles. The porous MgO supports were prepared by thermoplastic extrusion, based on the procedure developed by Ramachandran *et al.* [25] The used MgO feedstocks for extrusion are based on MgO powders calcined at 900 °C, containing 1 wt.% Fe_2O_3 and 20 vol.% thermoplastic polymers for improved sintering. The resulting support tubes are 37 % porous, providing a gas permeability of $7 \times 10^{-15} m^2$ and a flexural strength of ca. 40 MPa.

Experimental set-up

Lab-scale testing unit - Membrane rig

Oxygen permeation experiments were carried out using an open flow setup with supplying air at the outer side of the tube (feed side) and N_2 , H_2 and simulated producer

gas at the inner side (permeate side). Alumina holders were used to support the oxygen membranes and to supply the permeate gas. The oxygen membranes were situated in the hot zone of a vertical furnace. The temperature of the sample was monitored by placing thermocouples inside the alumina tube at the inlet and outlet of the oxygen membrane.

The oxygen membranes were sealed on the alumina support using YS2B glass, with composition SiO₂, 67.94 wt.%, Al₂O₃, 14.91 wt.%, and Na₂O, 17.14 wt.%. Indication of the gas tightness was obtained by comparing the difference between the inlet and the outlet gas flow rate after high temperature sealing at 980 C for 1 h. In this study, for an inlet flow rate of 500 l·min⁻¹ of N₂ an outlet flow rate of 500 l·min⁻¹ ± 3 ml·min⁻¹ was obtained. Additionally, the membrane was slightly pressurized with an inside overpressure corresponding to ca. 20 mm of H₂O (2x10⁻³ atm). The leak was below the measurement error of the outlet flow rate. Therefore, a leak-less membrane was assumed and the data were not leakage-corrected.

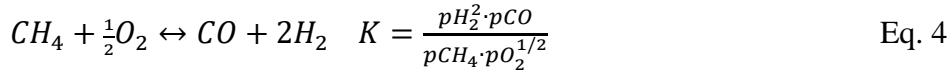
The active membrane area, calculated as the area between the seals on the outer diameter of the oxygen membrane, was 5 cm². A constant air flow on the feed side (2.0 l·min⁻¹) and a flow of different gasses (N₂, humidified H₂ at 25 °C, CO₂, CO, CH₄) on the permeate side (0.016 - 0.40 l·min⁻¹) were supplied. The gas flow rate was controlled and measured using mass-flow controllers (Brooks). The pO₂ was measured for the inlet (pO_{2(in)}) and the outlet gas (pO_{2(out)}) on the permeate side of the membrane using an in-house built ZrO₂-based sensor.

The membranes were tested in three different configurations, i) N₂ configuration, ii) H₂ configuration, and iii) simulated producer gas configuration. In all configurations air was supplied on the feed side of membrane. For testing in the N₂ and the simulated producer gas configuration the oxygen permeation flux was calculated by Eq.1.

$$J(O_2) = \frac{\phi_{inlet} (pO_{2\ outlet} - pO_{2\ inlet})}{A} \quad \text{Eq. 1}$$

ϕ_{inlet} is the total flow rate of gasses into the membrane and A is the active surface area of the membrane. For the N₂ configuration $pO_{2\ (outlet)}$ and $pO_{2\ (inlet)}$ are measured by partial oxygen pressures using the ZrO₂-based sensor. For the simulated producer gas configuration, the pO_2 values were calculated from the known total amount of C and H

in the system, measured pO_2 and from known temperature dependent equilibrium constants for reactions described by Eq. 2 – 4.



In the H_2 configuration, the equilibrium condition described by Eq. 2, was assumed and the oxygen permeation flux was calculated by Eq. 5.

$$J(O_2) = \frac{\Phi_{H_2O(outlet)} - \Phi_{H_2O(inlet)}}{2A} \quad \text{Eq. 5}$$

The volume flow rates of water (ϕ_{H_2O}) were calculated from measured pO_2 and the known equilibrium constant (K_{eq-1}) (Eq. 2), as described by Chatzichristodoulou et al. [26]

Test unit for producer gas

A specific open flow setup was designed to carry out tests with H_2 , N_2 and producer gas from a side stream of the LT-CFB gasifier after the gas filter. The membrane was placed in the setup with the inner side as a permeate side and the outer side as a feed side. Alumina spacers pre-sealed on Kanthal® holders with YS2B glass at 850 °C were fixed with Inconel fittings to the testing setup (

Fig. 2.a). The YS2B glass paste was applied to the contact area and the oxygen membranes were placed between the alumina spacers (

Fig. 2.b-c).

The oxygen membranes were placed in the hot zone of the furnace, which was heated up to 850 °C with heating rate of 5 °C·min⁻¹. The oxygen membrane was sealed in-situ at 850 °C for 30 min under compression using 1 kg load provided by a pulley and counterweight system (Fig. 3a). The active membrane area was ca. 35 cm² between the seals of the 10 cm long membrane tube, mounted on the outer diameter at the end of the tube.

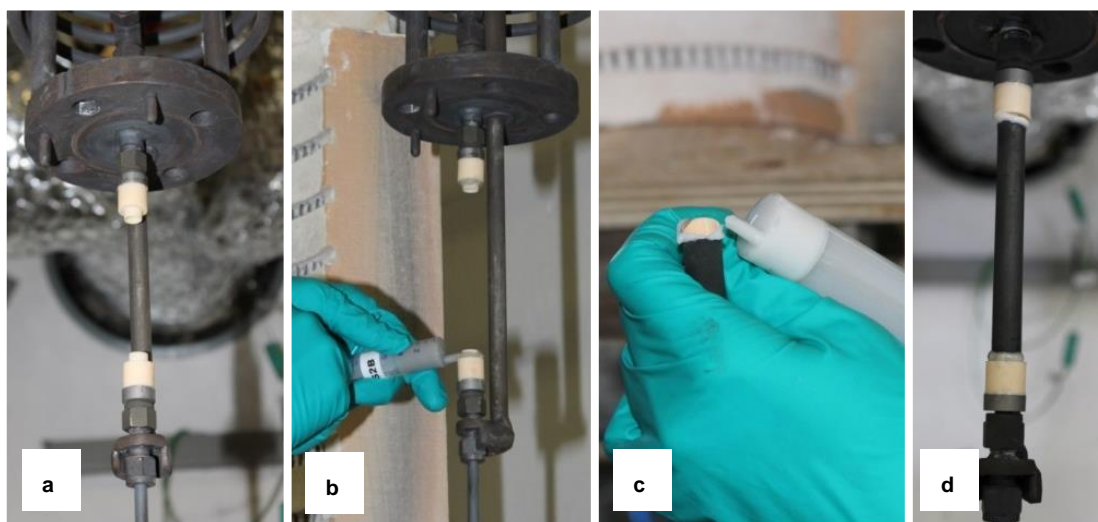


Fig. 2. Designed set-up for the oxygen membrane testing: a) alumina spacers pre-sealed on the Kanthal holder with Inconel fittings; b-c) application of the NAS glass paste to the contact area between membranes and alumina spacers; d) oxygen membrane in place in the set-up unit

The oxygen membrane was covered with a stainless steel cylinder that included the air preheating section, as well as the fresh air inlet and oxygen depleted air outlet for the O_2 concentration measurement (Fig. 3a-d). The lower part of the cylinder was open, so the rest of the oxygen-depleted air could freely leave the unit. Three gasometers were installed to measure the air flow (IGA Type AC-5M B733), H_2/N_2 (IGA Type AC-5M B733) and oxygen depleted air flow (Gallus 2100 TCE – G4 T) into the pO_2 sensor. These gasometers are made to measure capacities between 0.25 to $100 \text{ Nl}\cdot\text{min}^{-1}$. Having flows close to the lower limit ($1\text{-}3 \text{ Nl}\cdot\text{min}^{-1}$) could affect the accuracy of the results. Selection of these gasometers was based on a compromise between the accuracy of the experiments and expected operation flows in the pilot-scale gasifier. The highly accurate measurements of the membrane rig were used as reference. The system was equipped with three thermocouples to measure the inlet air temperature, the N_2/H_2 /producer gas inlet temperature and the furnace temperature. Additionally, the temperature of the producer gas before and after the main valve of the side stream was measured. To prevent condensation of tars the connecting part between the producer gas stream and the gasifier testing unit was heated to ca. $300 \text{ }^\circ\text{C}$.

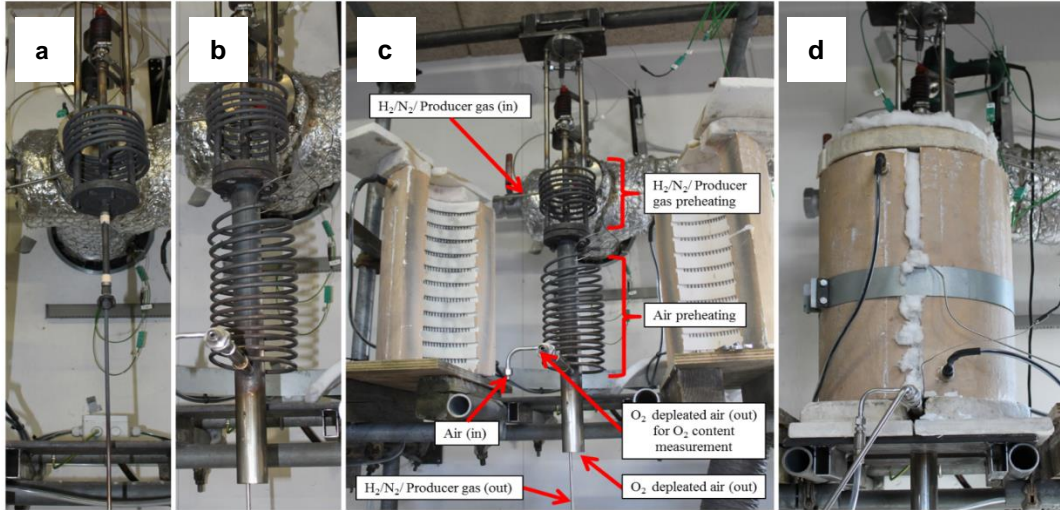


Fig. 3. Designed set-up for the oxygen membrane testing on a side stream of the LT-CFB gasifier: a) oxygen membrane placed in the set-up unit. Pulley and counterweight system to keep the membrane under a load is observed on the top of the unit. b) detail of the stainless steel cylinder covering the membrane with the air preheating section; c) overall view of the all set-up placed inside the furnace; d) set-up with of the furnace close and insulated.

Testing of membranes in N₂ and H₂

Adequacy, robustness and sensitivity of the developed partial oxidation test unit were evaluated by testing in N₂ and H₂ as sweep gas and air as feed gas. The sealing of the membrane was done at 850 °C for 30 min and flowing only air on the outside of the membrane. Afterwards, the supply tube system and the inside of the membrane were flushed with N₂ (1 l·min⁻¹) for 15 min. This was followed by supplying 0.35 - 0.85 l·min⁻¹ of H₂ inside the membrane for 60 min. At the end, the system was flushed with N₂ (2 l·min⁻¹) for 15 min and the membrane was passively cooled to room temperature.

During the test, pre-heated air with a flowrate of 3 l·min⁻¹ was supplied to the feed side of the oxygen membrane. A sample of the air (100 – 250 ml·min⁻¹) that passed the membrane was pumped through an in-house built ZrO₂-based oxygen sensor to monitor the change of the oxygen concentration in air.

The oxygen permeation flux was calculated by Eq. 6:

$$J(O_2) = \frac{pO_2(air) - pO_2(outlet)}{A} \quad \text{Eq. 6}$$

pO₂(air) and pO₂(outlet) are the oxygen partial pressures of air (0.205 atm.) and the oxygen-depleted air at the outlet, respectively.

Testing with producer gas

The LT-CFB gasifier was pre-warmed up for 12 h before the combustion of fuel was started. Crushed wheat straw pellets were used as fuel and air at atmospheric pressure as gasifying agent. The oxygen membrane tests and tar measurements in the producer gas were carried out when stable operation conditions were reached ca. 4 hours after the start-up. The oxygen membranes were prepared for this test following the same procedure as described for testing in N₂ and H₂ configurations. The membrane was sealed at 850 °C in air and the system was flushed with N₂ (ca. 2 l·min⁻¹) for 30 min. The main valve to the side stream of the producer gas was opened and the gas flow through the membrane was monitored by measuring pressure difference before (13 mm H₂O) and after the valve (10 mm H₂O). The producer gas was pre-heated to the membrane temperature before entering the membrane. The test with producer gas was carried out for 90 min, due to lack of stability in the operation of the gasifier. After the test, the main valve was closed and the system was flushed with N₂ for 15 min (ca. 2 l·min⁻¹). After the test, the oxygen membrane was cooled down with rate ca. 7 °C·min⁻¹ from 850 °C to room temperature.

Samples of the producer gas tars were taken simultaneously at the input and output streams of the partial oxidation unit for analysis. Producer gas was analysed using FLSmidth GASloq on-line gas analysers, where filters for tar-removal were set before the analysers. Additionally, off-line samples using gas pipets attached directly to the output stream of the partial oxidation unit were taken. Tar compositions were obtained by off-line solid phase adsorption technique (SPA) using a Hewlett Packard HP 6890 gas chromatograph interfaced to a HP5973 Mass Selective Detector (Agilent, Denmark).

Microstructure characterization

The microstructure of the membrane before and after testing was analysed using an optical and a scanning electron microscope (SEM Merlin, Zeiss). After testing, the membrane was cut into three pieces relative to the gas flow: i) inlet, ii) middle part and iii) outlet. The polished cross sections and longitudinal sections of the membranes were prepared in an epoxy resin and the microstructure of them was analysed using a Hitachi TM3000 scanning electron microscope (SEM) equipped with a Bruker energy dispersive X-ray spectroscopy (EDS) system.

Results

Characteristics of tars and producer gas

The LT-CFB gasifier was warmed up several hours before the start up with wheat straw crushed pellets. After few hours of operation, the gasifier reached steady state of operation. This was determined from the stability of the overall mass balance and the stability of the temperature and pressure curves during operation with fixed process settings. Tars and gas compositions at the outlet of the gasifier were obtained once it reached steady state of operation, Table 2 and Table 3 show the composition of tars and the producer gas respectively.

Table 2. Composition of tars of producer gas during stable operation of a LT-CFB gasifier

Primary tars [$\text{mg}\cdot\text{m}^{-3}$]		Secondary tars [$\text{mg}\cdot\text{m}^{-3}$]		PAH [$\text{mg}\cdot\text{m}^{-3}$]	
Phenol	821	Naphtalene	123	Acenaphthene	12
Dimethylphenol	202	Methylnaphtalene	98	Acenaphthylene	21
Cresol	547	Ethylnaphtalene	5	Fluorene	19
Ethyl-methylphenol	172	Dimethylnaphtalene	16	Anthracene	24
Ethylphenol	30	Vinylnaphtalene	3	Methylanthracene	8
Total	1772	Total	245	Pyrene	8
				Total	92

Table 3. Producer gas composition during stable operation of the LT-CFB gasifier

Parameter	Results [vol%]
CH ₄	3.3
CO	11.3
CO ₂	19.5
H ₂	3.7

Oxygen permeation flux measurements

Oxygen transport membranes from the same production batch were tested in two different tests units in i) the membrane rig and ii) the gasifier test unit for producer gas. The tests that were carried out in the clean lab conditions of the membrane rig are considered highly accurate and are used as reference to evaluate and benchmark the results obtained in the gasifier test unit.

In the membrane rig the membranes were tested in three different configurations, using i) N₂, ii) H₂, and iii) simulated producer gas on the permeate site as a sweep gas. The parallel tests in the gasifier test unit were conducted in two different configurations: i) flow of pure H₂ on the permeate site and ii) direct flow of the producer gas synthesized during combustion of the biomass in the LT-CFB gasifier. For all configurations, air was supplied to the feed side of the membrane.

In the following sections, the different configurations will be separately discussed and the results obtained in the membrane rig will be compared with the results obtained in the gasifier test unit.

Oxygen permeation flux in the N₂ and H₂ configurations

In Fig. 4 the oxygen permeation flux of the membrane as a function of temperature and flow rate of the sweep gas is shown. Maximum oxygen fluxes of 0.75 l/min and 6.14 l/min were measured at 850 °C using 0.4 l/min of N₂ and H₂, respectively. The oxygen permeation flux was strongly influenced by the increase of the flow rate of the sweep gasses.

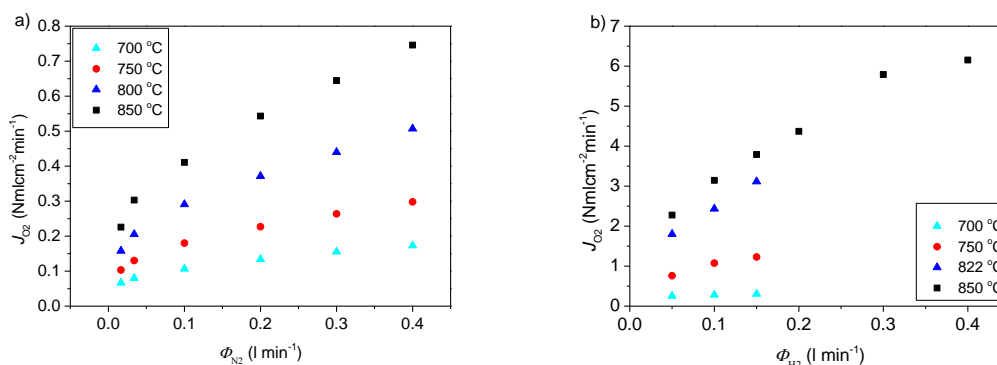


Fig. 4. Oxygen permeation flux of an infiltrated Ce_{0.9}Gd_{0.1}O_{1.95} – La_{0.6}Sr_{0.4}FeO_{3-d} membrane in the experimental test rig in a) nitrogen, b) hydrogen with a membrane area of 5 cm².

This can be directly correlated to an increased driving force of oxygen permeability, due to faster dilution of the permeated oxygen. Additionally, the oxygen permeation flux is strongly temperature-dependent. The activation energy for the p_{O_2} of the outlet gas of 0.02 atm (for the N₂ configuration) was 112 kJ/mol and for the p_{O_2} of 10⁻¹⁸ atm (for the H₂ configuration) was ca. 190 kJ/mol. A similar activation energy of 153 kJ/mol was reported by Cheng et al. [22] for planar asymmetric CGO-LSF composite membranes

with LSC electro-catalyst on the feed side for air/He configuration. The high activation energy indicates that the oxygen transport through the membrane is most probably limited by the surface exchange.

Fig. 5a shows an overview of the oxygen flux measurement in the gasifier test unit in H₂ configuration. The temperature was kept constant during the test at ca. 850 °C. A slight difference between the air and the sweep gas inlet temperature was observed (Fig. 5a). The membrane was first tested in N₂, then in H₂ and at the end of the test, the measurement in N₂ was repeated. The oxygen permeation flux in the N₂ configuration was ca. 0.5 Nml/cm² min for a flow of nitrogen of 1 l/min and. This oxygen flux was 2.7 times lower than expected from the parallel measurements in the membrane rig. The test in the N₂ configuration was repeated after 60 min of testing in the H₂ configuration. A slight degradation of the oxygen permeation flux after testing in H₂ compared to the initial performance in N₂ was observed (Fig. 5a).

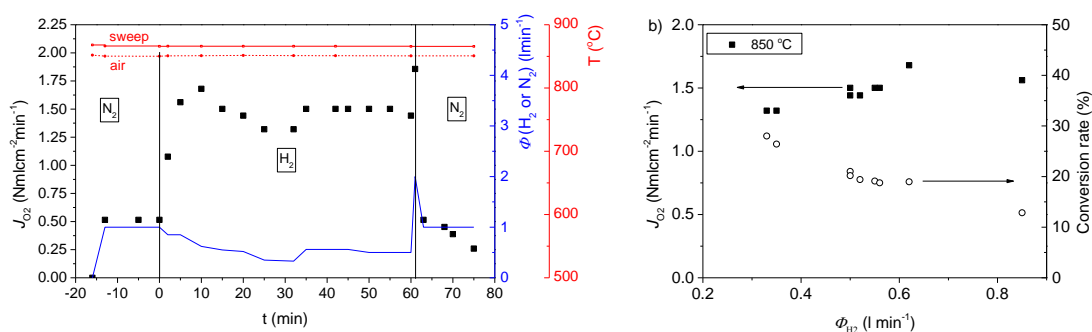


Fig. 5. a) Oxygen permeation flux Ce_{0.9}Gd_{0.1}O_{1.95} – La_{0.6}Sr_{0.4}FeO_{3-d} membrane in producer gas for a) a 80 hour test and b) oxygen permeation flux and conversion rate as a function of hydrogen for a membrane surface area of 35 cm²

In the H₂ configuration the flow rate of H₂ was varied. The dependence of the oxygen permeation flux on the H₂ flow rate is shown in Fig. 5b. A similar trend of an increased oxygen permeation flux with an increased sweep gas flow rate was observed for tests in both test units. As expected, by increasing the flow rate the conversion rate was decreased, as shown in Fig. 5b. The maximal conversion rate for the 10 cm long tubular membrane was 28 %. However, the flux measured in the gasifier test unit for the same testing conditions (850 °C, 0.4 l/min) was ca. 4 times smaller than in the membrane rig. This difference can be ascribed to several different reasons. Firstly, the driving force of the oxygen permeation is reduced along the membrane length as described by Puig-Arnau, et al., where a decrease of 13 % of the oxygen flux was calculated in the first 10 cm of a

MIEC tubular membrane working with air/vacuum gradient at 850 °C. [20] Therefore, for a longer membrane operating under the same conditions a lower total oxygen permeation flux is expected. Secondly, the membrane rig was under a slight over pressure compared to the gasifier test unit, which can result in different oxygen flux. Finally, the difference can also partly originate from potentially lower accuracy related to the used setup and the used equipment, as described below.

The oxygen permeation flux for the test rig was calculated from the flow rates of formed water. This (more accurate) measurements cannot be used in the gasifier unit, because the tar presents in the producer gas would destroy the sensitive oxygen sensors. Instead, the oxygen flux for the gasifier test unit was calculated from the depletion of oxygen on the air side. An additional concern can be leakage due to pinholes in the membrane or in the sealing area, which was not monitored for the gasifier test unit. The open flow setup used for this study should ensure a minimal pressure gradient between feed and permeate side. Higher pressure is expected in the permeate side, where H₂, N₂, or producer gas flows. For a small leak, the measured oxygen concentration will change due to cross of gas from the permeate side to the feed side, which would result in a lower pO₂ and consequently a higher oxygen flux would be estimated.

Testing with simulated producer gas

Fig. 6 shows the results of preliminary tests of the membranes stability in the simulated producer gas. Short-term tests were performed in the membrane rig. Different gas compositions were chosen to simulate the ratio of gasses in producer gas. Two different conditions were tested: i) “clean” gas with only H₂ and N₂ and ii) simulated producer gas with flow rate ratio of CO:CO₂:H₂:N₂:CH₄ = 2.3:3.1:1:8.9:0.7. In Fig. 6a a test over a duration of 50 h in the clean gas mixture with a N₂:H₂ flow rate ratio of 8.9:1 at 822°C is presented. The ratio N₂ to H₂ was chosen to resemble the estimated N₂:H₂ ratio in the producer gas. An initial value of 0.86 Nml·cm⁻²·min⁻¹ and a degradation of 0.07 Nml·cm⁻²·min⁻¹ (8.1 %) over the 50 h of the test were observed. Long-term stability studies of a CGO-LSF membrane on a MgO porous support in H₂ and CO₂ are described in a previous work. [27] In that study, the CGO-LSF membrane registered an initial value of 1.28 Nml·cm⁻²·min⁻¹ with a degradation of -0.16 Nml·cm⁻²·min⁻¹ (12.1%) in the first 50 h of operation when working at 700 °C and flowing 200 Nml·min⁻¹ of H₂ in the feed side.

After that, no more degradation was observed over the total 275 h of the test. This is in accordance to the long-term test for the N₂:H₂ flow rate ratio of 8.9:1 at 822 °C observed in Fig. 6b.

The variation of the oxygen permeation flux with the gas composition and temperature is shown in Fig. 6b. As expected, the oxygen flux was reduced by decreasing the concentration of H₂ in the sweep gas from 2.5 Nml·cm⁻²·min⁻¹ for a N₂:H₂ ratio of 1:1 to 0.86 Nml·cm⁻²·min⁻¹ for a N₂:H₂ ratio of 8.9:1 measured at 822 °C. Lower oxygen permeation flux of 0.38 Nml·cm⁻²·min⁻¹ at 822 °C and ca. 0.7 Nml·cm⁻²·min⁻¹ at 850 °C were measured for the simulated producer gas, although the ratio of inert gasses (N₂, CO₂) to gasses that react with the permeated O₂ (CO, H₂, CH₄) was increased to 3:1. For the simulated producer gas, the process was strongly temperature dependent. A temperature increase of 28 °C led an to increase of oxygen permeation flux for 25 – 50 %.

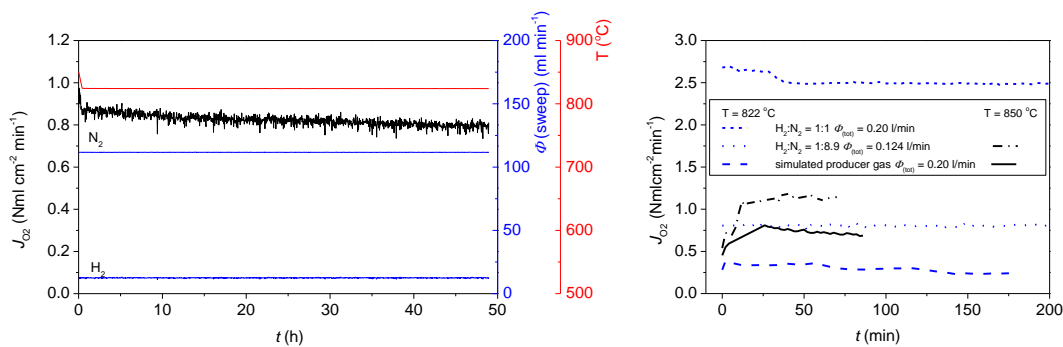


Fig. 6. Oxygen permeation flux measurements of a CGO-LSF membrane in the experimental test rig as a function of time a) for a H₂:N₂ mixture of 1:8.9 at 850 °C and b) for different H₂:N₂ ratios and the simulated producer gas at 822 °C and 850 °C (membrane area in both tests was 5 cm²).

Test of partial oxidation of tars

Fig. 7a shows an overview of the tests performed in the tars partial oxidation unit attached to the LT-CFB gasifier. The temperature of the inlet gasses was kept constant at ca. 850 °C throughout the test. The membrane was first tested in N₂, then in producer gas for ca.120 min and finally N₂ was flown to determine the degradation of the membrane. The initial performance of the membrane for a N₂ flow rate of 1.8 l·min⁻¹ was 0.9 Nml·cm⁻²·min⁻¹. The final performance in N₂ after the test in the producer gas was reduced to 0.5 Nml·cm⁻²·min⁻¹. These values are similar to the one carried out in the tests shown in Fig. 5. In producer gas conditions, oxygen flux values with relative stability in the region

of $0.5 \text{ Nm}^3 \cdot \text{cm}^{-2} \cdot \text{min}^{-1}$ were obtained. Test using producer gases was carried out only for 2 h because the lack of stability in the operation conditions of gasifier occurred.

The lower performance of the membrane in gasification conditions can be ascribed to different factors. i) As a consequence of clogging of the MgO porous support with the carbon or other impurities or ii) due to a degradation of the membrane's catalyst, LaCoO₃. The degradation of perovskite based membranes tested in CH₄ was reported by several groups. [17,28,29]. For example, for the Co based perovskites (catalyst in this study) the degradation is mostly connected with the Co segregation, which can be explained by the kinetic de-mixing mechanism of multicomponent materials in a thermodynamic potential gradient. [30] Another variable that could affect the obtained results is the accuracy of the used instruments in the setup, since the gas flows are in the lower detection limits of the used gasometers.

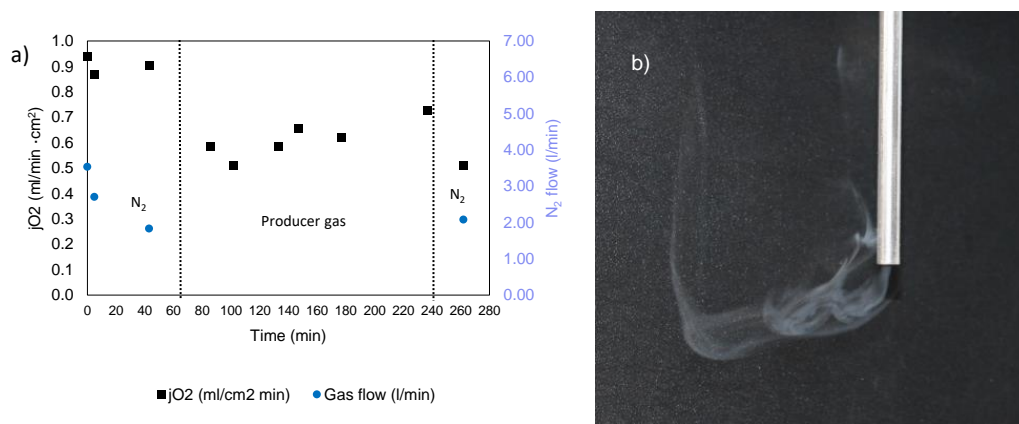


Fig. 7. a) Oxygen permeation flux measurement as a function of time of a 35 cm² CGO-LSF membrane tested in the partial oxidation test unit adjacent to a LT-CFB gasifier at 850 °C. b) White producer gas at the output of the membrane indicating the partial oxidation of the tars.

During the partial oxidation of tars, two different products at the membrane outlet were observed: i) condensed water and ii) white smoke, as shown in Fig. 7b. Formed water indicates that a partial combustion of H₂ or/and tar occurred during the test. From the observed white smoke it can be speculated that the outlet gas contained some remaining secondary and/or tertiary tars. The partial oxidation of tars in the used gasifier was studied by Ahrenfeldt et al. [6] in more detail. It was shown that a temperature of 950 °C was needed to partially oxidize primary tars, and that the predominating compound in the gas after partial oxidation was naphthalene. A detailed analysis of the tars compositions before and after the partial oxidation unit is shown in Fig. 8a. It is noticed that phenol and

naphthalene are fully decomposed when the gas reached the outlet of the membrane, but formation of tertiary tars, such as fluorene, anthracene and pyrene were identified in the SAP analysis. This indicates that partial oxidation of the tars is being carried out. This conversion might be driven by oxygen provided by the membrane, thermal decomposition or both. In order to define if tars conversion is related to thermal processes, a 10 cm dense alumina tube, labelled “blank”, which avoids the cross of oxygen or air to the permeate side, was set in the partial oxidation unit and tested with producer gas in the same operation conditions used for the actual membrane test. The results of the tars conversion of the blank are shown in Fig. 8b. Similar when operating the membrane, phenol and naphthalene are fully decomposed and only tertiary tars are observed at the outlet of the blank. This might indicate that decomposition of these type of tars could be linked to thermal processes.

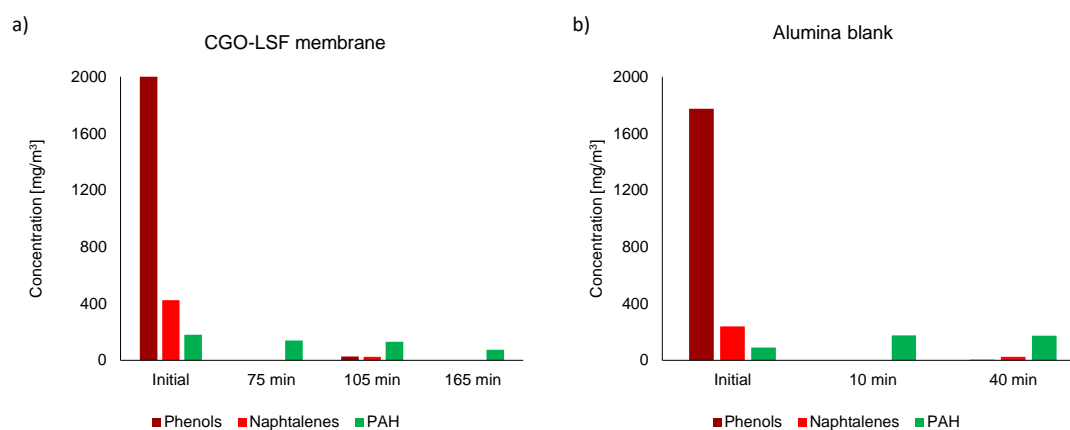


Fig. 8. Tars composition after treatment in a partial oxidation unit i) using an alumina blank and b) using a CGO-LSF membrane. Tests were carried out at 850 °C using air in the feed side.

However, the concentration of tertiary tars after the membrane is lower than that obtained in the alumina blank, even if the initial concentration of total phenols was higher in the membrane test. At the end of the test, tertiary tars are ca. $100 \text{ mg}\cdot\text{m}^{-3}$ lower than those observed in the blank, considering an equivalent initial phenols concentration, which is equivalent to ca. 65% of the tars in the producer gas. When comparing the oxygen flux (Fig. 7a) and formation of tertiary tars (Fig. 8a), a correlation between the values is observed, which might indicate that a fraction of the tars conversion is linked to the OTM contribution.

Table 4. Composition of the producer gas in oxidation unit using a membrane and an inner blank.

Parameter	Membrane CGO-LSF			Alumina blank		
	Producer gas	Membrane	% change	Producer gas	Blank	% change
O ₂	0.1	0.7	600%	0.1	0.6	500%
H ₂	3.7	8.5	130%	3.7	6.6	78%
CO	12.2	12.1	-1%	13	13.4	3%
CO ₂	19.5	17.4	-11%	16.9	16	-5%
CH ₄	2.9	4.9	69%	3.5	5.2	49%
N ₂	61.7	56.4	-9%	62.9	58.2	-7%

Table 4 shows the composition of the producer gas at the inlet and outlet of the partial oxidation unit when using the membrane and the alumina blank. It is noticed that gases such as H₂, CH₄ and CO are generated when using the alumina blank, which confirms the partial oxidation of tars due to thermal processes. Nevertheless, when using the membrane, ca. 50% and 20% more H₂ and CH₄ respectively are obtained than using the blank, while the concentration of CO remains similar. This data, together with the lower concentration of tertiary tars, indicates that the membrane partly contributes to the partial oxidation of the tars and formation of permanent gases.

Post-mortem analysis

The post-mortem analysis of the oxygen membrane tested in the partial oxidation unit is presented in Fig. 9 – Fig. 11. For the samples tested with H₂ sweep, no degradation or changes in the microstructure were observed. Fig. 9 shows a photo of a membrane after test with producer gas. The membrane was removed from the testing unit by breaking it close to the sealing area. Traces of black material were observed in the inner part of the tube in the inlet side.

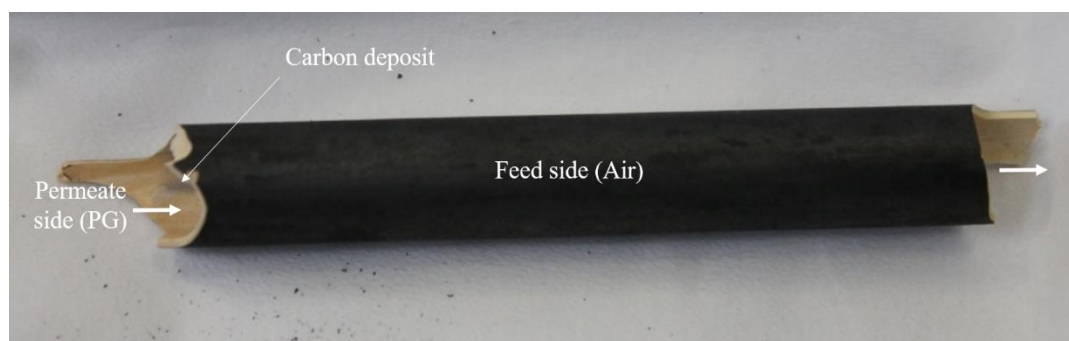


Fig. 9. Oxygen membrane after producer gas testing with carbon deposition (black colour) on the permeate side.

Fig. 10a shows optical microscopy images of a polished longitudinal section of the membrane's porous support after testing with the producer gas. On the inlet side of the tube a residual carbon contamination (black phase) was observed with the depth of few millimetres. In the middle and on the outlet side of the tube the residual carbon was not visible by optical microscopy. It can be concluded, that the carbon was formed during the partial oxidation of methane and tars, when the concentration of permeated oxygen was not sufficient for the formation of CO and H₂.

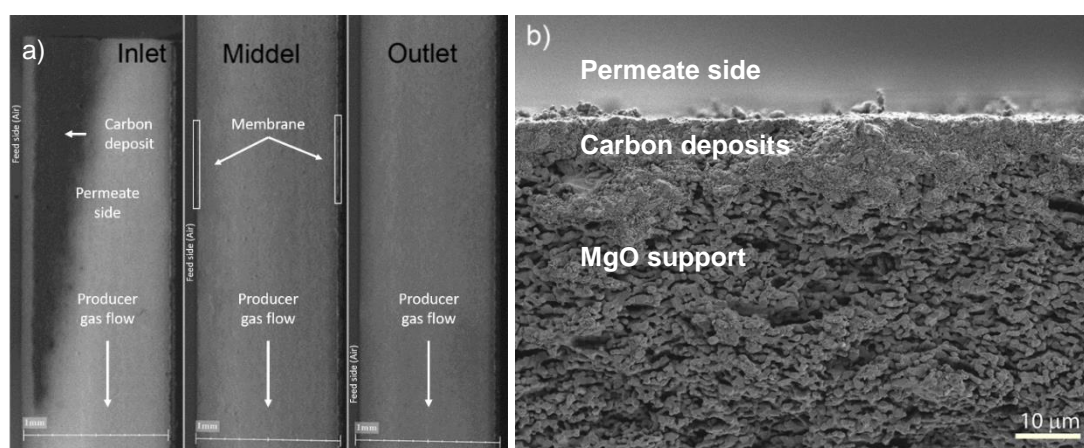


Fig. 10. a) Optical microscopy images of longitudinal sections of the membrane: inlet side, middle and outlet side, b) SEM micrographs of fractured cross section of the inlet side (permeate) of the inlet side of the MgO support tested with producer gas.

The residual carbon area in the porous support observed in Fig. 10a – Inlet matches with the fact that the concentration of CH₄ and tars is the highest at the inlet of gasses and is reduced along the tube. The main disadvantage of the carbon deposition inside the pores is clogging and therefore a consequent reduction of the membrane area where partial oxidation can occur. The residual carbon is also clearly observable in Fig. 10b, where SEM micrographs of the fractured surface on the inlet side of the MgO support is shown. The clogging of the pores was almost complete at the inlet of producer gas. The thickness of clogged area was ca. 10 μm micrometres. Below this layer the usual microstructure of the MgO support was observed.

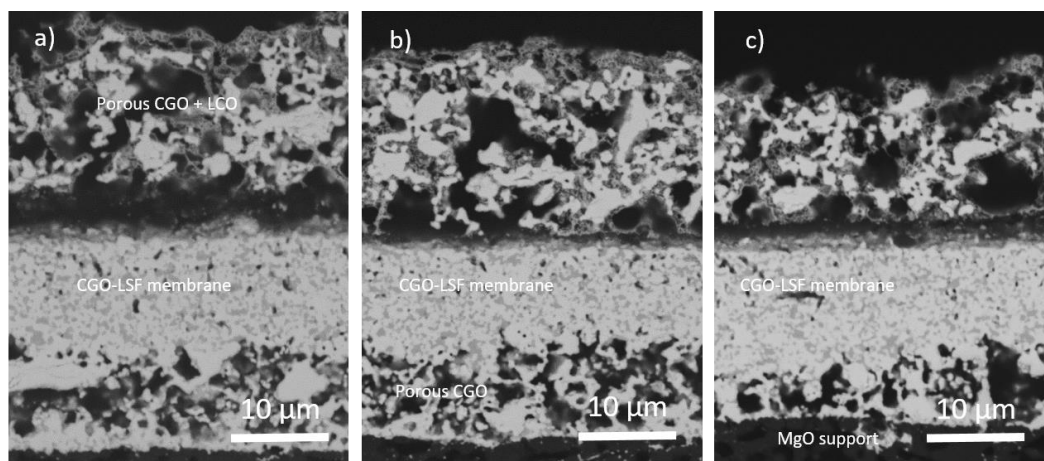


Fig. 11. Micrographs of the CGO-LSF membrane tube and the membrane layer after testing in the gasifier test unit with the producer gas of a) inlet, b) middle, c) outlet.

Fig. 11 shows the polished cross section SEM micrographs of the membrane and the CGO-porous layers of different sections along the tube. EDS analysis performed on the membrane revealed that no additional elements are present in the feed side and no visible degradation was observed. In addition, the membrane layer was well attached to the MgO porous support, and the electro-catalyst infiltrated into the outer porous CGO layer did not coarse during testing.

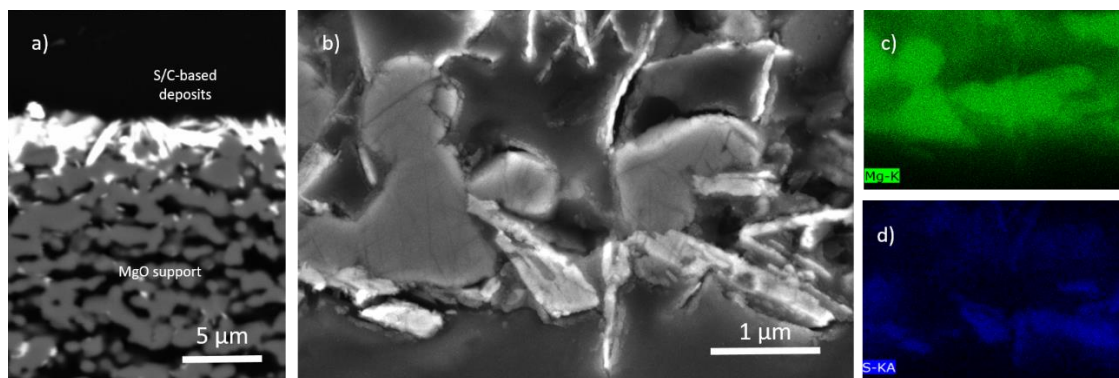


Fig. 12. a/b) Micrographs of post-mortem samples showing needle-like structures on the permeate side of the MgO support. c/d) EDS mapping of the needles and nearby components.

Fig. 12 shows a polished micrograph of the permeate side of the MgO support observed in Fig. 10b. It is observed that needle-like structures are formed on the surface of the MgO support. A higher resolution micrograph (Fig. 11b) as well as its EDS mapping (Fig. 11c and Fig. 11d) shows that the observed deposits are composed not only of C, C_xH_y or tars but also contain sulphur-based compounds. These compounds were not observed within the MgO support, but only on surface of the permeate side (producer gas side).

Although the random distribution of these compounds might not affect the diffusion of the gases throughout the porous support, it might be possible that during long-term operation they could negatively affect the performance of the membrane.

One of the potential improvements for the tested CGO-LSF membranes is their mechanical stability towards reducing conditions. After testing, attempts to cool down and heat up the membrane led to severe delamination of the membranes. The delamination might occur due to thermal expansion coefficient (TEC) mismatch of the materials. MgO has a TEC of $15.6 \times 10^{-6} \text{ K}^{-1}$ (30-1000 °C) and $14.4 \times 10^{-6} \text{ K}^{-1}$ (30-850 °C) [31], LSF doped with 40% Sr has a TEC of $17.9 \times 10^{-6} \text{ K}^{-1}$ (30-1000 °C) [32] and the CGO of $12.72 \times 10^{-6} \text{ K}^{-1}$ (30-850) [33]. In addition, at temperatures higher than 700 °C and reducing conditions, a relaxation of the CGO lattice occurs, causing chemical expansion. [34]. This could create mechanical stresses and weakening of the CGO porous layer between the membrane and the MgO support, causing delamination of the dip-coated layers. Although results in the tests with producer gas demonstrates that the tested membranes are capable to oxidize the tars and generate permanent gases, the delamination of the layers would limit the use of the membranes in practical applications. Thus, development of chemically stable and mechanically resistant oxygen transport membranes is required if their integration in biomass gasification units is pursued.

Conclusions

Tubular oxygen transport membranes based on a $\text{Ce}_{0.9}\text{Gd}_{0.1}\text{O}_{1.95} - \text{La}_{0.6}\text{Sr}_{0.4}\text{FeO}_{3-d}$ (CGO-LSF) supported on porous MgO were successfully integrated and tested in a biomass gasification for the first time. The partial oxidation of tars in the producer gas of a LT-CFB gasifier was investigated in a specially designed testing unit. The combination of heat and oxygen provided by the membrane process led to a 65% reduction in tertiary tars and an additional 50% and 20% higher conversion of the tars into H_2 and CH_4 when comparing with the purely thermal conversion of these tars.

Besides to the actual tests in the biomass gasifier, the performance of the membranes in H_2 and simulated producer gas were investigated under clean laboratory conditions.

Maximum oxygen fluxes of 0.7 NI/min and 4.4 NI/min were measured at 850 °C using 0.2 l/min of simulated producer gas and H₂, respectively.

The oxygen flux through the 10 cm long membrane in air/H₂ gradient at 850 °C measured in the gasifier unit was 1.5 Nml·cm⁻²·min⁻¹, which corresponded to 28 % of H₂ conversion. The short-term stability of the CGO-LSF membrane operating at 850 °C with air/producer gas gradient demonstrated

Post-mortem analysis of the membranes revealed that the performance decrease after exposure to the producer gas is most likely related to i) the deposition of carbon and sulphur-based compounds in the porous structure of the MgO support in the inlet area of the membrane and the ii) the deactivation of the catalyst. Although the mechanical robustness of the components towards thermal cycling must be increased, the proof-of-concept of using oxygen membranes for partial oxidation of tars was successfully demonstrated.

Acknowledgments.

Authors acknowledge financial support from “Highly Flexible Energy Production by Oxy-Fired Biomass Gasification (HighFlex)” EUDP grant No.: 64018-0028 –before 12403– , "Highly Flexible Energy Production by Oxy-Fired Biomass Gasification (HighFlex)"

References.

- [1] DONG Energy, 2011. News - From LT-CFB to Pyroneer. DONG Energy.
- [2] Nielsen, R.G.; Stoholm, P.; Nielsen, M.B; Krogh, J.; Nørholm, N.; Antonsen, S.; Sander, B.; Henriksen, U.B; Qvale, E.B. LT-CFB Gasifier – First Test Results From the 500 Kw Test Plant. Biomass for energy, industry and climate protection. 2005.
- [3] Stoholm, P.; Fock, M.W.; Henriksen, U.B. Low Temperature CFB Gasifier. Conceptual Ideas and Applications. Proceedings of the 15th International Conference on Fluidized Bed Combustion — 1999

- [4] Yang, T.; Jia, K.; Kai, X.; Sun, Y.; Li, Y.; Li, R. A Study on the Migration Behavior of K, Na, and Cl during Biomass Gasification. *Bioresources* (2016) Volume 11, Issue 3. 10.15376/biores.11.3.7133-7144
- [5] Larsen, H. H.; Sønderberg P.L. DTU International Energy Report 2012: Energy efficiency improvements: A key element in the global transition to non-fossil energy. Technical University of Denmark. 2012, Denmark. DTU_Energy_Report_2012.pdf
- [6] Ahrenfeldt, J.; Thomsen, T.; Henriksen, U.B., Clausen, L.R. Biomass gasification cogeneration – A review of state of the art technology and near future perspectives. *Applied Thermal Engineering* 2013, 50(2), 1407- 1417. 10.1016/j.applthermaleng.2011.12.040
- [7] DONG Energy A/S. Gasolution – Enables efficient power and gas production. ForskEL 2011 – PSO project 10730. Energinet. September 2015. 10730_gasolution_final_report.pdf
- [8] Zwart, R.; van der Heijden, S.; Emmen, R.; Dall Bentzen, J.; Ahrenfeldt, J.; Stoholm, P.; Krogh, J. (2010). Tar removal from low-temperature gasifiers. Petten: Energy Research Centre of the Netherlands (ECN). ECN-E-10- 008.
- [9] Sansaniwal, S.K.; Rosen, M.A.; Tyagi, S.K. Global challenges in the sustainable development of biomass gasification: An overview. *Renew Sustain Energy Rev* 2017; 80:23–43. 10.1016/j.rser.2017.05.215
- [10] Ruiz JA, Juárez MC, Morales MP, Muñoz P, Mendívil MA. Biomass gasification for electricity generation: Review of current technology barriers. *Renew Sustain Energy Rev* 2013;18:174–83. 10.1016/j.rser.2012.10.021
- [11] Milne, T.A.; Evans, R.J.; Abatzoglou, N. Biomass Gasifier “Tars”: Their Nature, Formation, and Conversion. National Renewable Energy Laboratory. November 1998, NREL/TP-570-25357. nrel.gov/docs/fy99osti/25357.pdf

- [12] Ravenni, G. (2018). Diss. Application of biomass char to tar conversion and producer gas upgrading to syngas. Kgs. Lyngby: Technical University of Denmark. orbit.dtu.dk/Giulia_Ravenni.pdf
- [13] Fjellerup, J.; Ahrenfeldt, J.; Henriksen, U.; Gøbel, B. (2005). Formation, Decomposition and Cracking of Biomass Tars in Gasification. Kgs. Lyngby: Technical University of Denmark. Department of Mechanical Engineering. orbit.dtu.dk/pyrotar2.pdf
- [14] Ahrenfeldt, J.; Egsgaard, H.; Stelte, W.; Thomsen, T.; Henriksen, U.B. The influence of partial oxidation mechanisms on tar destruction in Two Stage biomass gasification. *Fuel*. 2013;112:662-680. 10.1016/j.fuel.2012.09.048
- [15] Wei, Y.; Yang, W.; Caro, J.; Wang, H. Dense ceramic oxygen permeable membranes and catalytic membrane reactors. *Chem Eng J*. 2013;220:185-203. 10.1016/j.cej.2013.01.048
- [16] Den Exter, Marcel J.; Haije, W.G.; Vente, J.F. Viability of ITM technology for oxygen production and oxidation processes: Material, system, and process aspects. *Inorganic Membranes for Energy and Environmental Applications — 2009*, pp. 27-51.
- [17] Bouwmeester, HJM. Dense ceramic membranes for methane conversion. In: *Catalysis Today*. Vol 82. (2003) 141-150. 10.1016/S0920-5861(03)00222-0
- [18] Gupta, S; Adams, J.J.; Wilson, J.R.; Eddings, E.G.; Mahapatra, M.K.; Singh, P. Performance and post-test characterization of an OTM system in an experimental coal gasifier. *Appl Energy*. 2016;165:72-80. 10.1016/j.apenergy.2015.12.077
- [19] Kaiser, A.; Foghmoes, S.P.V.; Chatzichristodoulou, C.; Søggaard, M.; Glasscock, J.; Frandsen, H.L.; Hendriksen, P.V. Evaluation of thin film ceria membranes for syngas membrane reactors—Preparation, characterization and testing. *Journal of Membrane Science — 2011*, Volume 378, Issue 1-2, pp. 51-60. DOI: 10.1016/j.memsci.2010.12.012[16]

- [20] Puig-Arnavat, M.; Soprani, S.; Søggaard, M.; Engelbrecht, K.; Ahrenfeldt, J.; Henriksen, U.B.; Hendriksen, P.V. Integration of mixed conducting membranes in an oxygen–steam biomass gasification process. *Rsc Advances* — 2013, Volume 3, Issue 43, pp. 20843-20854. 10.1039/c3ra44509g
- [21] Yuan R.H.; He, W.; Zhang, Y.; Gao J.F.; Chen, C. Preparation and characterization of supported planar $Zr_{0.84}Y_{0.16}O_{1.92}-La_{0.8}Sr_{0.2}Cr_{0.5}Fe_{0.5}O_{3-\delta}$ composite membrane. *Journal of Membrane Science* (2016) 499: 335-342. 10.1016/j.memsci.2015.10.066
- [22] Cheng, S.; Huang, H.; Ovtar, S.; Simonsen, S.B.; Chen, M.; Zhang, W.; Søggaard, M.; Kaiser, A.; Hendriksen, P.V.; Chen, C. High-Performance Microchanneled Asymmetric $Gd_{0.1}Ce_{0.9}O_{1.95-\delta}-La_{0.6}Sr_{0.4}FeO_{3-\delta}$ -Based Membranes for Oxygen Separation *ACS Applied Materials and Interfaces* — 2016, Volume 8, Issue 7, pp. 4548-4560. 10.1021/acsami.5b10714
- [23] Garcia-Fayos, J.; Vert, V.B.; Balaguer, M.; Solís, C.; Gaudillere, C.; Serra, J.M. Oxygen transport membranes in a biomass/coal combined strategy for reducing CO₂ emissions: Permeation study of selected membranes under different CO₂-rich atmospheres. *Catalysis Today* (2015) Volume 257, Issue 2, pp. 221-228. 10.1016/j.cattod.2015.04.019
- [24] Gorauskis, J.; Ovtar, S.; Kaiser, A.; Søggaard, M.; Hendriksen, P.V. Ceria Based Composite Membranes for Oxygen Separation. *ECS Transactions* (2014); 64(2): 251-258. 10.1149/06402.0251ecst
- [25] Ramachandran, D.K.; Clemens, F.; Glasscock, A.J.; Søggaard, M.; Kaiser, A. Tailoring the microstructure of porous MgO supports for asymmetric oxygen separation membranes: Optimization of thermoplastic feedstock systems. *Ceramics International* — 2014, Volume 40, Issue 7, pp. 10465-10473. 10.1016/j.ceramint.2014.03.017

- [26] Chatzichristodoulou, C.; Søggaard, M.; Glasscock, J.; Kaiser, A.; Foghmoes, S.P.V.; Hendriksen, P.V. Oxygen Permeation in Thin, Dense Ce_{0.9}Gd_{0.1}O_{1.95}-delta Membranes II. Experimental Determination. *Journal of the Electrochemical Society* — 2011, Volume 158, Issue 5, pp. F73-F83. 10.1149/1.3559189
- [27] Ovtar, S.; Gorauskis, J.; Haugen, B.A.; Chatzichristodoulou, C.; Kaiser, A.; Hendriksen, P.V. Oxygen transport properties of tubular Ce_{0.9}Gd_{0.1}O_{1.95}-La_{0.6}Sr_{0.4}FeO₃-d composite asymmetric oxygen permeation membranes supported on magnesium oxide. *Journal of Membrane Science* — 2017, Volume 523, pp. 576-587. 10.1016/j.memsci.2016.09.060
- [28] Trunec, M.; Cihlar, J.; Diethelm, S.; Van Herle, J. Tubular La_{0.7}Ca_{0.3}Fe_{0.85}Co_{0.15}O₃ Perovskite Membranes, Part II: Performance and Stability. *Journal of the American Ceramic Society* — 2006, Volume 89, Issue 3, pp. 955-959. 10.1111/j.1551-2916.2005.00811.x
- [29] Zhu, X.; Yang, W. Composite membrane based on ionic conductor and mixed conductor for oxygen permeation. *AIChE Journal*. 2008;54(3):665-672. 10.1002/aic.11410
- [30] Martin, M. Materials in thermodynamic potential gradients. *Pure and Applied Chemistry* — 2003, Volume 75, Issue 7, pp. 889-903. 10.1351/pac200375070889
- [31] Rao, A.S.Madhusudhan¹; Narender, K. Studies on thermophysical properties of CaO and MgO by γ -ray attenuation. *Journal of Thermodynamics* — 2014, Volume 2014, pp. 123478. DOI: 10.1155/2014/123478
- [32] Hansen, K.K. Evaluation of LSF based SOFC cathodes using cone-shaped electrodes and EIS. *Solid State Ionics* — 2020, Volume 344, pp. 115096. DOI: 10.1016/j.ssi.2019.115096

- [33] Hayashi, H.; Kanoh, M.; Quan, C.J.; Inaba, H.; Wang, S.; Dokiya, M.; Tagawa, H. Thermal expansion of Gd-doped ceria and reduced ceria. *Solid State Ionics* — 2000, Volume 132, Issue 3, pp. 227-233. DOI: 10.1016/s0167-2738(00)00646-9
- [34] Bishop, S.R.; Marrocchelli, D.; Chatzichristodoulou, C.; Perry, N.H.; Mogensen, M.B.; Tuller, H.L.; Wachsman, E.D. Chemical Expansion: Implications for Electrochemical Energy Storage and Conversion Devices. *Annual Review of Materials Research* — 2014, Volume 44, Issue 1, pp. 205-239. 10.1146/annurev-matsci-070813-113329

5.2 Exploring the processing of tubular chromite- and zirconia-based oxygen transport membranes.

One of the main requirements for the integration of oxygen transport membranes (OTMs) in biomass gasification is the high stability towards temperatures ca. 1000 °C and oxygen partial pressures as low as 10-20 atm. Thus, the adequate selection of materials capable to withstand these conditions and provide high electronic and ionic conductivity is crucial.

This section includes the paper with the title “Exploring the processing of tubular chromite and zirconia-based oxygen transport membranes”, published in the journal “Ceramics” in 2018. [Ceramics, 1(2) 2018, 229-245].

This paper investigates the development of an asymmetric tubular dual-phase oxygen membrane based on chemically stable materials for gasification conditions. $(Y_2O_3)_{0.01}(Sc_2O_3)_{0.10}(ZrO_2)_{0.89}$ –ScYSZ– was selected as ionic-conducting phase and $LaCr_{0.85}Cu_{0.10}Ni_{0.05}O_{3-\delta}$ –LCCN– as electronic-conducting phase. $(Y_2O_3)_{0.03}(ZrO_2)_{0.97}$ –3YSZ– tubular porous supports were chosen due to their outstanding chemical and mechanical stability. Both, the dual phase composite (Pirou, et al. 2018) and the porous supports (Haugen, et al. 2016) have been previously investigated at DTU Energy. Tubular porous supports were fabricated by thermoplastic extrusion and the dual-phase composite functional layers were deposited using dip-coating.

The high co-sintering temperature (1450 °C) required to densify the 10ScYSZ-LCCN membrane on the 3YSZ porous supports caused evaporation of chromium (Cr) from the LCCN. This led to side reactions and formation of $La(OH)_3$ that caused longitudinal cracks on the membrane. Transversal cracks were also developed, which might be related to thermal expansion coefficient mismatch between the membrane and porous supports materials. Additionally, formation of a lanthanum zirconate insulating-phase was also observed.

Therefore, the LCCN is not suitable as electronic conducting-phase in tubular membranes using this architecture, unless means to lower the sintering temperature and reduce the chromium evaporation are found.

Exploring the processing of tubular chromite- and zirconia-based oxygen transport membranes

Astri Bjørnetun Haugen,^{1*} Lev Martinez Aguilera,¹ Kawai Kwok,^{1,a} Tesfaye Molla,^{1,b} Kjeld Bøhm Andersen,¹ Stéven Pirou,¹ Andreas Kaiser,¹ Peter Vang Hendriksen¹ and Ragnar Kiebach¹

¹ Department of Energy Conversion and Storage, Technical University of Denmark, Frederiksborgvej 399, 4000 Roskilde, Denmark

^a Currently at: University of Central Florida, Department of Mechanical and Aerospace Engineering 12760 Pegasus Blvd, P. O. Box 162450, Orlando, FL 32816-2450

^b Currently at: Department of Mechanical Engineering, Melbourne School of Engineering, The University of Melbourne, 173 Wilson Ave, Parkville VIC 3052, Australia

* Correspondence: ahua@dtu.dk; Tel.: +4521560919

Received: 31 August 2018; Accepted: 27 September 2018; Published: 29 September 2018

Abstract: Tubular oxygen transport membranes (OTMs) that can be directly integrated in high temperature processes have a large potential to reduce CO₂ emissions. However, the challenging processing of these multilayered tubes, combined with strict material stability requirements, has so far hindered such direct integration. We have investigated if a porous support based on (Y₂O₃)_{0.03}(ZrO₂)_{0.97} (3YSZ) with a dense composite oxygen membrane consisting of (Y₂O₃)_{0.01}(Sc₂O₃)_{0.10}(ZrO₂)_{0.89} (10Sc1YSZ) as an ionic conductor and LaCr_{0.85}Cu_{0.10}Ni_{0.05}O_{3-δ} (LCCN) as an electronic conductor could be fabricated as a tubular component, since these materials would provide outstanding chemical and mechanical stability. Tubular components were made by extrusion, dip coating and co-sintering, and their chemical and mechanical integrity was evaluated. Sufficient gas permeability ($\geq 10^{-14}$ m²) and mechanical strength (≥ 50 MPa) could be achieved with extruded 3YSZ porous support tubes. The high co-sintering temperature required to densify the 10ScYSZ/LCCN membrane on the porous support, does however, cause challenges related to evaporation of chromium from the membrane. This chemical degradation caused loss of the LCCN electronic conducting phase, formation of secondary lanthanum zirconate compounds and fractures. LCCN is therefore not suitable as the electronic conductor in a tubular OTM, unless means to lower the sintering temperature and reduce the chromium evaporation are found that are applicable to large-scale fabrication of tubular components.

Keywords: oxygen transport membranes; yttria-stabilized zirconia; extrusion; thermoplastic; LaCrO₃; dip coating; co-sintering; tubular membranes; porosity.

1. Introduction

Oxygen transport membranes (OTMs) have a large potential to reduce CO₂ emissions from high temperature processes such as combustion and gasification [1,2]. Oxy-blown (oxygen rather than air) gasification or combustion would both reduce energy consumption through less inactive gas volume (N₂) that has to be heated, and provide a N₂ and NO_x –free flue gas from which CO₂ can easily be captured [1]. For biomass gasification, the higher oxygen content in an oxy-blown gasification will also significantly lower the tar content in the producer gas [3], which increases its commercial value and enables its use in gas turbines. OTMs are dense ceramic membranes that only allow the transport of oxygen via migration of oxygen vacancies [4]. If thermally and chemically integrated in e.g. gasification plants such that the thermal energy for diffusion and driving force in form of a pO₂ gradient are supplied, OTMs will be a cost-efficient alternative to bottled oxygen produced by cryogenic distillation or pressure-swing adsorption [5].

However, such direct chemical and thermal integration of OTMs in real operating conditions has not yet been realized, due to manufacturing challenges and tough requirements on materials and components during operation. Single phase, mixed electronic and ionic conductors such as Ba_{0.5}Sr_{0.5}Co_{0.8}Fe_{0.2}O_{3-δ} (BSCF) as the membrane material can provide high oxygen flux [6], but these materials are often chemically and thermally unstable [7,8]. Changing from a mixed conductor to a composite membrane with two separate, percolating phases of an electron and oxygen ion conducting material gives more flexibility to choose the most stable material combination for a given operation condition. Fluorite-structured oxides based on ceria or zirconia are well known ionic conductors [9,10]. Doping ZrO₂ with Y and/or Sc increases its ionic conductivity, in (Y₂O₃)_{0.01}(Sc₂O₃)_{0.10}(ZrO₂)_{0.89} (10Sc1YSZ) up to 0.12 S cm⁻¹ at 850 °C while stability in CO₂, SO₂ and reducing conditions is retained [11]. Lanthanum-based perovskite-structured oxides with e.g. Cr, Fe and Sr are common choices for the electronic conductor. LaCrO₃ is difficult to sinter due to the high volatility of Cr, but has an excellent stability over a wide pO₂ range (0.21-10⁻²² atm), and can upon acceptor doping reach high electronic conductivity [12]. The composition LaCr_{0.85}Cu_{0.10}Ni_{0.05}O_{3-δ} (LCCN) was recently shown to reach 11.4 S cm⁻¹ at 800 °C and have excellent stability in a wide pO₂

range [13]. A composite membrane of 30 vol% LCCN and 70 vol% 10Sc1YSZ reached an oxygen flux of $1.02 \text{ ml cm}^{-2} \text{ min}^{-1}$ at $950 \text{ }^\circ\text{C}$ in N_2/air in the shape of a planar thick film [13].

Thin OTMs are advantageous compared to bulk OTMs [6,14,15]. Reducing the thickness of the membrane and hence the diffusion length of oxygen ions increases the oxygen flux, until a critical thickness is reached where reduction and oxidation of oxygen at the membrane surfaces takes over as the rate-limiting steps. Porous activation layers to increase the surface area and/or infiltrate catalysts for these surface exchange reactions are therefore often added on either side of the thin membrane. When reducing the thickness it is also critical that the membrane is dense and gas tight (no percolating porosity) such that the gas separation remains 100 % selective of oxygen via the ionic diffusion.

Since these thin membranes cannot be free-standing, asymmetric oxygen membranes are made, with the membrane and activation layers deposited on a thicker porous support [16]. Supports which are a porous version of the membrane material [17] exclude chemical or thermal expansion mismatches. However, since the support needs to be highly porous for sufficient gas permeability and at the same time strong enough for integration in continuous operation in, e.g. a biomass gasifier, inherently stronger ceramics are advantageous. Target values are permeability of $\geq 10^{-14} \text{ m}^2$ and a strength of $\geq 50 \text{ MPa}$, based on considerations from references [17,18] respectively. ZrO_2 with 3 mol% Y_2O_3 (3YSZ) has superior strength and toughness while being chemically stable, and is therefore a commonly used porous support in solid oxide fuel cells and OTM [13,19].

Tubular membranes have advantages compared to planar, such as easier sealing and higher tolerance for thermal gradients [15]. Pilot-scale stand-alone units for oxygen production using tubular BSCF under compressed air/vacuum has already been made [16,19,20], and there are a few reports on the lab-scale fabrication and testing of other tubular OTM systems [22–24], as it stands, tubular membranes with thermochemical stability for direct integration has not yet been made. Techniques to make flat and defect-free planar OTMs, such as stress relief through bending (camber), top loads for controlling this camber. The sophisticated manufacture required for tubular, asymmetric

OTMs limits their widespread use. Techniques to make flat and defect free planar OTMs, such as stress relief through slight bending (camber), top loads for controlling this camber, two-step sintering, and enclosed crucibles or sacrificial powder beds, [13,24], are not easily transferrable to large-scale processing of tubular systems.

In this work, we investigate if the combination of 3YSZ as porous support and LCCN/10Sc1YSZ as composite membrane is feasible for tubular OTM made by large-scale fabrication techniques. This membrane composition has demonstrated decent oxygen fluxes in a planar configuration [13], and the support composition has been proven suitable for high gas permeability [26,27], but it has not yet been established whether sufficient mechanical and chemical integrity can be obtained after the more challenging co-sintering of a tubular system. Indeed, our work shows that while we can make strong and permeable 3YSZ support tubes, the high temperature required for co-sintering of LCCN/10Sc1YSZ on 3YSZ followed by evaporation of chromium makes LCCN unsuitable for large-scale fabrication of tubular OTMs.

2. Materials and Methods

Tubular supports were made by thermoplastic extrusion [28] of feedstocks containing 3YSZ powders, pore formers and thermoplastic binders. The pore formers consist of a 2:1 volumetric ratio of graphite (SG FormulaBT SLA1518, Superior Graphite, USA) to polymethylmethacrylate (PMMA) (MR-10G, Esprix, USA) and the thermoplastic binders a 2:1 volumetric ratio of ethylene-vinyl acetate copolymer (Elvax© 250, DuPont, USA) and paraffin wax (melting point 53–57 °C, Sigma-Aldrich, USA). Two different feedstock compositions were extruded in this work, feedstocks which in the shape of small discs provide the desired permeability ($\geq 10^{-14} \text{ m}^2$) over a wide sintering temperature range [26]. The first was with 40 vol% pore formers, 25 vol% 3YSZ (TZ-3YS-E, Tosoh, Japan) coated with 2.48 wt% stearic acid (Sigma Aldrich, USA) and 35 vol % thermoplastic binders, such that the pore formers constitute 61.5 vol% of the solid content (3YSZ powder and pore formers). The second feedstock composition was with 45 vol% pore formers, 25 vol% 3YSZ powder (TZ-3Y-E, Tosoh, Japan) coated with 5.36 wt% stearic acid (Sigma-Aldrich, USA) and 30 vol% thermoplastic, where the pore formers constitute 64.3 vol% of the solid content. The feedstocks were mixed and kneaded at 100 °C (Type BK20, Linden, Germany), and then extruded (Model 19/20DN, Brabender,

Germany) at 100-110 °C as 1 m long tubes of 14 mm diameter and 1 mm wall thickness. Binder-burnout and sintering in air was performed with the following program: 15 °C/h to 200 °C (2 h hold), 15 °C/h to 360 °C (2 h hold), 15 °C/h to 600 °C (4 h hold), 30 °C/h to the sintering temperature (1225–1400 °C) (2 h hold) and finally cooling at 120 °C/h. More details on the thermoplastic feedstocks can be found in reference [26]. Microstructure, porosity, Darcy gas permeability coefficient and flexural strength of the sintered porous 3YSZ tubes were characterized by scanning electron microscopy (SEM) (TM3000, Hitachi, Japan), Hg porosimetry (Poremaster© GT, Quantachrome Instruments, USA), and gas flow under total pressure gradient (self-constructed setup, more details in [26]).

Flexural strength of porous 3YSZ tubes was tested using four-point bending of semi-cylindrical samples. The test methodology is fully described in [29]. The main advantage of this methodology is that, upon flexure, the maximum tensile stress is created in the middle region on the outer tube surface far away from any cut surfaces. The measured strength data will therefore not be affected by flaws introduced during machining. Time-consuming polishing of samples is thus not needed. Semi-cylindrical specimens also provide flat surfaces for contact with the loading pins. Semi-cylindrical porous 3YSZ samples were prepared by wet and dry cutting using diamond cutting tools. Four-point bending tests were conducted using a specially designed equipment for continuous testing of multiple specimens under controlled environments [29]. Porous 3YSZ were bent until fractured at room temperature. At least six specimens were fractured for each type of porous 3YSZ, 32 for the composition with 61.5 vol% pore former sintered at 1300 °C. The peak stress was determined from the recorded peak load via finite element analyses using the commercial software Abaqus. The measured fracture stresses of sample 61.5 vol% pore former sintered at 1300 °C were analyzed using the Weibull theory [30] to calculate the Weibull strength of porous YSZ.

Dip coating of membrane and activation layers onto the porous support and co-sintering was used to fabricate multilayered, asymmetric tubular OTMs. The general procedure was to first dip coat an inner porous layer directly on the as-extruded tubes, calcine, dip coat one layer of the composite membrane, pre-sinter, dip coat a second layer of the membrane and one outer porous activation layer followed by the final sintering.

All dip coating was performed at 2 mm/s without any hold. The calcination program was similar to the debinding temperature profile described above, just with a lower final holding temperature of 1100 °C (instead of 1250-1400 °C). Pre-sintering was done with heating rate of 60 °C/h, 1 h dwell at 600 °C, 2 h dwell at 1150 °C and cooling at 120 °C/h. The sintering program was identical to the presintering, except with a final dwell temperature varied from 1250 to 1450 °C and dwell time from 2-6 h.

Slurries for dip coating were made according to Table 1, based on previously developed OTMs [31]. A version of the activation layer slurry for increasing the porosity was made by increasing the pore former content to 10.59 wt% and decreasing the backbone content to 21.08 wt%, and a version with LCCN also in the porous layer to suppress evaporation of Cr was made by further replacing 50 vol% of the 10Sc1YSZ with LCCN. All slurries were made by ball milling for 24 h (porous slurries)-72 h (dense slurries). Pore former was added after 24 h and only ball milled with the slurry for 30 minutes. After milling, the slurries were stored while rolling and used within 3 months. The dense slurry was re-dispersed by ultrasound immediately before dip coating.

Table 1. Components of the slurries for dip coating the functional layers.

Activation layers			Membrane layer		
Function	Component	wt%	Function	Component	wt%
Solvent	Ethanol (Reactant grade, Sigma Aldrich)	61.8	Solvent	Ethanol (Reactant grade, Sigma Aldrich)	67.6
Dispersant	Polyvinyl pyrrolidone (PVP K30, Sigma Aldrich)	1.3	Dispersant	Polyvinyl pyrrolidone (PVP K15, Sigma Aldrich)	1.5
Binder	Polyvinyl butyral (B30 HH Mowital, Kuraray, USA)	3.1	Binder	Polyvinyl pyrrolidone (PVP K30, Sigma Aldrich)	1.5
Backbone	10Sc1YSZ (Daiichi, Japan) calcined at 900 °C	25.8	Ionic conductor	10Sc1YSZ (Daiichi, Japan) calcined at 900 °C	19.8
Plasticizer	Dibutyl sebacate (Sigma Aldrich)	2.2	Electronic conductor	LCCN (Cerpotech, Norway)	8.8
Pore former	Graphite (UF-1, Graphit Kropfmühl, Germany)	5.8	Sintering aid	NiO (Product 12359, Alfa Aesar) planetary ball milled for 90 min.	0.9

The microstructure of the sintered tubes were characterized by SEM (TM3000, Hitachi, Chiyoda ku, Japan and SUPRA35, Carl Zeiss, Oberkochen, Germany) and energy-dispersive spectroscopy (EDS) (JEOL JSM6400). Linear shrinkage was measured by contact dilatometry (Netzsch 402, Selb, Germany). Porosity in the membrane layer was estimated by segmenting the SEM images with the software ThreshAlyzer. Leak tightness of the membrane layer was evaluated by pouring ethanol into the tube and visually inspecting if any leakage occurred through the membrane.

3. Results

3.1. Porous 3YSZ support tubes

Figure 1 shows strength vs. sintering temperature and porosity of the two thermoplastic feedstocks for porous 3YSZ extruded into tubes in this work. Both compositions show a porosity content which is in good agreement with the amount of pore former, and decreasing strength with increasing porosity, as expected. While the tubes made with 64.3 vol% pore formers are too fragile at low sintering temperatures, the ones with 61.5 vol% pore formers fulfil the desired strength of 50 MPa after sintering in the entire studied sintering temperature range. The 61.5 vol% pore former composition was therefore chosen for further development of the asymmetric OTM in this work. Figure 1(c) shows the Weibull plot for room temperature strength of the specimens with 61.5 vol% pore former and sintered at 1300 °C. The measured strengths of the specimens are shown with the assigned probabilities of failure (P_f) and a fit of a Weibull distribution. Results of the Weibull fit show that the specimens have a characteristic strength and Weibull modulus of 92.19 MPa and 12.20, respectively.

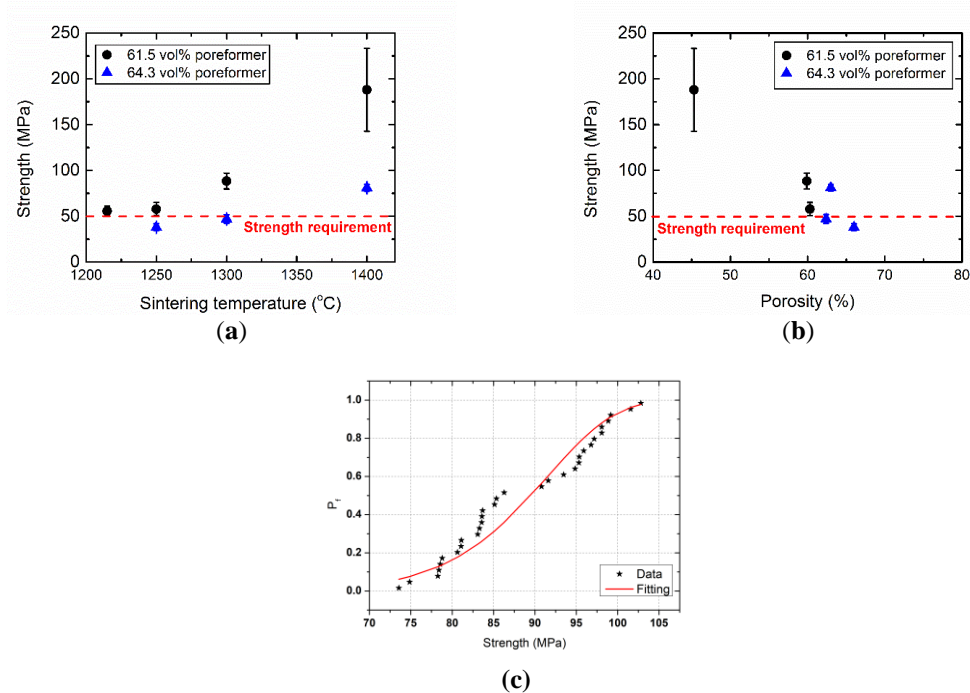


Fig. 1. Flexural strength of tubular, porous 3YSZ supports plotted vs. (a) sintering temperature and (b) porosity. (c) Weibull plot of room temperature strength of specimens with 61.5 vol% pore former and sintered at 1300 °C.

The microstructure of the porous 3YSZ tubes with 61.5 vol% pore former at various sintering temperatures is shown in Figure 2. The material contains large spherical and large irregular pores, which are assumed to originate from PMMA and graphite, respectively. There are also some small ($<1 \mu\text{m}$) pores within the 3YSZ matrix structure. The shape of the large pores are unaffected by the sintering temperature, but the small pores in the 3YSZ matrix structure are diminishing with increasing temperature. The porosity and gas permeability of the 3YSZ tubes with 61.5 vol% pore former are listed in Table 2. The porosity decreases as expected and the pore size increases with increasing sintering temperature, with values similar as the initial studies on small discs of the same compositions [26]. Especially the size of the smallest pores, represented by d_{10} , increase with the sintering temperature. At all studied sintering temperatures, the gas permeability fulfils the target of $\geq 10^{-14} \text{ m}^2$.

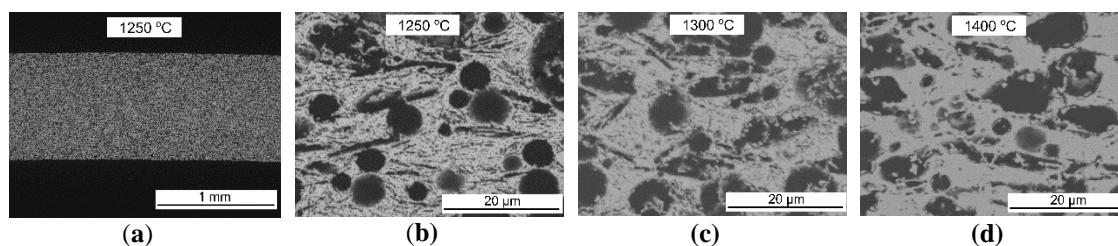


Fig. 2. Micrographs of the porous 3YSZ support tubes with 61.5 vol% pore formers after sintering for 2 h at different temperatures. (a) and (b) 1250 °C, (c) 1300 °C, and (d) 1400 °C.

Table 2. Properties of the porous 3YSZ support with 61.5 vol% pore formers.

Sintering temp. (°C)	Gas permeability coefficient (m^2)	Porosity (vol%)	Pore size, d_{10} (μm)	Pore size, d_{50} (μm)	Pore size, d_{90} (μm)	Strength (MPa)
1250	1.80×10^{-14}	60.3	0.27	1.19	1.66	57.8
1300	1.00×10^{-14}	59.9	0.34	1.31	1.69	88.3
1400	1.10×10^{-14}	45.3	0.60	1.33	1.85	188

3.2 Co-sintering of membrane and activation layers on the porous support tubes

Dilatometry curves of 30 vol % LCCN, 70 vol % 10Sc1YSZ (membrane composition), and 3YSZ (porous support composition) are shown in Figure 3. Both materials were measured in the form of pellet (compressed powder) and with organics for shaping (thermoplastic feedstock for the support tube, and a tape [13] as a substitute for the membrane dip coating slurry). The LCCN/10Sc1YSZ pellets densifies at $<1400 \text{ }^\circ\text{C}$, in good agreement with previous reports that pellets of the 70/30 composite membrane can

be sintered dense at 1400 °C for 6 h [13]. The LCCN/10Sc1YSZ also densifies faster at a lower temperature than the 3YSZ. However, it is known that the sintering behavior can change upon addition of organics (different green density), pore formers, and with a change from bulk to thick film [6]. The free sintering of the membrane layer is not possible, but similar sintering behaviour for the dip coated membrane layer as for the tape can be expected. Compared to the pellets, the tape and tube show a high initial shrinkage due to the presence of organic additives, a similar onset temperature for sintering, and a reversed order of sintering activity; in this case, the densification of the 3YSZ tube is much higher than the LCCN/10Sc1YSZ tape.

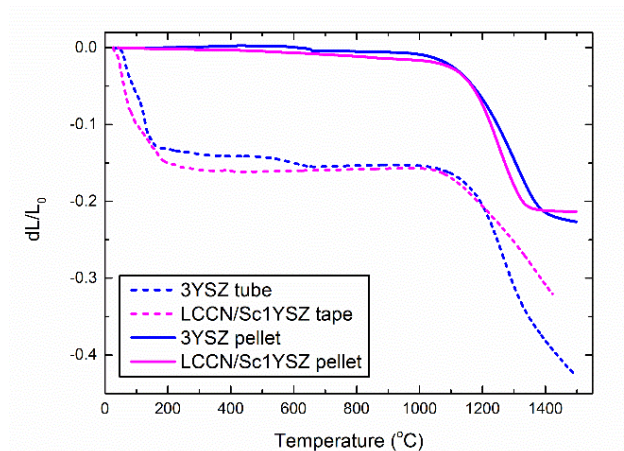


Fig. 3. Dilatometry of 3YSZ and 30/70 vol% LCCN/10Sc1YSZ as pellets and as the actual thermoplastic feedstock with 61.5 vol% pore formers for the support as a tube, and the 30/70 vol% LCCN/10Sc1YSZ as a casted tape rolled up to a cylinder.

Figure 4 shows photographs of the tubular OTM at different stages of the processing. Micrographs of cross sections of the OTM multilayers sintered at different temperatures and dwell times are shown in Figure 5. From top to bottom in each image is the outer activation layer (~5–15 μm), the composite membrane layer (~30–40 μm), the inner activation layer (~5–15 μm), and the porous support (only the first few μm visible). The bright phase in the membrane layer is expected to be LCCN, the darker 10Sc1YSZ. The black areas are pores. A membrane with sufficient density to be leak-tight (only a few small, leaky spots observed during leak testing) was obtained after sintering for 6 h at 1425 or 1450 °C. Sintering at 1425 °C for 6 h was therefore used as the standard procedure in further work. It is obvious that higher temperature is needed to densify the LCCN/10Sc1YSZ as a multilayer compared to previous reports on the bulk ceramic [13]. These findings are in accordance with dilatometry result (Figure 3). We can also see that

some thin, longitudinal cracks are present in the membrane part of the as-sintered tubes after sintering at 1450 °C for 6 h (Figure 5d). In the other samples, such cracks can be observed to a lesser extent. These cracks are expected to be the origin of the leakage spots observed in the leakage test.

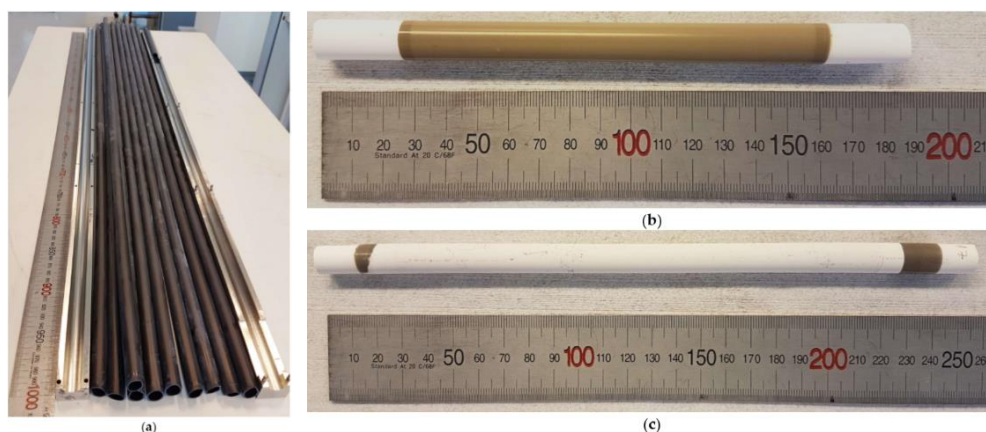


Fig. 4. Photographs of (a) as-extruded support tubes, (b) tubes coated with inner activation layer and membrane layer after calcination and pre-sintering (the white parts on the ends are uncoated support), and (c) tubes after application of all layers (the white parts on the ends are uncoated support, the white part in the middle is the outer 10Sc1YSZ activation layer. The ruler shows length in millimeters).

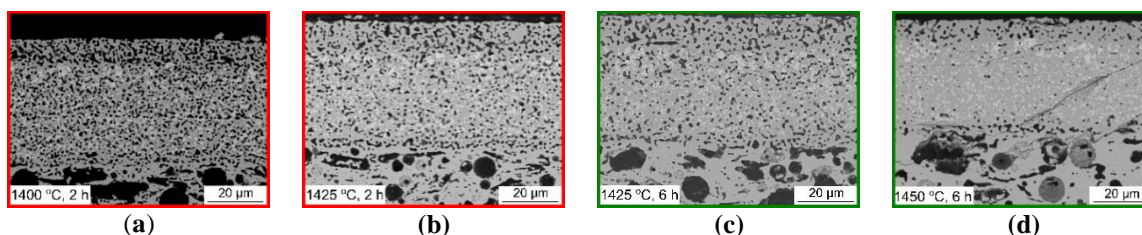


Fig. 5. SEM micrographs of the tubular OTM layers, from top to bottom outer activation layer, composite membrane, inner activation layer and porous support, after sintering at (a) 1400 °C, 2 h (leaks), (b) 1425 °C, 2 h (leaks), (c) 1425 °C, 6 h (tight) and (d) 1450 °C, 6 h (tight, with some leaky spots).

However, the leak-tight and apparently defect-free membrane sintered at 1425 and 1450 °C for 6 h was, upon closer inspection, found to have significant defects. Re-inspecting sintered tubes after heating to 300 °C for infiltration of catalyst in the activation layers, regularly separated cracks were observed by naked eye. Such *macroscopic* cracks were also observed to a lesser extent after storage for several weeks in ambient conditions, without any post-sintering treatment. In the less dense and leaky membranes sintered at 1400 °C, cracks were only visible by SEM microscopy investigation after a few weeks of storage. In general, the cracks were more pronounced and more advanced (visible immediately after storage) in the denser membrane layers sintered at higher temperature for a longer time. The cracks can be seen in Figure 6a. In contrast to the smaller, longitudinal cracks observed by microscopy immediately after sintering, these cracks

are transverse (radial) through all the functional layers (membrane, inner, and outer porous layers) and separated by regular intervals. Adding a 10 h hold at 1100 °C (in which the creep rate in YSZ is still high [25]) during cooling after sintering did not prevent subsequent transversal cracking.

The membranes presented so far have a thickness of 30–40 μm. To avoid cracking, experiments to reduce the membrane thickness and number of layers were carried out. It was expected that thinner layers hold less energy and have a higher tolerance for strain mismatches [32]. Figure 6 shows how the kind of fracture appears to be related to the membrane thickness. The transverse cracks are only visible in thick (>30 μm) membranes (Figure 6a). Finer, longitudinal cracks or slight delamination of the outer membrane occur also in thinner membranes (8–20 μm) (Figure 6b), while very thin membranes (~4 μm) (Figure 6c) do not show any fractures. For oxygen transport, we need the membrane layer to be dense and gas tight. Whether or not the membrane leaks (as observed by the ethanol leak test) after sintering depends on a combination of its density and its thickness. Figure 7 shows that while 30 μm membranes can be leak-tight already at 86% density, membranes below 10 μm leak also when 95% dense.

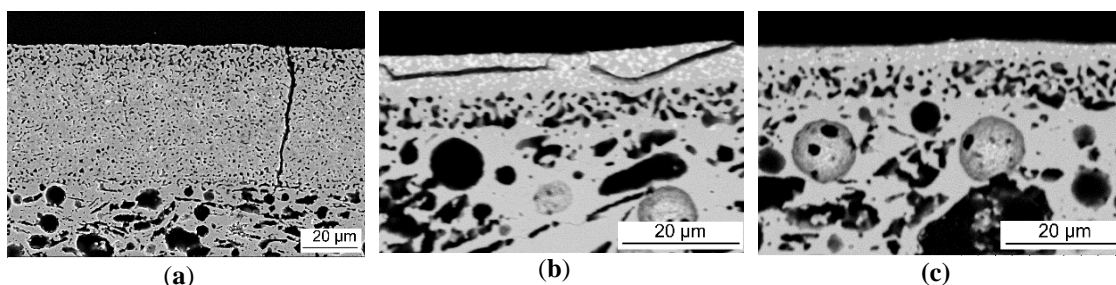


Fig. 6. Effect of thickness on crack formation in the tubular OTMs. a) Transversal crack in thick membranes. b) longitudinal cracks and c) thin membrane without cracks, but severe loss of electronic conducting phase.

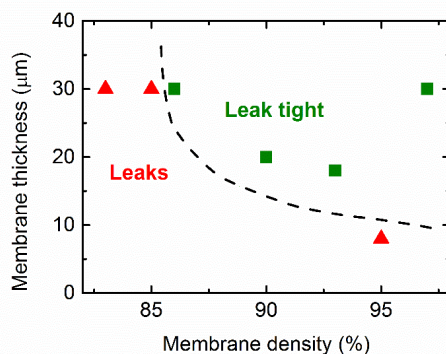


Fig. 7. Leakage dependence on thickness and density of the LCCN/10Sc1YSZ asymmetric membranes, with a qualitative estimate of regimes where the membrane leaks or is leak tight.

3.3. Cr evaporation during co-sintering

The sintered top surface of a membrane layer without additional outer porous layer was analyzed to understand the chemical distribution of elements within our membrane after co-sintering. The micrograph in Figure 8 shows the regular, expected distribution of what appears to be the LCCN and 10Sc1YSZ phases in the composite membrane surface, and in addition two regions with other phases. EDS analysis reveal that these phases are Cr-rich regions (not present in the thinnest membranes of only 4 μm) and La-rich needle-shaped agglomerates. Although the membrane surface is neither visible in most tubes (since it is covered by an outer porous activation layer), nor a correct representation of the membrane-outer porous layer interface in the membranes with an outer porous activation layer, it indicates how the LCCN phase is prone to decompose and forms other La and Cr rich phases.

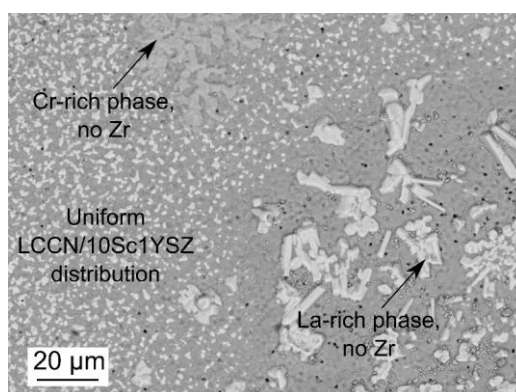


Fig. 8. Micrograph of the top surface of a tubular OTM (without outer porous activation layer) showing decomposition of the LCCN phase into Cr and La rich regions.

Figure 8 shows the cross-section of the OTM (here including the porous activation catalyst layers) with the typical longitudinal fracture observed in the intermediate thickness membranes and a close-up EDS study of the region around the longitudinal crack. La is evenly distributed both above and below the crack, while Cr is mainly present in the region of the membrane closer to the inner porous activation layer and support, and almost completely depleted on the side of the crack facing the outer porous activation layer. The chemical composition within the bright spots for the outer part of the membrane has a La:O ratio of 0.33, indicating presence of $\text{La}(\text{OH})_3$, while the bright spots on the inner side still has Cr remaining in the position of the LCCN phase. These bright

grains are also larger in the outer part (see circle in Figure 9) than the inner part, indicating that the nominal LCCN grains grow when the Cr has been depleted. Upon closer inspection it was found that the outer 4-10 μm of the membrane in all the components made with 10Sc1YSZ as the outer porous layer are depleted of Cr, while thin membranes without an outer activation layer (Figure 6(c)) show a complete loss of Cr from the membrane layer.

In the next set of experiments, additional LCCN (40 vol %) was added to the outer porous activation layer. Here the intention was that evaporation from this layer can saturate the environment immediate to the membrane surface with chromium and lower the driving force for evaporation from the membrane layer. Nevertheless, outer porous activation layers with higher fraction of LCCN than 40 vol % could not be sintered. Figure 10 shows the cross-section micrograph and EDS signals of Zr, La, and Cr with this approach. The SEM image shows a bright layer at the membrane-outer porous layer interface. This layer was found by EDS to contain La with Zr instead of Cr, in a Zr:La ratio of 2.1:1 and O:La of 7.6:1, indicating a LaZr_2O_7 secondary phase. Upon closer inspection, La,Zr secondary phases were observed also in membranes made without an outer porous activation layer or with the initial 10Sc1YSZ outer porous activation layer. Cr is present in the inner part of the membrane in Figure 10, associated with the bright phase in the SEM picture similar as seen in Figure 9. However, the stoichiometry does not add up to the LCCN phase, and the Cr:La is 0.55 rather than 0.85 as in the nominal LCCN phase. Also, Zr and Sc were found in the same spot, with a Zr:La of 20–60:1, indicating that most of the LCCN phase has decomposed and been replaced by a Sc,Y-doped ZrO_2 phase. Due to low concentration of Ni and Cu in the sample, it is difficult to see their elemental distribution in the EDS maps, but results indicate an enrichment within the 10Sc1YSZ phase.

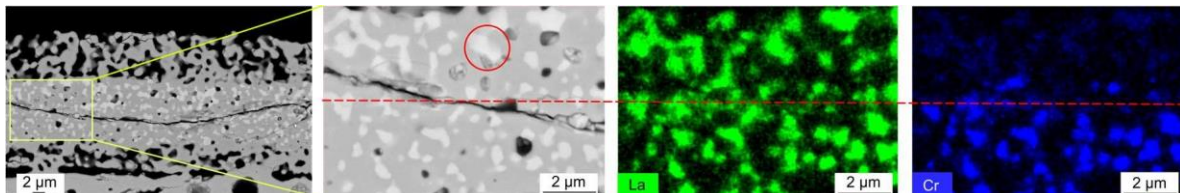


Fig. 9. SEM image (left) and EDS signals of La and Cr from a close-up of the tubular OTMs, showing evaporation of Cr and coarsening of the nominal LCCN grains (red circle) from the outer side from the crack (above the red line).

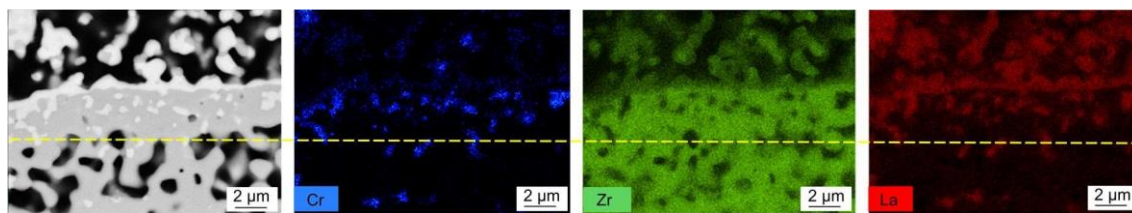


Fig. 10. SEM image (left) and EDS signals from Cr, Zr and La from the same area of a cross-section of the tubular OTMs with outer porous activation layer containing 60/40 vol% LCCN/10Sc1YSZ. The yellow line is a guide for the eye.

4. Discussion

4.1 Ceramic processing of 3YSZ porous support tubes

Thermoplastic extrusion has proven to be a suitable technique for the fabrication of porous support tubes for oxygen transport membranes. With 3YSZ as membrane support material, both high gas permeability and high strength could be achieved. Since the temperature required to densify the LCCN/10Sc1YSZ membrane was higher than expected (>1400 °C), and the membrane supports are quite dense and more than strong enough at 1400 °C, higher amounts of pore formers than 61.5 and 64.3 vol % could be considered to retain high gas permeability too after sintering at $\gg 1400$ °C. The strength of our 3YSZ tubes (Table 2) is similar to previously reported planar 3YSZ porous supports (~ 150 MPa at 45% porosity and ~ 100 MPa at 55% porosity) [19], twice as strong as porous MgO tubes (82 MPa at 42% porosity) [33], and more than four times as strong as porous BSCF tubes (20–36 MPa at 41% porosity) [6]. The gas permeability of the 3YSZ tubes is at the same time improved by an order of magnitude compared to those of MgO (4.7×10^{-16} m²) at similar porosity (42%) [33]. We have thus been successful at preparing strong, porous 3YSZ tubes that can be used for OTM supports integrated in mechanically and chemically harsh environments, or be used in other applications.

4.2 Crack formation during co-sintering of tubular, asymmetric oxygen transport membranes

Fractures, like the transverse and longitudinal cracks in our membranes, originate from stress mismatches within the membrane. Such stresses can be introduced during sintering, cooling after sintering, or storage. In an asymmetric, co-sintered system we

expect that the thickest layer, in our case the porous support, dictates the total shrinkage of the multi-layered system [34].

The transverse cracks (Figure 6a) indicate that the membrane and the adjacent layers (inner and outer porous activation layers) have been under tensile stress. The similar shape of either side of the cracks also points towards the membrane fracturing while in its elastic regime, i.e., during cooling from sintering and below creep temperatures. Tension in this regime can originate from a higher thermal expansion coefficient (TEC) of the membrane compared to the support. TEC mismatches are known [35] to cause failures similar to those observed here, and would be our initial suggestion to explain the transverse cracks. Based on the average width and separation of the transverse cracks, the expansion, and hence also the TEC of the membrane, could be estimated to be 103% of the support. This TEC difference exceeds the acceptable TEC mismatch estimated (using equations from [32] and data for 8YSZ from [36]) for our >20 μm thick membranes. There are no previous reports on the TEC of the specific LCCN composition. The TEC of LaCrO_3 ($4.6 \times 10^{-6} \text{ K}^{-1}$ in the range 40–275 $^\circ\text{C}$, $9.4 \times 10^{-6} \text{ K}^{-1}$ in the range 290–1050 $^\circ\text{C}$, and $9.8 \times 10^{-6} \text{ K}^{-1}$ in the range 1100–1395 $^\circ\text{C}$) [37,38] can be adjusted by doping to be similar to fluorite structured materials like zirconia [12]. Ni is expected to slightly decrease the TEC of LaCrO_3 , and Cu is not expected to increase it as much as elements with spin transitions such as Co [39]. We are therefore assuming LCCN to have a TEC of $\sim 9.5 \times 10^{-6} \text{ K}^{-1}$. Comparing the estimated TEC of each layer in our tubular OTMs (Table 3), however, we cannot find any support for our hypothesis that TEC mismatches cause the transverse cracks, since the literature data clearly point towards the TEC of the membrane layer being *smaller* than that of the support.

Table 3. Thermal expansion coefficients of each layer of the asymmetric membrane.

Layer	Material	Thermal expansion coef. (10^{-6} m/K)	Reference
Support	3YSZ	10.5	[36]
Activation layers	10Sc1YSZ	≤ 10.0	Based on reports on $\text{Sc}_2\text{O}_3\text{-ZrO}_2\text{-Y}_2\text{O}_3$ [40,41]
Composite membrane	30 vol% LCCN, 70 vol% 10Sc1YSZ	~ 9.9	Volumetric average of 10Sc1YSZ and LCCN ($9.5 \times 10^{-6} \text{ m/K}$).

Other possible causes of tension in the membrane and the transverse cracks are chemical reactions causing a volume reduction of the membrane, or a higher sintering rate of the

membrane layer compared to the support. No secondary phases indicating chemical reactions were observed at the fracture surface of the transverse cracks. The most plausible cause of the transverse cracks is therefore sintering stresses. Relative differences in sintering onset temperature and sintering rates are known to strongly affect the mechanical stability of multilayered ceramics [6,42,43], and the thin layer that is in tension in the early stage of sintering is most susceptible to failure [44]. A higher sintering rate of the LCCN/10Sc1YSZ membrane compared to the 3YSZ support from ~1200 °C is seen in the dilatometry studies on pellets (Figure 3). This places the membrane layer under tension, and the resulting stress-buildup is released by cracking, either immediately during sintering, during cooling, or possibly later when triggered by, e.g., thermal stress during infiltration.

Longitudinal cracks were also observed in many of the membranes and were spatially correlated with depletion of Cr (Figure 9). When sufficient amounts of Cr have evaporated from the outer part of the membrane, the LCCN perovskite will decompose and La-based secondary phases, e.g., La_2O_3 , form. La_2O_3 is known to easily hydrate to $\text{La}(\text{OH})_3$, accompanied by a large volume increase [45]. This local expansion might cause the longitudinal cracks in the zone between the Cr-depleted and the nominal regions within the dense membrane. It is also not possible to exclude TEC mismatches as the cause of some of the transverse cracks seen after sintering at high temperature (Figure 5d). The adherence between the different layers is strong, since we do not see delamination between them [25].

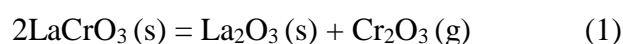
The cracks, both transverse and longitudinal, are only observed in the thickest membranes and after a certain degree of densification. The lower stiffness of porous compared to dense layers can make porous layers more able to tolerate strain [18]. Furthermore, thinner membranes are in general expected to be more crack-resistant, since the total energy to be released is smaller than for thicker layers [32]. Still, reducing the thickness of the membrane (e.g., to below 8 μm) to avoid cracking is not a viable solution, since it jeopardizes the leak-tightness crucial for selective transport of oxygen by ionic diffusion through the OTMs and causes depletion of Cr throughout most of the membrane thickness. Completely establishing the origin of the different mechanical

failures in our system would require its own designated study and is out of scope of this work.

4.3 Evaporation of Cr

The volatility of chromium in LaCrO_3 at high temperatures is a well-known challenge [12]. Since a high sintering temperature (≥ 1425 °C) was required to densify the composite membrane in our work, it is not surprising that we also encountered loss of Cr from the outer membrane part. Additionally, the LCCN in the inner part of the membrane, where the LCCN phase initially appeared intact as bright areas in the SEM images, are probably compromised, since these areas also contain Zr and less Cr than nominally, and since Ni and Cu are found outside of the nominal LCCN regions. Some of the Cr observed by EDS might also be from Cr redistributed by evaporation and condensation [12], similar to the Cr-rich agglomerates observed on the membrane surface in Figure 9. Upon evaporation of Cr (and possibly also Ni and Cu) from the B-site of the perovskite LCCN, it decomposes, and La reacts with Zr from 10Sc1YSZ instead. The LaZr_2O_7 phase observed in significant amounts at the interface between the membrane and outer porous layer is an insulating phase and is detrimental to the electrical conductivity of the OTM. Similar negative effects of such a La,Zr phase at interfaces were reported before in solid oxide fuel cells [46,47].

The evaporation in oxidizing atmospheres is assumed to occur according to Equation (1) [12]:



Thus, the creation of a local atmosphere at the membrane surface saturated with Cr_2O_3 (g) will shift the reaction (1) towards the left and stabilize the solid perovskite. This approach is used in many systems with volatile components, by adding top plates, powder beds, and/or closed crucibles. These configurations are not feasible for large, tubular components, but we aimed to achieve a similar effect by adding LCCN to the outer porous activation layer, where the high surface area should promote evaporation of Cr from the porous layer rather than the membrane and thus saturate the atmosphere to limit further evaporation. This approach was, however, not sufficient to reduce the evaporation and avoid secondary phase formation.

We can also see that the Cr in LCCN hinders the sintering; the particles are larger when depleted of Cr. The sintering temperature is expected to increase with the vol % of LCCN in the membrane, and decreasing the LCCN content could therefore be a way of lowering the sintering temperature and thus the evaporation of Cr. However, the initial amount of LCCN in the composite membrane is already low (30 vol %), and by reducing it further we risk losing percolation of the electronic conductor. The same LCCN powder (<1 μm particle size) has been successfully prepared into a planar LCCN/10Sc1YSZ composite membrane, but with a two-step sintering where high densification could be reached without loss of Cr [13]. It is also possible that finer powder (<100 nm particle size) could improve the densification (in both planar and tubular systems). However, two-step sintering or small batch-synthesized nano powder are not compatible with our ambitions to develop a membrane suitable for production in sizes and volumes for process integration. For a LaCrO_3 -based perovskite to be suitable as an electronic conductor, we would need to use other dopants than in the LCCN to allow sintering at lower temperatures, or combine it with an ionic conductor that sinters easier than 10Sc1YSZ.

5. Conclusions

3YSZ is a suitable support material for tubular oxygen transport membranes, whereas $\text{LaCr}_{0.85}\text{Cu}_{0.10}\text{Ni}_{0.05}\text{O}_{3-\delta}$ (LCCN), as the electronic conductor in a composite membrane, is extremely difficult to densify defect free in a tubular multi-layer configuration. A thermoplastic feedstocks with 61.5 vol % graphite and PMMA as pore formers resulted in porous 3YSZ supports with both sufficient gas permeability ($\geq 10^{-14} \text{ m}^2$) and mechanical strength ($\geq 50 \text{ MPa}$) for integration in gasification plants. The high sintering temperature ($\geq 1425 \text{ }^\circ\text{C}$) required to densify the LCCN/10Sc1YSZ composite membrane during co-sintering caused evaporation of Cr from the electronic conductor, formation of longitudinal cracks, and an insulating lanthanum zirconate-based secondary phase. A way of reducing the sintering temperature and thus the evaporation of Cr needs therefore to be identified before a LCCN/10Sc1YSZ-supported 3YSZ multilayer can be realized as a tubular, high performance, stable oxygen transport membrane.

Author Contributions: Investigation, A.B.H., L.M.A., K.K., T.M., K.B.A., and S.P.; Supervision, A.B.H., A.K.,P.V.H., and R.K.; Writing—original draft, A.B.H. and L.M.A.; Writing—review & editing, A.B.H., L.M.A., K.K., T.M., K.B.A., S.P., A.K., P.V.H., and R.K.

Funding: This research was funded by Energinet.dk through grant number 12403 “Highly Flexible Energy Production by Oxy-Fired Biomass Gasification”.

Acknowledgments: The authors would like to thank Dr. Simona Ovtar for valuable discussions, and Pernille Hedemark Nielsen, Marianne Nielsen and Jens Østergaard for technical assistance.

Conflicts of Interest: The authors declare no conflict of interest. The funders had no role in the design of the study; in the collection, analyses, or interpretation of data; in the writing of the manuscript, and in the decision to publish the results.

References

1. Stadler, H.; Beggel, F.; Habermehl, M.; Persigehl, B.; Kneer, R.; Modigell, M.; Jeschke, P. Oxyfuel coal combustion by efficient integration of oxygen transport membranes. *Int. J. Greenh. Gas. Control* **2011**, *5*, 7–15. [[CrossRef](#)]
2. Wei, Y.; Yang, W.; Caro, J.; Wang, H. Dense ceramic oxygen permeable membranes and catalytic membrane reactors. *Chem. Eng. J.* **2013**, *220*, 185–203. [[CrossRef](#)]
3. Ahrenfeldt, J.; Egsgaard, H.; Stelte, W.; Thomsen, T.; Henriksen, U.B. The influence of partial oxidation mechanisms on tar destruction in TwoStage biomass gasification. *Fuel* **2013**, *112*, 662–680. [[CrossRef](#)]
4. Bouwmeester, H.J.M.; Gellings, P.J. *Handbook of Solid State Electrochemistry*; CRC Press: Boca Raton, FL, USA, 1997.
5. Puig-Arnabat, M.; Soprani, S.; Søggaard, M.; Engelbrecht, K.; Ahrenfeldt, J.; Henriksen, U.B.; Hendriksen, P.V. Integration of mixed conducting membranes in an oxygen–steam biomass gasification process. *RSC Adv.* **2013**, *3*, 20843. [[CrossRef](#)]

6. Pippardt, U.; Böer, J.; Kiesel, L.; Kircheisen, R.; Kriegel, R.; Voigt, I. Co-firing technology for the preparation of asymmetric oxygen transporting membranes based on BSCF and Zr-doped BSCF. *AIChE J.* **2014**, *60*, 15–21. [[CrossRef](#)]
7. Shao, Z.; Yang, W.; Cong, Y.; Dong, H.; Tong, J.; Xiong, G. Investigation of the permeation behavior and stability of a $\text{Ba}_{0.5}\text{Sr}_{0.5}\text{Co}_{0.8}\text{Fe}_{0.2}\text{O}_{3-\delta}$. *J. Membr. Sci.* **2000**, *172*, 177–188. [[CrossRef](#)]
8. Švarcová, S.; Wiik, K.; Tolchard, J.; Bouwmeester, H.J.M.; Grande, T. Structural instability of cubic perovskite $\text{BaxSr}_{1-x}\text{Co}_{1-y}\text{FeyO}_{3-\delta}$. *Solid State Ionics* **2008**, *178*, 1787–1791. [[CrossRef](#)]
9. Brett, D.J.L.; Atkinson, A.; Brandon, N.P.; Skinner, S.J. Intermediate temperature solid oxide fuel cells. *Chem. Soc. Rev.* **2008**, *37*, 1568. [[CrossRef](#)] [[PubMed](#)]
10. Zhu, X.; Yang, W. *Critical Factors Affecting Oxygen Permeation Through Dual-phase Membranes*, 1st ed.; Elsevier BV: Amsterdam, The Netherlands, 2011; Volume 14.
11. Artemov, V.G.; Kuritsyna, I.E.; Lebedev, S.P.; Komandin, G.A.; Kapralov, P.O.; Spektor, I.E.; Kharton, V.V.; Bredikhin, S.I.; Volkov, A.A. Analysis of electric properties of $\text{ZrO}_2\text{-Y}_2\text{O}_3$ single crystals using terahertz IR and impedance spectroscopy techniques. *Russ. J. Electrochem.* **2014**, *50*, 690–693. [[CrossRef](#)]
12. Gupta, S.; Mahapatra, M.K.; Singh, P. Lanthanum chromite based perovskites for oxygen transport membrane. *Mater. Sci. Eng. R Rep.* **2015**, *90*, 1–36. [[CrossRef](#)]
13. Pirou, S.; Bermudez, J.M.; Na, B.T.; Ovtar, S.; Yu, J.H.; Hendriksen, P.V.; Kaiser, A.; Reina, T.R.; Millan, M.; Kiebach, R. Performance and stability of $(\text{ZrO}_2)_{0.89}(\text{Y}_2\text{O}_3)_{0.01}(\text{Sc}_2\text{O}_3)_{0.10}\text{-LaCr}_{0.85}\text{Cu}_{0.10}\text{Ni}_{0.05}\text{O}_{3-\delta}$ oxygen transport membranes under conditions relevant for oxy-fuel combustion. *J. Membr. Sci.* **2018**, *552*, 115–123. [[CrossRef](#)]

14. Baumann, S.; Serra, J.M.; Lobera, M.P.; Escolástico, S.; Schulze-Küppers, F.; Meulenber, W.A. Ultrahigh oxygen permeation flux through supported $\text{Ba}_{0.5}\text{Sr}_{0.5}\text{Co}_{0.8}\text{Fe}_{0.2}\text{O}_{3-\delta}$ membranes. *J. Membr. Sci.* **2011**, *377*, 198–205. [[CrossRef](#)]
15. Schulz, M.; Pippardt, U.; Kiesel, L.; Ritter, K.; Kriegel, R. Oxygen permeation of various archetypes of oxygen membranes based on BSCF. *AIChE J.* **2012**, *58*, 3195–3202. [[CrossRef](#)]
16. Baumann, S.; Meulenber, W.A.; Buchkremer, H.P. Manufacturing strategies for asymmetric ceramic membranes for efficient separation of oxygen from air. *J. Eur. Ceram. Soc.* **2013**, *33*, 1251–1261. [[CrossRef](#)]
17. Kaiser, A.; Foghmoes, S.P.; Pecanac, G.; Malzbender, J.; Chatzichristodoulou, C.; Glasscock, J.A.; Ramachandran, D.; Ni, D.W.; Esposito, V.; Søgaaard, M.; et al. Design and optimization of porous ceramic supports for asymmetric ceria-based oxygen transport membranes. *J. Membr. Sci.* **2016**, *513*, 85–94. [[CrossRef](#)]
18. Kwok, K.; Frandsen, H.L.; Søgaaard, M.; Hendriksen, P.V. Stress analysis and fail-safe design of bilayered tubular supported ceramic membranes. *J. Membr. Sci.* **2014**, *453*, 253–262. [[CrossRef](#)]
19. Klemensø, T.; Boccaccini, D.; Brodersen, K.; Frandsen, H.L.; Hendriksen, P.V. Development of a Novel Ceramic Support Layer for Planar Solid Oxide Cells. *Fuel Cells* **2014**, *14*, 153–161. [[CrossRef](#)]
20. Beggel, F.J.; Nauels, N.; Modigell, M. *CO₂ Separation via the Oxyfuel Process with O₂-Transport Membranes in Coal Power Plants*; Wiley-VCH-Verl.: Weinheim, Germany, 2011; pp. 405–430.
21. Pfaff, E.M.; Kaletsch, A.; Broeckmann, C. Design of a Mixed Ionic/Electronic Conducting Oxygen Transport Membrane Pilot Module. *Chem. Eng. Technol.* **2012**, *35*, 455–463. [[CrossRef](#)]
22. Ramachandran, D.K.; Søgaaard, M.; Clemens, F.; Gorauski, J.; Kaiser, A. Fabrication and performance of a tubular ceria based oxygen transport membrane on a low cost MgO support. *Sep. Purif. Technol.* **2015**, *147*, 422–430. [[CrossRef](#)]

23. Ovtar, S.; Gurauskis, J.; Haugen, A.B.; Chatzichristodoulou, C.; Kaiser, A.; Hendriksen, P.V. Oxygen transport properties of tubular $\text{Ce}_{0.9}\text{Gd}_{0.1}\text{O}_{1.95}\text{-La}_{0.6}\text{Sr}_{0.4}\text{FeO}_{3-\delta}$ composite asymmetric oxygen permeation membranes supported on magnesium oxide. *J. Membr. Sci.* **2017**, *523*, 576–587. [[CrossRef](#)]
24. Dahl, P.I.; Fontaine, M.-L.; Ahouanto, F.; Denonville, C.; Paulsen, O.; Larring, Y.; Peters, T.; Henriksen, P.P.; Bredeesen, R. Fabrication, sealing and high pressure testing of tubular $\text{La}_2\text{NiO}_{4+\delta}$ membranes for air separation. *Energy Procedia* **2012**, *23*, 187–196. [[CrossRef](#)]
25. Charlas, B.; Frandsen, H.L.; Brodersen, K.; Henriksen, P.V.; Chen, M. Residual stresses and strength of multilayer tape cast solid oxide fuel and electrolysis half-cells. *J. Power Sources* **2015**, *288*, 243–252. [[CrossRef](#)]
26. Haugen, A.B.; Gurauskis, J.; Kaiser, A.; Sjøgaard, M. Graphite and PMMA as pore formers for thermoplastic extrusion of porous 3Y-TZP oxygen transport membrane supports. *J. Eur. Ceram. Soc.* **2017**, *37*, 1039–1047. [[CrossRef](#)]
27. Haugen, A.B.; Geffroy, A.; Kaiser, A.; Gil, V. MgO as a non-pyrolyzable pore former in porous membrane supports. *J. Eur. Ceram. Soc.* **2018**, *38*, 3279–3285. [[CrossRef](#)]
28. Clemens, F. Thermoplastic Extrusion for Ceramic Bodies. In *Extrusion in Ceramics*; Händle, F., Ed.; Springer: Berlin, Germany, 2009; pp. 295–311.
29. Kwok, K.; Kiesel, L.; Frandsen, H.L.; Sjøgaard, M.; Hendriksen, P.V. Strength characterization of tubular ceramic materials by flexure of semi-cylindrical specimens. *J. Eur. Ceram. Soc.* **2014**, *34*, 1423–1432. [[CrossRef](#)]
30. Weibull, W. A statistical distribution function of wide applicability. *J. Appl. Mech.* **1951**, *18*, 293–297.
31. Gurauskis, J.; Ovtar, S.; Kaiser, A.; Sjøgaard, M.; Hendriksen, P.V. Ceria Based Composite Membranes for Oxygen Separation. *ECS Trans.* **2014**, *64*, 251–258. [[CrossRef](#)]

32. Hendriksen, P.V.; Høgsberg, J.R.; Kjeldsen, A.M.; Sørensen, B.F.; Pedersen, H.G. *Failure Modes of Thin Supported Membranes*; Wiley-Blackwell: Hoboken, NJ, USA, 2008; pp. 347–360.
33. Ramachandran, D.K.; Kwok, K.; Søgaard, M.; Clemens, F.; Glasscock, J.; Kaiser, A. The role of sacrificial fugitives in thermoplastic extrusion feedstocks on properties of MgO supports for oxygen transport membranes. *J. Eur. Ceram. Soc.* **2015**, *35*, 1527–1537. [[CrossRef](#)]
34. Molla, T.T.; Ramachandran, D.K.; Ni, D.W.; Esposito, V.; Teocoli, F.; Olevsky, E.; Bjørk, R.; Pryds, N.; Kaiser, A.; Frandsen, H.L. Modeling constrained sintering of bi-layered tubular structures. *J. Eur. Ceram. Soc.* **2015**, *35*, 941–950. [[CrossRef](#)]
35. Mahapatra, M.K.; Lu, K. Seal glass for solid oxide fuel cells. *J. Power Sources* **2010**, *195*, 7129–7139. [[CrossRef](#)]
36. Sarantaridis, D.; Atkinson, A. Redox cycling of Ni-based solid oxide fuel cell anodes: A review. *Fuel Cells* **2007**, *7*, 246–258. [[CrossRef](#)]
37. Höfer, H.E.; Kock, W.F. Crystal Chemistry and Thermal Behavior in the La(Cr,Ni)O₃ Perovskite System. *J. Electrochem. Soc.* **1993**, *140*, 2889–2894. [[CrossRef](#)]
38. Gupta, S.; Mahapatra, M.K.; Singh, P. Phase transformation, thermal expansion and electrical conductivity of lanthanum chromite. *Mater. Res. Bull.* **2013**, *48*, 3262–3267. [[CrossRef](#)]
39. Christie, G.M.; Middleton, P.H.; Steele, B.C.H. Liquid phase sintering, electrical conductivity, and chemical stability of lanthanum chromite doped with calcium and nickel. *J. Eur. Ceram. Soc.* **1994**, *14*, 163–175. [[CrossRef](#)]
40. Son, H.J.; Lim, T.H.; Shin, D.R.; Song, R.H.; Kim, S.H. Investigation of Scandia Stabilized Zirconia (ScSZ)—Yttria Stabilized Zirconia (YSZ) Composite Electrolyte for Intermediate Temperature Fuel Cells. *Solid State Phenom.* **2007**, *124–126*, 795–798. [[CrossRef](#)]

41. Hirano, M.; Watanabe, S.; Kato, E.; Mizutani, Y.; Kawai, M.; Nakamura, Y. Fabrication, electrical conductivity and mechanical properties of Sc₂O₃-doped tetragonal zirconia ceramics. *Solid State Ionics* **1998**, *111*, 161–169. [[CrossRef](#)]
42. Kaiser, A.; Foghmoes, S.; Chatzichristodoulou, C.; Søggaard, M.; Glasscock, J.A.; Frandsen, H.L.; Hendriksen, P.V. Evaluation of thin film ceria membranes for syngas membrane reactors—Preparation, characterization and testing. *J. Membr. Sci.* **2011**, *378*, 51–60. [[CrossRef](#)]
43. Le, S.; Sun, K.N.; Zhang, N.; Zhu, X.; Sun, H.; Yuan, Y.X.; Zhou, X. Fabrication and evaluation of anode and thin Y₂O₃-stabilized ZrO₂ film by co-tape casting and co-firing technique. *J. Power Sources* **2010**, *195*, 2644–2648. [[CrossRef](#)]
44. Cheng, T.; Raj, R. Flaw Generation During Constrained Sintering of Metal-Ceramic and Metal-Glass Multilayer Films. *J. Am. Ceram. Soc.* **1989**, *72*, 1649–1655. [[CrossRef](#)]
45. Fleming, P.; Farrell, R.A.; Holmes, J.D.; Morris, M.A. The Rapid Formation of La(OH)₃ from La₂O₃ Powders on Exposure to Water Vapor. *J. Am. Ceram. Soc.* **2010**, *93*, 1187–1194. [[CrossRef](#)]
46. Acharya, K.; Mazumder, S.K.; Burra, R.K.; Williams, R.; Haynes, C. System-interaction analyses of solid-oxide fuel cell (SOFC) power-conditioning system. In Proceedings of the 38th IAS Annual Meeting on Conference Record of the Industry Applications Conference, Salt Lake City, UT, USA, 12–16 October 2003; IEEE: Piscataway, NJ, USA, 2003; Volume 3, pp. 2026–2032.
47. Van Heuveln, F.H.; Bouwmeester, H.J.M. Electrode Properties of Sr-Doped LaMnO₃ on Ytria-Stabilized Zirconia. *J. Electrochem. Soc.* **1997**, *144*, 134–140. [[CrossRef](#)]



© 2018 by the authors. Submitted for possible open access publication under the terms and conditions of the Creative Commons Attribution (CC BY) license (<http://creativecommons.org/licenses/by/4.0/>).

5.3 $\text{Y}_{0.8}\text{Ca}_{0.2}\text{Cr}_{0.8}\text{Co}_{0.2}\text{O}_{3-\delta}$ -based dual phase membranes for oxyfuel and syngas applications.

In Chapter 5.2, it was demonstrated that the development of thin $(\text{Sc}_2\text{O}_3)_{0.10}(\text{Y}_2\text{O}_3)_{0.01}(\text{ZrO}_2)_{0.89} - \text{LaCr}_{0.85}\text{Cu}_{0.10}\text{Ni}_{0.05}\text{O}_{3-\delta}$ oxygen transport membranes (OTMs) was limited by challenges related to Cr evaporation from the $\text{LaCr}_{0.85}\text{Cu}_{0.10}\text{Ni}_{0.05}\text{O}_{3-\delta}$ perovskite after sintering at 1450 °C. After loss of Cr, La formed secondary phases, such as $\text{La}(\text{OH})_3$ and $\text{La}_2\text{Zr}_2\text{O}_7$ that affected the functionality and mechanical integrity of the membrane. In order to avoid side-reactions during the processing of the dual-phase membranes, a La-free perovskite would be needed. $\text{Y}_{0.8}\text{Ca}_{0.2}\text{Cr}_{0.8}\text{Co}_{0.2}\text{O}_{3-\delta}$ (YCCC) has been investigated as electronic-conducting material in solid oxide fuel cells applications [Yoon, et al. 2011; Yan, et al. 2016] and it could be used as electronic conducting phase in dual-phase OTMs.

This section contains the paper “ $\text{Y}_{0.8}\text{Ca}_{0.2}\text{Cr}_{0.8}\text{Co}_{0.2}\text{O}_{3-\delta}$ -based dual phase membranes for O_2 separation in oxyfuel and syngas applications”. The manuscript was written in cooperation with the Instituto de Tecnología Química (ITQ). Staff of ITQ are the first and corresponding authors of this paper.

This study analysed the compatibility of the YCCC with high-performance oxygen-ion conductors: $\text{Ce}_{0.9}\text{Gd}_{0.1}\text{O}_{2-\delta}$, $(\text{Y}_2\text{O}_3)_{0.08}(\text{ZrO}_2)_{0.92}$, and $(\text{Sc}_2\text{O}_3)_{0.10}(\text{Y}_2\text{O}_3)_{0.01}(\text{ZrO}_2)_{0.89}$. It was found that the composites using ZrO_2 -based materials formed a Cr_2CoO_4 secondary phase and showed lack of densification after thermal treatment at 1300 °C in air. On the other hand, the composite using $\text{Ce}_{0.9}\text{Gd}_{0.1}\text{O}_{2-\delta}$ (CGO) was fully dense. EDS-analysis revealed high chemical stability of the composite after sintering. The onset temperature of the composite was obtained at 937 °C, which might be originated by the interaction of the Co from the YCCC and the CGO phase. The composite did not resist low reducing conditions ($\sim 10^{-20}$ atm), since cracks along the CGO grains were formed, probably caused by chemical expansion of the CGO.

Oxygen permeability tests of the composite resulted on $0.78 \text{ Nml} \cdot \text{min}^{-1} \cdot \text{cm}^{-2}$ for 0.7 mm thick membrane pellets in an Air/ CO_2 gradient at 1000 °C. Stability tests showed that the composite withstood the exposition to 25% CO_2 -Ar/Air gradient at 900 °C over 1800 hours, which makes it promising candidate material for oxyfuel applications.

Y_{0.8}Ca_{0.2}Cr_{0.8}Co_{0.2}O₃-based dual phase membranes for oxyfuel and syngas applications

Julio Garcia-Fayos¹, Lev Martinez Aguilera², Astri Bjørnetun Haugen², Wolff-Ragnar Kiebach², Jose M. Serra*¹

¹ Instituto de Tecnología Química (Universitat Politècnica de València – Consejo Superior de Investigaciones Científicas), E-46022 Valencia, Spain

² Department of Energy Conversion and Storage, Technical University of Denmark, 2800 Kgs. Lyngby, Denmark

* Corresponding author. jmserra@itq.upv.es

Abstract.

Dual-phase composites based on Y_{0.8}Ca_{0.2}Cr_{0.8}Co_{0.2}O₃ as electronic conducting phase and (Sc₂O₃)_{0.10}(Y₂O₃)_{0.01}(ZrO₂)_{0.89}, Ce_{0.9}Gd_{0.1}O_{2-δ}, and (Y₂O₃)_{0.08}(ZrO₂)_{0.92} as ion conductors were investigated to determine their potential use as oxygen transport membrane materials. The composite Ce_{0.9}Gd_{0.1}O_{2-δ} – Y_{0.8}Ca_{0.2}Cr_{0.8}Co_{0.2}O₃ was the only feasible composite to analyse. The composite has a sintering temperature onset of 937 °C and a total conductivity of 4.5 S·cm⁻¹ at 825 °C. No variation of the conductivity was observed within the pO₂ range 2x10⁻⁵ to 1 bar. Oxygen permeability tests of the composite resulted on 0.70 Nml·min⁻¹·cm⁻² in Air/Ar gradient and 0.78 Nml·min⁻¹·cm⁻² in an Air/CO₂ at 1000 °C by using a 0.7 mm thick pellet. Negligible degradation was registered after exposing the composite to a gradient 25% CO₂-Ar/Air at 900 °C over 24 hours. This demonstrates the Ce_{0.9}Gd_{0.1}O_{2-δ} – Y_{0.8}Ca_{0.2}Cr_{0.8}Co_{0.2}O₃ composite is suitable as oxygen transport membrane for oxyfuel applications.

1. Introduction.

In the past recent years there is a significant interest from governments and administrations for implementing policies oriented to achieve an industry carbon neutrality while gaining in efficiency and competitiveness [1]. This will require from a profound transformation of energy-intensive industries via the switching to (i) renewable and clean energy solutions, (ii) technical approaches enabling the reduction or removal of GHG emissions, and (iii) alternative and secondary raw materials that currently are not considered nor exploited. The reduction of GHG emissions such as CO₂ can be

accomplished by integrating oxy-combustion solutions along with carbon capture and storage (CCS) [2-4]. Regarding the carbon-neutral exploitation of alternative raw materials, it can be achieved by conducting the production of commodity intermediates and building blocks (such as H₂ and carbon-based compounds like syngas, methane, methanol or ethylene) by using sustainable feedstocks (e.g. biogas from biomass residues) and renewable energy [5-7]. A way for implementing both strategies is by making use of oxygen technologies, i.e. application of CCS by conducting fuel combustions with pure O₂ and production of high added value chemicals (syngas, ethylene...) with methane partial oxidation and oxidative dehydrogenation of alkanes [8-13]. Such approaches require from an O₂ source, e.g. an Air Separation Unit (ASU) integrated within such processes.

Current commercial technologies enabling on-site O₂ production are (i) cryogenic distillation of air and (ii) pressure swing adsorption, being only the first a valid option capable of continuously satisfying the O₂ demands in terms of purity for the considered applications. Nevertheless, cryo-O₂ production is high energy intensive and only economically viable for large installations in the range of 30,000–50,000 Nm³ O₂/h [14]. In this context, Oxygen Transport Membranes (OTMs) based on ceramic materials is being considered as an alternative for the O₂ production in small and medium scale applications [15], enabling almost a 50% reduction in energy consumption per ton of produced O₂ [16], as well as a reduction in O₂ production costs of up to 35% with regard to traditional technologies [17]. Furthermore, OTMs application in industrial processes permits a synergetic integration of two processes, O₂ supply and chemical reaction, in one single unit device [18]. Such an approach presents several advantages: (i) gain in process simplicity for several processes are integrated in only one process unit, (ii) important energy savings and reduction of waste emissions, (iii) achievement of higher yields and conversion rates, and (iv) conduction of reaction in a safer way (avoidance of explosive atmospheres).

Under applications conditions (reducing atmospheres, presence of CO₂...), the typical mixed ionic-electronic conducting (MIEC) materials used as OTMs are not chemically nor mechanically stable [19-23]. Nevertheless, recent investigations conducted on composite materials have demonstrated a good behaviour and performance of these when

exposed to harsh environments [24-27]. Amongst them, dual-phase materials with composition based on $\text{Fe}_2\text{NiO}_4 - \text{Ce}_{0.8}\text{Tb}_{0.2}\text{O}_{2-d}$ and $(\text{Y}_2\text{O}_3)_{0.01}(\text{Sc}_2\text{O}_3)_{0.10}(\text{ZrO}_2)_{0.89} - \text{MnCo}_2\text{O}_4$ have shown an outstanding stability and a promising performance [28-30], even in presence of harmful compounds such as CO_2 , SO_2 and H_2O . Ca- and Co-doped yttrium chromite (YCCC) has been considered in several studies as a good interconnect material for solid oxide fuel cells due to its excellent electronic conductivity and stability [31, 32] and also as electronic conductive phase in dual-phase membranes combined with Sm-doped ceria, resulting in highly stable material for continuous operation under H_2 - CO_2 environments [33].

The present work is focused on the production and characterization of $\text{Y}_{0.8}\text{Ca}_{0.2}\text{Cr}_{0.8}\text{Co}_{0.2}\text{O}_3$ -based dual phase membranes for O_2 separation in low $p\text{O}_2$ applications. For that aim it has been evaluated the chemical compatibility of several compositions (YCCC in combination with yttrium stabilized zirconia, scandium doped YSZ and gadolinium doped ceria), as well as studying their stability under reducing environments at very high temperature. Once selected the most compatible and stable material, it has been conducted a thorough characterization including microstructural, electrochemical and oxygen permeation studies, thus completely determining the material capabilities for its consideration in the prospected applications.

2. Experimental.

2.1. Samples preparation.

YCCC powders were prepared by Pechini method. For conducting this synthesis, the corresponding metal nitrates were dissolved in an aqueous solution ($\text{Y}(\text{NO}_3)_3 \cdot 6\text{H}_2\text{O}$, $\text{Ca}(\text{NO}_3)_2 \cdot 4\text{H}_2\text{O}$, $\text{Cr}(\text{NO}_3)_3 \cdot 9\text{H}_2\text{O}$ and $\text{Co}(\text{NO}_3)_2 \cdot 6\text{H}_2\text{O}$ provided by Sigma Aldrich. Once obtained a complete dissolution, citric acid (Sigma Aldrich) was added as chelating agent to prevent partial segregation of metal components and ethylene glycol to polymerize with chelating agent and produce an organometallic polymer (in a molar ratio 1:2:4, respectively). This complexation is followed by dehydration at low temperature (up to 270°C) and finally, the thermal decomposition of the precursors at 1100°C forms the structural phase.

For the conduction of a chemical compatibility study, YCCC powder obtained by Pechini method was mixed with different fluorites from commercial suppliers such as $\text{Ce}_{0.8}\text{Gd}_{0.2}\text{O}_2$ (CGO, Treibacher), $(\text{Y}_2\text{O}_3)_{0.08}(\text{ZrO}_2)_{0.92}$ (YSZ, Tosoh) and $(\text{Y}_2\text{O}_3)_{0.01}(\text{Sc}_2\text{O}_3)_{0.10}(\text{ZrO}_2)_{0.89}$ (ScSZ, Marion Technologies). YCCC-CGO, YCCC-YSZ and YCCC-ScSZ composite powders were obtained after mixing the corresponding perovskite-fluorite phases in a 1:1 volume ratio and subsequent ball milling in acetone for 48 hours. After drying, the composite powders were uniaxially pressed on a 26 mm diameter steel die (50 MPa) to form green disks. The disks were sintered at 1300 °C for 6 h in air.

Samples for Electrical Conductivity (EC) characterization were produced by uniaxial pressing of YCCC powder in a 4 x 0.4 x 0.2 cm³ rectangular steel die at 125 MPa during 1 minute and subsequent sintering at 1350 °C for 5 hours in air.

For electrochemical impedance spectroscopy (EIS) measurements, 30 µm-thick porous layers of YCCC-CGO were screen-printed on both sides of a CGO electrolyte disk. Ink for screen-printing was made by mixing in a three roll mill a 1:2 weight ratio of previously ball-milled YCCC-CGO and an ethyl cellulose (6 wt%) solution in terpineol. After deposition, the obtained composite ceramic structures were sintered in air at 1100 °C for 2 h.

Low surface area $\text{Ce}_{0.9}\text{Gd}_{0.1}\text{O}_{2-\delta}$, CGO (FuelCell Materials) and $\text{Y}_{0.8}\text{Ca}_{0.2}\text{Cr}_{0.8}\text{Co}_{0.2}\text{O}_{3-\delta}$, YCCC (Jülich Forschungszentrum) powders were mixed in volumetric proportion 70:30, ball-milled in ethanol for 72 hours and dried. Samples of single YCCC and CGO powders were ball-milled in similar conditions as the composite to ensure the same particle size when assessing their individual stability and sintering properties. CGO, YCCC and CGO-YCCC composite pellets were prepared by cold uniaxial pressing with 1 ton·cm⁻² (98 MPa) using 3 w% PVA as binder. Pellets were sintered at 1300°C in air for 2 hours using heating and cooling rates of 60 and 120°C·min⁻¹ respectively and then exposed to reducing conditions (5% H₂-Ar) for 24 hours at 900°C, in order to analyse the microstructural stability of the composite.

2.2. Samples characterization.

Crystalline phases in produced samples were identified by using a PANalytical Cubix fast diffractometer, using $\text{CuK}\alpha 1$ radiation ($\lambda = 1.5406 \text{ \AA}$) and an X'Celerator detector in Bragg–Brentano geometry. XRD patterns recorded in the 2θ range from 20° to 90° were analyzed using X'Pert Highscore Plus software. Cross section analysis of the sintered materials after and before tests were conducted by performing scanning electron microscopy (SEM) and energy dispersive X-ray (EDX) characterization using a ZEISS Ultra55 field emission scanning electron microscope. Furthermore, backscattered electrons detector (BSD) was used to provide images with compositional contrast that differentiate grains and element distribution.

Field emission scanning electron microscope (FE-SEM) (Merlin, Zeiss) working with secondary and backscattered electron detectors and accelerating voltage of 15 kV was used for the microstructural analysis of the samples. The composition of the untreated (before sintering), sintered and reduced composite pellets was analyzed by using EDS (Quantax70) working at 15 kV.

High temperature X-ray diffraction analysis (HT-XRD) was done to identify structural changes and secondary phase formation during the sintering process of the composite. Diffractograms were obtained using a high resolution X-ray diffractometer (Smartlab, Rigaku) varying 2θ in the interval 10° to 140° with a step of 0.0152° . In total 27 XRD measurements were taken in-situ between room temperature (RT) and 1100°C .

Sintering curves of CGO, YCCC and CGO-YCCC composite up to 1200°C were obtained using a dilatometer (DIL 402C, Netzsch). Heating ramp of $1^\circ\text{C}\cdot\text{min}^{-1}$, cooling ramp of $10^\circ\text{C}\cdot\text{min}^{-1}$ and air flow of $20 \text{ l}\cdot\text{min}^{-1}$ were used in all the dilatometry analyses.

EC measurements were conducted by standard four-point DC technique on the rectangular bars. Silver wire and paste were used for contacting electrodes. The measurements were carried out after 2 h of stabilization at 800°C by cooling down at a rate of $1^\circ\text{C}\cdot\text{min}^{-1}$ in constant O_2 containing atmospheres (Linde calibrated gas mixtures). The constant current was supplied by a programmable current source (Keithley 2601) and the voltage drop through the sample was detected by a multimeter (Keithley 3706).

Permeation tests were performed on a gastight YCCC-CGO composite disk sintered at 1400 °C for 10 hours, with final membrane thickness of 0.55 mm. YCCC-CGO membrane was screen-printed on both sides with a 15 µm-thick BSCF porous layer including graphite pore former and 5% wt. of Pd nanoparticles. After deposition and drying the layer was calcined at 1050 °C in air for 2 hours. The permeation tests were conducted in a lab-scale reactor consisting of a cylindrical two chambers quartz reactor, in which synthetic air (21%, vol. O₂) or pure O₂ was fed into the oxygen-rich chamber, while argon, Ar/CO₂ mixtures and 10% CH₄ in Ar were used as sweep gases on the permeate side chamber, in a 4-end mode configuration. Both streams were fed at atmospheric pressure. Inlet gases were preheated in order to ensure the correct gas temperature for contact with the membrane surface. This is particularly important when high gas flow rates are employed. All streams were individually mass flow controlled. The temperature was measured by a thermocouple attached to the membrane. Membrane gas leak-free conditions were achieved using gold rings on both sides of the membrane, which were heated to 1000 °C for 4 h immediately prior to the measurement. The permeate was analysed at steady state by online gas chromatography using a micro-GC Varian CP-4900 equipped with Molsieve5A, Pora-Plot-Q glass capillary, and CP-Sil modules. Membrane gas leak-free conditions were ensured by continuously monitoring the N₂ concentration in the product gas stream. An acceptable sealing was achieved when the ratio between the oxygen flow leak and the oxygen flux was lower than 3%. The data reported here were achieved at steady state after 1 h in the reaction stream. Each test was repeated three times to minimize the analysis error. The experimental analytical error was below 0.5%.

3. Results and discussion

3.1. Microstructural study.

Chemical compatibility of YCCC-based composites

YCCC has been considered in several studies as a good interconnect material for solid oxide fuel cells due to its excellent electronic conductivity and stability [31, 32]. Aiming to produce a dual-phase material presenting high mixed ionic-electronic conductivity which subsequently results in high O₂ permeation fluxes, it was considered the

formulation of three different YCCC-based composites including fluorites as ionic phases: (i) 50% YCCC – 50% CGO, (ii) 50% YCCC – 50% YSZ, and (iii) 50% YCCC – 50% ScSZ. A balanced 50-50 vol.% ratio was selected in order to ensure a proper distribution of electronic and ionic percolation paths. It was studied the chemical compatibility of the considered phases by uniaxial pressing of the composite powders and sintering at 1300 °C in air during 6 hours. The resulting specimens were analysed by XRD and FE-SEM. As can be seen in Figure 1, only YCCC-CGO material presents a chemical compatibility between its constituting phases with the achievement of a high degree of density for ensuring membrane gas-tightness. On the other hand, YCCC-YSZ and YCCC-ScSZ sintering results in the formation of a Cr_2CoO_4 phase in both compositions. Furthermore, FE-SEM analysis shows a lack of sinterability for YCCC-YSZ and YCCC-ScSZ, resulting in porous structures with presence of small aggregates corresponding to the detected Cr_2CoO_4 phase. Therefore, dual-phase material consisting of YCCC and CGO can be considered as suitable for the production of composite membranes for O_2 production.

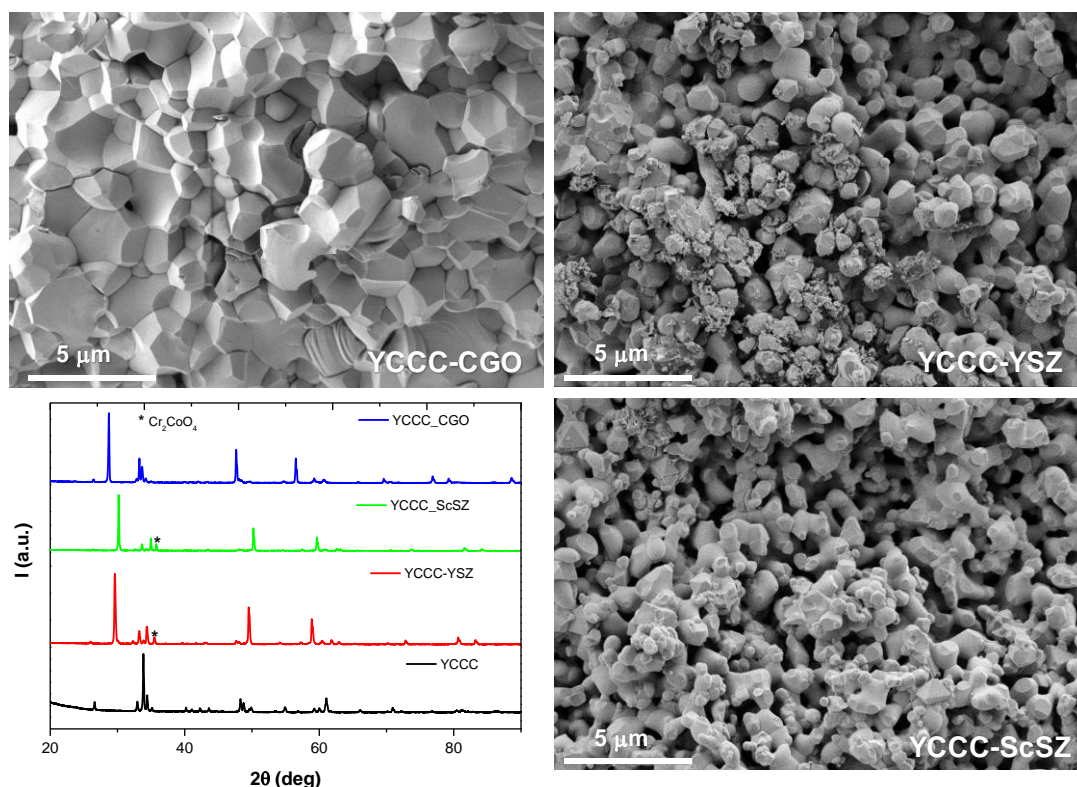


Figure 1. FE-SEM images corresponding to YCCC composites cross sections and XRD patterns of the depicted samples.

YCCC-CGO stability under reducing environments

YCCC-CGO sintered pellets were exposed to 5% H₂ in Ar atmosphere for 24 hours at 900 °C, in order to analyse the microstructural stability of the composite under reducing conditions. SEM cross-section micrographs of pellets sintered at 1300°C before and after exposure to reducing conditions at 900°C show changes in the microstructure of the composite. After sintering, uniform distribution of YCCC-CGO phases and 5% porosity was homogeneously observed across the pellet's surface and bulk. Once the sample was exposed to reducing conditions, cracks along CGO grains were observed, probably caused by chemical expansion of CGO. [34] No changes in porosity were noticed.

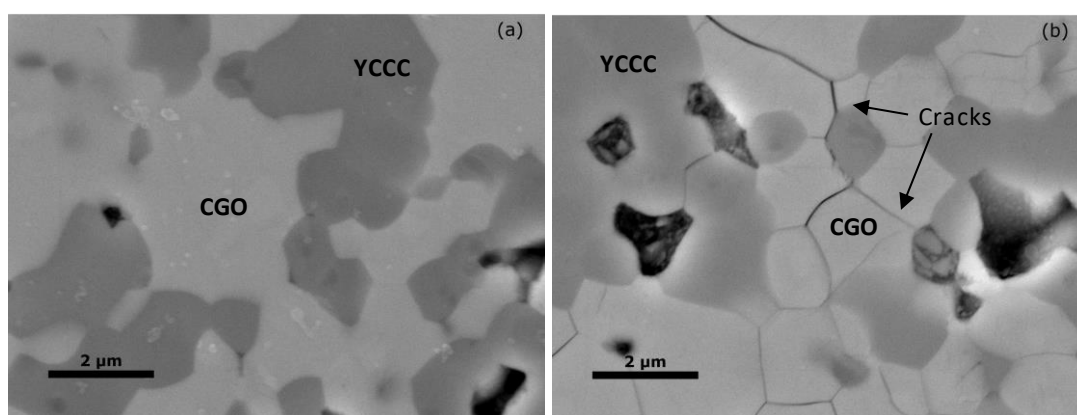


Figure 2. SEM micrographs of the CGO-YCCC composite after (a) sintering in air at 1300°C and (b) after sintering and applying reducing conditions 5% H₂-Ar for 24h at 900°C.

Table 1 shows the EDS analysis of the different YCCC metals in the untreated, as-sintered and reduced composite pellets. It is observed that the Y, Ca, Cr and Co atomic proportions in the untreated pellet are close to the theoretical values; however, once the sample is sintered, a Y deficiency is observed. After applying reducing conditions, a decrease in the Cr and Co quantities is noticed.

Table 1. Atomic composition of YCCC in different samples using EDS (Normalized data to Y = 0.80)

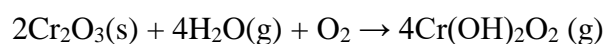
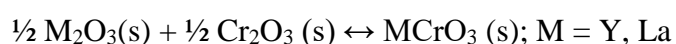
Element	Ca	Cr	Co
Theoretical	0.20	0.80	0.20
Not treated.	0.25	0.81	0.19
As-sintered	0.31	1.20	0.36
Reduced	0.26	0.87	0.20

An analysis of the CGO phase of the as-sintered sample shows the presence of Y in atomic proportion ~1:1 to Ce. Different authors [35-38] have studied Y-Ce solid solutions for different applications. Among them, Tessier et al. [38] obtained stable compounds with stoichiometry from CeO₂ to Ce_{0.5}Y_{0.5}O_{1.75} at 900°C. It might be possible that during sintering at 1300°C of the CGO-YCCC composite, Y formed a solid solution within the CGO phase. However, additional analysis for the structure determination, properties and formation mechanisms of the Y-Ce compounds can be matter of further investigations.

Some authors have proposed that an under-stoichiometry of the perovskite's A-site might result in the exsolution of B-site species into their oxides in an attempt to reestablish the stoichiometry in both sites of the perovskite [39].

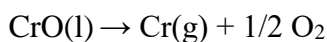
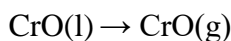
One of the major drawbacks of YCCC and any other chromite at high temperatures is the loss of Cr and other metal species in the B sites of the perovskite, which enhance the electrical conductivity and stability towards reducing conditions, among other properties [40].

Cr vaporization has been studied by different authors [41-43] finding that decomposition in oxidizing conditions occurs above 900 °C, and highly accelerated above ~1250 °C [41]. Different Cr species are formed due to reaction with oxygen, and if water vapor is present in the air, decomposition increases significantly due to formation of hydroxide species [40, 44]. The main reactions during the decomposition are:

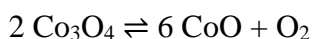


In reducing conditions, Cr vaporization might be associated to reduction and decomposition of Cr₂O₃ into Cr²⁺ and Cr⁰ species [13]. Peres et al. [45] have studied the Cr₂O₃ dissociation in reducing conditions (pO₂ in the range 10⁻²¹ – 10⁻¹¹ atm) and have found that different reactions may form gaseous Cr compounds, which could explain the loss of Cr after sintering and treatment in reducing atmospheres.



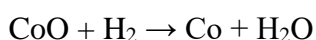
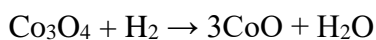


Regarding Co, Tsvetkov et al. [39] have studied cobaltite double perovskites decomposition and suggested the formation of Co_3O_4 at $T < 950^\circ\text{C}$ and CoO at $T > 950^\circ\text{C}$ as perovskite's exsolution products. Co_3O_4 has a boiling point of 895°C and it decomposes at 920°C in oxidizing conditions with $p\text{O}_2 < 1$ according to [46]



After 950°C , CoO is stable in oxidizing conditions [47]. Thus, it is likely that during the sintering process, vaporization and decomposition of Co_3O_4 may take part.

In hydrogen reducing conditions, two main reactions are carried out at 300°C and 700°C respectively [48].



Li et al. [47] have suggested a five step mechanism with intermediate species up to elemental Co where all the reactions occur in the range $192^\circ\text{C} - 750^\circ\text{C}$. In addition, Ernst et al. [49] studied the catalytic effect of CeO_2 over 40 w% in the reduction of Co_3O_4 to Co finding that the reduction reaction was completed at 527°C . It might be possible that an interaction of the CeO_2 from the CGO may occur and promote the reduction of the exsolved Co_3O_4 from the YCCC perovskite, which could cause the loss of Co from the studied composite.

YCCC-CGO composite sintering behaviour

Onset temperatures obtained from YCCC, CGO and CGO-YCCC dilatometry curves (Figure 3) and HT-XRD diffractograms of CGO-YCCC (Figure 4) show the interaction between the composite's components. While single CGO and YCCC have similar sintering rates and temperature onsets approximated to 1042°C and 1116°C , respectively (Figure 3), the composite's onset drops considerably to 937°C .

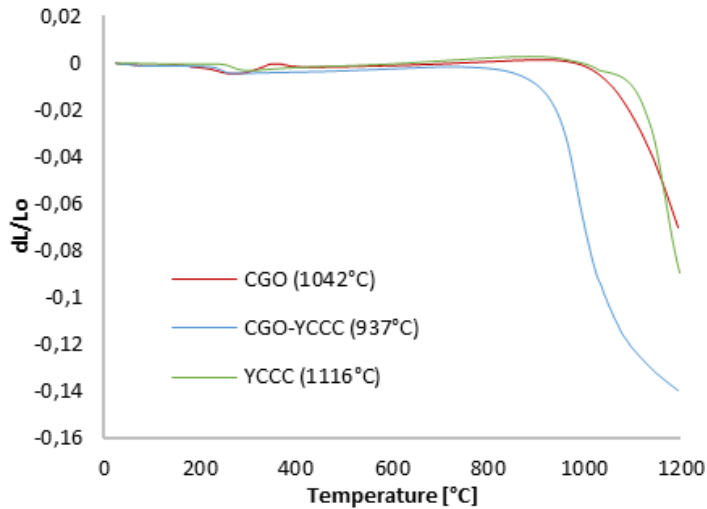


Figure 3. Dilatometry curves of CGO, YCCC and CGO-YCCC composite. Onset point in brackets.

Change in the crystal structure can be observed in the HT-XRD analysis. After sintering at 1100°C, broadening of the YCCC peaks at 33.5° and 60.5° (Figure 4b and c) occurs between 925°C and 950°C and remains after cooling, which might indicate a change in the YCCC lattice parameters. The HT-XRD diffractograms mainly show the reflections from CGO because the YCCC peaks overlap with the CGO, the main phase of the composite. The full HT-XRD analysis between RT and 1100°C is shown in the appendix.

As discussed above, Co_3O_4 decomposition in oxidizing conditions occurs between 920°C and 950°C, which matches with the range of temperature where the YCCC lattice parameters changed. Zhang et al. [50] studied the system Co_3O_4 -doped $\text{Ce}_{0.8}\text{Gd}_{0.2}\text{O}_{2-\delta}$ (CGO20). They found that Co precipitates at the CGO20 grain boundaries as a thin film of cubic CoO and it increased with increasing temperature in the interval 890°C - 1150°C [50, 51]. Other authors [52, 53] also found Co segregated at the CGO grain boundaries as a 2-4 nm transient liquid-phase layer.

Several studies [51-55] have demonstrated cobalt's effectivity as sintering aid, where quantities as low as 1 mol% can significantly accelerate the CGO sintering process. Thus, it is likely that a similar mechanism and interaction between the CGO and the exsolved Co_3O_4 occurred, lowering the composite's temperature onset.

A detailed qualitative and quantitative EDS-TEM analysis could be confirm the presence of CoO in the CGO grain boundaries.

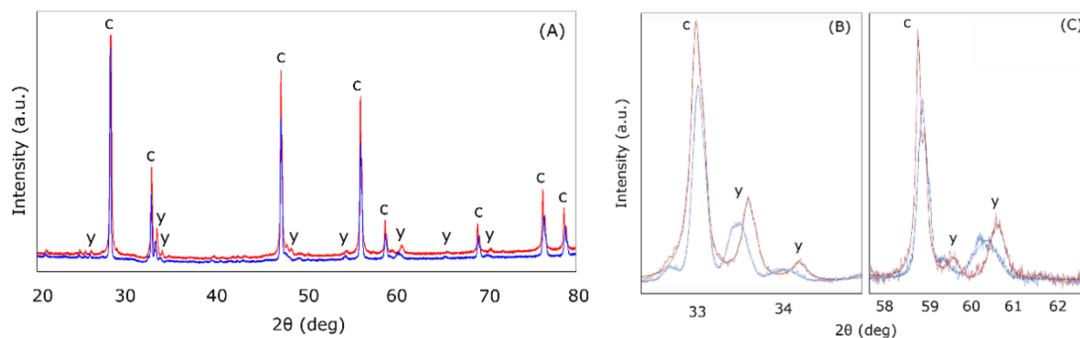


Figure 4. XRD diffractograms of CGO-YCCC composite taken at 500°C during heating (red) and cooling (blue) before and after sintering in air at 1100°C. (A) Relevant 2θ range, (B) and (C) YCCC peaks at 33.5° and 60.5° respectively. c: CGO, y: YCCC.

Functionality of the dual phase.

Small amounts of Co or other transition metals oxides, such as Fe and Cu, are very effective as sintering aids but can also modify the conductivity of CGO [54]. Doping with Co can increase the ionic conductivity and also develop p-type electronic conductivity; which would allow the extension of the mixed ionic–electronic conduction to higher oxygen partial pressures (10^{-5} to 10^{-1} atm) [55]. Minor dopant additions (<2%) have negligible effect in the total ionic conductivity of CGO. However, p-type conduction can increase 8-30 times at 1173-1473°C, because it increases the grain boundary intrinsic conductivity [52, 53].

Both Ca and Co are dopants that enhance the electrical conductivity of YCrO_3 . Therefore, loss of these species from YCCC through mobility or vaporization might reduce the electrical conductivity of YCCC, and thus the performance of the active membrane during oxygen transport might decay.

3.2. Electrochemical studies.

Once proved the chemical compatibility between YCCC and CGO phases, the transport properties of the YCCC-CGO composite were studied. Figure 5a shows the total electrical conductivity (σT) in dependence of the reciprocal temperature measured in air for the YCCC and CGO single phases, and the YCCC-CGO composite. As it can be seen, YCCC presents the highest conductivity amongst the measured samples, achieving $41 \text{ S}\cdot\text{cm}^{-1}$ at 825 °C in air. Such values are in accordance with previous EC measurements conducted in YCCC [31, 32]. With regard to YCCC-CGO composite, the total conductivity decreases significantly down to $4.5 \text{ S}\cdot\text{cm}^{-1}$ when combined with CGO. This is ascribed

to the ionic contribution of CGO phase, which presents a conductivity of $0.03 \text{ S}\cdot\text{cm}^{-1}$ at $825 \text{ }^\circ\text{C}$ in air, thus reducing the electrical properties of the composite. Furthermore, it was also studied the total conductivity of YCCC, CGO and YCCC-CGO as a function of $p\text{O}_2$ at $800 \text{ }^\circ\text{C}$ (Figure 5b). As can be seen, no significant variation in σ is observed for the considered materials when varying $p\text{O}_2$ from $2\cdot 10^{-5}$ to 1 bar. This suggest that the electronic conductivity is the predominant transport mechanism of the considered composite material.

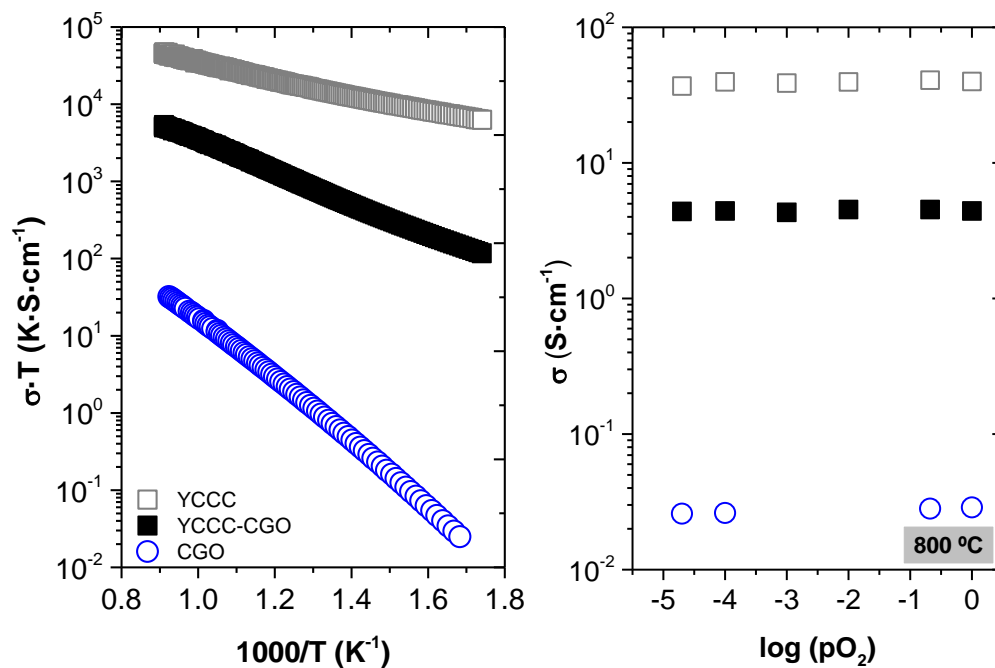


Figure 5. a) Arrhenius plot of the total electrical conductivity in air for the single phase YCCC, CGO, and the composite phase YCCC-CGO. b) total electrical conductivity in dependence of $p\text{O}_2$ at $800 \text{ }^\circ\text{C}$ of the YCCC, CGO and YCCC-CGO composite

EIS measurements were performed on symmetric cells consisting of YCCC-CGO electrodes deposited on CGO electrolytes. This was done in order to study the surface electrochemistry of the dual-phase material as well as the effect of CO_2 in the oxygen surface reactions. For that aim, different tests were conducted at $850 \text{ }^\circ\text{C}$ when considering different gas atmospheres: 21% O_2 in N_2 (feed side conditions), 5% O_2 in CO_2 (clean sweep side conditions) and 5% O_2 in CO_2 (oxy-fuel sweep side conditions). As can be seen in Figure 6a, lower impedance values are obtained under air feeding conditions, whereas it is experienced a significant increase in polarization resistance (R_p) values when decreasing O_2 content in the gas stream. R_p increases from 0.46 to $0.65 \text{ }\Omega\cdot\text{cm}^2$ when

switching from 21% O₂ to 5% O₂ in N₂. This is due to oxygen surface semi-reactions are favored by high O₂ concentrations. When replacing N₂ by CO₂ for mimicking oxy-fuel conditions only a minor increase is observed. This reversible effect is ascribed to the CO₂ competition with the O₂ for the surface active sites, which results in a blocking of these sites and, subsequently, in the diminution of the oxygen permeation [29, 56]. All these variations in impedance take place at low and medium frequencies, as results from Nyquist plot observation in Figure 6b, being this significant of the influence of pO₂ conditions and CO₂ presence on the surface reactions. In Figure 6c it is compared the performance of different dual-phase materials with YCCC-CGO material when exposed to the same considered environments at 850 °C. The selected cases correspond to already reported EIS studies conducted on Fe₂NiO₄ – Ce_{0.8}Tb_{0.2}O₂ (60-40 vol%) [56], MnCo₂O₄ - (Y₂O₃)_{0.01}(Sc₂O₃)_{0.10}(ZrO₂)_{0.89} (30-70 vol.%) and MnCo₂O₄ - (Y₂O₃)_{0.01}(Sc₂O₃)_{0.10}(ZrO₂)_{0.89} (60-40 vol.%) [28] composite materials. As displayed in Figure 6c, YCCC-CGO composite presents the lowest R_p values amongst the considered materials for all the tested conditions. Then, it would be expected a better oxygen permeation performance for a membrane consisting of YCCC-CGO.

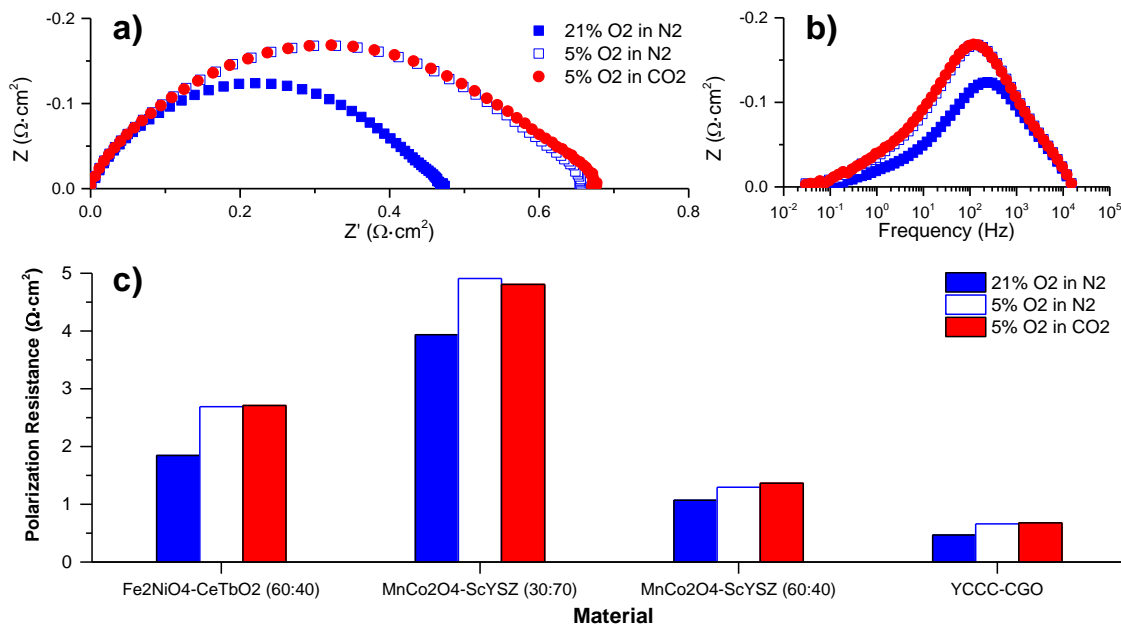


Figure 6. a) BODE plot of YCCC-CGO at 850 °C. b) Nyquist plot of YCCC-CGO at 850 °C. c) Polarization resistance values of various composites at 850 °C.

3.3. Oxygen permeation tests

In order to characterize the oxygen permeation of YCCC-CGO, it was tested a 0.55 mm-thick membrane. For minimizing the limitation of surface kinetics it was added on both membrane sides a 15 μm -thick porous catalytic layer consisting of BSCF impregnated with 5% wt. Pd. The oxygen permeation was studied in the temperature range from 700 to 1000 $^{\circ}\text{C}$ when exposing the membrane to several environments and gradients. Figure 7a depicts the oxygen permeation evolution with temperature when feeding with air and sweeping with Ar, CO_2 and 10% CH_4 in Ar, and when feeding with pure O_2 and sweeping with Ar. The different sweep gases were considered for mimicking the conditions that can be found in real environments, i.e. clean atmospheres (Argon), oxy-fuel applications (CO_2) and syngas production (10% CH_4 in Argon). The use of pure O_2 as feed gas intends to replicate a 5 bar pressurized air feeding, which is typically considered in practical applications. A maximum $J(\text{O}_2)$ of ca. $0.7 \text{ ml}\cdot\text{min}^{-1}\cdot\text{cm}^{-2}$ is obtained at 1000 $^{\circ}\text{C}$ under an Air/Ar gradient, whereas higher fluxes of 0.79 and $0.95 \text{ ml}\cdot\text{min}^{-1}\cdot\text{cm}^{-2}$ are obtained with Air/ CO_2 and O_2 /Ar gradients, respectively. Addition of methane in the sweep gas also produces an oxygen flux improvement in the tested temperatures. This can be ascribed to the reduction from Ce^{+4} to Ce^{+3} which provides CGO with n-type electronic conductivity and therefore the YCCC-CGO ambipolar conductivity is increased [8]. Moreover, the induction of reducing environments also implies a lower $p\text{O}_2$ at permeate side than the resulting with Argon sweeping, thus increasing the $p\text{O}_2$ gradient and subsequently the $J(\text{O}_2)$ [57]. As can be seen in Figure 5a, the oxygen permeation follows an Arrhenius behavior for all the tested conditions, with a higher activation energy and a stronger dependency with temperature for the case of CO_2 sweeping. This marked effect of CO_2 presence on $J(\text{O}_2)$ loss can be ascribed to the use of the BSCF catalytic layer, which is well-known for its sensitivity when exposed to CO_2 environments. In the literature, there is only one work studying oxygen permeation on YCCC-based composite membranes. The study, conducted on $\text{Y}_{0.8}\text{Ca}_{0.2}\text{Cr}_{0.8}\text{Co}_{0.2}\text{O}_3 - \text{Ce}_{0.8}\text{Sm}_{0.2}\text{O}_{1.9}$ membranes (50% wt. of each phase), resulted in a $J(\text{O}_2)$ of $0.31 \text{ ml}\cdot\text{min}^{-1}\cdot\text{cm}^{-2}$ at 950 $^{\circ}\text{C}$ for a 1.3 mm-thick membrane [33]. Despite the difference in composition and thickness, the oxygen permeation performance of the YCCC-based composite membranes is comparable. It was also tested the oxygen permeation influence when varying the sweep gas flow rate under

Air/Ar and O₂/Ar gradients. The results, displayed in Figure 5b, show that the higher the flow rate the higher the oxygen permeation. This is related with concentration polarization resistances taking place on permeate side surface, where the permeated O₂ remains adsorbed on the active sites thus requiring a sweeping agent for getting desorbed and diffuse to the permeate stream. This accumulation of O₂ molecules results in an increase in pO₂ that produces a lower pO₂ gradient across the membrane, thus affecting negatively the oxygen permeation.

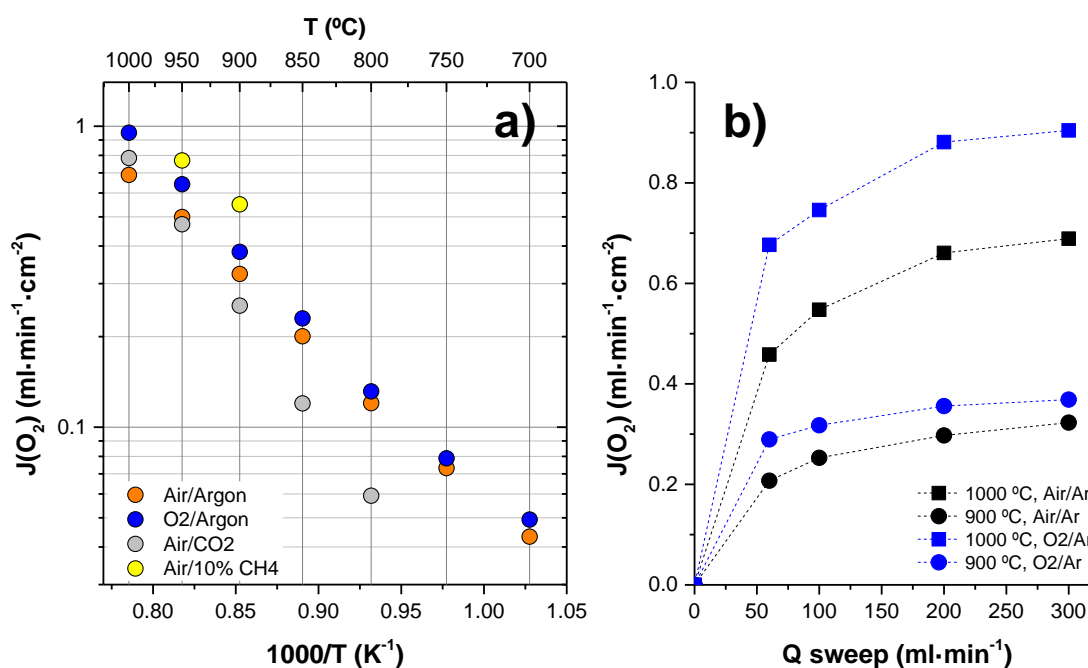


Figure 7. a) Oxygen permeation of YCCC-CGO membrane in dependence of temperature when exposed to different gradients. Q_{feed} and $Q_{sweep} = 300$ ml·min⁻¹. b) Oxygen permeation as function of sweep gas flow for different temperatures and feeding modes. $Q_{feed} = 300$ ml·min⁻¹.

The suitability of YCCC-CGO material for being considered in the fabrication of OTM modules for the O₂ supply system in oxy-fuel applications has been checked by the conduction of O₂ permeation tests where CO₂ mixtures were used as sweep gas. This is based on the fact that when integrating OTM modules within oxy-fuel applications the flue gas (mainly consisting of CO₂ and H₂O) is used for heating up the module to its working temperature and also for sweeping the permeated O₂. Therefore, it is of great interest conducting the characterization of materials in conditions of high temperature (>850 °C) and high CO₂ concentrations (>70% CO₂). First, it was tested the influence of CO₂ content on membrane performance at different temperatures (850-1000 °C). As it can be seen in Figure 6a, CO₂ content in sweep gas has a negative effect in $J(O_2)$ at

temperatures below 950 °C, being more significant the lower the temperature. At 900 °C, the O₂ permeation decreases from 0.3 to 0.25 ml·min⁻¹·cm⁻² when varying CO₂ content from 0 to 100%. This negative effect in J(O₂) is reversible, since original O₂ fluxes were completely recovered once CO₂ was withdrawn for all the temperatures. Contrarily, CO₂ improves permeation at 1000 °C, achieving a J(O₂) of 0.78 ml·min⁻¹·cm⁻² under full-CO₂ sweeping. Such behavior has been previously observed in several studies [58,59] and it is related with the better sweeping properties of CO₂ at very high temperatures (>900 °C) due to the higher CO₂ thermal emissivity, which can produce a local increase in temperature, thus improving the oxygen permeation along with the higher shear rate of CO₂ [60]. In order to check YCCC-CGO performance under a continuous operation in a CO₂ atmosphere, it was conducted a stability test for 24 hours keeping a constant sweeping of 25% CO₂ in Argon at 900 °C. Figure 6b depicts the O₂ permeation evolution of the stability test. It can be observed that, after an initial J(O₂) loss when switching from Ar to 25% CO₂ in Ar, O₂ flux experiences a slight recovery until it gets stabilized around 0.24 ml·min⁻¹·cm⁻².

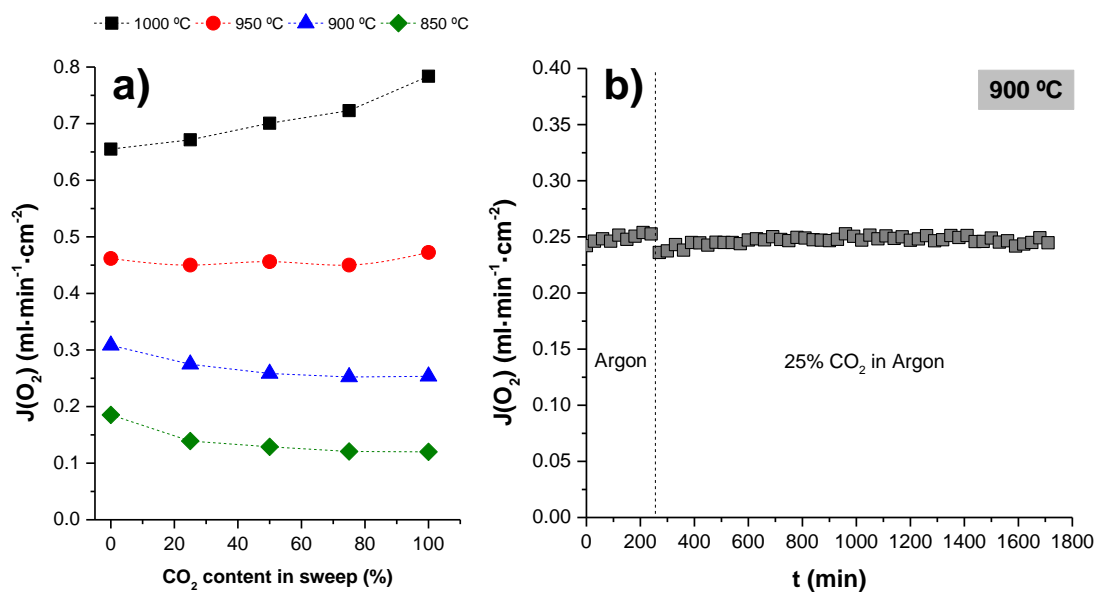


Figure 8. a) Oxygen permeation dependence of the CO₂ content in the sweep at different temperatures. b) Oxygen permeation evolution with time at 900 °C under different sweep gas atmospheres. $Q_{\text{feed}}, Q_{\text{sweep}} = 300 \text{ ml}\cdot\text{min}^{-1}$. Air feeding in both tests.

Once tested, the YCCC-CGO membrane was checked by XRD and FE-SEM techniques in order to check material stability after the continuous exposure to the considered environments (Ar, CH₄ and CO₂). As it can be seen in Figure 9, no additional phases to

the initial YCCC and CGO peaks are detected on the tested sample. Only peaks belonging to the sealing with gold O-rings are detected in addition to the composite material. Peaks corresponding the BSCF catalytic layer are missing, probably due to a degradation suffered after the exposure to the CO₂ and reducing environments that resulted in layer delamination. In fact, after disassembling the sample from the reactor no signs of the porous layer were visible on the sweep surface, and thus, no rests of carbonates were left for XRD detection. The XRD measurement corresponding to fresh sample included in Figure 9 was taken before BSCF coating, since XRD measurement after the deposition would have resulted in a catalytic layer breakage due to the sample holding system. SE and BSD images also confirm YCCC-CGO stability after the O₂ permeation tests, for no signs of pores, cracks or phases degradation can be observed.

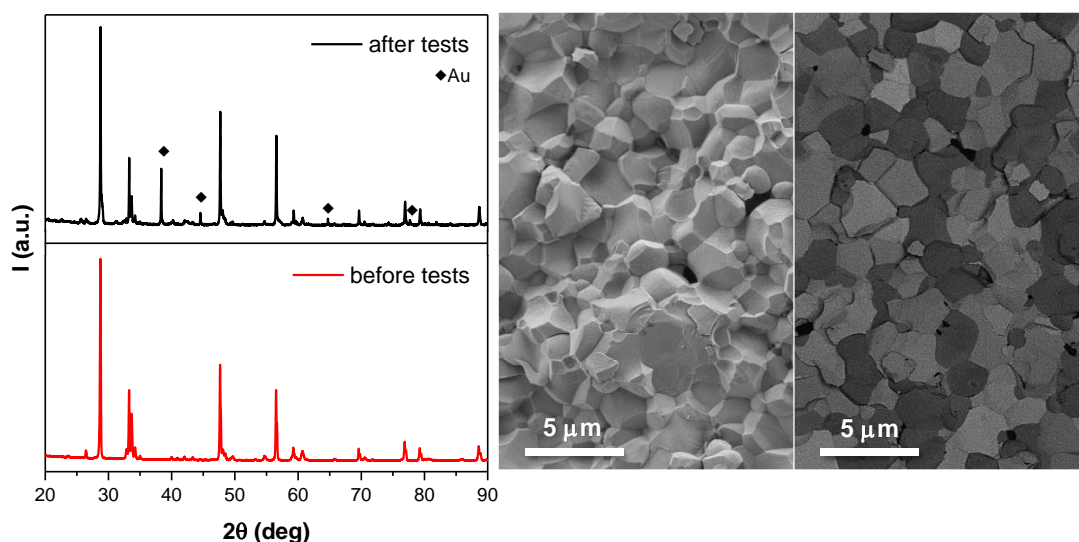


Figure 9. (left) XRD measurements of YCCC-CGO membranes before (no BSCF activation) and after oxygen permeation tests. Au peaks belong to membranes sealing. (right) SE and BSD FE-SEM images of YCCC-CGO membrane after testing.

4. Conclusions.

Different dual-phase composites containing $Y_{0.8}Ca_{0.2}Cr_{0.8}Co_{0.2}O_3$ electronic conducting perovskite and fluorite-type ion-conducting materials, $(Sc_2O_3)_{0.10}(Y_2O_3)_{0.01}(ZrO_2)_{0.89}$, $Ce_{0.9}Gd_{0.1}O_{2-\delta}$, and $(Y_2O_3)_{0.08}(ZrO_2)_{0.92}$ were studied to verify their compatibility and possible use as oxygen transport membranes. The ZrO₂-based materials were unable to sinter in air at 1300 °C and formed a Cr₂CoO₄ secondary phase. However, the composite

$\text{Ce}_{0.9}\text{Gd}_{0.1}\text{O}_{2-\delta} - \text{Y}_{0.8}\text{Ca}_{0.2}\text{Cr}_{0.8}\text{Co}_{0.2}\text{O}_3$ showed densification >95% and high chemical stability after sintering. The onset temperature of the composite was obtained at 937 °C. This could be originated by the interaction between the CGO and the Co from the YCCC, which might act as sintering aid. The total conductivity of the composite was $4.5 \text{ S}\cdot\text{cm}^{-1}$ when measured in air at 825 °C, with no variation within the $p\text{O}_2$ range 2×10^{-5} to 1 bar, suggesting the electronic conductivity is the predominant transport mechanism of the composite material. Oxygen permeability tests of the composite resulted on $0.70 \text{ Nml}\cdot\text{min}^{-1}\cdot\text{cm}^{-2}$ in Air/Ar gradient and $0.78 \text{ Nml}\cdot\text{min}^{-1}\cdot\text{cm}^{-2}$ in an Air/ CO_2 at 1000 °C for 0.7 mm thick pellet. An stability tests showed that the composite withstood the exposition to 25% CO_2 -Ar/Air gradient at 900 °C over 24 hours with negligible degradation. After the composite was exposed to $p\text{O}_2 \sim 10^{-20}$ atmosphere at 900 °C, it developed cracks along the CGO grains, which might be caused by the chemical expansion of the CGO. Although the use of the CGO-YCCC composite for syngas applications might be limited, this study demonstrated that this dual-phase composite is a candidate material to be used as oxygen transport membrane for oxyfuel applications.

References

- [1] E. Comission, Roadmap for a competitive low-carbon Europe, in, 2018.
- [2] N. Perrin, R. Dubettier, F. Lockwood, J.-P. Tranier, C. Bourhy-Weber, P. Terrien, Oxycombustion for coal power plants: Advantages, solutions and projects, Applied Thermal Engineering, 74 (2015) 75-82.
- [3] M. Lupion, I. Alvarez, P. Otero, R. Kuivalainen, J. Lantto, A. Hotta, H. Hack, 30 MWth CIUDEN Oxy-CFB Boiler - First experiences, Ghgt-11, 37 (2013) 6179-6188.
- [4] J. Monne, C. Prinet, Lacq-Rousse Industrial CCS reference project: Description and operational feedback after two and half years of operation, Ghgt-11, 37 (2013) 6444-6457.
- [5] W. Wang, S.P. Wang, X.B. Ma, J.L. Gong, Recent advances in catalytic hydrogenation of carbon dioxide, Chem Soc Rev, 40 (2011) 3703-3727.

- [6] M. Balaguer, C.-Y. Yoo, H.J. Bouwmeester, J.M. Serra, Bulk transport and oxygen surface exchange of the mixed ionic–electronic conductor $\text{Ce}_{1-x}\text{Tb}_x\text{O}_{2-\delta}$ ($x=0.1, 0.2, 0.5$), *Journal of Materials Chemistry A*, 1 (2013) 10234-10242.
- [7] S.G. Jadhav, P.D. Vaidya, B.M. Bhanage, J.B. Joshi, Catalytic carbon dioxide hydrogenation to methanol: A review of recent studies, *Chemical Engineering Research and Design*, 92 (2014) 2557-2567.
- [8] M.P. Lobera, J.M. Serra, S.P. Foghmoes, M. Søggaard, A. Kaiser, On the use of supported ceria membranes for oxyfuel process/syngas production, *Journal of Membrane Science*, 385–386 (2011) 154-161.
- [9] J. Caro, T. Schiestel, S. Werth, H. Wang, A. Kleinert, P. Kölsch, Perovskite hollow fibre membranes in the partial oxidation of methane to synthesis gas in a membrane reactor, *Desalination*, 199 (2006) 415-417.
- [10] L. Olivier, S. Haag, C. Mirodatos, A.C. van Veen, Oxidative coupling of methane using catalyst modified dense perovskite membrane reactors, *Catalysis Today*, 142 (2009) 34-41.
- [11] H. Jiang, Z. Cao, S. Schirmer, T. Schiestel, J. Caro, A Coupling Strategy to Produce Hydrogen and Ethylene in a Membrane Reactor, *Angewandte Chemie International Edition*, 49 (2010) 5656-5660.
- [12] M.P. Lobera, S. Valero, J.M. Serra, S. Escolástico, E. Argente, V. Botti, Optimization of ODHE membrane reactor based on mixed ionic electronic conductor using soft computing techniques, *Chemical Engineering Science*, 66 (2011) 6308-6317.
- [13] M. Pilar Lobera, S. Escolastico, J.M. Serra, High Ethylene Production through Oxidative Dehydrogenation of Ethane Membrane Reactors Based on Fast Oxygen-Ion Conductors, *Chemcatchem*, 3 (2011) 1503-1508.
- [14] M. den Exter, W. Haije, J. Vente, Viability of ITM Technology for Oxygen Production and Oxidation Processes: Material, System, and Process Aspects, in: A. Bose (Ed.) *Inorganic Membranes for Energy and Environmental Applications*, Springer New York, 2009, pp. 27-51.

- [15] P. Markewitz, J. Marx, A. Schreiber, P. Zapp, Ecological evaluation of coal-fired Oxyfuel power plants -cryogenic versus membrane-based air separation, *Ghgt-11*, 37 (2013) 2864-2876.
- [16] M. Puig-Arnabat, S. Soprani, M. Søggaard, K. Engelbrecht, J. Ahrenfeldt, U.B. Henriksen, P.V. Hendriksen, Integration of mixed conducting membranes in an oxygen–steam biomass gasification process, *RSC Advances*, 3 (2013) 20843-20854.
- [17] S. Smart, C.X.C. Lin, L. Ding, K. Thambimuthu, J.C. Diniz da Costa, Ceramic membranes for gas processing in coal gasification, *Energy & Environmental Science*, 3 (2010) 268-278.
- [18] X. Tan, K. Li, *Inorganic Membrane Reactors: Fundamentals and Applications*, *Inorganic Membrane Reactors: Fundamentals and Applications*, (2015) 1-290.
- [19] S. McIntosh, J.F. Vente, W.G. Haije, D.H.A. Blank, H.J.M. Bouwmeester, Oxygen stoichiometry and chemical expansion of $\text{Ba}_{0.5}\text{Sr}_{0.5}\text{Co}_{0.8}\text{Fe}_{0.2}\text{O}_{3-\delta}$ measured by in situ neutron diffraction, *Chemistry of Materials*, 18 (2006) 2187-2193.
- [20] S. McIntosh, J.F. Vente, W.G. Haije, D.H.A. Blank, H.J.M. Bouwmeester, Structure and oxygen stoichiometry of $\text{SrCo}_{0.8}\text{Fe}_{0.2}\text{O}_{3-\delta}$ and $\text{Ba}_{0.5}\text{Sr}_{0.5}\text{Co}_{0.8}\text{Fe}_{0.2}\text{O}_{3-\delta}$, *Solid State Ionics*, 177 (2006) 1737-1742.
- [21] S. McIntosh, J.F. Vente, W.G. Haije, D.H.A. Blank, H.J.M. Bouwmeester, Phase stability and oxygen non-stoichiometry of $\text{SrCo}_{0.8}\text{Fe}_{0.2}\text{O}_{3-\delta}$ measured by in situ neutron diffraction, *Solid State Ionics*, 177 (2006) 833-842.
- [22] D.N. Mueller, R.A. De Souza, T.E. Weirich, D. Roehrens, J. Mayer, M. Martin, A kinetic study of the decomposition of the cubic perovskite-type oxide $\text{Ba}_x\text{Sr}_{1-x}\text{Co}_{0.8}\text{Fe}_{0.2}\text{O}_{3-\delta}$ (BSCF) ($x=0.1$ and 0.5), *Physical Chemistry Chemical Physics*, 12 (2010) 10320-10328.
- [23] J. Yi, M. Schroeder, High temperature degradation of $\text{Ba}_{0.5}\text{Sr}_{0.5}\text{Co}_{0.8}\text{Fe}_{0.2}\text{O}_{3-\delta}$ membranes in atmospheres containing concentrated carbon dioxide, *Journal of Membrane Science*, 378 (2011) 163-170.

- [24] F. Liang, H. Luo, K. Partovi, O. Ravkina, Z. Cao, Y. Liu, J. Caro, A novel CO₂-stable dual phase membrane with high oxygen permeability, *Chemical Communications*, 50 (2014) 2451-2454.
- [25] H. Luo, T. Klande, Z. Cao, F. Liang, H. Wang, J. Caro, A CO₂-stable reduction-tolerant Nd-containing dual phase membrane for oxyfuel CO₂ capture, *Journal of Materials Chemistry A*, 2 (2014) 7780-7787.
- [26] H. Luo, H. Jiang, K. Efimov, F. Liang, H. Wang, J. Caro, CO₂-Tolerant Oxygen-Permeable Fe₂O₃-Ce_{0.9}Gd_{0.1}O_{2-δ} Dual Phase Membranes, *Industrial & Engineering Chemistry Research*, 50 (2011) 13508-13517.
- [27] H. Luo, K. Efimov, H. Jiang, A. Feldhoff, H. Wang, J. Caro, CO₂-Stable and Cobalt-Free Dual-Phase Membrane for Oxygen Separation, *Angewandte Chemie International Edition*, 50 (2011) 759-763.
- [28] S. Pirou, J. García-Fayos, M. Balaguer, R. Kiebach, J.M. Serra, Improving the performance of oxygen transport membranes in simulated oxy-fuel power plant conditions by catalytic surface enhancement, *Journal of Membrane Science*, 580 (2019) 307-315.
- [29] J. Garcia-Fayos, M. Balaguer, J.M. Serra, Dual-Phase Oxygen Transport Membranes for Stable Operation in Environments Containing Carbon Dioxide and Sulfur Dioxide, *ChemSusChem*, 8 (2015) 4242-4249.
- [30] M. Balaguer, J. Garcia-Fayos, C. Solis, J.M. Serra, Fast Oxygen Separation Through SO₂- and CO₂-Stable Dual-Phase Membrane Based on NiFe₂O₄-Ce_{0.8}Tb_{0.2}O_{2-δ}, *Chemistry of Materials*, 25 (2013) 4986-4993.
- [31] W. Li, M. Gong, X. Liu, H₂ oxidation on doped yttrium chromites/yttrium stabilized zirconia anode of solid oxide fuel cell, *Journal of Power Sources*, 241 (2013) 494-501.
- [32] K.J. Yoon, C.N. Cramer, E.C. Thomsen, C.A. Coyle, G.W. Coffey, O.A. Marina, Calcium- and Cobalt-Doped Yttrium Chromites as an Interconnect Material for Solid Oxide Fuel Cells, *Journal of The Electrochemical Society*, 157 (2010) B856-B861.

- [33] K.J. Yoon, O.A. Marina, Highly stable dual-phase $\text{Y}_{0.8}\text{Ca}_{0.2}\text{Cr}_{0.8}\text{Co}_{0.2}\text{O}_{3-\text{Sm}_{0.2}\text{Ce}_{0.8}\text{O}_{1.9}}$ ceramic composite membrane for oxygen separation, *Journal of Membrane Science*, 499 (2016) 301-306.
- [34] S.R. Bishop, D. Marrocchelli, C. Chatzichristodoulou, N.H. Perry, M.B. Mogensen, H.L. Tuller, E.D. Wachsman, Chemical Expansion: Implications for Electrochemical Energy Storage and Conversion Devices, *Annual Review of Materials Research*, 44 (2014) 205-239.
- [35] S. Grieshammer, Defect Interactions in the $\text{CeO}_2\text{-ZrO}_2\text{-Y}_2\text{O}_3$ Solid Solution, *The Journal of Physical Chemistry C*, 121 (2017) 15078-15084.
- [36] R. Wallenberg, R. Withers, D.J.M. Bevan, J.G. Thompson, P. Barlow, B.G. Hyde, The fluorite-related “solid solutions” of $\text{CeO}_2\text{-Y}_2\text{O}_3$ I: A re-examination by electron microscopy and diffraction, *Journal of the Less Common Metals*, 156 (1989) 1-16.
- [37] S.K. Tadokoro, E.N.S. Muccillo, Influence of the precursor purity and the precipitating agent on impedance spectroscopy of $\text{CeO}_2\text{:Y}_2\text{O}_3$ ceramics, *Journal of Alloys and Compounds*, 374 (2004) 190-193.
- [38] F. Tessier, F. Chevire, F. Muñoz, O. Merdrignac-Conanec, R. Marchand, M. Bouchard, C. Colbeau-Justin, Powder preparation and UV absorption properties of selected compositions in the $\text{CeO}_2\text{-Y}_2\text{O}_3$ system, *Journal of Solid State Chemistry*, 181 (2008) 1204-1212.
- [39] D.S. Tsvetkov, I.L. Ivanov, D.A. Malyshkin, A.Y. Zuev, Oxygen content, cobalt oxide exsolution and defect structure of the double perovskite $\text{PrBaCo}_2\text{O}_{6-\delta}$, *Journal of Materials Chemistry A*, 4 (2016) 1962-1969.
- [40] K. Hilpert, D. Das, M. Miller, D.H. Peck, R. Weiß, Chromium Vapor Species over Solid Oxide Fuel Cell Interconnect Materials and Their Potential for Degradation Processes, *Journal of The Electrochemical Society*, 143 (1996) 3642-3647.
- [41] S.A. Suvorov, A.P. Shevchik, Chemical Equilibria Involving Lanthanum Chromite, *Refractories and Industrial Ceramics*, 45 (2004) 94-99.

- [42] E. Povoden, M. Chen, A.N. Grundy, T. Ivas, L.J. Gauckler, Thermodynamic Assessment of the La-Cr-O System, *Journal of Phase Equilibria and Diffusion*, 30 (2009) 12-27.
- [43] E.J. Opila, D.L. Myers, N.S. Jacobson, I.M.B. Nielsen, D.F. Johnson, J.K. Olminky, M.D. Allendorf, Theoretical and Experimental Investigation of the Thermochemistry of $\text{CrO}_2(\text{OH})_2(\text{g})$, *The Journal of Physical Chemistry A*, 111 (2007) 1971-1980.
- [44] S.P.S. Badwal, R. Deller, K. Foger, Y. Ramprakash, J.P. Zhang, Interaction between chromia forming alloy interconnects and air electrode of solid oxide fuel cells, *Solid State Ionics*, 99 (1997) 297-310.
- [45] V. Peres, L. Favergeon, M. Andrieu, J.C. Palussière, J. Balland, C. Delafoy, M. Pijolat, High temperature chromium volatilization from Cr_2O_3 powder and Cr_2O_3 -doped UO_2 pellets in reducing atmospheres, *Journal of Nuclear Materials*, 423 (2012) 93-101.
- [46] A. Małeckı, J.A.K. Tareen, J.P. Doumerc, L. Rabardel, J.C. Launay, Kinetics of thermal decomposition of Co_3O_4 powder and single crystals, *Journal of Solid State Chemistry*, 56 (1985) 49-57.
- [47] C.e. Li, L. Wong, L. Tang, N.V.Y. Scarlett, K. Chiang, J. Patel, N. Burke, V. Sage, Kinetic modelling of temperature-programmed reduction of cobalt oxide by hydrogen, *Applied Catalysis A: General*, 537 (2017) 1-11.
- [48] N.G. Gallegos, J.M.P. Lopez, Kinetic study of cobalt oxides reduction by hydrogen, *Materials Chemistry and Physics*, 19 (1988) 431-446.
- [49] B. Ernst, L. Hilaire, A. Kiennemann, Effects of highly dispersed ceria addition on reducibility, activity and hydrocarbon chain growth of a Co/SiO₂ Fischer–Tropsch catalyst, *Catalysis Today*, 50 (1999) 413-427.
- [50] Z. Zhang, W. Sigle, M. Rühle, E. Jud, L.J. Gauckler, Microstructure characterization of a cobalt-oxide-doped cerium-gadolinium-oxide by analytical and high-resolution TEM, *Acta Materialia*, 55 (2007) 2907-2917.

- [51] M. Mori, Z. Wang, T. Itoh, Sintering Mechanisms of Cobalt-Doped Ceria and Zirconia Electrolytes in Intermediate-Temperature Solid Oxide Fuel Cells, in: ECS Transactions, ECS, 2009.
- [52] D.P. Fagg, V.V. Kharton, J.R. Frade, P-Type Electronic Transport in $\text{Ce}_{0.8}\text{Gd}_{0.2}\text{O}_{2-\delta}$ – δ : The Effect of Transition Metal Oxide Sintering Aids, *Journal of Electroceramics*, 9 (2002) 199-207.
- [53] S. Taub, K. Neuhaus, H.-D. Wiemhöfer, N. Ni, J.A. Kilner, A. Atkinson, The effects of Co and Cr on the electrical conductivity of cerium gadolinium oxide, *Solid State Ionics*, 282 (2015) 54-62.
- [54] L. Villas Boas, P. Nascente, R. Landers, M. Campos, D. Souza, The Effect of Co and Zn Addition on Densification and Electrical Properties of Ceria-Based Nanopowders, *Materials Research*, 19 (2016).
- [55] W. Fang, F. Liang, Z. Cao, F. Steinbach, A. Feldhoff, A Mixed Ionic and Electronic Conducting Dual-Phase Membrane with High Oxygen Permeability, *Angewandte Chemie-International Edition*, 54 (2015) 4847-4850.
- [56] J. García-Fayos, R. Ruhl, L. Navarrete, H.J.M. Bouwmeester, J.M. Serra, Enhancing oxygen permeation through $\text{Fe}_2\text{NiO}_4\text{-Ce}_{0.8}\text{Tb}_{0.2}\text{O}_{2-\delta}$ composite membranes using porous layers activated with Pr_6O_{11} nanoparticles, *Journal of Materials Chemistry A*, 6 (2018) 1201-1209.
- [57] Z. Shao, G. Xiong, H. Dong, W. Yang, L. Lin, Synthesis, oxygen permeation study and membrane performance of a $\text{Ba}_{0.5}\text{Sr}_{0.5}\text{Co}_{0.8}\text{Fe}_{0.2}\text{O}_{3-\delta}$ oxygen-permeable dense ceramic reactor for partial oxidation of methane to syngas, *Separation and Purification Technology*, 25 (2001) 97-116.
- [58] J. Garcia-Fayos, M. Balaguer, J.M. Serra, Dual-Phase Oxygen Transport Membranes for Stable Operation in Environments Containing Carbon Dioxide and Sulfur Dioxide, *ChemSusChem*, (2015) n/a-n/a.
- [59] J.M. Serra, J. Garcia-Fayos, S. Baumann, F. Schulze-Kueppers, W.A. Meulenber, Oxygen permeation through tape-cast asymmetric all- $\text{La}_{0.6}\text{Sr}_{0.4}\text{Co}_{0.2}\text{Fe}_{0.8}\text{O}_{3-d}$ membranes, *Journal of Membrane Science*, 447 (2013) 297-305.

- [60] D. Catalán-Martínez, A. Santafé-Moros, J.M. Gozávez-Zafrilla, J. García-Fayos, J.M. Serra, Characterization of oxygen transport phenomena on BSCF membranes assisted by fluid dynamic simulations including surface exchange, *Chemical Engineering Journal*, 387 (2020) 124069.

5.4 Co-sintering and interaction of $Y_{0.8}Ca_{0.2}Cr_{0.8}Co_{0.2}O_{3-\delta} - Ce_{0.9}Gd_{0.1}O_{2-\delta}$ dual phase oxygen transport membranes with tubular $Zr_{0.97}Y_{0.6}O_{2.03}$ supports

In the previous section (CH5.3), the $Y_{0.8}Ca_{0.2}Cr_{0.8}Co_{0.2}O_{3-\delta} - Ce_{0.9}Gd_{0.1}O_{2-\delta}$ composite (CGO-YCCC) was found to be a suitable candidate for operation in oxyfuel applications. The use of this composite to fabricate thin-oxygen transport membranes supported on $Zr_{0.97}Y_{0.6}O_{2.03}$ (3YSZ) porous tubes is explored in this manuscript with the title “Sintering and interaction of $Y_{0.8}Ca_{0.2}Cr_{0.8}Co_{0.2}O_{3-\delta} - Ce_{0.9}Gd_{0.1}O_{2-\delta}$ dual-phase oxygen transport membranes on tubular $Zr_{0.97}Y_{0.6}O_{2.03}$ ”. Different fabrication attempts and limitation for the manufacturing of this architecture are described. 3YSZ porous supports developed and used in CH5.2 were selected due to their high chemical, thermal and mechanical stability, as well as their good permeability. The porous supports were fabricated via thermoplastic extrusion. The CGO-YCCC dense membrane and functional layers were deposited using dip-coating.

One of the features of the CGO-YCCC composite is its low sintering onset temperature, which was found to be ca. 940 °C (CH5.3). In contrast, the sintering onset of the 3YSZ is >1100 °C. This mismatch could cause considerable stresses during the co-sintering of the two components. By using sintering aids for the porous support, it is expected to decrease the sintering onset mismatch with the CGO-YCCC composite. Fe_2O_3 was selected as sintering aid, due to its ability to ease the sintering of ZrO_2 -based materials, as well as its high availability. Along the performed experiments in this section, it was observed that thermal expansion coefficient (TEC, α) of the 3YSZ was also modified by the addition of sintering aid.

Different tests were carried out in order to define a possible fabrication route to co-sinter the CGO-YCCC membranes on 3YSZ supports; however, although the sintering temperature of the 3YSZ supports was lowered and the sintering onset mismatch was decreased to 99 °C, it was not possible to diminish the TEC mismatch $\Delta\alpha \leq 1 \times 10^{-6} K^{-1}$. This led to severe structural damages such as cracks and delamination of the dip-coated layers. Although the fabrication of the CGO-YCCC membranes on tubular 3YSZ-based materials was unsuccessful, different manufacturing approaches were identified and applied in these studies, such as using sintering aids as modification tool for tailoring the TEC.

Co-sintering and interaction of $Y_{0.8}Ca_{0.2}Cr_{0.8}Co_{0.2}O_{3-\delta}$ – $Ce_{0.9}Gd_{0.1}O_{2-\delta}$ dual phase oxygen transport membranes with tubular $Zr_{0.97}Y_{0.06}O_{2-\delta}$ supports

Lev Martinez Aguilera, Astri Bjørnetun Haugen, Andreas Kaiser, Ragnar Kiebach*

Department of Energy, Technical University of Denmark, 2800 Kgs. Lyngby, Denmark

** Corresponding author: woki@dtu.dk*

Abstract.

The fabrication of multilayer $Ce_{0.9}Gd_{0.1}O_{2-\delta}$ – $Y_{0.8}Ca_{0.2}Cr_{0.8}Co_{0.2}O_{3-\delta}$ oxygen transport membrane layers on porous, tubular $Zr_{0.97}Y_{0.06}O_{2-\delta}$ support structures was performed and studied using microstructural and dilatometry analysis. The use of Fe_2O_3 as sintering aid for the porous supports was investigated. In the sintering process, mechanical failure of the membrane has been observed after cooling down of the membrane assembly. The thermal expansion coefficient mismatch up to of $3.9 \times 10^{-6} K^{-1}$ between the support and the membrane resulted in severe cracks and delamination of the membrane, observed by optical and scanning electron microscopy. It was determined that some elements present in YCCC are mobile at 1250°C. Ca migrates towards the $Zr_{0.97}Y_{0.06}O_{2-\delta}$, although only slight variations of Co and Cr were identified. Although a successful fabrication method of the multilayers systems was not possible, it was demonstrated that the shrinkage of the tubular supports has an important impact in the densification of the membrane, and that sintering aids can be used as a tool to decrease the thermal expansion coefficient and sintering temperature mismatch, broadening the perspective of combination of materials.

Introduction.

Oxygen transport membranes (OTM) are an attractive technology to be integrated in oxy-fuel applications, such as carbon capture and storage (CCS). By removing the N_2 from the combustion air, it would be possible to increase the quality of the output gases, eliminating the need of additional gas separation processes. However, oxyfuel is a process with low pO_2 conditions, thus the use of stable and resilient materials in reducing environments and high temperature are needed. Dual-phase composites have been recently studied as an alternative to mixed ionic-electronic conducting materials (MIEC). Although MIEC have high oxygen-ionic and electronic conductivity, they have a limited

pO_2 operation range, undergoing chemical decomposition at pO_2 values below 10^{-12} . By using dual-phase composites, it is possible to take advantage of highly stable ionic conducting and electronic conducting materials. [1-6]

$(Sc_2O_3)_{0.10}(Y_2O_3)_{0.01}(ZrO_2)_{0.89} - LaCr_{0.85}Cu_{0.10}Ni_{0.05}O_{3-\delta}$ composites have been studied as OTM material for oxyfuel applications. These components are highly stable but sintering temperatures above $1450\text{ }^\circ\text{C}$ are needed to achieve full densification of the composite, which is required for the use as a gas separation membrane. The high temperatures cause the vaporization of species, formation of cracks and formation of insulating phases, such as lanthanum zirconate, $La_2Zr_2O_7$ (LZO). [7,8] $Y_{0.8}Ca_{0.2}Cr_{0.8}Co_{0.2}O_{3-\delta}$ (YCCC) has been studied as electronic conductor in solid oxide cells interconnects [9-10] and it can be an attractive option as La-free electronic-conducting material in dual-phase OTMs, by avoiding the formation of LZO. Nevertheless, previous studies have shown that dual-phase composites using YCCC and ZrO_2 -based ion-conductors may not be able to densify due to formation of a Ca–Cr–O transient liquid phase that interacts with Zr, forming $CaZrO_3$. [11,12] By using $Ce_{0.9}Gd_{0.1}O_{2-\delta}$ (CGO) as ionic-conducting phase and YCCC as electronic conductor, it was possible to obtain a dual-phase composite that could withstand oxyfuel conditions and providing oxygen fluxes of up to $0.78\text{ ml}\cdot\text{min}^{-1}\cdot\text{cm}^{-2}$ for 0.7 mm thick membrane pellets in an Air/ CO_2 gradient at $1000\text{ }^\circ\text{C}$. [12] The use of thin-film CGO-YCCC composite in asymmetric OTMs, could further improve the oxygen fluxes and allow the integration in carbon capture applications.

In previous work, $Zr_{0.97}Y_{0.06}O_{2-\delta}$ (3YSZ) porous tubular structures were used in oxygen membranes due to the remarkable chemical and mechanical stability of the 3YSZ structures with sufficiently high gas permeability coefficient of 1.8 m^2 . [8] Due to different thermomechanical properties, such as different thermal expansion and densification behavior, the co-integration of CeO_2 -based and ZrO_2 -based materials into tubular multilayer structures is challenging. Nevertheless, in planar solid oxide cells, CGO has been successfully integrated as protective layer between the cathode material and a $Zr_{0.92}Y_{0.16}O_{2.08}$ (8YSZ) electrolyte. [13-15]

An approach to decrease the thermo-mechanical stresses when using CGO and 8YSZ has been studied by Mehranjani, et al. [16] It was shown that the addition of Fe_2O_3 as sintering

aid could help to match the onset of the sintering temperatures at about 1100 °C as well as equalizing their sintering rates, resulting in the successful co-sintering of CGO and 8YSZ layers. This study analyses an attempt to fabricate multilayer CGO-YCCC oxygen membranes supported on 3YSZ porous tubular supports, as well as methods to minimize the thermomechanical properties mismatch of the materials by using Fe₂O₃.

Experimental.

Tubular oxygen transport membranes (OTM) were fabricated using a multi-layer architecture as shown in Fig. 1. All functional layers were deposited using dip-coating ethanol-based slurries. An active dense membrane (AM) made of CGO-YCCC, with volumetric proportions 70:30 (CY7030), was set in between of inner porous (IL) and an outer porous (OL) activation layers. The layers were deposited on 3YSZ-based tubular porous supports (PS) and co-sintered.

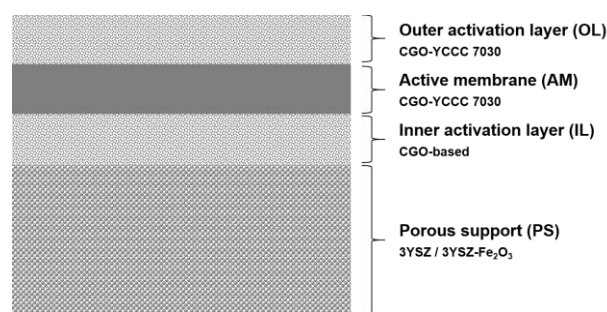


Fig. 1. Schematics of the different components of the studied oxygen transport membrane.

Powder preparation.

Low surface area CGO (FuelCell Materials) and YCCC (Jülich Forschungszentrum) powders were mixed in volumetric proportion 70:30 and ball-milled in ethanol at 50 rpm for 72 hours to obtain mean particle size of ca. 250 nm. The obtained composite powders were dried and used for the different analyses and fabrication of the functional layers. CGO+1 mol% Co₃O₄ (Alpha Aesar), CGO+1 mol% Fe₃O₄ (Alpha Aesar), 3YSZ (Tosho) and 3YSZ+3 mol% Fe₂O₃ (Alpha Aesar) were prepared in similar conditions for analysis and fabrication of the activation layers (IL and OL) and porous supports (PS).

Oxygen membranes fabrication.

Porous tubular supports were fabricated via thermoplastic extrusion according to Haugen et al. [8]. Two feedstocks were prepared, one using pure 3YSZ and an another adding

3 mol% Fe₂O₃ to the formulation (3YSZ-Fe₃). Debinding and calcination of the tubes prior deposition of the layers was done by slowly heating up in air at a rate of 15 °C·h⁻¹ to avoid excessive generation of gases from the organic phase thermal decomposition. Dwells of 2 h at 200 °C, 360 °C and 600 °C were kept to burn specific fraction of organics. After the dwell at 600 °C, a ramp of 30°C·h⁻¹ was used up to 1100 °C or 950 °C. Cooling after calcination was done with a rate of 120 °C·h⁻¹.

Table 1. Formulation of the active membrane and porous activation layers slurries

Function	Dense active membrane	wt. %	Porous activation layers	wt. %
Solvent	Ethanol	67.5	Ethanol	61.8
Oxides	CY7030	28.6	CY7030/CGO-Co/CGO-Fe	25.8
Dispersant	PVPK15 (Sigma Aldrich)	1.5	PVPK15 (Sigma Aldrich)	1.3
Binder	PVPK30 (Sigma Aldrich)	1.5	B30HH (Kuraray)	3.1
Plasticiser	--		Dibutyl sebacate (Sigma Aldrich)	2.2
Pore former	--		Graphite UF-1 (Graphit Kropfmühl)	5.8

Slurries for the IL, AM and OL were prepared according to the general formulations shown in Table 1. The layers were deposited using an in-house built dip-coater, adjusting the deposition speeds such as to obtain layers with thicknesses between 5–10 µm. The fabrication process of the membranes is summarised in the block diagram shown in Fig. 2. Between each deposition, a calcination at 950 °C was required to fix the layers to the substrate. Co-sintering of the PS and the dip-coated layers was carried out at 1250 °C for 2 °C·h⁻¹ and cooling rate of 120 °C·h⁻¹. 2 h dwells were kept at 360 °C and 600 °C.

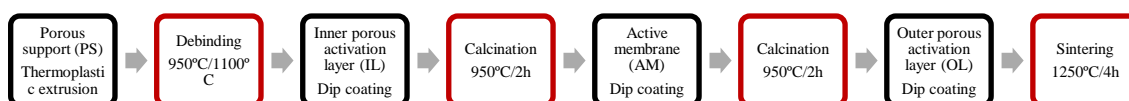


Fig. 2. Fabrication process of the asymmetric tubular oxygen transport membranes. Thermal processes are outlined in red.

Table 2 summarizes the membrane configurations to analyse different variables, combinations and alternative materials. Initially, a test to define the compatibility of the CY7030 AM on the 3YSZ PS was carried out (Test 1). Test 2 and 3 are related to the compatibility of CY7030 as IL and OL using 3YSZ PS. Tests 4 was performed to verify the compatibility of the CGO-Co (CGO+1 mol%Co₃O₄) as IL.

Table 2. Configurations of CY7030 membranes fabricated during this study

Component	Test 1	Test 2	Test 3	Test 4	Test 5	Test 6	Test 7
OL	---	---	CY7030	---	CY7030	CY7030	---
AM	CY7030	CY7030	CY7030	CY7030	CY7030	CY7030	CY7030
IL	---	CY7030	---	CGO-Co	CGO-Co	CGO-Co	CGO-Fe
PS	3YSZ	3YSZ	3YSZ	3YSZ	3YSZ	3YSZ-Fe ₃	3YSZ

Test 1: Initial compatibility tests. Test 2: CY7030 IL effect on AM. Test 3: CY7030 IL effect on AM. Test 4: Use of CGO-Co as IL. Test 5: Alternative architecture on 3YSZ. Test 6: Alternative architecture on 3YSZ-Fe₃. Test 7: Study of effect of Fe₂O₃ in the AM.

Test 5 and 6 consist on the fabrication of full membranes using CGO-Co as IL and 3YSZ and 3YSZ-Fe₃ (3YSZ+3 mol% Fe₂O₃) porous supports. In Test 7, CGO-Fe (CGO+1 mol% Fe₂O₃) was used as IL to analyse the effect of the Fe₂O₃ on the densification of CY7030 AM.

Microstructural analysis.

Microstructural characterization of the membranes was made using a Hitachi TM3000 scanning electron microscope (SEM) working with secondary and backscattered electron detectors and accelerating voltage of 15 kV. Composition of the as-received YCCC and sintered AM were analyzed by using EDS X-Flash 6|60 working at 15 kV and 176 pA.

Dilatometry studies.

3YSZ, 3YSZ-Fe₃ (3YSZ + 3 mol% Fe₂O₃) and CGO-YCCC composite pellets of 6 mm diameter and ca. 7 mm length were prepared by cold uniaxial pressing with a pressure of 1 ton·cm⁻². 3 wt.% PVA was used as binder. Sintering profiles and thermal expansion coefficients (TEC) were obtained using a dilatometer Netzsch DIL 402C working at T max 1200°C. Heating ramp of 1 °C·min⁻¹ was set to simulate the ramp used in the sintering process. Airflow of 20 l·min⁻¹ was set in all the dilatometry analyses. Thermal expansion coefficients were obtained by using heating and cooling ramps of 2 °C·min⁻¹ in pre-sintered pellets at 1350 °C.

Results and discussion.

Sintering curves and thermal expansion coefficients (TEC) measured by dilatometry of the CGO-YCCC 70:30 (CY7030) composite for the active membrane, AM (red), the 3YSZ porous support, PS (orange) and a doped 3YSZ-Fe₃ PS (yellow) are shown in Fig.

3a and 3b, respectively. The TECs in Fig 3b are given in 4 different intervals of temperature to simplify the analysis.

As observed in Fig. 3a, CY7030 composite has a sintering onset temperature of 937 °C. Sintering onsets of 3YSZ and 3YSZ-Fe₃ were respectively registered at 1103 °C and 1036 °C. Although the intrinsic auto-sintering aid effect, of the CY7030 composite [12,17-20] might be desirable to avoid vaporization of the species from the perovskite, such as Cr⁶⁺, it can also create additional transient stresses during the manufacturing of the membranes. A sintering mismatch of 166 °C between the CY7030 AM and 3YSZ PS can be decreased to 99 °C by adding 3 mol% Fe₂O₃ to the 3YSZ PS.

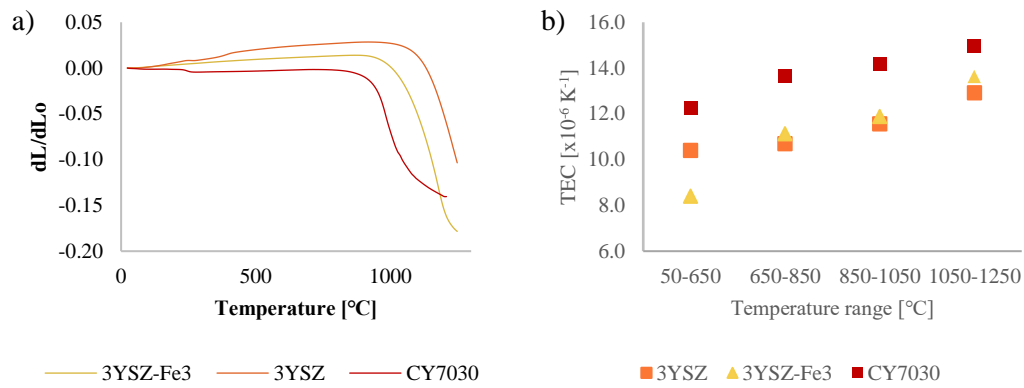


Fig. 3. Dilatometry analysis of the membrane and porous support materials CGO-YCCC, 3YSZ and 3YSZ-Fe₃ (a) sintering curves and (b) thermal expansion coefficients.

In Fig. 3b, it is observed that thermal expansion coefficient (TEC) mismatch between the CY7030 AM and the 3YSZ-based PS is considerable. The TEC mismatch ($\Delta\alpha$) are shown in Table 3. As observed, Fe₂O₃ slightly modifies the TEC values of the 3YSZ PS in such a way that at high temperatures (1050 – 1250 °C), the TEC mismatch between CY7030 AM and 3YSZ PS is decreased from $2 \times 10^{-6} \text{ K}^{-1}$ to $1.3 \times 10^{-6} \text{ K}^{-1}$ when Fe₂O₃ is added. Nevertheless, at lower temperatures (50 – 650 °C) the TEC mismatch increases considerably, reaching differences up to $3.9 \times 10^{-6} \text{ K}^{-1}$.

Table 3. Thermal expansion coefficient mismatch ($\Delta\alpha$) between the CY7030 membrane and the YSZ-based porous supports

Interval of temperature [°C]	50-650	650-850	850-1050	1050-1250
3YSZ [10 ⁻⁶ K ⁻¹]	1.9	3.0	2.6	2.0
3YSZ-Fe ₃ [10 ⁻⁶ K ⁻¹]	3.9	2.6	2.3	1.3

Although microstructure plays an important role in the mechanical stability of two components, e.g. thickness, porosity, deposition method, it is usually defined that an $\Delta\alpha \leq 1 \times 10^{-6} \text{K}^{-1}$ between two materials would allow their co-sintering. Since in all the cases, the obtained $\Delta\alpha > 1 \times 10^{-6} \text{K}^{-1}$, it is likely that the structural problems might be observed during the processing of the membranes.

Analysis of the co-firing process of the multilayer membrane

Fig. 4 shows the micrographs of a pellet and a thin active membrane of CY7030 sintered at 1250 °C. Although CY7030 pellets showed high densification after sintering, once the CY7030 is deposited on calcined 3YSZ PS (at 1100 °C) and sintered at 1250 °C, high porosity of the CY7030 AM was observed (Fig. 4b and Fig. 4c). By analysing Fig. 3a, it is possible to observe that at 1100 °C the 3YSZ PS already started the sintering process. This would decrease the shrinkage potential of the 3YSZ-tubes by approximately half.

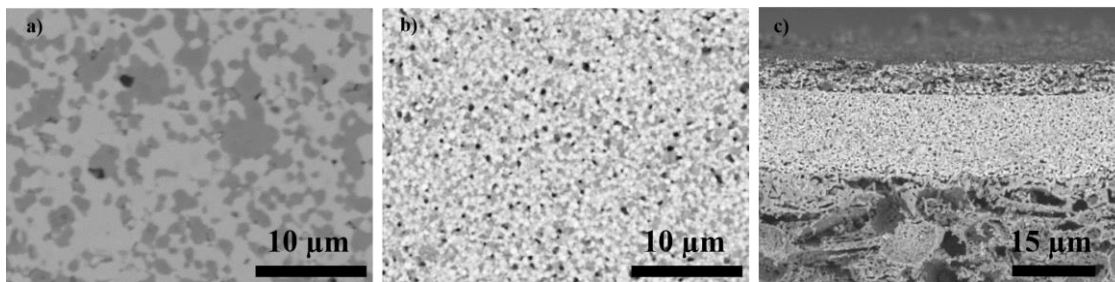


Fig. 4. SEM micrographs of CGO-YCCC sintered at 1250 °C in air. a) pressed pellet, b) surface of thin membrane on 3YSZ support, and c) cross section of thin membrane on 3YSZ support,

By calcining the PS at 950 °C, it was possible to reach densification of the membrane after sintering. This can be explained by the fact that CY7030 AM and the 3YSZ PS require having similar linear shrinkages during the densification process. In the case of CY7030 AM, a total linear shrinkage of 15.8 % occurs during its densification. Calcined 3YSZ PS at 1100 °C will only provide ca. 7 % linear shrinkage, which would prevent the densification of the AM. Thus, additional shrinkage of the supports is needed, which can be obtained by decreasing the calcination temperature of the tubes before or close to the sintering onset temperature of the support's material.

By experimental measurements, which are in correlation with the dilatometry studies, the linear shrinkage potential of the tube could be estimated to be 13.2 %. In the case of the 3YSZ-Fe₃, a full shrinkage potential of 18.5 % was obtained. In addition, during the

shrinkage of tubular systems, an effect of 2-dimensional pressing aids the sintering of the membranes. [21-23]

It is important to point out that the calcination temperature at 1100 °C of the 3YSZ tubular supports allows the handling of the tubes for dip-coating depositions. Calcining at lower temperatures increases the fragility of the tubes and the challenges during handling. A temperature of 950 °C for the PS calcination was found to be the best compromise between sufficient shrinkage potential and enough mechanical strength to handle the samples.

Structural integrity of the membranes during co-sintering.

The effect of the thermomechanical properties mismatch between the AM and the tubular PS can be observed in the cross-section SEM micrographs of the CY7030 AM deposited directly on 3YSZ PS (Fig. 5a), on CGO-Co IL/3YSZ PS (Fig. 5b) and on CGO-Co IL/3YSZ-Fe₃ PS (Fig. 5c) and sintered at 1250 °C. 1 mol% Co₃O₄ was added to the CGO IL to allow its adhesion on the calcined PS, prior the AM deposition. Co₃O₄ would also reduce the sintering mismatch behaviour between the CGO and CY7030, facilitating the sintering of the multilayer system. Although tests using CY7030 as IL were performed, unsuccessful results were obtained due to complete delamination of the membranes caused by the lack of contacting points between the 3YSZ-based PS and CY7030 IL, as well as the TEC mismatch of the materials.

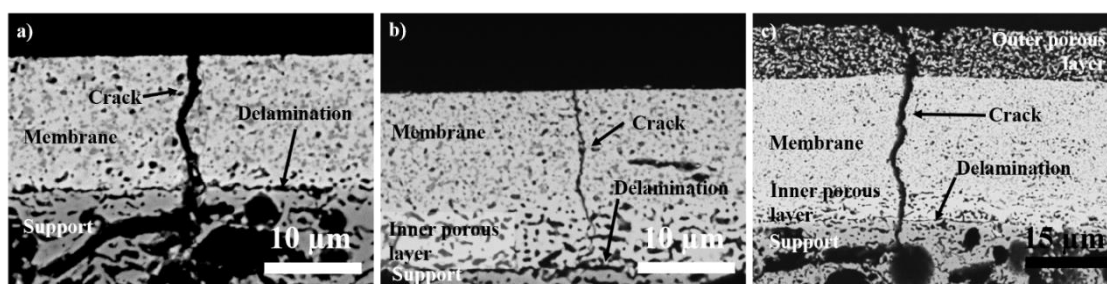


Fig. 5. SEM-micrographs of CY7030 membranes on 1) 3YSZ PS, 2) CGO-Co IL/3YSZ PS and 3) CGO-Co IL/3YSZ-Fe₃ PS.

As observed in Fig. 6, all the cases show similarities on the structural failures: Severe transversal cracks along all the tubular structure and delamination or weak AM/PS or IL/PS interfaces. By using the CGO-Co IL, delamination could be reduced; however weak interfaces were yet obtained and transversal cracks were extensively observed.

The structural damages are attributed to the sintering onset and TEC mismatch between the AM and PS materials, as shown in the performed dilatometry analysis (Fig. 3b) and Table 3.

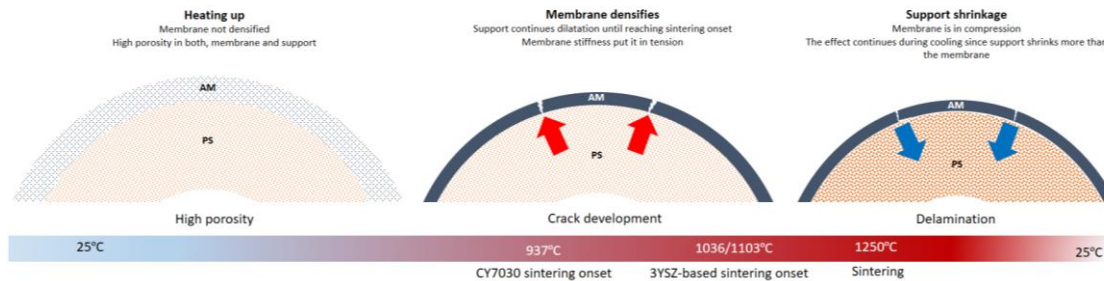


Fig. 6. Possible observation of failure during the co-sintering of CY7030 membranes and 3YSZ-based porous support.

Fig. 6 depicts the possible mechanism of cracks formation and delamination, according to the thermo-physical properties of the CY7030 AM and the 3YSZ-based PS. Before densification of the AM, no fractures were observed, probably due to the high porosity and lower stiffness of the materials. However, once the AM densifies, the membrane is subjected to stresses and cracks occur.

After reaching the CY7030 sintering onset temperature at 937 °C, the AM starts densifying, increasing its stiffness. While the AM densifies, the 3YSZ-based PS continues its dilatation due to rising temperature, which puts the recently densified membrane in tension. In this stage, the formation of cracks might occur. At 1036 °C/1103 °C, the sintering process of the PS begins, causing shrinkage of the porous structure and in consequence putting the membrane in compression, which besides cracks, it could also cause delamination. Finally, during the cooling process and due to the TEC mismatch, the PS would contract more than the membrane, which can increase the compression on the membrane.

Therefore, it can be concluded that CGO-YCCC AM are incompatible with 3YSZ/3YSZ-Fe₃ PS for the fabrication of OTM. However, it could be possible to use other materials as PS, such as CGO-based materials or other less expensive options, such as MgO. With a TEC of $15.6 \times 10^{-6} \text{K}^{-1}$, MgO would be suitable as support for the CY7030 AM. Cheng et al. [24] successfully developed CGO-LSF thin membranes using MgO tubular supports. Even though MgO PS presented a limited flexural strength of 40 MPa, the high

permeability of $7 \times 10^{-15} \text{ m}^2$ would diminish diffusion limitations of the gases towards the membrane. An additional option would be using CY7030 composite in self-supported capillaries, which would eliminate the requirement of materials compatibility.

Chemical stability and reaction at the interfaces

EDS analysis performed on cross section samples of the AM before and after sintering indicates) mobility of some of the elements from the YCCC perovskite and b) their interaction with the PS. **Table 4** shows the results of the performed EDS analysis on AM areas adjacent to the IL and OL, as well as in the central part of the AM (bulk). As expected, vaporization is mainly observed on areas close to the IL and OL interface, affecting ca. 2 μm within the AM. On the other hand, the central region of the membrane show similar values of those obtained for the untreated YCCC, demonstrating the chemical integrity of the phase in general.

Table 4. EDS analysis of YCCC in the sintered dual-phase membrane

	Ca	Cr	Co
Theoretical	0.20	0.80	0.20
Untreated	0.16	0.70	0.17
AM/IL interface	0.08	0.70	0.15
AM bulk	0.09	0.74	0.18
AM/OL interface	0.06	0.68	0.12

Ca as A-site cation was affected the most, decreasing ca. 62 at% of the initial Ca content. Through an EDS mapping scan (Fig. 7), deposits of Ca were found in the PS, in areas adjacent to the CY7030 AM/3YSZ PS interface. According to Carter et al. [11], mobility of Ca is likely due to the system Cr-Ca-O, which could be able to diffuse towards the 3YSZ PS, due to the affinity of these components. Co and Cr content remain similar despite the mobility of Ca, and no structural changes or secondary-phase formation was observed. By using CGO-Co IL, the mobility of Ca was diminished.

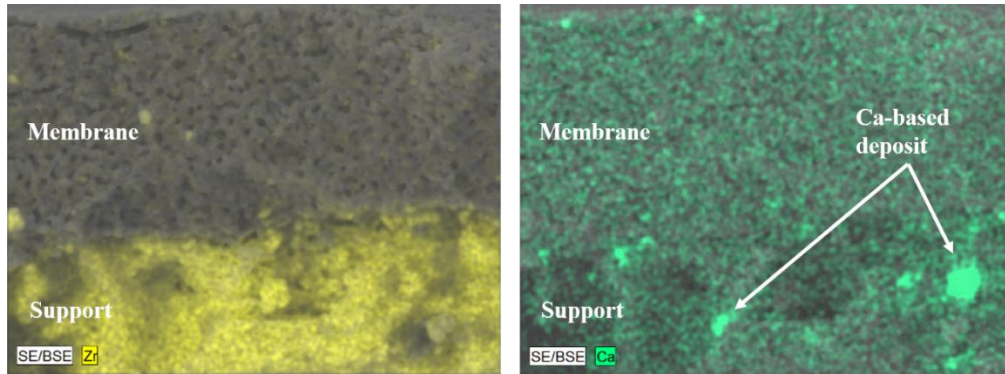


Fig. 7. EDS mapping of Zr and Ca of the CY7030 membrane – 3YSZ support interface.

When using 3YSZ-Fe3 PS, it was found that direct contact between the membrane and the support could cause lack of membrane densification in the adjacent areas to the support. In order to verify this result, CY7030 + 1 mol% Fe₂O₃ pellets were sintered in air at 1250 °C. A total porosity of 21 % was registered. In contrast pellets made of only CY7030 show 7% porosity. An additional analysis using CGO + 3 mol% Fe₂O₃ IL on 3YSZ supports showed that Fe affects ca. 1µm of the CY7030 AM after sintering, as observed in Fig. 8.

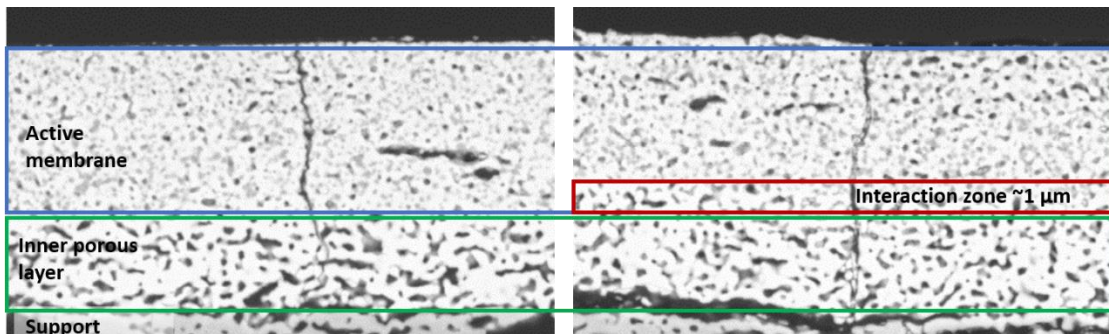


Fig. 8. Interaction of Fe on the membranes CY7030 using 3YSZ tubular supports using a) CGO-Co inner activation layer and b) CGO-Fe inner activation layer. Lack of densification is observed within 1 µm of the membrane when Fe is used as dopant.

Sintering studies developed by Nicholas, et al. [25], found that Fe-doped CGO can slightly retard the sintering onset of the CGO when doped with 1-3 mol% Fe₂O₃, however, the sintering rate is faster than pure CGO, reaching full densification at 1100 °C. On the other hand, Yoon et al. [10] studied the sintering behaviour of the single perovskite Y_{0.8}Ca_{0.2}Cr_{0.9}M_{0.1}O_{3-δ} (M=Co, Fe). When substituting with Co or Fe similar sintering onsets temperatures ca. 1100 °C were obtained; however, the sintering rate of the Co-substituted perovskite was found two times faster than the one of the Fe-substituted perovskite.

It might be possible that during the sintering process at 1250 °C, Fe-diffused from the 3YSZ-Fe₃ PS could partially displaced or substitute the Co from the B-site of YCCC, modifying its crystal structure, retarding its sintering and causing the observed porosity. Additional XRD analysis is needed to determine the Fe-substitution in the B-site of the YCCC perovskite. Nevertheless, electronic conductivity of the perovskite might not be affected, since $Y_{0.8}Ca_{0.2}Cr_{0.9}Co_{0.1}O_{3-\delta}$ and $Y_{0.8}Ca_{0.2}Cr_{0.9}Fe_{0.1}O_{3-\delta}$ have similar conductivity properties with values ca. $6\text{ S}\cdot\text{cm}^{-1}$ and $10\text{ S}\cdot\text{cm}^{-1}$ respectively, when measured at 1000 °C and a $pO_2 = 10^{-17}$ atm. [10].

Conclusions.

The interaction of $Y_{0.8}Ca_{0.2}Cr_{0.8}Co_{0.2}O_{3-\delta}$ – $Ce_{0.9}Gd_{0.1}O_{2-\delta}$ 70:30 vol.% (CY7030) oxygen membranes and $Zr_{0.97}Y_{0.6}O_{2.03}$ (3YSZ) / $Zr_{0.97}Y_{0.6}O_{2.03}+3\text{ mol}\%$ Fe_2O_3 (3YSZ-Fe₃) tubular porous supports was studied. Dilatometry analysis showed a considerable difference in sintering temperature onsets and thermal expansion coefficients between the CY7030 and the 3YSZ-based porous support. The structural effect of this mismatch was observed in the extensive structural damages in the tubular membranes, such as transversal cracks and delamination.

The use of Fe_2O_3 as sintering aid was successfully used to modify the sintering onset. TEC of the 3YSZ tubular supports was also modified, although not to the needed degree to match the properties to the CY7030 composite used in the active membrane.

The chemical stability of the CY7030 was found to be satisfactory after sintering. Cr remained in the perovskite along the membrane, although approximately 62% of the Ca and 30% of the Co were lost from the perovskite. Ca was found in the surface layers of the 3YSZ-based porous supports, probably due to high mobility of the Cr-Ca-O liquid system. Nevertheless, no structural effects or secondary phase formation due to loss of cations was observed in the membrane. It was found that Fe from the 3YSZ-Fe₃ support could affect the densification of the membrane due to possible substitution of the Fe in the B-site of the YCCC perovskite, however, additional studies are necessary to confirm it.

The CY7030 composite is a good and stable candidate to be studied as oxygen transport membrane; however, it is necessary to select a porous support with similar thermomechanical properties to diminish possible mechanical stresses during the fabrication of the membranes. The use of self-supported capillaries could be other option. The use of Fe₂O₃ has proven to be a tool to modify the sintering onset temperature and the TEC of the porous support, which could broaden the options to fabricate stable and structurally strong oxygen membranes.

Acknowledgments.

Authors acknowledge financial support from “Highly Flexible Energy Production by Oxy-Fired Biomass Gasification (HighFlex)” EUDP grant No.: 64018-0028 –before 12403– , "Highly Flexible Energy Production by Oxy-Fired Biomass Gasification (HighFlex)"

References.

- [1] Smart, S.; Diniz Da Costa, J.C. Oxygen transport membranes for power plant applications. *Advanced membrane science and technology for sustainable energy and environmental applications*, Chapter 9. Woodhead Publishing Limited, 2011. United Kingdom. DOI: 10.1533/9780857093790
- [2] Puig-Arnavat, M.; Soprani, S.; Søggaard, M.; Engelbrecht, K.; Ahrenfeldt, J.; Henriksen, U.B.; Hendriksen, P.V. Integration of mixed conducting membranes in an oxygen–steam biomass gasification process. *Rsc Advances* — 2013, Volume 3, Issue 43, pp. 20843-20854. 10.1039/c3ra44509g
- [3] Stadler, H.; Beggel, F.; Habermehl, M.; Persigehl, B.; Kneer, R.; Modigell, M.; Jeschke, P. Oxyfuel coal combustion by efficient integration of oxygen transport membranes. *International Journal of Greenhouse Gas Control* — 2011, Volume 5, Issue 1, pp. 7-15. 10.1016/j.ijggc.2010.03.004

- [4] Milne, T.A.; Evans, R.J.; Abatzoglou, N. Biomass Gasifier “Tars”: Their Nature, Formation, and Conversion. National Renewable Energy Laboratory. November 1998, NREL/TP-570-25357. nrel.gov/docs/fy99osti/25357.pdf
- [5] Niedrig, C.; Menesklou, W.; Wagner, S.F.; Ivers-Tiffée, E. High-temperature pO₂ stability of metal oxides determined by amperometric oxygen titration. *Journal of the Electrochemical Society* — 2013, Volume 160, Issue 2, pp. F135-F140. DOI: 10.1149/2.063302jes
- [6] Zhu, X.; Yang, W. Critical Factors Affecting Oxygen Permeation Through Dual-phase Membranes. *Membrane Science and Technology* — 2011, Volume 14, pp. 275-293. DOI: 10.1016/b978-0-444-53728-7.00012-4
- [Carter] Carter, J.D.; Appel, C.C.; Mogensen, M.B. Reactions at the calcium doped lanthanum chromite-yttria stabilized zirconia interface. *Journal of Solid State Chemistry* — 1996, Volume 122, Issue 2, pp. 407-415. DOI: 10.1006/jssc.1996.0134
- [7] Pirou, S.; Bermudez, J.M.; Tak Na, B.; Ovtar, S.; Yu, J.H.; Hendriksen, P.V.; Kaiser, A.; Ramirez Reina, T.; Millan, M.; Kiebach, R. Performance and stability of (ZrO₂)_{0.89}(Y₂O₃)_{0.01}(Sc₂O₃)_{0.10}-LaCr_{0.85}Cu_{0.10}Ni_{0.05}O_{3-δ} oxygen transport membranes under conditions relevant for oxy-fuel combustion. *Journal of Membrane Science* — 2018, Volume 552, pp. 115-123. DOI: 10.1016/j.memsci.2018.01.067
- [8] Haugen, A.B.; Martinez Aguilera, L.; Kwok, K.; Molla, T.; Andersen, K.B.; Pirou, S.; Kaiser, A.; Hendriksen, P.V.; Kiebach, R. Exploring the Processing of Tubular Chromite- and Zirconia-Based Oxygen Transport Membranes. *Ceramics* — 2018, Volume 1, Issue 2, pp. 229-245. DOI: 10.3390/ceramics1020019
- [9] Yoon, K.J.; Cramer, C.N.; Thomsen, E.C.; Coyle, C.A.; Coffey, G.W.; Marina, O.A. Calcium- and cobalt-doped yttrium chromites as an interconnect material for solid oxide fuel cells. *Journal of the Electrochemical Society* — 2010, Volume 157, Issue 6, pp. B856-B861. DOI: 10.1149/1.3337156

- [10] Yoon, K.J.; Cramer, C.N.; Stevenson, J.W.; Marina, O.A. Improvement of sintering, thermal behavior, and electrical properties of calcium- and transition metal-doped yttrium chromite. *Electrochemical and Solid-state Letters* — 2010, Volume 13, Issue 9, pp. B101-B105. DOI: 10.1149/1.3456525
- [11] Carter, J.D.; Appel, C.C.; Mogensen, M.B. Reactions at the calcium doped lanthanum chromite-yttria stabilized zirconia interface. *Journal of Solid State Chemistry* — 1996, Volume 122, Issue 2, pp. 407-415. DOI: 10.1006/jssc.1996.0134
- [12] Garcia-Fayos, J.; Martinez Aguilera, L.; Haugen, A.B.; Kiebach, W.R., Serra, J.M. Y_{0.8}Ca_{0.2}Cr_{0.8}Co_{0.2}O₃-based dual phase membranes for O₂ separation in oxyfuel and syngas applications. Instituto de Tecnología Química - Technical University of Denmark. Unpublished.
- [13] Kammer Hansen, K.; Menon, M.; Knudsen, J.; Bonanos, N.; Mogensen, M.B. The Effect of a CGO Barrier Layer on the Performance of LSM/YSZ SOFC Cathodes. *Journal of the Electrochemical Society* — 2010, Volume 157, Issue 3, pp. B309-B313. DOI: 10.1149/1.3273194
- [14] Knibbe, R.; Hjelm, J.; Menon, M.; Pryds, N.; Søggaard, M.; Wang, H.J.; Neufeld, K. Cathode-Electrolyte Interfaces with CGO Barrier Layers in SOFC : Cathode-Electrolyte Interfaces in IT-SOFCs. *Journal of the American Ceramic Society* — 2010, Volume 93, Issue 9, pp. 2877-2883. DOI: 10.1111/j.1551-2916.2010.03763.x
- [15] Laguna-Bercero, M.A.; Monzón, H.; Larrea, A.; Orera, V.M. Improved stability of reversible solid oxide cells with a nickelate-based oxygen electrode. *Journal of Materials Chemistry a* — 2016, Volume 4, Issue 4, pp. 1446-1453. DOI: 10.1039/c5ta08531d
- [16] Mehranjani, A.S.; Cumming, D.J.; Sinclair, D.C.; Rothman, R.H. Low-temperature co-sintering for fabrication of zirconia/ceria bi-layer electrolyte via tape casting using a Fe₂O₃ sintering aid. *Journal of the European Ceramic Society* — 2017, Volume 37, Issue 13, pp. 3981-3993. DOI: 10.1016/j.jeurceramsoc.2017.05.018

- [17] Zhang, Z.; Sigle, W.; Rühle, M.; Jud, E.; Gauckler, L.J. Microstructure characterization of a cobalt-oxide-doped cerium-gadolinium-oxide by analytical and high-resolution TEM. *Acta Materialia* — 2007, Volume 55, Issue 8, pp. 2907-2917. DOI: 10.1016/j.actamat.2006.12.039
- [18] Mori, M.; Wang, Z.; Itoh, T. Sintering mechanisms of cobalt-doped ceria and zirconia electrolytes in intermediate-temperature solid oxide fuel cells. *ECS Transactions* — 2009, Volume 25, Issue 2, pp. 1625-1634. DOI: 10.1149/1.3205699
- [19] Fagg, D.P.; Kharton, V.V.; Frade, J.R. P-type electronic transport in Ce_{0.8}Gd_{0.2}O_{2-δ}: The effect of transition metal oxide sintering aids. *Journal of Electroceramics* — 2002, Volume 9, Issue 3, pp. 199-207. DOI: 10.1023/a:1023269326651
- [20] Taub, S.; Neuhaus, K.; Wiemhöfer, H.D.; Ni, N.; Kilner, J.A.; Atkinson, A. The effects of Co and Cr on the electrical conductivity of cerium gadolinium oxide. *Solid State Ionics* — 2015, Volume 282, pp. 54-62. DOI: 10.1016/j.ssi.2015.09.024
- [21] Liang, B.; Suzuki, T.; Hamamoto, K.; Yamaguchi, T.; Fujishiro, Y.; Awano, M.; Ingram, B.J.; Carter, J.D. Anode-supported tubular SOFC at low temperature using Ni, Fe, GDC, and YSZ based anode support. *ECS Transactions* — 2011, Volume 35, Issue 1, pp. 705-711. DOI: 10.1149/1.3570049
- [22] Zyryanov, V.V.; Nemudry, A.P.; Sadykov, V.A. Nanostructured Perovskites for the Fabrication of Thin Ceramic Membranes and Related Phenomena. *Membranes for Membrane Reactors: Preparation, Optimization and Selection* — 2011, pp. 201-225. DOI: 10.1002/9780470977569.ch6
- [23] Suzuki, T.; Funahashi, Y.; Yamaguchi, T.; Fujishiro, Y.; Awano, M. Development of Fabrication/Integration Technology for Micro Tubular SOFCs. *Micro Fuel Cells* — 2009, pp. 141-177. DOI: 10.1016/B978-0-12-374713-6.00004-4
- [24] Cheng, S.; Huang, H.; Ovtar, S.; Simonsen, S.B.; Chen, M.; Zhang, W.; Søggaard, M.; Kaiser, A.; Hendriksen, P.V.; Chen, C. High-Performance Microchanneled

Asymmetric $\text{Gd}_{0.1}\text{Ce}_{0.9}\text{O}_{1.95-\delta}$ – $\text{La}_{0.6}\text{Sr}_{0.4}\text{FeO}_{3-\delta}$ -Based Membranes for Oxygen Separation ACS Applied Materials and Interfaces — 2016, Volume 8, Issue 7, pp. 4548-4560. 10.1021/acsami.5b10714

- [25] Nicholas, J.D.; De Jonghe, L.C. Prediction and evaluation of sintering aids for Cerium Gadolinium Oxide. Solid State Ionics — 2007, Volume 178, Issue 19-20, pp. 1187-1194. DOI: 10.1016/j.ssi.2007.05.019

5.5 Effective method to manufacture stable $(\text{Sc}_2\text{O}_3)_{0.10}(\text{Y}_2\text{O}_3)_{0.01}(\text{ZrO}_2)_{0.89}$ – $\text{LaCr}_{0.85}\text{Cu}_{0.10}\text{Ni}_{0.05}\text{O}_{3-\delta}$ asymmetric tubular ceramic oxygen transport membranes.

This section includes the manuscript “Effective method to manufacture stable dense asymmetric tubular ceramic oxygen transport membranes”, which objective is the study of an alternative method to obtain dense ceramic membranes based on 70:30 and 60:40 volume $(\text{Sc}_2\text{O}_3)_{0.10}(\text{Y}_2\text{O}_3)_{0.01}(\text{ZrO}_2)_{0.89}$ – $\text{LaCr}_{0.85}\text{Cu}_{0.10}\text{Ni}_{0.05}\text{O}_{3-\delta}$ composites. The study considers the use of Fe_2O_3 as sintering aid to match the thermo-mechanical properties of the membrane’s components, in order to diminish the transient stress during manufacturing and lower the sintering temperature to <1300 °C to avoid vaporization of the species, destabilization of the perovskite and formation of secondary phases.

$(\text{Y}_2\text{O}_3)_{0.03}(\text{ZrO}_2)_{0.97}$ porous tubular supports were fabricated by thermoplastic extrusion. Catalytic porous layers and dense active membrane were deposited via dip coating on the porous support. Dilatometry studies were used to identify the sintering behaviour and the thermal expansion coefficients of the materials used in the fabrication of the components to find a feasible combination and an adequate and successful sequence to fabricate the membranes. Several iterations were made until obtaining highly stable 6-10 μm , crack-free dense active membranes. The microstructure of the activation layers was optimized, in order to create enough triple phase boundaries to carry out the oxygen transport across the membrane.

In order to investigate the functionality of the fabricated tubular membrane, oxygen permeability tests were performed in gradients Air/ N_2 , Air/ CO_2 , Air/ CH_4 , and Air/5% H_2 - N_2 between 850 °C and 950 °C. Oxygen fluxes in the range of 0.28 $\text{ml}\cdot\text{min}^{-1}\cdot\text{cm}^2$ were obtained at 950 °C in gradient Air/ N_2 . The performance of the membrane showed no changes after every test, which indicates high thermo-chemical stability of the membrane towards different atmospheres, including highly reducing conditions, which makes it suitable for further testing and development for syngas applications.

The oxygen permeability tests developed in this study were carried out considering the in the time-framework of the project and the availability of the testing rigs. Additional analysis is required to complement the results shown in this section.

**Effective method to manufacture stable $(\text{Sc}_2\text{O}_3)_{0.10}(\text{Y}_2\text{O}_3)_{0.01}(\text{ZrO}_2)_{0.89}$ –
 $\text{LaCr}_{0.85}\text{Cu}_{0.10}\text{Ni}_{0.05}\text{O}_{3-\delta}$ asymmetric tubular ceramic oxygen transport membranes.**

Lev Martinez Aguilera ^a, Astri Bjørnetun Haugen ^a, Peter Vang Hendriksen ^a, Andreas Kaiser ^a, Steven Pirou ^a, Peyman Khajavi ^a, Henrik Lund Frandsen ^a, Julio Garcia Fayos ^b, Jose Manuel Serra ^b, Ragnar Kiebach ^{a*}

a Department of Energy Conversion and Storage, Technical University of Denmark, 2800 Kgs. Lyngby, Denmark.

b Instituto de Tecnología Química (Universitat Politècnica de Valencia – Consejo Superior de Investigaciones Científicas), E-46022 Valencia, Spain.

** Corresponding author: woki@dtu.dk*

1. Abstract.

Dense $(\text{Sc}_2\text{O}_3)_{0.10}(\text{Y}_2\text{O}_3)_{0.01}(\text{ZrO}_2)_{0.89}$ – $\text{LaCr}_{0.85}\text{Cu}_{0.10}\text{Ni}_{0.05}\text{O}_{3-\delta}$ ceramic membranes supported on porous tubular $(\text{Y}_2\text{O}_3)_{0.03}(\text{ZrO}_2)_{0.97}$ were fabricated by doping the materials with Fe_2O_3 . The addition of Fe_2O_3 allowed lowering the sintering temperature of the system, as well as matching the thermo-mechanical properties between the composite membrane layer and the porous support. Fully densification of the membrane was obtained at 1250 °C.

Thermoplastic extrusion was used to fabricate robust, chemical and mechanical stable $(\text{Y}_2\text{O}_3)_{0.03}(\text{ZrO}_2)_{0.97}$ tubular supports. By doping the supports with 3 mol% Fe_2O_3 , 49 vol% of porosity, gas permeability of 2.2×10^{-14} cm² and flexural strength of more than 138 MPa was obtained. With a total shrinkage of 26 % of these supports, full densification of the membrane layer could be achieved.

The interaction among the porous activation layers, active membrane and porous support was analysed. The fraction of $\text{LaCr}_{0.85}\text{Cu}_{0.10}\text{Ni}_{0.05}\text{O}_{3-\delta}$ perovskite material in the dual-phase composite of the active membrane layer is limited to 90 vol% and to 70 vol% in the two catalytic layers to allow densification. Increasing the load of the perovskite in any of these layers would hinder the densification of the membrane, which might be related to the high vapour pressure of the Cr^{+6} in the perovskite at the studied sintering temperature. The dual phase $\text{LaCr}_{0.85}\text{Cu}_{0.10}\text{Ni}_{0.05}\text{O}_{3-\delta}$ - $(\text{Sc}_2\text{O}_3)_{0.10}(\text{Y}_2\text{O}_3)_{0.01}(\text{ZrO}_2)_{0.89}$ membranes showed an oxygen flux of 0.28 ml·min⁻¹·cm⁻² in an Air/N₂ atmosphere at 950 °C. Furthermore, the membranes revealed stable oxygen flux using an Air/N₂

gradient after measurements in different atmospheres, including Air/H₂ gradient. The development of a fabrication method for lanthanum chromite based dual phase membranes, which are stable in reducing atmospheres (e.g. in H₂, CO₂, CH₄) opens the possibility for optimization of this membrane system for integration in syngas or oxy-combustion applications.

2. Introduction.

Oxygen is an important worldwide commodity with several industrial applications and which market is expected to continue growing in the following years. [1,2] Currently, the market of industrial production of oxygen is dominated by two technologies: 1) fractional distillation of liquefied air (cryogenic distillation), which is a large-scale production technology capable to generate high purity oxygen (>99.5%) and 2) pressure swing adsorption (PSA), that uses pressurized systems and absorbents like carbon molecular sieves or zeolites to remove N₂ and CO₂ from the air. Oxygen production via PSA economically viable but achieving O₂ purities above 97% makes the process technically and economically unfeasible [1,3]

Oxygen transport membranes (OTMs) are a promising alternative to separate oxygen from air in high temperature processes. An OTM is a gas-tight ceramic layer permeable to oxygen and electrons and impermeable to other species, allowing a theoretical oxygen selectivity of 100%. Oxygen ions are transported via oxygen vacancies and the total oxygen flux depends on the bulk permeability and the reaction rate of molecular oxygen at the interfaces membrane/gas, where the splitting and recombination of oxygen molecules. The difference in partial oxygen pressure, pO₂, between the feed and the permeate side of the membrane provides the driving force for the process. [4,5]

Promising applications for the OTM are oxy-fuel combustion for capture and storage (CCS) and oxygen blown gasification. When air is used in combustion processes, N₂, an inactive gas that shares ~79 % of the air's volume, needs to be heated up, lowering the efficiency of the process. It also increase the capital costs of the combustion equipment, since dimensioning the systems to handle the inactive N₂ is needed. [1,7,8]

Previous studies, have shown first investigations to integrate oxygen membranes into biomass gasification processes, showing the feasibility of this concept. However, in order

to use OTMs under large scale and real operation conditions, technical challenges related to the stability and performance of the membrane materials under operating conditions of biomass gasification (ca 1000 °C and pO_2 of 10^{-20} atm) still need to be addressed. [4,6]

Perovskites, with the general structure ABO_3 , have been identified as the most common and promising candidates for use in oxygen transport membranes due to their high ionic and electronic conduction. [4] Several studies have demonstrated that mixed ionic-electronic conducting (MIEC) perovskites with the composition $A_xSr_{1-x}Co_yFe_{1-y}O_{3-d}$ (A=La, Ba) have high oxygen-ionic and electronic conductivity, which are the basic requirements for an OTM material. However, these perovskites have a limited pO_2 operation range and can undergo chemical decomposition at low pO_2 values ($\sim 10^{-12}$ atm), depending on their exact composition. [9]

By using dual-phase composites of electron and oxygen conducting materials, it is possible to seize stability and performance features of both components. [10] Fluorite-structured oxides based on Y_2O_3 stabilized ZrO_2 have been widely studied as ionic conductors due to their highly stable conductivity in the pO_2 range between $1 - 10^{-21}$. [11,12] By doping YSZ with Sc, a non-transformable tetragonal phase and ionic conductivity up to $0.12 \text{ S}\cdot\text{cm}^{-1}$ at 850 °C is obtained, such as in the case of $(Sc_2O_3)_{0.10}(Y_2O_3)_{0.01}(ZrO_2)_{0.89} - ScYSZ$. [13,14]

Lanthanum chromite-based perovskites $La_{1-x}A_xB_yCr_{1-y}O_{3-\delta}$ (A= Sr, Ca; B = Fe, Cu, Mn, Co) have been studied as interconnects due to their high electronic conductivity, thermochemical stability at high temperatures (~ 1000 °C) and stability in reducing environments ($pO_2 \sim 10^{-20}$ atm). [15,16] When doped with Ca or Sr, lanthanum chromite have a high electronic conductivity that can reach up to $25 \text{ S}\cdot\text{cm}^{-1}$ and $6 \text{ S}\cdot\text{cm}^{-1}$ at 1000 °C in air and reducing conditions, respectively. [15,17-20] In addition, it has been demonstrated that Sr-containing perovskites can accelerate the oxygen exchange kinetics at the surface. [21] However, in $pO_2 < 10^{-7}$ and temperatures above 600 °C, Sr segregates and an exponential decrement of the electronic conductivity is observed. [18,21,22] Thus, the use of a Sr-free chromite could offer the possibility to keep the stability of the perovskite structure in highly reducing environments and temperatures as high as 1000 °C, operations conditions foreseen for OTMs in gasification processes.

Pirou et al. [23] have studied $\text{LaCr}_{0.85}\text{Cu}_{0.10}\text{Ni}_{0.05}\text{O}_{3-\delta}$ – LCCN – in dual phase OTMs with ScYSZ, demonstrating that this composite could be used in oxygen membranes for oxy-fuel applications. Haugen et al. [24] used this composite supported on porous $(\text{Y}_2\text{O}_3)_{0.03}(\text{ZrO}_2)_{0.97}$ – 3YSZ – to manufacture asymmetric tubular oxygen membranes. However, successful fabrication of the system was not possible due to several drawbacks caused by the stability of the materials at the used sintering temperature of 1450 °C. Some of the shortcomings observed by Haugen et al. were: 1) formation of transversal cracks in the membrane caused by thermal expansion mismatch between the dual-phase composite and the porous support; 2) longitudinal cracks caused by vaporization of Cr from the perovskite and subsequent reaction of the La_2O_3 with humidity to form $\text{La}(\text{OH})_3$, and 3) formation of insulating lanthanum zirconate phase on the surface of the membrane.

Lowering the sintering temperature is a cornerstone to decrease the vaporization of Cr from the chromite based perovskite [25], avoiding the formation of secondary phases and keeping the stability of the system. In order to achieve this, the use of effective sintering aids for the ZrO_2 -phase is an option to lower the sintering temperature of the system, as well as modifying the thermal expansion coefficient (TEC) of the materials to reduce the thermo-mechanical stress during the sintering process and operation of the membrane.

This study describes an alternative method to fabricate asymmetrical multilayer ScYSZ-LCCN oxygen membranes supported on 3YSZ tubular porous supports by using Fe_2O_3 as sintering aid and as a tool to tailor the thermo-mechanical properties of the membrane's components. It was possible to obtain dense membranes at 1250 °C, which reduce the Cr vaporization of the membrane. The obtained oxygen membranes are robust and show high tolerance towards reducing conditions.

3. Experimental.

The asymmetric tubular oxygen transport membranes (OTMs) consist of three different layers: 1) an inner porous activation layer (IL), 2) a dense active membrane (AM) and, 3) an outer porous activation layer (OL) that are dip coated on a robust tubular porous support (PS). The support is fabricated by thermoplastic extrusion. A schematic of the architecture of the membrane is shown in Fig. 1.

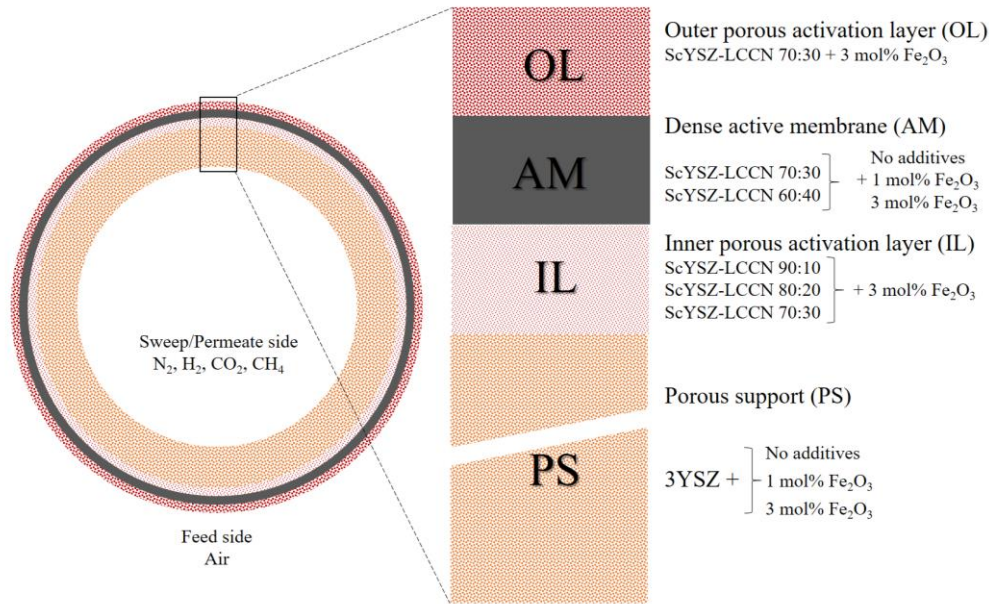


Fig. 1. Schematic of the studied oxygen transport membrane's architecture and materials analysed in this study.

The dip coated layers are based in dual-phase composites $(\text{Sc}_2\text{O}_3)_{0.10}(\text{Y}_2\text{O}_3)_{0.01}(\text{ZrO}_2)_{0.89} - \text{LaCr}_{0.85}\text{Cu}_{0.10}\text{Ni}_{0.05}\text{O}_{3-\delta}$ (ScYSZ-LCCN) and single ScYSZ. The PS was fabricated via thermoplastic extrusion using $(\text{Y}_2\text{O}_3)_{0.03}(\text{ZrO}_2)_{0.97}$ (3YSZ), as described in section 3.2 further below. Fe₂O₃ was added in the IL, OL, AM and PS as sintering aid. The fabrication process of the dual phase membranes in this study is summarised in Fig. 2, including the fabrication techniques and thermal processes. Two fabrication routes are shown: i) a 3-step route where the de-binding of the PS and the calcination of the IL are carried out in a single process (Fig. 2a) and ii) a 4-step route where de-binding and calcination of the IL are done independently (Fig. 2b).

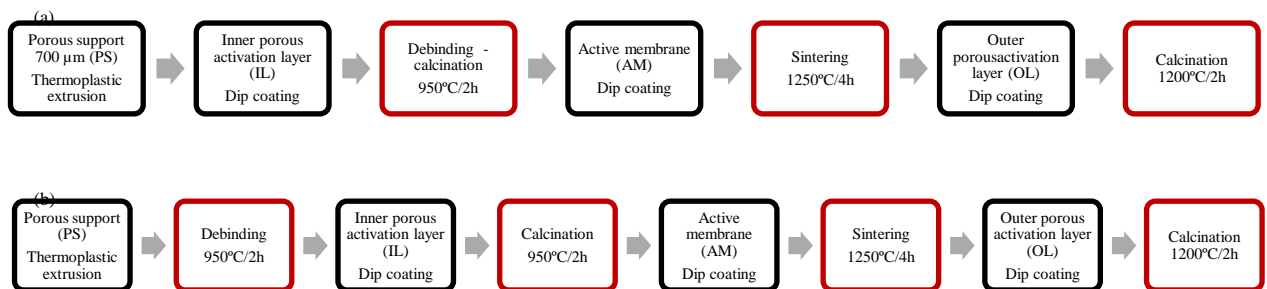


Fig. 2. Manufacturing steps of the asymmetric tubular oxygen transport membranes: a) 3-step route and b) 4-step route. Thermal processes are outlined in red.

In the sections 3.1 – 3.5, a more detailed description of the different manufacturing steps for the preparation of the OTMs are described. These steps include the pre-treatment of the powders, formulation of the dip-coating slurries and the preparation of the extrusion feedstocks. In section 3.5, the characterization methods of the powders, slurries, PS and membranes (PSD, XRD, Rheometry, Darcy permeability, Hg Porosimetry, flexural strength, oxygen permeability) are listed and the instrument setting are described.

3.1 Pre-treatment of the powders

$(\text{Sc}_2\text{O}_3)_{0.10}(\text{Y}_2\text{O}_3)_{0.01}(\text{ZrO}_2)_{0.89}$ – ScYSZ (Daiichi, Japan) – powder and $\text{LaCr}_{0.85}\text{Cu}_{0.10}\text{Ni}_{0.05}\text{O}_{3-\delta}$ – LCCN, (CerPoTech, Norway) – powder were mixed in different volumetric proportions between 90:10 – 50:50 ScYSZ-LCCN, to prepare the different dual-phase composites investigated in this work. The single powders of LCCN, ScYSZ and $(\text{Y}_2\text{O}_3)_{0.03}(\text{ZrO}_2)_{0.97}$ – 3YSZ (Tosoh, Japan) were also investigated to assess their individual stability and sintering properties. Fe_2O_3 (Alfa Aesar, USA) was added in 1 mol% and 3 mol% to adjust the sintering behaviour of the different composites and single ScYSZ and 3YSZ powders according to Table 1. The function of each layer in the multilayer membrane is specified in the table. The powders were mixed and ball milled in ethanol using 5 mm ZrO_2 milling media until obtain powders with mean particle size of 250 nm. Powders were dried at 50 °C overnight.

Table 1. Matrix of tested components in the ScYSZ-LCCN multilayer tubular systems.

Component	ScYSZ:LCCN [vol.%]	Fe content [mol %] to Zr-based phase.		
		0 %	1 %	3 %
Porous support (PS) 3YSZ	---	✓	✓	✓
Inner porous activation layer (IL) ScYSZ-LCCN	100:0	✓	✓	✓
	90:10	✓	-	✓
	80:20	✓	-	✓
	70:30	✓	-	✓
Dense active membrane (AM) ScYSZ-LCCN	60:40	✓	✓	✓
	70:30	✓	✓	✓
Outer porous activation layer (OL) ScYSZ-LCCN	70:30	✓	-	✓
	60:40	✓	-	✓
	50:50	✓	-	✓

3.2 Porous supports manufacturing.

Tubular PS were prepared by thermoplastic extrusion process following the procedure described by Ramachandran, et al. [26,27] and Haugen et al. [24]. A volumetric-based mixture of graphite (Superior Graphite, USA), poly-methyl-methacrylate (Esprix, USA) ethylene-vinyl acetate copolymer (DuPont, USA) and paraffin wax (Sigma-Aldrich, USA) was added to 3YSZ powders coated with stearic acid (Sigma-Aldrich, USA). Three different feedstocks were prepared. One feedstock containing single 3YSZ, and two more with 1 mol% Fe₂O₃ (3YSZFe1) and 3 mol% Fe₂O₃ (3YSZFe3) respectively. The feedstocks were mixed and homogenized for 2 h at 100 °C using a BK20 mixer (Linden International, Germany). Tubes of 14 mm outer diameter were extruded at 85 °C using a single screw extruder 19/20DN (Brabender, Germany).

3.3 Preparation of dip-coating slurries.

Dip coating slurries for the AM, IL and OL were made by mixing the ScYSZ and ScYSZ-LCCN powders with the organic additives according to the formulations described in Table 2. Ethanol was used as solvent, polyvinyl-pyrrolidone PVPK15 (Sigma-Aldrich, USA) as dispersant, polyvinyl-pyrrolidone PVPK30 (Sigma-Aldrich, USA) and polyvinyl-butyrac PVB Mowital B30HH (Kuraray, USA) as binders, dibutyl sebacate DBS (Sigma Aldrich, USA) as plasticizer and graphite UF-1 (Graphit Kropfmühl, Germany) as pore former.

Table 2. Formulation of the active membrane and porous activation layers slurries

Function	Dense active membrane	wt. %	Porous activation layer	wt. %
Solvent	Ethanol	67.5	Ethanol	61.8
Oxides	ScYSZ-LCCN (Fe)	28.6	ScYSZ, ScYSZ-LCCN, ScYSZ (Fe)	25.8
Dispersant	PVPK15	1.5	PVPK15	1.3
Binder	PVPK30	1.5	B30HH	3.1
Plasticiser	--		DBS	2.2
Pore former	--		Graphite UF-1	5.8

The slurries for the IL and OL were prepared by ball-milling the oxide powders, dispersant and the solvent for 72 h. Afterwards, the binder and plasticizer were added and subsequently ball-milled for 24 h. For 2AM slurries were prepared by ball-milling the oxide powders and the dispersant for 72 hours. The PVP binder was added after the milling

process, allowing additional mixing for 2 hours more. All the slurries were filtrated using a 20 μm mesh and kept stored in constant rotation at 15 rpm to avoid agglomeration of the powders.

3.4 Fabrication of the tubular membranes and thermal treatment.

The inner activation layer (IL) was deposited on the tubular porous supports (PS) using an in-house built dip coater [28] varying the deposition speeds from 0.05 to 0.5 $\text{cm}\cdot\text{s}^{-1}$, in order to obtain between 4-10 μm thick layers. Deposition of this layer was done on a) green PS and b) de-binded PS for the 3-step and 4-step fabrication route, as described in Fig. 2.

In the case of the 3-step route (Fig. 2a), binder burnout of the PS and calcination of the IL was done by heating up with ramp of 15 $^{\circ}\text{C}\cdot\text{h}^{-1}$ in order to allow controlled removal of gases. Dwells of 2 h at 200 $^{\circ}\text{C}$, 360 $^{\circ}\text{C}$ and 600 $^{\circ}\text{C}$ were kept to burn specific fraction of organics. A maximum temperature of 950 $^{\circ}\text{C}$ for 2 h was kept to complete the calcination, followed by cooling with a rate of 120 $^{\circ}\text{C}\cdot\text{h}^{-1}$. The same cooling rate was used in all the thermal profiles for the fabrication of the OTMs.

In the case of a 4-step route, de-binding of the PS was carried out before the IL was deposited. Then, the coated tube was calcined in air at 950 $^{\circ}\text{C}$ for 2 h. Heating ramp of 60 $^{\circ}\text{C}\cdot\text{h}^{-1}$ with 2 dwells at 360 $^{\circ}\text{C}$ and at 600 $^{\circ}\text{C}$ were used in the thermal profile as depicted in Fig. 3b.

The active membrane (AM) was deposited on the calcined IL. The deposition was controlled by means of dip-coating speed to have uniform layers with thickness of 5-8 μm . Sintering of the membrane was done using heating ramp of 60 $^{\circ}\text{C}\cdot\text{h}^{-1}$ with 2 dwells at 360 $^{\circ}\text{C}$ and at 600 $^{\circ}\text{C}$ for 2 hours. Two ramps were used between 600 $^{\circ}\text{C}$ and 1250 $^{\circ}\text{C}$: 1) 60 $^{\circ}\text{C}\cdot\text{h}^{-1}$ and b) 200 $^{\circ}\text{C}\cdot\text{h}^{-1}$, according to Fig. 3c. Sintering temperature was set at 1250 $^{\circ}\text{C}$ for 4h to ensure densification of the membrane.

Deposition of the outer activation layer (OL) was done on the sintered and densified AM. Calcination was done using a thermal profile similar to the sintering one: using a heating rate of 200 $^{\circ}\text{C}\cdot\text{h}^{-1}$ between 600 $^{\circ}\text{C}$ and the pre-sintering temperature of 1200 $^{\circ}\text{C}$ for 2 hours, according to Fig. 3d.

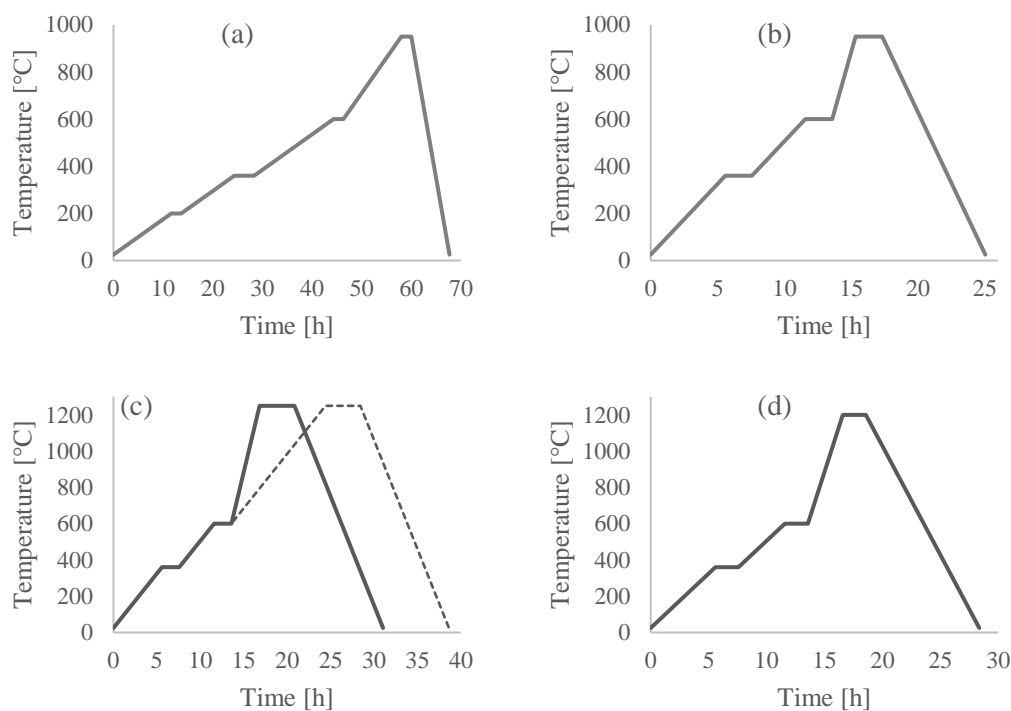


Fig. 3. Thermal profiles for (a) green tubes debinding at 950 °C, (b) inner activation layer / 1st activation membrane layer calcination at 950 °C, (c) sintering of active membrane at 1250 °C, and (d) firing of outer activation layer at 1200 °C.

3.5 Characterization methods

3.5.1 Particle size and slurries characterization.

Particle sizing of the different slurries was measured with a laser diffraction particle size analyser LS 13 320 (Beckman Coulter, USA) using ethanol as vehicle and a 5 mW laser diode with a wavelength of 750 nm (or 780 nm) as the main illumination source.

Rheological properties of the slurries were obtained using a MCR302 rheometer (Anton Paar, Austria) with a 25 mm stainless steel parallel plate (PP25). The gap between the PP50 and the rheometer's fixed plate was set at 0.5 mm. Viscosity was measured in a shear rate interval between 1 s⁻¹ to 100 s⁻¹. FFT (Fast Fourier Transformed) smoothing method was used to determine the viscosity during the preparation of the solutions.

3.5.2 X-ray diffraction.

X-ray diffraction analysis was performed to identify the possible secondary phase formation in LCCN powder after sintering at 1300 °C and after exposition to 5%H₂-N₂ gas mixture for 24 h. ScYSZ-LCCN 70:30 vol. (SL7030) sintered at 1300 °C was also

analysed. Diffractograms were obtained using a D8 X-ray diffractometer (Bruker, Germany). XRD diffractograms were obtained varying 2θ in the interval $10^\circ - 90^\circ$ with step of 0.019° . Voltage of 40 kV and current of 40 mA were used.

3.5.3 Dilatometry studies.

Sintering curves and thermal expansion coefficients (TEC) of the different composites and single-phase powders were obtained using a dilatometer DIL402CD (Netzsch, Germany). Measurements were done on 1 cm long pellets prepared by cold uniaxial pressing using a 6 mm diameter die and a pressure of $1 \text{ ton}\cdot\text{cm}^{-2}$. 6 mm long alumina rods were used as references. Air at a constant rate of $20 \text{ ml}\cdot\text{min}^{-1}$ was used in all the tests. Measurements were done using differential method.

For the sintering curves, as-prepared pellets were heated with a rate of $1 \text{ }^\circ\text{C}\cdot\text{min}^{-1}$ up to $1250 \text{ }^\circ\text{C}$ and cooled using a ramp of $10 \text{ }^\circ\text{C}\cdot\text{min}^{-1}$. For TEC measurements, as-prepared pellets were sintered in a chamber furnace in stagnant air at $1350 \text{ }^\circ\text{C}$ for 2 hours using heating and cooling ramps of $1 \text{ }^\circ\text{C}\cdot\text{min}^{-1}$ and of $2 \text{ }^\circ\text{C}\cdot\text{min}^{-1}$, respectively. TEC measurements were performed using heating and cooling ramps of $2 \text{ }^\circ\text{C}\cdot\text{min}^{-1}$ with 1 dwell at $1250 \text{ }^\circ\text{C}$. Analysis of the dilatometry data was done using Netzsch Proteus software.

3.5.4 Flexural strength of porous supports.

Flexural strength was tested using four-point bending of the different support samples. The test rig, methodology and peak stress data analysis are described by Kwok et al. [29]. 6 cm long tubes were longitudinally diamond saw-cut by the half to obtain semi-cylindrical pieces. At least 6 pieces of each PS, 3YSZ, 3YSZ + 1 mol% Fe_2O_3 (3YSZFe1) and 3YSZ + 3 mol% Fe_2O_3 (3YSZFe3) were tested, in order to obtain representative data. A maximum load of 10 N was applied during the tests at room temperature.

3.5.5 Gas permeability through the porous support.

Permeability experiments were carried out on the PS using a special rig based on Darcy's Law [30], which states that the flow rate of a single phase fluid through a porous medium is proportional to the potential energy within the fluid according to Eq. 1:

$$Q = \frac{Ak\Delta P}{\mu\Delta x} \quad (\text{Eq. 1})$$

Where Q is the flow [$\text{m}^3\cdot\text{s}^{-1}$], A is the cross section area to flow [m^2], ΔP is the pressure drop [Pa], k is the intrinsic permeability of the medium [m^2], μ the viscosity of the fluid [$\text{Pa}\cdot\text{s}$], and Δx is the length where the pressure drop occurs [m] [31]. Measurements were done using N_2 from 0.23 to 4 bars at room temperature in 1 cm and 0.7 cm sections of the 3YSZ-based PS. It is expected that values of k larger than 10^{-14} m^2 provide sufficient gas permeability from the bulk to the membrane and avoid limitation in the gas supply to the membrane. [30].

3.5.6 Porous support porosity.

Porosity of the 3YSZ-based PS was obtained through Hg-intrusion using an automatic pore size analyser PoreMaster 33 (Quantachrome, USA) and through microstructure analysis using a desktop scanning electron microscope TM3000 (Hitachi, Japan) working with secondary electron detector at 15 kV. Image J (open source software) was used for the SEM data analysis.

3.5.7 Oxygen flux characterization.

Oxygen permeability through the membrane was tested in an in-house built open flow rig supplying air at the feed side (outer side) while sweeping was performed at the permeate side (inner side). Gas flows were monitored by Brooks mass flow controllers.

The rig is made of two alumina tubes that act as holders to set the sample in the hot zone of a vertical furnace. Temperature was monitored at the inlet and the outlet of the membrane in the sweeping gas side by two thermocouples. The membrane was sealed to the alumina holders using YS2B glass, with composition of SiO_2 , 67.94 wt.%, Al_2O_3 , 14.92 wt.%, and Na_2O , 17.14 wt.%. The sealing procedure comprises heating up to $1000 \text{ }^\circ\text{C}$ by using a rate of $1 \text{ }^\circ\text{C}\cdot\text{min}^{-1}$. A dwell of 2 h was kept at this temperature before cooling down to $850 \text{ }^\circ\text{C}$.

To verify the gas tightness, N_2 was fed at the permeate side and flows were monitored at the inlet and outlet of the membrane. A difference of flows below 3% was considered as gas tight. The air flow at the permeate side was set to $1 \text{ l}\cdot\text{min}^{-1}$ for all the tests. N_2 , CO_2 , CH_4 , 5% H_2 balanced with N_2 and H_2 , were used as sweeping gas using flows between

24 ml·min⁻¹ and 500 ml·min⁻¹. Tests were performed at three temperatures: 850 °C, 900 °C and 950 °C. Between each change of gas, measurements in N₂/Air gradient at 850 °C were carried out, in order to check the effect of the sweep gas on the performance of the membrane.

Oxygen flux was calculated according to Eq. 2 [23],

$$J_{O_2} = \frac{\phi_{in}(p_{O_2(out)} - p_{O_2(in)})}{A} \quad (\text{Eq. 2})$$

Where J_{O_2} is the oxygen flux [ml·min⁻¹·cm⁻²], A is the active surfaced area of the membrane [cm²], ϕ_{in} is the total gas flow at the inlet of the membrane [ml·min⁻¹], $p_{O_2(out)}$ and $p_{O_2(in)}$ are the oxygen partial pressures at the outlet and inlet of the membrane respectively. Oxygen flux for gradient H₂/Air was calculated using Eq. 3 [32], where $\phi_{H_2O}^{out}$ and $\phi_{H_2O}^{in}$ are the flows rates of produced water [ml·min⁻¹] considering that the reaction $H_{2(g)} + O_{2(g)} \rightarrow H_2O_{(g)}$ is in equilibrium and can be described with a known equilibrium constant, $K_{eq}(T)$. [33].

$$J_{O_2} = \frac{\phi_{H_2O}^{out} - \phi_{H_2O}^{in}}{A} \quad (\text{Eq. 3})$$

Microstructural analysis of the AM, IL and OL, as well as the interaction among the membrane components was done using scanning electron microscopes TM3000 (Hitachi, Japan) and FE-SEM Merlin (Zeiss, Germany) working with secondary and backscattered electron detectors and accelerating voltage of 15 kV. Composition of the membranes was analysed by using EDS (Quantax70) working at 15 kV.

3.5.8 Stability of the membranes towards cycling

Cyclic cooling and heating treatments were applied to the fabricated membranes, in order to investigate the mechanical and chemical stability of the membranes after such conditions. The cyclic treatment consisted on heating up a sample of the manufactured membrane to 1000 °C with ramp of 2 °C·min⁻¹, keeping a 30 min dwell and then cooling down with the same rate. This cycle was repeated 4 times in air and 3 times in 5% H₂-N₂. A final cycle in air was carried out to re-oxidise the sample.

4. Results and discussion.

This section shows the results from the characterization tests of the porous supports (PS) and the dense active membranes (AM). Section 4.1 analyses the stability of the dual-phase composite in relevant conditions for the processing and operation of the membrane. XRD-analysis, SEM and dilatometry are used to investigate the possible mechanisms for the densification of the composites.

The main characteristics of the Fe₂O₃-doped 3YSZ PS is summarised in section 4.2. SEM, flexural strength, porosimetry and dilatometry are used to analyse the effect of the sintering aid in the physical properties of the PS and to determine its possible use in the fabrication of the membranes.

Section 4.3 describes and analyses the effects of the variation in the composition of the electronic-conducting phase and the addition of Fe₂O₃ in the dual-phase composite. Possible effects on the ion-conductivity of the ZrO₂-based phase and modification of the thermo-mechanical properties are also described.

Section 4.4 analyses the compatibility of thermal expansion coefficients between the AM and PS materials and accordingly to the results, the selection of possible AM/PS combinations is also given.

A detailed analysis of the interaction of the different components of the OTM is presented in Section 4.5. Due to the membrane complexity and challenges in the processing, eight subsections describe the different interactions among the porous support, the active membrane and the activation layers, as well as the sintering conditions used to obtain highly stable tubular membranes. SEM-EDS is widely used to investigate the microstructure of the membranes.

Performance of the membranes was measured by oxygen permeation tests. In section 4.6, the results of the tests are displayed and discussed. Hypotheses are given to explain the moderate oxygen permeability obtained in different atmospheres. In addition, some options to improve the membrane performance in the future are described.

4.1 Stability of $\text{LaCr}_{0.85}\text{Cu}_{0.10}\text{Ni}_{0.05}\text{O}_{3-\delta}$, $(\text{Sc}_2\text{O}_3)_{0.10}(\text{Y}_2\text{O}_3)_{0.01}(\text{ZrO}_2)_{0.89}$ and composite in relevant conditions

4.1.1 Electron conducting phase stability

Fig. 4 shows the X-ray diffractograms of (a) pristine $\text{LaCr}_{0.85}\text{Cu}_{0.10}\text{Ni}_{0.05}\text{O}_{3-\delta}$ (LCCN) powder, (b) LCCN powder sintered at 1300 °C for 2h, and (c) LCCN sintered at 1300 °C and exposed to reducing conditions (5% $\text{H}_2\text{-N}_2$) for 24 h.

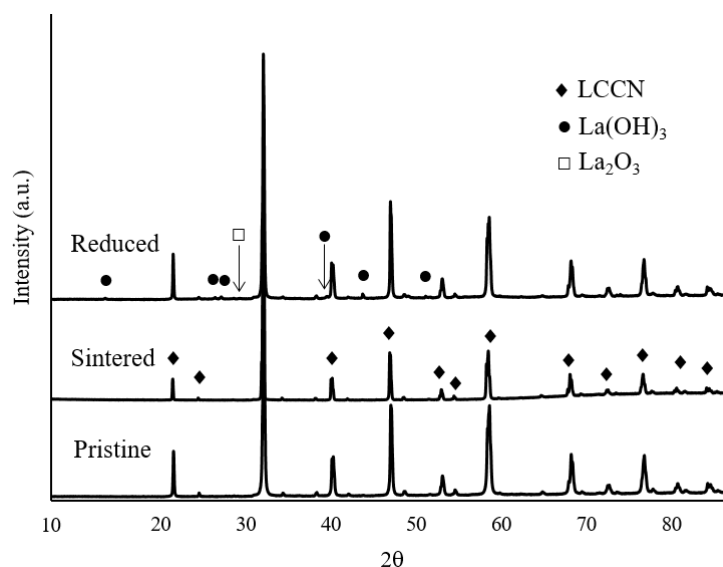
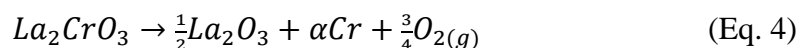


Fig. 4. XRD analysis of LCCN as a) untreated raw powder, b) sintered LCCN pellet in air at 1300 °C/2 h and c) sintered LCCN pellet exposed to reducing conditions 5% H_2N_2 at 900 °C for 24 hours.

As shown in Fig. 4, after sintering in air, the LCCN perovskite structure is kept. No secondary phases were identified; however, after exposing it to reducing conditions at 900 °C, peaks corresponding to La_2O_3 (not shown in figure due to scale) and $\text{La}(\text{OH})_3$ were found. Povoden et al. [34] have studied the system La-Cr-O in different atmospheres and determined that lanthanum chromite decomposes at low $p\text{O}_2$ and high temperatures. At a temperature of 900 °C and an oxygen partial pressures of $\sim 10^{-21}$ atm, the lanthanum chromite would decompose according to the reaction:



The formation of $\text{La}(\text{OH})_3$ could be the result of a hydration of the La_2O_3 when it is exposed to humidity, according to the reaction [35]:



In this process, a volume expansion between 40% to 60% occurs, which could lead to severe mechanical stresses in the composite. Fleming et al. [35] have observed the formation of $\text{La}(\text{OH})_3$ already at a temperature of 700 °C. However, Nagao et al. [36] reported the formation of hydroxides in rare-earth oxides even at temperatures as low as room temperature when exposed to an atmosphere with high humidity. High-temperature XRD analysis in controlled atmosphere of the ScYSZ-LCCN composite would allow determining if $\text{La}(\text{OH})_3$ was formed during the reduction tests performed on the composite.

Volume expansion during the formation of $\text{La}(\text{OH})_3$ could cause an excessive stress in the active membrane during its fabrication, which would affect its integrity. Studies performed with ScYSZ-LCCN 70:30-containing membranes [23,24] revealed the formation of the $\text{La}(\text{OH})_3$ and its consequences. It was found that vaporization of Cr^{6+} was linked to the La_2O_3 and subsequent $\text{La}(\text{OH})_3$ formation on the surface layers of the membrane. This led to longitudinal cracks that sometimes propagate transversally across the membrane causing a leak and affecting the functionality of the AM.

4.1.2 Sintering of $\text{LaCr}_{0.85}\text{Cu}_{0.10}\text{Ni}_{0.05}\text{O}_{3-\delta}$, $(\text{Sc}_2\text{O}_3)_{0.10}(\text{Y}_2\text{O}_3)_{0.01}(\text{ZrO}_2)_{0.89}$ composites.

Fig. 5a displays the sintering curves of the single phases $(\text{Sc}_2\text{O}_3)_{0.10}(\text{Y}_2\text{O}_3)_{0.01}(\text{ZrO}_2)_{0.89}$ (ScYSZ), $\text{LaCr}_{0.85}\text{Cu}_{0.10}\text{Ni}_{0.05}\text{O}_{3-\delta}$ (LCCN) and the composite $(\text{Sc}_2\text{O}_3)_{0.10}(\text{Y}_2\text{O}_3)_{0.01}(\text{ZrO}_2)_{0.89}$ - $\text{LaCr}_{0.85}\text{Cu}_{0.10}\text{Ni}_{0.05}\text{O}_{3-\delta}$ (ScYSZ-LCCN) with volumetric ratio 70:30 (SL7030) from room temperature to 1250 °C. The measurements show that the dual-phase composite has a slightly lower sintering onset temperature than any of the single phases that constitute it (SL7030 has a sintering onset at 977.3 °C, while ScYSZ and LCCN have onsets of 986.6 °C and 993.4 °C, respectively). Neither LCCN nor SL7030 reaches full densification in the studied temperature range. It is observed that the ScYSZ has a shrinkage of ~18 %, while the LCCN and the ScYSZ-LCCN composite show a shrinkage of ~8 %. LCCN has a multi-step sintering process and, despite being the minority phase with 30 vol%, it considerably influences the sintering rate and densification of the composite.

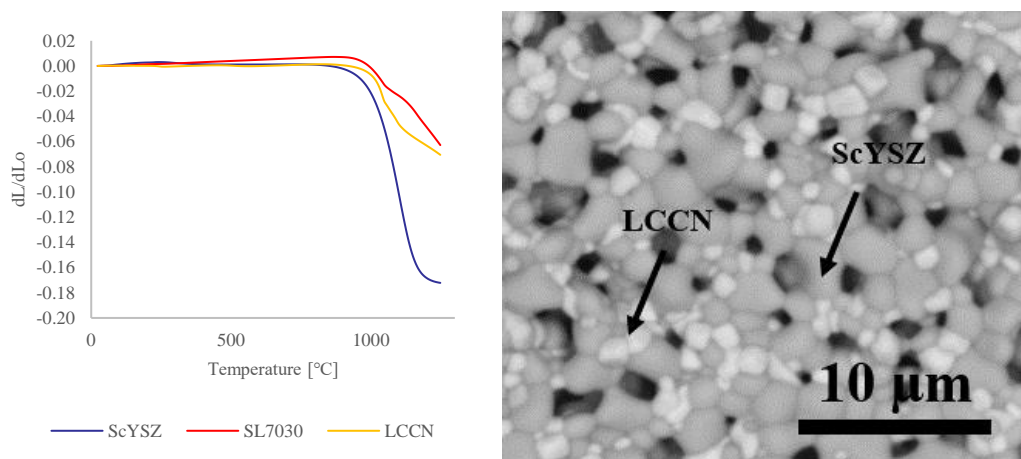
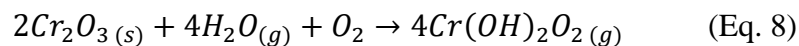
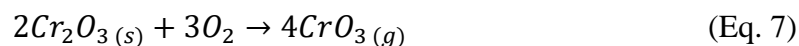


Fig. 5. Sintering curves of a) ScYSZ-LCCN 7030 components using a sintering rate of 1 °C·min⁻¹, and b) a SEM micrograph of the composite surface after sintering at 1300 °C in air.

Pellets of SL7030 composite showed a total porosity of 26% after being sintered at 1300 °C for 2 hours, as observed in Fig. 5b. Lanthanum chromite is known to be poorly sinterable in air due to the high vapour pressure of Cr⁶⁺ containing species. [25] Molin et al. [37] studied the sintering behaviour of 8YSZ in presence of Cr₂O₃. They found that Cr₂O₃ hindered the sintering of 8YSZ. After sintering 8YSZ with 6 mol% Cr₂O₃ at 1400 °C, they observed 19 vol% porosity. The hindering effect might be related to the high melting point of the Cr₂O₃, 2435 °C and vaporization of Cr⁶⁺. Additionally, Cr₂O₃ will decrease the ionic conductivity of 8YSZ during operation of the membrane due to grain boundary blocking. Decomposition of chromites in oxidizing conditions (Eq. 6 and Eq.7) occurs above 900 °C, and highly emphasized above ~1250 °C [25,34,38]. If water vapour is present during the sintering process, decomposition rate increases significantly due to formation of hydroxide species (Eq. 8). [7,12]



The decomposition of LaCrO₃ leads to the vaporization of Cr⁶⁺ species. An excess of La₂O₃ will remain in the perovskite's structure, which could lead to side reactions. In order to diminish the vaporization of Cr, it is essential to lower the sintering temperature of the system without compromising neither the densification of AM nor its mechanical integrity.

The effect of LCCN on the composite's sintering behaviour can be observed in Fig. 6a, where the sintering curves of dual-phase composites with 60, 70 and 80 vol.% LCCN are shown. By increasing the electronic-conducting phase in the composite, the sintering onsets are slightly modified. Onsets sintering temperatures were obtained at 963.1 °C, 977.3 °C and 946.9 °C for SL6040, SL7030 and SL8020, respectively. The multi-step sintering behaviour created by the LCCN, which was described in Fig. 5a, is smoother with the increase of the ScYSZ phase. However, the sintering rates do not change and low shrinkage and low densification of the composites is obtained.

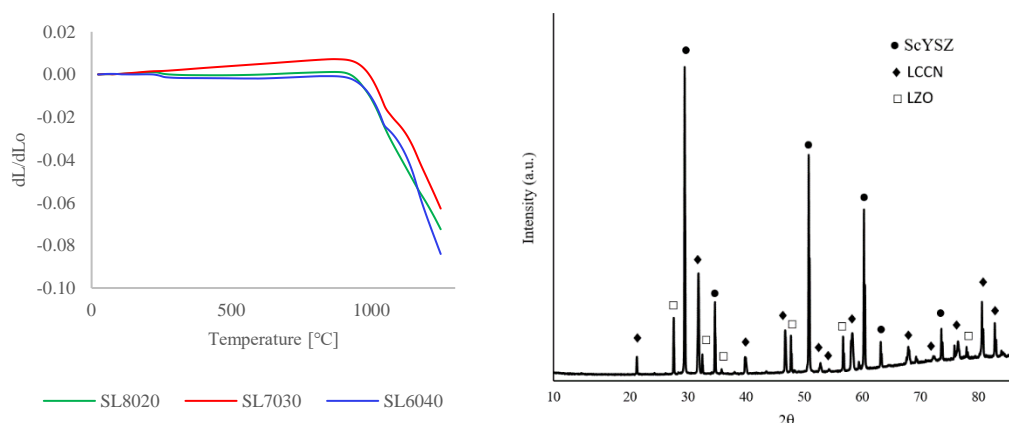


Fig. 6. a) Sintering curves of the ScYSZ-LCCN composites with 60, 70 and 80 vol% LCCN using a heating rate of 1 °C·min⁻¹. b) XRD analysis of ScYSZ-LCCN 7030 composite sintered in air at 1300 °C showing the ScYSZ, LCCN and LZO phases.

Fig. 6b shows the X-ray diffractograms of ScYSZ-LCCN 7030 (SL7030) composite sintered at 1300 °C in air. Beneath the two composite materials, ScYSZ and LCCN, La₂OZr₂O₇ (LZO) was identified as secondary phase. Different studies have analysed the interaction between LaCrO₃-based perovskites and (Y₂O₃)_{0.08}(ZrO₂)_{0.92} (8YSZ). It has been reported that both components are compatible and no reactions are expected in both, oxidizing and reducing conditions. [15,39] At 1200 °C in air, LaCrO₃ and 8YSZ do not react. However, Sr or Ca-doped LaCrO₃ might form insulating zirconate phases, such as SrZrO₃ or CaZrO₃ at 1100 °C. [39,40] LZO pyrochlore structure is not expected to be formed, unless La₂O₃ is available to react according to Eq. 9. [39]:



LZO is formed from the reaction between ZrO₂ and La₂O₃ starting at 1100 °C in air. [41] Above 1500 °C, LZO phase is fully formed. [41,42] As previously described, above 900 °C in oxidizing atmospheres, vaporization of Cr⁶⁺ from the chromite structure occurs,

increasing its rate formation after 1250 °C and precipitating La₂O₃ in this process. It is likely that during the sintering process of the OTM at 1250 °C, ScYSZ and La₂O₃ precipitates from LCCN react and form LZO. Additional analysis would be necessary to determine the moment of formation of the insulating phase.

Avoiding the formation of LZO in electrochemical devices, like solid oxide cells or oxygen transport membranes, is advisable due to its insulating properties. In order to diminish the LZO formation, changing the stoichiometric composition of the lanthanum-based perovskite to A-site deficient has been proposed. [42] However, reducing the sintering temperature to avoid the formation of LZO is typically the preferred route. [43]

4.2 Effect of Fe₂O₃ on supports and dual-phase composites.

As mentioned above, one of the main cornerstones to produce free-defect membranes using the system (Sc₂O₃)_{0.10}(Y₂O₃)_{0.01}(ZrO₂)_{0.89} – LaCr_{0.85}Cu_{0.10}Ni_{0.05}O_{3-δ} (ScYSZ-LCCN) is related to the sintering temperature. It has been described that temperatures in the region of 1450 °C are needed to reach full densification of the ScYSZ-LCCN membranes. [23,24] In this process, Cr vaporization occurs, which leads to the formation of La(OH)₃ and La₂Zr₂O₇ (LZO and crack development. In addition, possible thermal expansion coefficient mismatch might be also related to transversal cracks. By lowering the sintering temperature, it might be possible to minimise the Cr loss and in this way, keeping the functionality of the membrane and avoiding damages caused by side-reactions of La.

The use of sintering aids for the dense active membrane may enhance its densification at lower temperatures than 1450 °C, which could also reduce the Cr vaporization and the formation of La-based secondary phases. If sintering aid is used in the porous support, it might increase the shrinkage of the supports and aid with the densification of the membrane due to 2-dimensional compression caused by the tubular geometry.

Thus, the use of sintering aids for the (Y₂O₃)_{0.03}(ZrO₂)_{0.97} (3YSZ) porous supports and the (Sc₂O₃)_{0.10}(Y₂O₃)_{0.01}(ZrO₂)_{0.89} (ScYSZ) from the dual-phase composite of the active membranes has been considered for this study.

Studies regarding 8YSZ have demonstrated that Bi and Fe are able to lower the sintering temperature considerably when added in small quantities (< 1 mol%) to the

(Y_2O_3)_{0.08}(ZrO_2)_{0.92} (8YSZ). The decrease in the sintering onset is approximately 100 °C when 8YSZ is doped with 3 mol% of Fe. The dopant has no considerable effect in the sintering rate of the 8YSZ. [44,45] The increased Zr^{4+} diffusion coefficient is mainly responsible for the rapid densification rate of the Fe_2O_3 doped 8YSZ, which is caused by the Fe^{3+} ions interstitial diffusion mechanism due to the co-existence of substitutional and interstitial Fe^{3+} ions. [45]

Other thermomechanical properties, such as thermal expansion coefficient (TEC), may be modified when using sintering aids. This parameter acquires significant importance when a multilayer system is used. The different sintering behaviours of the components cause transient stresses that might hinder or facilitate the densification in each layer, creating processing defects, such as cracks or delamination. [46] Thus, decreasing the mismatch of the thermomechanical properties of the membrane's components, e.g. TECs, sintering onsets and sintering rates, could decrease both, the temporary stress during sintering and the sintering temperature of the system.

4.2.1 *Fe_2O_3 as modifier of the thermomechanical properties of the studied materials.*

Dilatometry analysis of the membrane's components was done in order to assess the effect of Fe_2O_3 in their thermo-mechanical properties. Table. 3 displays the TEC of single, 1 mol% and 3 mol% Fe_2O_3 -doped ScYSZ-LCCN composites, including single ScYSZ and LCCN measured in air. Data is shown at four different temperature intervals to ease the analysis of the materials. TEC values of single components, 3YSZ, ScYSZ and LCCN are in accordance with literature. [47-49] Experimental sintering temperature onsets are also shown.

As observed, Fe_2O_3 affects both PS and dual-phase composites. TEC values of 3YSZ decrease with increasing the Fe content at temperatures below 650 °C. A difference of $2 \times 10^{-6} \text{ K}^{-1}$ was registered in the interval 50-650 °C between pure 3YSZ and 3YSZFe3 (3 mol% Fe_2O_3). However, the effect is inverted at higher temperatures and TEC of 3YSZFe3 is $0.71 \times 10^{-6} \text{ K}^{-1}$ higher than the one of 3YSZ in the range 1050-1250 °C.

On the other hand, dual-phase composites show a slight decrease of TEC values when increasing the Fe content along all the studied temperatures. TEC values difference

increases with increasing temperature. Thus, differences of 0.26 and $0.57 \times 10^{-6} \text{ K}^{-1}$ were observed in the interval 50-650 °C and 1050-1250 °C respectively between SL7030 and SL7030Fe3. Similar effects were observed in other composites where Fe slightly affected the TEC values.

Table 3. Thermal expansion coefficients and sintering onsets of Fe-doped membrane's components

Material	50-650 °C	650-850 °C	850-1050 °C	1050-1250 °C	Onset [°C]
ScYSZ	10.1	12.1	13.1	13.8	986.6
LCCN	9.5	10.8	11.7	12.2	993.4
3YSZ	10.4	10.7	11.6	12.9	1103.1
3YSZFe1	9.7	10.5	12.3	13.0	1036.3
3YSZFe3	8.4	11.1	11.9	13.6	1025.1
SL7030	9.4	11.4	12.9	13.7	977.3
SL7030Fe1	9.4	11.2	12.6	13.5	996.7
SL7030Fe3	9.1	11.1	12.4	13.1	1035.2
SL6040	8.9	11.0	12.6	13.2	963.1
SL6040Fe3	8.5	11.2	12.5	13.4	---
SL8020	9.5	11.6	12.9	13.5	946.9
SL9010	9.0	11.7	12.7	13.2	---
SL9010Fe3	8.6	11.1	12.5	13.1	1036.2

Fig. 7a illustrates the sintering curves of Fe-doped 3YSZ pellets. A decrease of 67 °C in the onset temperature was observed by adding 1 mol% Fe_2O_3 (3YSZFe1). The sintering effectiveness of the Fe_2O_3 decreases considerable between 3YSZFe1 and 3YSZFe3 since only a decrease of 10 °C was registered. In the case of 3YSZ-based PS materials, the decrease in the sintering onset by increasing the Fe_2O_3 is in accordance with other authors. [44,45] Sintering rates are not affected by the addition of Fe_2O_3 and remain similar in the three analysed samples.

Fig. 7b shows the effect of Fe_2O_3 doping on the sintering behaviour of SL7030. Surprisingly, onset temperatures increased with the addition of dopant. Sintering onsets of SL7030Fe1 and SL7030Fe3 are only 1 °C and 10 °C mismatched with 3YSZFe1 PS material. A difference of 40 °C and 28 °C were respectively obtained when using 3YSZFe3.

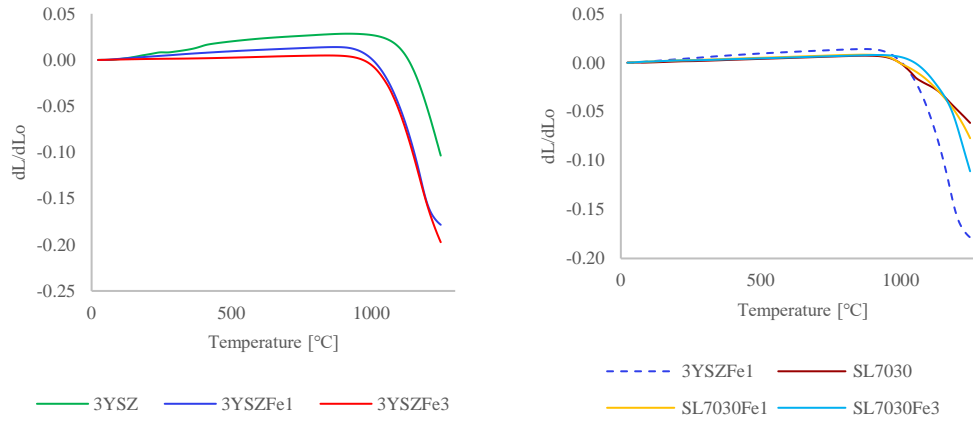


Fig. 7. a) Sintering curves of porous support materials. 3YSZ, 3YSZFe1 (1 mol% Fe₂O₃) and 3YSZFe3 (3 mol% doped Fe₂O₃), b) Sintering curves of Fe-doped 3YSZ and Fe-doped active membrane composite materials.

In addition, it is observed that sintering rates increased in such a way that when adding 3 mol% Fe₂O₃ to the ScYSZ-LCCN composite (SL7030Fe3), the mismatch on the sintering rates between this composite and 3YSZ-Fe based materials is decreased. Having similar sintering rates would lower the stresses caused in the sintering process.

4.2.2 Tubular supports characterization.

Porous tubular 3YSZ-based PS were fabricated via thermoplastic extrusion adding 1 mol% and 3 mol% Fe₂O₃ as dopant. Sintering was done in air at 1250 °C for 4 h. The main results of the different characterization tests are displayed in Table 4.

Table 4. Main features of the Fe₂O₃-doped 3YSZ porous supports

Sample	3YSZ (0 mol % Fe ₂ O ₃)	3YSZFe1 (1 mol % Fe ₂ O ₃)	3YSZFe3 (3 mol % Fe ₂ O ₃)
Porosity [vol.%]	59.9	53.4	48.6
Pore size [µm]	1.29	1.37	1.38
Darcy coefficient [10 ⁻¹⁴ cm ⁻²]	2.2	2.1	2.2
Average flexural strength [MPa]	82.8	114.2	>138.0
Onset temperature [°C]	1110	1040	1037
Diameter shrinkage [%]	19.9	24.9	25.7

Fig. 8 shows cross section SEM micrographs of the sintered tubes. Long irregular microchannel pores are formed by graphite, while PMMA provides the larger spherical pores. The porosity given by the PMMA is observed in all the samples; nevertheless, graphite porosity, observed in the single 3YSZ (Fig. 8a), is partially collapsed in 3YSZ-Fe1 (Fig. 8b) and 3YSZ-Fe3 (Fig. 8c). 3YSZ total porosity decreases by 11.3 vol.% when

doped with 3 mol% Fe_2O_3 . It is worth pointing out that reduction of graphite pores in the 3YSZ- Fe_3 surface might create limitations in the permeability and diffusion of the gases towards the membrane.

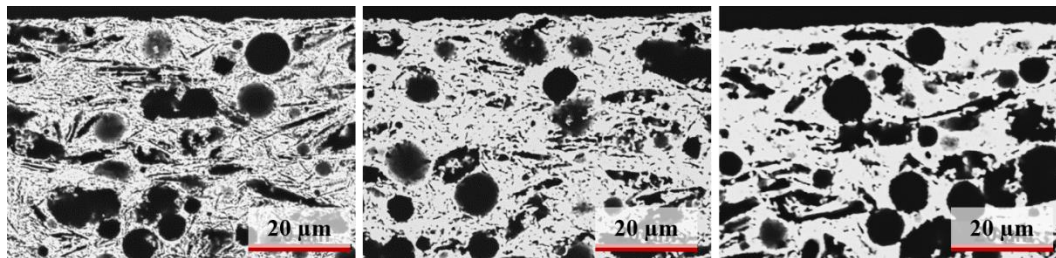


Fig. 8. Cross sectional SEM micrographs of Fe_2O_3 -doped 3YSZ tubular supports after sintering at 1250 °C. (a) Single phase 3YSZ, (b) 1 mol% doped Fe_2O_3 and (c) 3 mol% doped Fe_2O_3 .

Hg-intrusion and SEM analysis show that total porosity of 3YSZ (59.9 vol.%) is slightly lower than expected according to the method developed by Haugen, et al. (63.5 vol.%). [24] This observation could be the consequence of the extended sintering time at 1250 °C. In addition, in order to identify the effect that the addition of Fe_2O_3 could cause to the permeability of the PS, Darcy coefficients were calculated. The results reveal that Darcy's coefficients do not vary with the dopant content and remain in the range of $2.2 \times 10^{-14} \text{ m}^2$. This indicates that the permeability is not reduced despite increased sintering shrinkage (densification) and most likely relies on well connected, large enough pore channels, which were formed between the (larger) slit type pores from graphite and the spherical PMMA pores in the PS. It has been previously shown that the gas permeability in porous microstructure based on graphite/PMMA pore former systems depends on pore size distribution (mean pore size) pore connectivity and pore orientation. [50] Furthermore, for specific ranges of densification temperatures, densification can be achieved within these graphite/PMMA pore former systems without sacrificing gas permeability. [27] The three supports fulfil the requirement of Darcy coefficients $> 1 \times 10^{-14} \text{ m}^2$, thus limitations by insufficient gas permeability through the support are not expected [30]

Flexural strength tests using four points bending method demonstrated a relationship between the dopant content and the strength of the tube. By using 1 mol% Fe_2O_3 , the flexural strength of the 3YSZ PS increases by 38%. In the case of 3YSZ- Fe_3 , a flexural strength of $> 138 \text{ MPa}$ was calculated. The maximum testing load of the used rig (10 N) was held by the sample without breaking. The estimation of the flexural strength was based on the maximum load and the geometry of the sample.

Increase of mechanical properties of the PS is related to higher sinterability and densification of the Fe₂O₃-doped PS. Fig. 8 presents the sintering curves of 3YSZ and Fe-doped 3YSZ pellets. A decrease of 67 °C of the onset temperature was observed by adding 1 mol% Fe₂O₃ (3YSZ-Fe1). The sintering effectiveness of the Fe₂O₃ decreases considerably between 3YSZ-Fe1 and 3YSZ-Fe3 since only a decrease of 10 °C was registered. This effect is in accordance with previous publications regarding interaction between Fe₂O₃ and ZrO₂-based materials. [44] Sintering rates are not affected by the addition of Fe₂O₃ and remain similar for the three analysed samples.

4.2.3 *Effect of Fe₂O₃ in the ionic conductivity.*

The addition of a new phase to increase the sinterability and shrinkage of the membrane materials might create disruptions in other important properties, such as the ionic conductivity of the ScYSZ. Several studies [37,51-56] investigated the effect of Fe₂O₃ on the conductivity of the YSZ and other ZrO₂-based oxides. Simulations carried out by Chen et al. showed that oxygen ion conductivity could increase from 0.08 S·cm⁻¹ to 0.3028 S·cm⁻¹ at 700 °C when 3 mol% Fe₂O₃ was added to the 8YSZ. [53] Bohnke et al. experimentally determined that scandia stabilized zirconia's bulk conductivity is not affected by the addition of Fe₂O₃, keeping values close to 3x10⁻³ S·cm⁻¹ in air at 750 °C. [51] Van Hassel et al. [57] measured the ionic conductivity of an Fe-doped single crystal of (ZrO₂)_{0.83}(Y₂O₃)_{0.17} as function of pO₂ (H₂ and N₂ atmospheres) and temperature (500 °C – 900 °C). At 500 °C, the ionic conductivity was found to be one order of magnitude lower than the one of the single crystal. This has been explained by the possible incorporation Fe³⁺ on a Zr⁴⁺ lattice position in the YSZ lattice. Nevertheless, above 700 °C the ionic conductivities converge despite the used atmosphere. To the best of the authors' knowledge, no studies of conductivity of Fe-doped ScYSZ in reducing conditions have been done. However, it is expected that ScYSZ follows a similar behaviour than YSZ crystal structures. Thus, ionic conductivity of the ScYSZ is not expected to be affected by the addition of Fe₂O₃ when working above 700 °C.

4.2.4 *Brief summary of Fe₂O₃ as sintering aid.*

From the described above, the use of Fe₂O₃ as sintering aid for the porous support and the functional layers is a feasible option to decrease the sintering temperature of the

ScYSZ-LCCN system and, in this way, to minimise the Cr evaporation and to keep the mechanical and functional integrity of the membrane. Other authors have investigated the Fe₂O₃ as sintering aid in 8YSZ, lowering the sintering temperature up to ~100 °C when added in small quantities (< 1 mol%). [44,45] The use of Fe₂O₃ would also allow tailoring the thermal expansion coefficient and sintering onset temperature of the porous support (PS) and the active membrane (AM), which, by an adequate selection of the materials, would reduce the stresses during fabrication of the membranes. E.g. by using the 3 mol% Fe₂O₃ in the 3YSZ porous support and the ScYSZ-LCCN membrane, a sintering onsets mismatch can be decrease from 125.8 °C to 10 °C (Table 3).

By adding Fe₂O₃ in the 3YSZ porous supports, the flexural strength is increased from 82.8 MPa up to >138 MPa, and although porosity was reduced by ~10 %, the permeability of the supports was not affected, keeping values in the region of $2 \times 10^{-14} \text{ cm}^2$ (Table 4). Besides, the additional shrinkage of the 3YSZ support, could promote the densification of the membrane. According to literature, effects the ionic/electronic conductivity of the ScYSZ-LCCN membrane are not expected by the addition of Fe₂O₃.

In order to increase the possibilities to obtain a free-defect membrane, it is crucial to adequately select the porous support and membrane materials. The selection of materials based on the results shown in Table 3 is discussed in Section (4.3).

4.3 Analysis of porous supports – active membrane materials combinations.

With the purpose of minimise the transient stresses between the dense active membrane (AM) and porous support (PS) during the sintering and operation of the membrane, it is necessary to decrease the thermal expansion coefficient (TEC) and sintering onset mismatch of the components. This can be done by selecting materials with similar thermal properties or by tailoring them by means of sintering aids. Table 3 in Section 4.2.1 shows the TEC values of the different composites used in this study. Following, in Fig. 9, a graphic TEC analysis of ScYSZ-LCCN active membranes and 3YSZ-based porous supports is made. The figure shows a matrix of 3 porous support (PS) and 3 active membranes (AM). The analysed porous supports are: 3YSZ, 3YSZ+1 mol%Fe₂O₃ (3YSZFe1) and 3YSZ+3 mol%Fe₂O₃ (3YSZFe3). The analysed active membranes are:

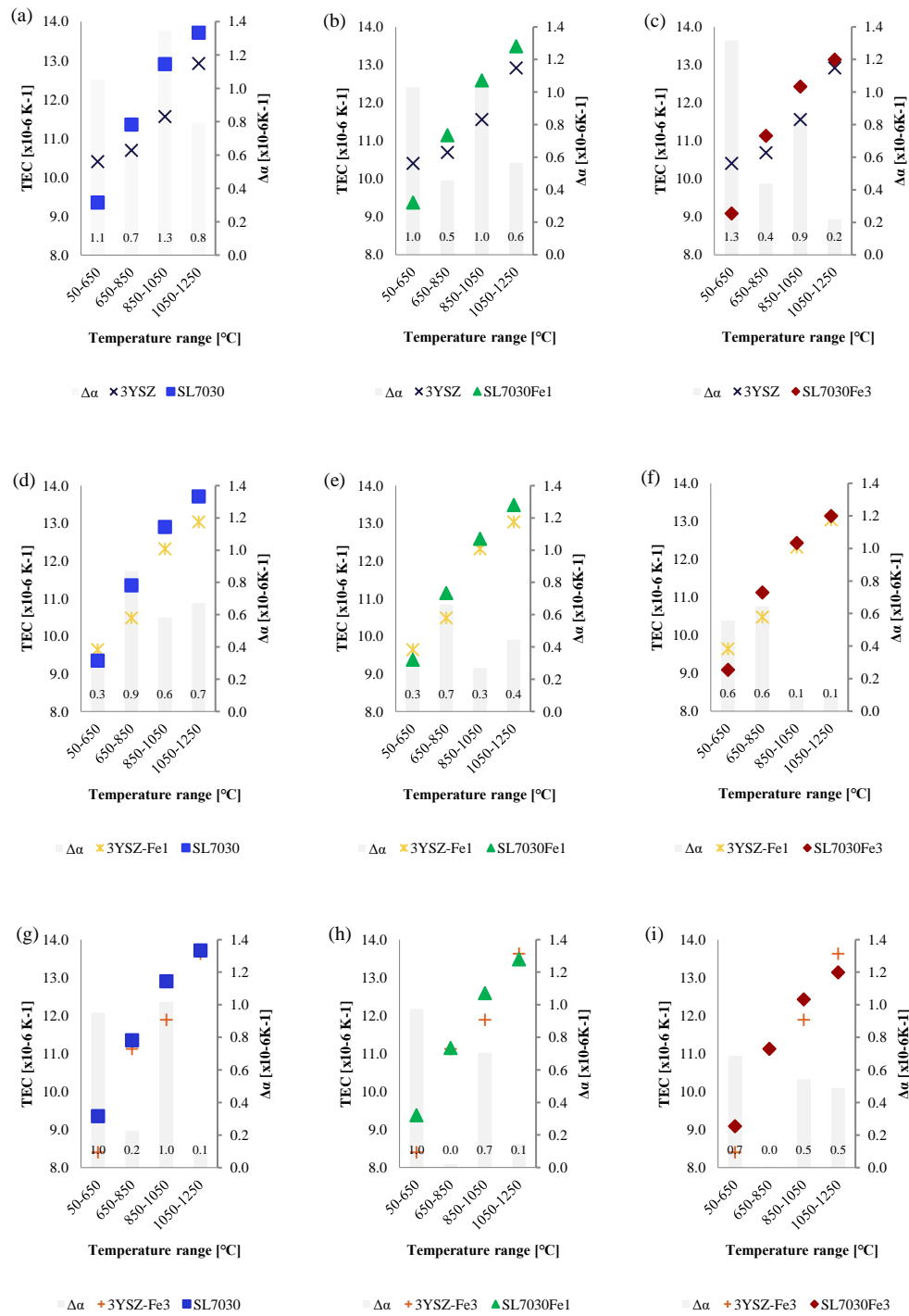


Fig. 9. TEC analyses of 3YSZ-based porous supports and ScYSZ-LCCN active membrane materials with different Fe₂O₃ concentrations as sintering aid.

ScYSZ-LCCN 70:30 (SL7030), ScYSZ-LCCN 70:30+1 mol%Fe₂O₃ (SL7030Fe1) and ScYSZ-LCCN 70:30+3 mol%Fe₂O₃ (SL7030Fe3).

As shown by Figure 9, the PS/AM combinations with lower TEC mismatches are 3YSZ/SL7030Fe3, 3YSZ-Fe1/SL7030Fe1, 3YSZFe1/SL7030Fe3. 3YSZFe3 supports are compatible with SL7030, SL7030Fe1 and SL7030Fe3 membranes. Similar analysis was made using Fe-doped SL6040 composites for the AM material. These composites have higher content of LCCN to ensure the percolation of the electronic-conductor phase within the membrane. Results showed that the combination 3YSZ-Fe3/SL6040Fe3 is a credible candidate for this study.

4.4 Fabrication of asymmetrical tubular oxygen membranes.

4.4.1 Initial approach for the co-sintering of all the membrane components..

As illustrated in Fig 1, the membrane architecture consist of four main components/layers: a dense active membrane (AM) between two porous layers – an inner porous activation layer (IL) and an outer porous activation layer (OL) – deposited on a porous support (PS). Deposition of the functional layers (IL, AM, and OL) on the PS was done by dip-coating. The powder slurries for the dense membranes and catalytic (activation) layers behaved as Newtonian fluids with approximated viscosities of 17 mPa·s and 23 mPa·s, respectively.

As initial approach, the IL, AM and OL were dip-coated on a calcined 3YSZFe3 PS and co-sintered in a single step at 1250 °C. The composite ScYSZ-LCCN 7030 (SL7030) was used in all the layers to minimise the possible thermo-mechanical stress in the membrane. The obtained membrane showed no cracks or structural damage; however, full densification of the AM was not reached. It is known that co-sintering of multilayer systems is a challenging process, because of the intrinsic sintering properties of each material and due to the different interactions among the materials to be sintered. [58,59]. Thus, it is necessary to assess the individual interaction/influence of the membrane's components, in order to analyse the different effects.

4.4.2 Active membrane – porous support interaction at different heating rates.

In order to analyse the interaction between the active membrane and the porous support, two different sets of samples consisting on ScYSZ-LCCN 70:30 (SL7030) and ScYSZ-

LCCN 60:40 (SL6040) membranes deposited on pre-sintered 3YSZFe₃ were prepared (SL7030/3YSZFe₃ and SL6040/3YSZFe₃). The samples were sintered in air at 1250 °C, according to Fig. 3c. Two different sintering rates between 600 °C and 1250 °C were used to analyse the possible effects caused by the different shrinkage of the materials. The first set of samples SL7030/3YSZFe₃ and SL6040/3YSZFe₃ was sintered with heating ramp of 60 °C·h⁻¹, while the second set was sintered with heating ramp of 200 °C·h⁻¹.

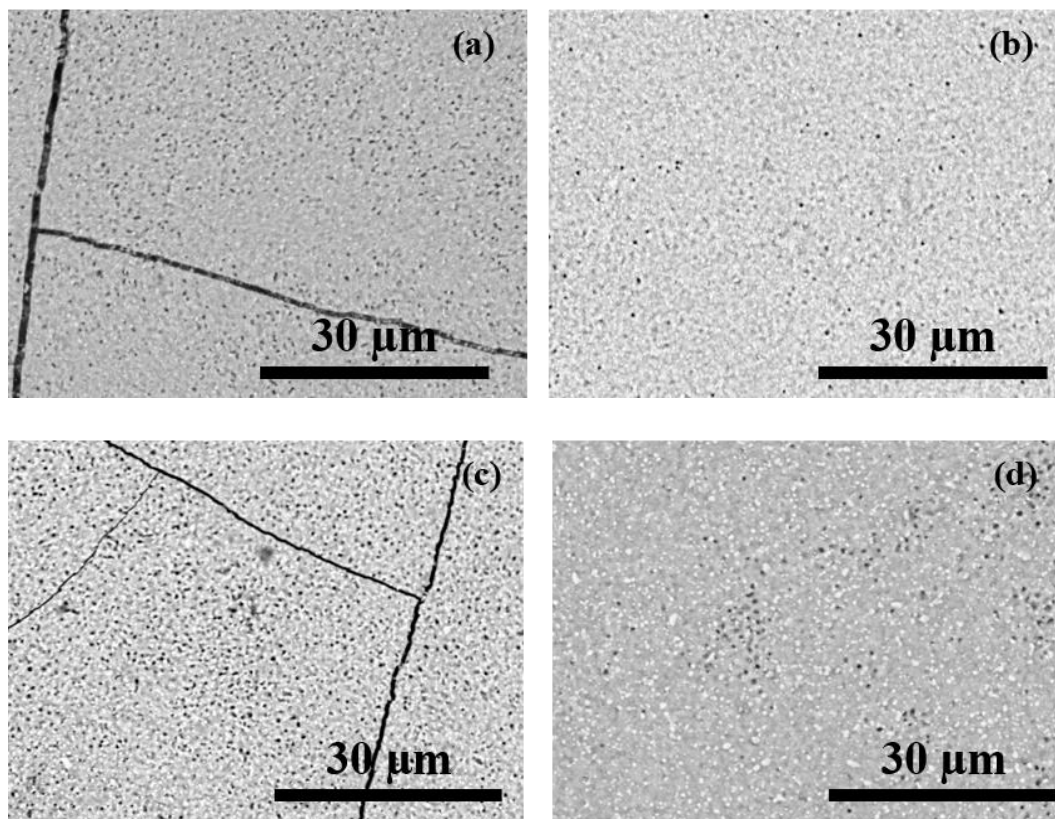


Fig. 10. Top-view of dual-phase membranes doped with 3 mol% Fe₂O₃ supported on 3YSZ+3 mol% Fe₂O₃ tubes using different heating rates and sintered at 1250 °C/4hours: a) ScYSZ-LCCN 70:30 at 60 °C·h⁻¹, b) ScYSZ-LCCN 70:30 at 200 °C·h⁻¹ c) ScYSZ-LCCN 60:40 at 60 °C·h⁻¹, b) ScYSZ-LCCN 60:40 at 200 °C·h⁻¹.

SEM analysis of the AM's surface (Fig. 10a and Fig. 10c) revealed extensive cracks on the set of samples sintered with ramp of 60 °C·h⁻¹; however, when using a heating rate of 200 °C·h⁻¹, free-crack membranes were obtained (Fig 10b and Fig.10d).

Taking the case of the sample SL7030Fe₃/3YSZFe₃ (AM/PS) and analysing Fig. 7b, it is noticed that total shrinkages of SL7030Fe₃ and 3YSZFe₃ after sintering at 1250 °C are ~11% and ~18%, respectively. Additionally, they shrink at different rates. In the range of temperature 950 °C–1150 °C, the 3YSZFe₃ support shrinks at higher rate than the SL7030Fe₃ membrane. If the heating rate is slow, the support has enough time to shrink

while the membrane shrinkage would be restricted by the already shrunk support. This could lead to transient stresses since the membrane would be subjected to tension if it has bonded to the support. In order to release the tension, the membrane would crack in some areas to locally sinter and densify. If the heating rate is increased, in this case to $200\text{ }^{\circ}\text{C}\cdot\text{h}^{-1}$, the 3YSZFe3 support has less time to shrink, allowing the membrane to shrink and densify.

Additionally, a higher densification of the membrane is obtained when the faster heating rate of $200\text{ }^{\circ}\text{C}\cdot\text{h}^{-1}$ is used. Since the membrane has no fractures, it would be subjected to the compression the 2-dimensional compression originated by the tubular geometry. [60-62] Densification of 98% and 95% was achieved in SL7030Fe3 and SL6040Fe3 membranes sintered at $200\text{ }^{\circ}\text{C}\cdot\text{h}^{-1}$, while, 92% and 89% densification was obtained for the same composites when using a heating ramp of $60\text{ }^{\circ}\text{C}\cdot\text{h}^{-1}$. It is also noticed that the densification of SL7030Fe3 is higher than the one of SL6040Fe3. This is in correlation with the previously described phenomenon, where LCCN has a sintering hindering effect when combined with ZrO₂-based materials.

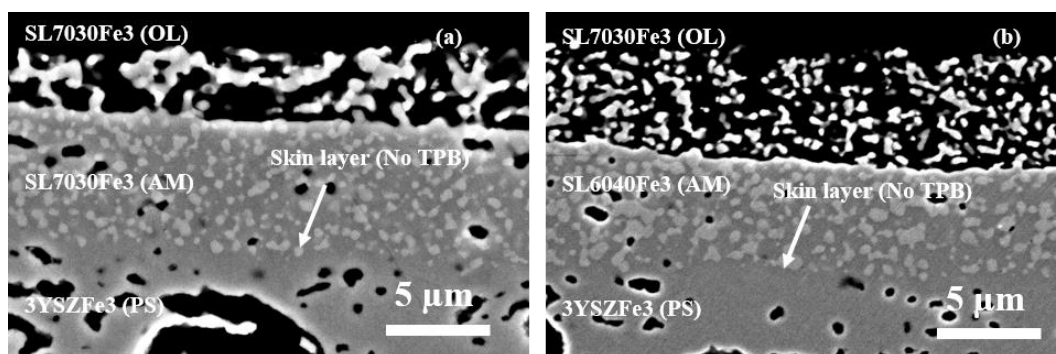


Fig. 11. SEM micrographs of membranes a) 3YSZFe3/SL7030Fe3 and 3YSZFe3/SL6040Fe3 after sintering at $1250\text{ }^{\circ}\text{C}$. Outer activation layer SL7030Fe3 is observed on the membrane.

Fig. 11 shows the cross section of 3YSZFe3/SL7030Fe3 (PS/AM). Uniform distribution of both ScYSZ and LCCN phases is observed in the AM, however, better percolation of LCCN (bright phase) is observed in the SL6040Fe3 membrane. No delamination or internal cracks were observed; however, a lack of TPB in the PS/AM interface was identified, since LCCN phase is embedded in the ScYSZ phase forming a dense ZrO₂-based layer between the AM and the PS. This effect would block active sites to carry out the oxygen exchange reactions, since electronic conductivity is required.

4.4.3 Effect of the inner activation layer.

In order to i) increase the quantity of triple phase boundaries (TPB) and ii) improve the gas diffusion from the gas stream to the TPBs, the use of an effective intermediate porous layer between the porous support (PS) and the active membrane (AM) is needed. The use of ScYSZ as activation layer in between the 3YSZ (PS) and ScYSZ-LCCN 7030 (SL7030) (AM) has been analysed in previous studies [24] and it could be an alternative to increase the TPB. A multilayer system using ScYSZ (IL) and ScYSZ-LCCN 6040+3 mol% Fe₂O₃ (SL6040Fe3) (AM) was fabricated using a pre-sintered 3YSZ+3 mol% Fe₂O₃ (3YSZFe3) (PS).

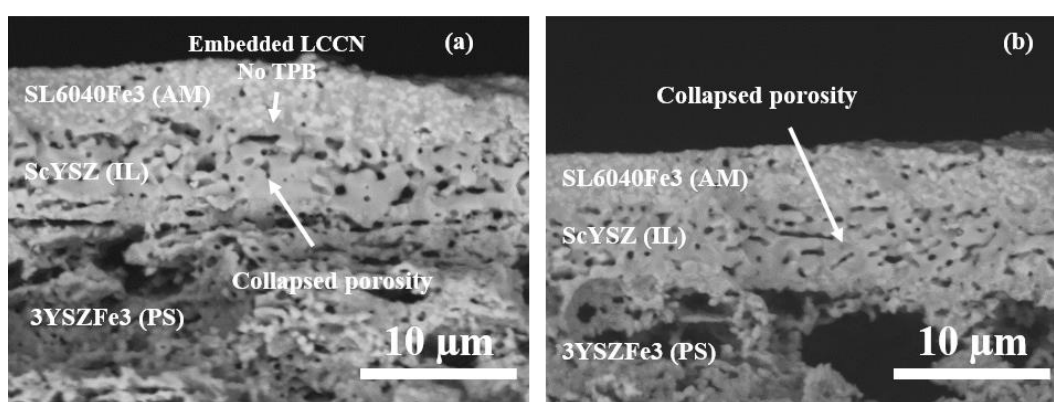


Fig. 12. SEM cross section micrographs of 3YSZFe3 (PS)/ScYSZ (IL)/SL6040Fe3 (AM) a) IL original formula, b) IL with double pore former quantity.

The membrane was gas-tight and no cracks were observed; however, the SEM-analysis indicated the collapsing of the ScYSZ (IL) and its partial densification (Fig. 12a). Pore formers of the ScYSZ slurry were duplicated as an attempt to increase the porosity of the layer; however, after sintering, negligible porosity increase was observed in the IL (Fig. 12b). In addition, LCCN was found embedded in the ScYSZ phase of the AM.

As mentioned, LCCN act as a densification hindering when added to ScYSZ. It was also pointed out that co-sintering with ScYSZ-LCCN porous layers led to porous AMs. Thus, the possibility of using LCCN as a non-pyrolisable pore former in the activation layers was investigated. Dual-phase composites SL9010Fe3, SL8020Fe3 and SL7030Fe3 were used as activation layer materials.

SEM-analysis of SL6040Fe3 membranes (AM) using SL9010Fe3, SL8020Fe3 and SL7030Fe3 inner activation layers (IL) deposited on pre-calcined 3YSZFe3 supports are shown in Fig. 13. It is noticed that the LCCN content of the IL affects the densification

of the SL6040Fe3 AM. Membrane densifications of 95%, 90% and 70% were obtained for SL9010Fe3, SL8020Fe3 and SL7030Fe3, respectively. The use of SL9010Fe3 allows forming active sites at the interface IL – AM but it also affects the densification of the membrane. Using composites for the IL with LCCN-content higher than 80 vol.% would lead to a not fully dense AM, as observed in Fig. 13c.

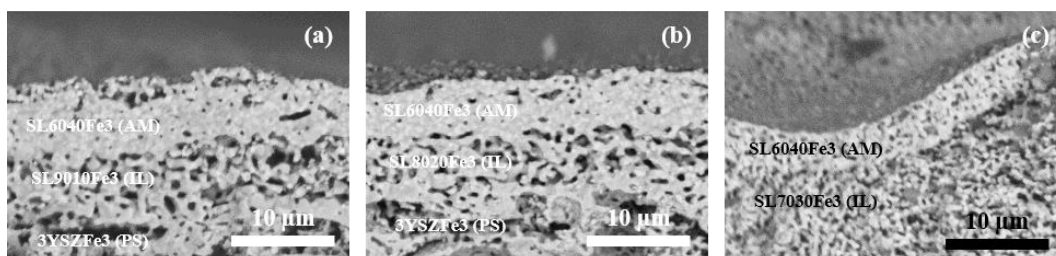


Fig. 13. SEM cross section images of membranes containing different amount of LCCN in the inner activation layer. : a) SL9010Fe3, b) SL8020Fe3 and c) SL7030Fe3. Porous support: 3YSZFe3 supports, active membrane: SL6040Fe3

If no sintering aid is used in the IL, temperatures as high as 1100 °C would be required to bond the layer to the PS, which would diminish the sinterability potential of the AM due to shrinkage of the PS. In co-sintering with the AM, the ScYSZ-LCCN 60:40 + 3 mol% Fe₂O₃ membrane did not reach densification.

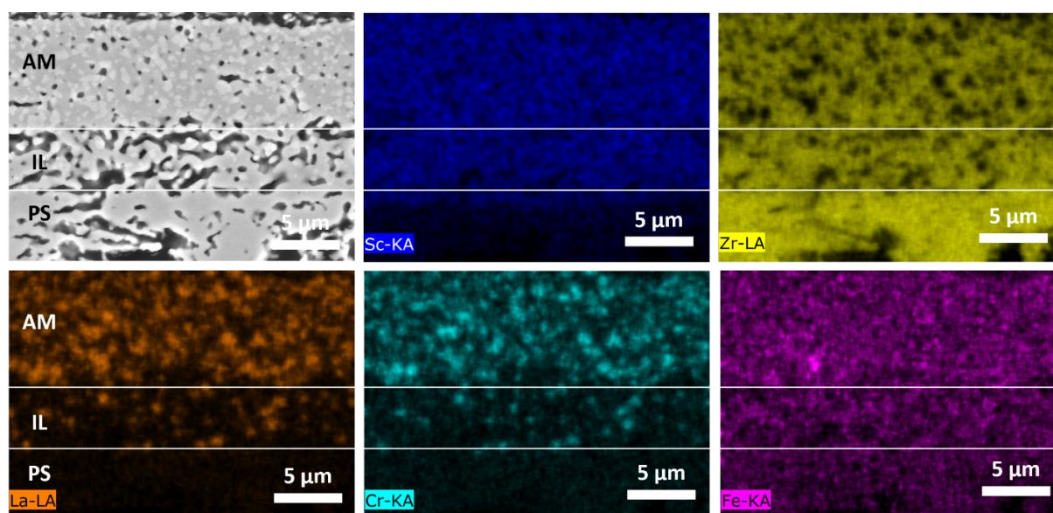


Fig. 14. EDS-map of the active membrane (AM), the inner activation layer (IL) and the porous support (PS).

Despite the formation of TPBs at the interface to the AM, the IL presents irregular porosity. Close to the PS the formation of a 3-4 µm semi-dense layer in the PS interface was observed, herein referred to as “skin layer”. This could be the result the deposition method. Since dip-coating is being made in a pre-calcined porous substrate, it might be possible that the slurry intrudes into the pores of the PS’s surface, causing the formation of dense structures after sintering.

Fig. 14 shows the EDS mapping of the AM and IL – PS interface. A reference line shows the limit of the PS, which is recognizable in the Zr map. It can be noticed that Sc diffuses into the 3YSZ PS by approximately 2 μm . Traces of Sc were observed at 5 μm deep in the PS. This diffusion can be related to the intrusion of the IL composite during dip-coating deposition of the layer on the PS.

The distribution of La and Cr of the LCCN-phase in the AM was also analysed. The EDS map shows that both elements are in contact with the IL, forming TPBs. No LZO was identified and Fe is distributed along all the three layers of the OTM.

In order to avoid the formation of dense structures on the surface of the PS, the activation layer was deposited on green 3YSZFe₃ PS. Simultaneous debinding of the PS and calcination of the IL was made using the thermal profile shown in Fig. 2a.

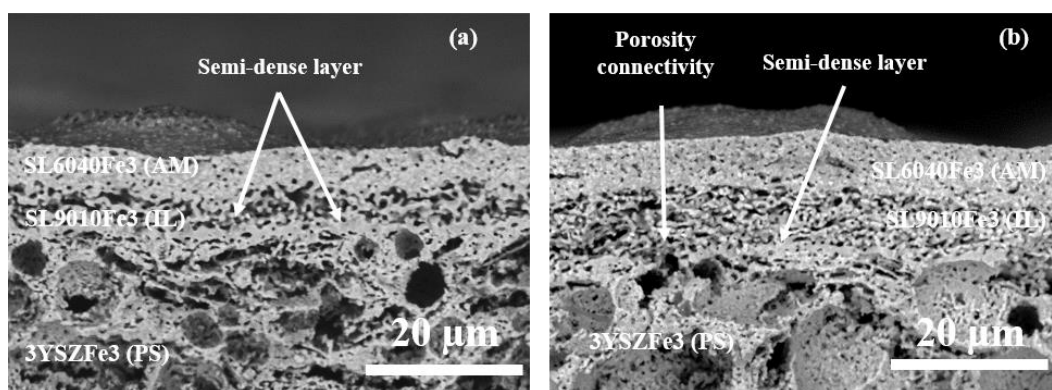


Fig. 15. Cross section micrographs of a) Skin layer formation in the activation layer-support interface when using a pre-sintered support. b) skin layer is diminished when using simultaneous debinding-calcination of the two components. System 3YSZFe₃ (PS)/SL9010Fe₃ (IL)//SL6040Fe₃ (PS).

Cross-sections SEM images of the fabricated membranes are shown in Fig. 15. It is observed that, despite the 3-4 μm partially dense layer is formed on the PS, it has no continuity and porosity of the PS is connected to porosity of the IL, which would lead to proper diffusion of the gases from the bulk to the TPBs. In green state, organics fill the porous system of the PS, avoiding that the dip-coating slurry invades the pores during the coating, minimizing the formation of the skin layer.

4.4.4 Effect of the porous support on dense active membrane.

In order to assess the influence of the porous support (PS) in the densification of the active membrane (AM), samples were fabricated using SL9010Fe₃ IL and SL6040Fe₃ AM on pre-sintered 3YSZ-based PS containing 0 mol%, 1 mol% and 3 mol Fe₂O₃.

After sintering in air at 1250 °C for 4h, a clear correlation between the densification of the AM and the shrinkage of the PS, given by the Fe₂O₃ doping, was found; the higher the Fe content in the PS, the higher densification of the AM (Fig. 16). 5% more shrinkage was obtained when 1 mol% Fe₂O₃ was added to the 3YSZ PS (Table 3), however, this increase in shrinkage did not allowed full densification of the AM. On the other hand, 1% difference shrinkage between 3YSZF3 and 3YSZFe1 was enough to allow full densification of the AM.

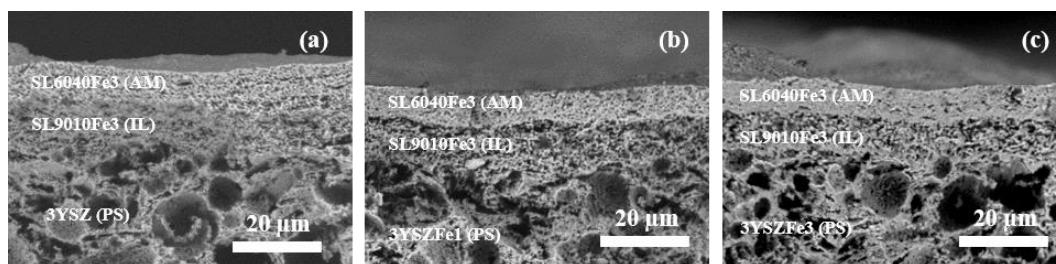


Fig. 16. Effect of the Fe-content on the 3YSZ porous support on the densification of SL6040Fe3 active membranes after sintering at 1250 °C: a) 3YSZ porous support, b) 3YSZFe1 and c) 3YSZFe3. SL9010Fe3 was used as inner activation layer.

Some proposed (PS/AM) combinations described in Section 4.3 considered the use of 3YSZ and 3YSZ+1 mol% Fe₂O₃ (3YSZFe1) PS. Nevertheless, the densification of the AM was not reached in any of the analysed options with these PS, no matter the Fe-content in the ScYSZ-LCCN membranes. In contrast, all the AM using 3YSZ+3 mol% Fe₂O₃ (3YSZFe3) PS showed >90% densification. This might indicate that densification of the AM might be strongly linked to the Fe₂O₃ in the PS and the change in the geometry of the PS during the sintering process.

4.4.5 Effect of Fe-content on the dense active membrane.

In order to analyse the effect of the Fe-content in the AM densification, tests using SL7030, SL7030Fe1 and SL7030Fe3 AM were deposited on 3YSZFe3 PS using SL9030Fe3 as IL. The results showed that all the membranes densified, regardless the quantity of Fe in the AM's formulation. However, SEM-EDS analysis showed that Fe diffused into the SL7030 membrane, which could act as sintering aid. Above 1050 °C Fe₂O₃ vaporizes. [63] Thus, it might be likely that during the sintering process at 1250 °C, Fe₂O₃ was vaporized from the 3YSZFe3 PS or the SL9030Fe3 IL and condensed in the AM. EDS composition of the SL7030, SL7030Fe1 and SL7030Fe3 AM when deposited on SL9010Fe3 IL and supported on 3YSZFe3 PS is shown in Table 5. Compositions are

normalized to Zr for the ScYSZ and to La in the case of the LCCN to ease the analysis. It is observed that Fe is found in any of the studied AM, including the SL7030 membrane, which was developed without Fe-doping. The quantities of Fe found in SL7030 were approximated to 3 mol% to Zr, which would be the expected composition of SL7030Fe3. In the case of SL7030Fe1 and SL7030Fe3, the quantities of Fe in the ion-conducting phase double the formulated expected quantity. It is important to point out that higher quantities of Fe were found in the electronic-conductor phase, which indicates Fe-doping of the perovskite structure.

Table 5. EDS elemental composition of the studied active membranes

Element	ScYSZ, Zr=0.89			LCCN, La=1			
	Sc	Y	Fe	Cr	Cu	Ni	Fe
Theoretical	0.20	0.02	-/0.01/0.03	0.85	0.10	0.05	-
SL7030	0.20	0.05	0.03	0.66	0.01	0.02	0.20
SL7030Fe1	0.19	0.04	0.06	0.60	0.02	0.02	0.28
SL7030Fe3	0.19	0.04	0.05	0.80	0.04	0.03	0.09

It is worth to point out that because of the average grain size of the LCCN (~330 nm) and the ScYSZ (~900 nm) in the AM, it is possible that the interaction volume of the electron beam of the SEM could get signals from both electron and ion-conducting phases. However, despite of this uncertainty, the diffusion of Fe from the PS or IL or both to the AM is confirmed.

As previously discussed, Fe may not interfere with the ionic-conduction of YSZ-based materials and instead, enhance the conductivity of the YSZ. Hartmanova et al. [64] studied the system 15YSZ doped with iron. They obtained that grain and bulk conductivity were enhanced when doping with Fe. Molin et al. [37] reported a slight decrease in the 8YSZ grain and grain boundary conductivity by increasing the Fe content up to 6 mol%. However, the total electrical conductivity increased from 0.15 to 0.3 S·cm⁻¹ at 850 °C in air. It was proposed that only 2 mol% Fe would segregate in the grain boundaries while the rest of the Fe would dissolve in the YSZ grains. The Fe solubility limits in ZrO₂-based materials has been studied by other authors [65,66], finding values of 2-3 mol% solubility at 1200 °C. Kuznezoff [65] has proposed that once the iron overpass the solubility limit, ionic conductivity would decrease. Yokokawa [66] studied the solubility of Fe in YSZ in different pO₂ atmospheres, finding that the maximum

solubility of Fe was 5.6 mol% between 2.5×10^{-14} and 10^{-15} . Nevertheless at $pO_2 < 10^{-18}$, solubility of Fe would decrease to zero since Fe reduces to metallic state. This might explain the low total conductivities of the YSZ-Fe system studied by Van Hassel et al. [57] by one order of magnitude when measured in H_2 ($pO_2 \sim 10^{-25}$) at temperatures below 700 °C. In that case, working at temperatures above 700 °C would be needed to overcome the low conductivity and increase the performance of the OTM.

4.4.6 *Effect of outer porous activation layer.*

As last step to obtain a full membrane, it is necessary to deposit an activation porous layer, which would allow the infiltration of catalyst materials to improve the oxygen-ion exchange reactions. Fabrication of full membranes using green 3YSZFe3 PS for the configuration 3YSZFe3/SL9010Fe3/SL7030Fe3 (PS/IL/AM) and ScYSZ-LCCN-based composites as OL was carried out. Co-sintering of the OL and the AM leads to densification inhibition of the membrane. Thus, the OL needs to be deposited on the sintered membranes. This could allow using high LCCN content composites for the OL; however, as previously analysed, larger quantities of LCCN decreases the sinterability of the composite and higher temperatures would be needed to bond it to the membrane. Different tests were carried out using SL7030Fe3, SL6040Fe3 and SL5050Fe3 OL. It was found that only SL7030Fe3 attached to the AM at 1200 °C. SL6040Fe3 and SL5050Fe3 calcined at 1250 °C formed an easily removable layer on the AM. To bond them to the substrate, temperatures higher than 1300 °C were necessary, which would lead to formation of LZO (see Section 4.1.2).

4.4.7 *Fabrication of full membranes: possible configurations and limitations.*

Based on the results presented in the previous sections, possible PS/AM combinations described in the TEC analysis (Section 4.3) are limited to those using only 3YSZ+3 mol% Fe_2O_3 (3YSZFe3) porous supports (PS) and inner activation layers (IL) based on ScYSZ-LCCN 90:10+3 mol% Fe_2O_3 . Feasible configurations considering the TEC matching are 3YSZFe3 (PS)/SL9010Fe3 (IL), SL7030(AM), SL7030Fe1 (AM) and SL6040Fe3 (AM) and SL7030Fe3 (OL). 30 cm long tubular membranes with the following configurations were fabricated:

- 1) 3YSZFe3/SL9010Fe3//SL7030//SL7030Fe3
- 2) 3YSZFe3/SL9010Fe3//SL7030Fe1//SL7030Fe3
- 3) 3YSZFe3/SL9010Fe3//SL6040Fe3//SL7030Fe3

The configuration using SL6040Fe3 (AM) was severely affected, since fractures occurred along all the membrane. Fractures were developed in the weakest points of the PS, matching the extrusion dice's spider, Although the thermomechanical properties of the SL7030Fe3 and SL6040Fe3 are relatively similar, the amount of LCCN affects drastically the mechanical integrity of the membrane.

Interestingly, a correlation between the total thickness of the dip-coated layers and the crack formation/fractures in the PS was found. A maximum thickness of 15 μm of all the layers allows mechanical integrity of the tube; however, this implies to use thin layers. It was observed that 6 μm thick membranes would allow gas-tightness of the membrane.

On the other hand, configurations using SL7030 (AM) and SL7030Fe3 (AM) show adequate densification of the membrane and no structural damage. Fig. 17 shows cross section SEM micrographs of full membranes using SL7030 and SL7030Fe1 as AM. The densification of the thin membranes was achieved in the same grade, no matter the Fe content in the AM. Membranes are gas tight and no delamination or cracks were observed, which makes the configurations using SL7030 (AM) or SL7030Fe1 (AM) feasible options for further study and characterization.

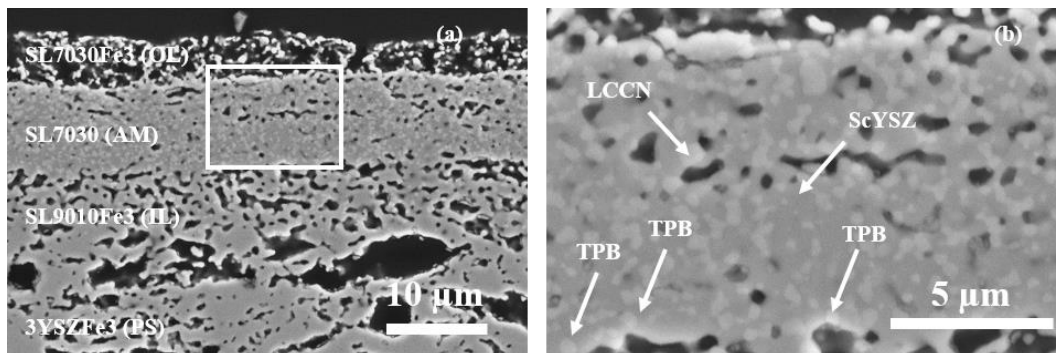


Fig. 17. SEM images of a) Full tubular OTM using 3YSZFe3 (PS), SL9010Fe3 (IL), SL7030 (AM) and SL7030Fe3 (OL); and b) zoom in of the SL7030Fe3 (AM)

4.5 Thermomechanical and chemical stability of the membranes.

Fig. 18 shows micrographs of a membrane with the configuration 3YSZFe3 (PS)/SL9010Fe3(IL)//SL7030Fe1(AM)//SL7030Fe3 (OL) which was subjected to

thermo-cycling in air, reducing conditions and re-oxidation in order to verify its mechanical and chemical integrity.

It was observed that membranes after each stage of the cyclic treatment withstood the conditions without crack formation, delamination or any other effects affecting its microstructure, which demonstrates the high mechanical stability of the PS, as well as strong interfaces among the IL, AM, OL and the PS. As observed in Fig. 18d, after reduction the color of the supports turn black due to possible reduction of the Fe^{4+} to Fe^{3+} and elemental Fe [67].

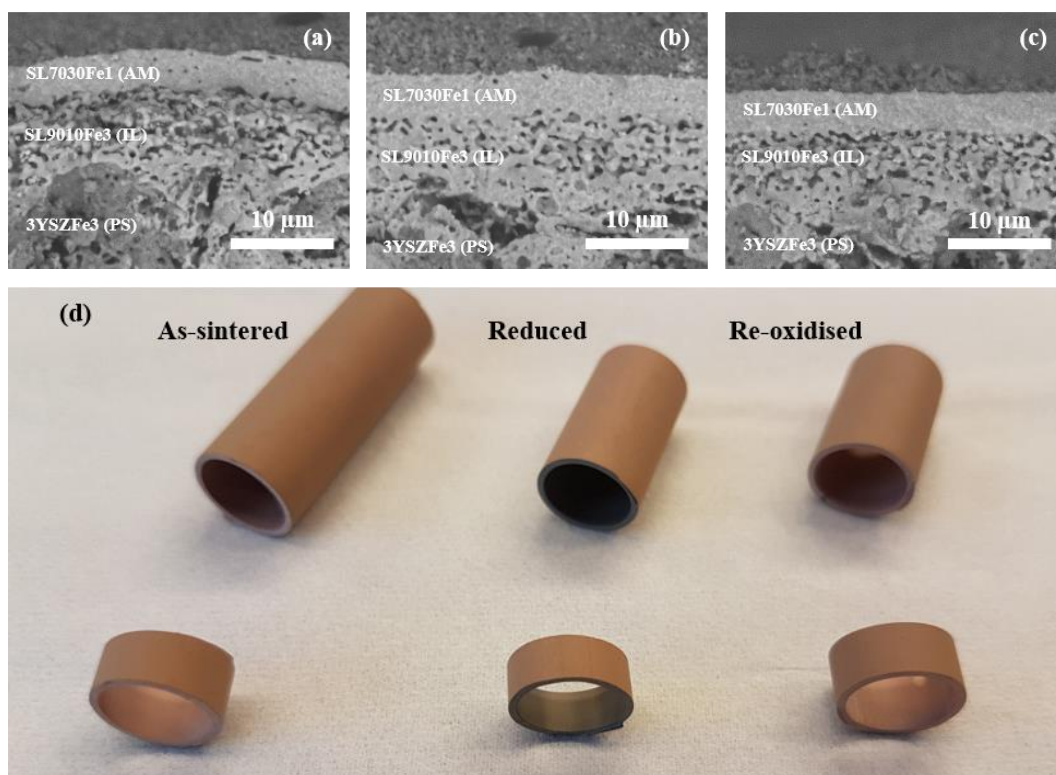


Fig. 18. SEM micrographs of SL7030Fe1 active membranes after cyclic treatment at 1000 °C in a) air, b) 5% H_2 - N_2 and c) re-oxidised sample, d) picture of the samples.

Table 6. EDS analysis of the SL7030Fe3 dual-phase dense membrane in different testing stages.

Element	Theoretical	Untreated	Sintered	Reduced
Zr	0.89	-	0.89	0.89
Y	0.02	-	0.04	0.04
Sc	0.20	-	0.14	0.10
La	1.00	1.00	1.00	1.00
Cr	0.85	0.90	0.78	0.78
Cu	0.10	0.09	0.04	0.04
Ni	0.05	0.05	0.04	0.04

SEM-EDS analysis of SL7030Fe3 (AM) untreated and after being sintered and exposed to reduction. The obtained results are shown in Table 6, where atomic values of the different components are normalised to Zr (for ScYSZ) and La (for LCCN). As observed, LCCN has an important loss of Cu (~50%) while ~13% less Cr is found in the perovskite after the sintering process. However, after reducing conditions were applied, the LCCN kept the same composition and no changes were observed.

4.6 Initial oxygen flux characterization.

In order to assess the performance of the developed membranes, a tubular section of the membrane ScYSZ-LCCN+1 mol%Fe₂O₃ with a length of ~3 cm was tested in an in-house built test rig. Tests were performed between 850 °C and 950 °C using the following feed gas/sweep gas gradients: Air/N₂, Air/CO₂, Air/5%H₂-N₂ and Air/H₂. Each testing cycle was 9 hours long. Fig. 19a shows the obtained results measured in Air/N₂ gradient. It is observed that the maximum oxygen flux, 0.28 Nml·cm⁻²·s⁻¹, obtained at 950 °C and using 500 ml·min⁻¹ is slightly higher than the oxygen flux obtained in a 1 mm pellet of ScYSZ-LCCN with the same operating conditions, this is one order of magnitude lower than the oxygen flux expected for a membrane of ~10µm thick. Oxygen flux data obtained using Air/CO₂, Air/5%H₂-N₂ and Air/H₂ gradients are not shown in this analysis due to a failure in the gasometers that affected the continuous and correct supply of the sweep gases. However, measuring in Air/N₂ was still possible.

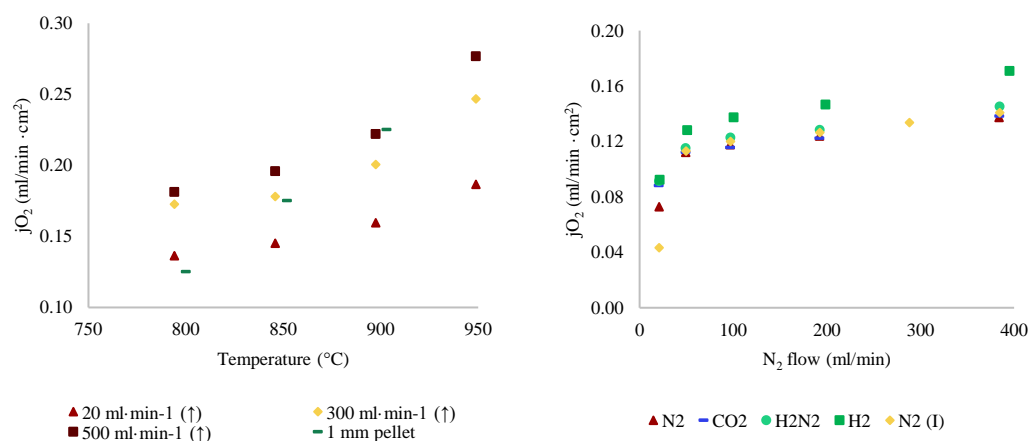


Fig. 19. Oxygen flux of tubular OTM based on SL7030Fe1 active membrane a) Oxygen flux using Air/N₂ gradient and varying the sweep gas flow, b) Reference measurements in Air/N₂ gradient at 850 °C after using different gradients.

Fig. 19b shows the reference oxygen fluxes obtained at 850 °C in Air/N₂ gradient after testing each of the studied gradients. It is observed that the oxygen flux measurements are relatively similar after test in Air/CO₂ and Air/5%H₂-N₂ gradients. A slightly higher oxygen flux was observed after measurements in Air/H₂, probably caused by activation of the membrane. The lower oxygen flux values obtained when using sweep gas flows of 20 ml·min⁻¹ might be related to diffusion limitations.

The stable oxygen flux values after the using different gradients clearly indicates that the membrane has an outstanding stability towards different atmospheres, including highly reducing conditions, fulfilling one of the main requirements for syngas applications.

Additional characterization of the fabricated membranes is required to identify the possible mechanisms involved in the limited oxygen permeability, including an extensive oxygen flux measurement campaign with relevant gases for syngas applications.

Other possible causes of the low oxygen permeability could be attributed to the lack of percolation of the electronic-conducting phase and formation of triple phase boundaries. This could be analysed by means of 3D SEM and statistical 2D SEM studies. Other possible cause could be related to effects on the ionic or electronic conductivity of the dual-phase composite caused by the addition or diffusion of Fe₂O₃ in the active membrane. This could be determined by electronic conductivity tests in relevant conditions, as well as XRD analysis to identify the possible substitution of Fe in the lattices of the crystal structure of the ScYSZ or LCCN. The possible formation of the lanthanum zirconate insulating phase could be also a possible cause. This could be analysed by means of TEM studies.

5. Conclusions.

Fabrication of (Sc₂O₃)_{0.10}(Y₂O₃)_{0.01}(ZrO₂)_{0.89} – LaCr_{0.85}Cu_{0.10}Ni_{0.05}O_{3-δ} (ScYSZ-LCCN) tubular oxygen membranes using (Y₂O₃)_{0.03}(ZrO₂)_{0.97} (3YSZ) porous supports was successfully achieved by doping the porous supports and the dense dual-phase membranes with 1 mol% and 3 mol% Fe₂O₃. The addition of Fe₂O₃ increased the sinterability of the materials and matched their thermal expansion coefficients, diminishing the thermo-mechanical stresses of the components during the sintering.

3YSZ porous supports un-doped and doped with 1 mol% and 3 mol% Fe_2O_3 were fabricated and characterized. By adding Fe, the sinterability of the supports increase considerably, obtaining ~6% additional shrinkage at 1250 °C in comparison with undoped 3YSZ. The addition of Fe also increased the flexural strength of the tubes, holding >137.7 MPa. Although the addition of Fe reduces the porosity by 11 vol.%, the permeability of the supports was unaffected since Darcy coefficients of $2.1 \times 10^{-14} \text{ cm}^{-2}$ were obtained in the three studied cases, making the 3 mol% Fe_3O_2 doped 3YSZ suitable to be used for the membrane fabrication.

Compatibility of materials and interactions between layers were studied for the fabrication of asymmetric membranes made of four different layers. It was found that the high LCCN content in the dense active membrane and in the activation layers affects the stability of the system and hinders the densification of the membrane due to the high vapour pressure of the Cr^{6+} . LCCN in the active membrane was restricted to 30 vol.%, where optimal densification was obtained at 1250 °C; however, percolation of the LCCN phase might be limited which would drastically affect the performance of the membranes. Optimal composition for the inner activation layer was defined as ScYSZ-LCCN 70:30 volume ratio. Lower quantities cause collapsing and partial densification of the activation layer, blocking the gas diffusion between the porous support and the membrane. A maximum content of 30 vol% LCCN was defined for the outer activation layer, which must be calcined at 1200 °C on the already sintered membrane. Larger quantities of LCCN would require >1300 °C to bond the outer activation layer to the active membrane, increasing the risk of lanthanum zirconate formation. Although porous activation layers require the addition of 3 mol% Fe_2O_3 to allow the fixation of the layers on the substrate, the active membrane does not require it since diffusion of Fe from the support and inner activation layer occurs during the sintering process.

Only the membranes using the 3 mol% Fe_2O_3 doped 3YSZ porous support reached sufficient densification. This demonstrates that the main driver for the densification of the membrane is the shrinkage of the support and not the quantity of dopant in the membrane.

Oxygen permeability measurements show low performances with oxygen flux values of approximately $0.28 \text{ ml} \cdot \text{min}^{-1} \cdot \text{cm}^2$ in Air/ N_2 gradient. However, the membrane shows high

stability after applying reducing conditions, maintaining the same performances and with high mechanical stability towards cycling. Possible causes of low performance might be related to: i) the lack of percolation of the electronic-conducting phase, ii) the formation of lanthanum zirconates or iii) effects of the Fe₂O₃ in the ionic/electronic conductivity of the membrane.

Although the interaction of the different components in the membrane make its fabrication challenging, a method to obtain highly mechanically stable membranes was obtained, as well as the main driver of the sinterability of tubular membranes was found, which could lead to additional studies to increase the performances of the membrane to be used in syngas or oxy-combustion applications.

6. Acknowledgments.

Authors acknowledge financial support from “Highly Flexible Energy Production by Oxy-Fired Biomass Gasification (HighFlex)” EUDP grant No.: 64018-0028 –before 12403– , "Highly Flexible Energy Production by Oxy-Fired Biomass Gasification (HighFlex)"

7. References.

- [1] Smart, S.; Diniz Da Costa, J.C. Oxygen transport membranes for power plant applications. *Advanced membrane science and technology for sustainable energy and environmental applications*, Chapter 9. Woodhead Publishing Limited, 2011. United Kingdom. DOI: 10.1533/9780857093790
- [2] Riaz, M.; Abdullah Butt, M. Oxygen Transport Membranes and their Role in CO₂ Capture and Syngas Production. *Journal of Membrane Science and Technology* — 2018, Volume 08, Issue 02. DOI: 10.4172/2155-9589.1000181
- [3] Banaszekiewicz, T.; Chorowski, M.; Gizicki, W. Comparative analysis of cryogenic and PTSA technologies for systems of oxygen production. *Aip Conference Proceedings* — 2014, Volume 1573, Issue 1, pp. 1373-1378. DOI: 10.1063/1.4860866

- [4] Julbe, A.; Farrusseng, D.; Guizard, C. Limitations and potentials of oxygen transport dense and porous ceramic membranes for oxidation reactions. IN *Catalysis Today* — 2005, Volume 104, Issue 2-4, pp. 102-113. DOI: 10.1016/j.cattod.2005.03.075
- [5] Den Exter, M.J.1; Haije, W.G.; Vente, J.F. Viability of ITM technology for oxygen production and oxidation processes: Material, system, and process aspects. *Inorganic Membranes for Energy and Environmental Applications* — 2009, pp. 27-51. DOI: 10.1007/978-0-387-34526-0_2
- [6] Kiebach, WR., ForskEL Project description: Highly Flexible Energy Production by Oxy-Fired Biomass Gasification. , 2016.
- [7] Puig-Arnavat, M.; Soprani, S.; Søgaaard, M.; Engelbrecht, K.; Ahrenfeldt, J.; Henriksen, U.B.; Hendriksen, P.V. Integration of mixed conducting membranes in an oxygen–steam biomass gasification process. *Rsc Advances* — 2013, Volume 3, Issue 43, pp. 20843-20854. DOI: 10.1039/c3ra44509g
- [8] Stadler, H.; Beggel, F.; Habermehl, M.; Persigehl, B.; Kneer, R.; Modigell, M.; Jeschke, P. Oxyfuel coal combustion by efficient integration of oxygen transport membranes. *International Journal of Greenhouse Gas Control* — 2011, Volume 5, Issue 1, pp. 7-15. DOI: 10.1016/j.ijggc.2010.03.004
- [9] Niedrig, C.; Menesklou, W.; Wagner, S.F.; Ivers-Tiffée, E. High-temperature pO₂ stability of metal oxides determined by amperometric oxygen titration. *Journal of the Electrochemical Society* — 2013, Volume 160, Issue 2, pp. F135-F140. DOI: 10.1149/2.063302jes
- [10] Zhu, X.; Yang, W. Critical Factors Affecting Oxygen Permeation Through Dual-phase Membranes. *Membrane Science and Technology* — 2011, Volume 14, pp. 275-293. DOI: 10.1016/b978-0-444-53728-7.00012-4
- [11] Nasrallah, M.M.; Douglass, D.L. Ionic and electronic conductivity in Y₂O₃-doped monoclinic ZrO₂. *J Electrochem Soc* — 1974, Volume 121, Issue 2, pp. 255-262.
- [12] Ishihara, T. Oxide Ion-Conducting Materials for Electrolytes. *Materials for High-temperature Fuel Cells* — 2012, pp. 97-132. DOI: 10.1002/9783527644261.ch3

- [13] Liu, H.; Li, S.; Li, Q.; Li, Y. Investigation on the phase stability, sintering and thermal conductivity of Sc₂O₃-Y₂O₃-ZrO₂ for thermal barrier coating application. *Materials and Design* — 2010, Volume 31, Issue 6, pp. 2972-2977. DOI: 10.1016/j.matdes.2009.12.019
- [14] Artemov, V.G.; Kuritsyna, I.E.; Lebedev, S.P.; Komandin, G.A.; Kapralov, P.O.; Spektor, I.E.; Kharton, V.V.; Bredikhin, S.I.; Volkov, A. A. Analysis of electric properties of ZrO₂-Y₂O₃ single crystals using terahertz IR and impedance spectroscopy techniques. *Russian Journal of Electrochemistry* — 2014, Volume 50, Issue 7, pp. 690-693. DOI: 10.1134/s1023193514070039
- [15] Gupta, S.; Mahapatra, M.K.; Singh, P. Lanthanum chromite based perovskites for oxygen transport membrane. *Materials Science and Engineering R: Reports* — 2015, Volume 90, pp. 1-36. DOI: 10.1016/j.mser.2015.01.001
- [16] Fergus, J.W. Lanthanum chromite-based materials for solid oxide fuel cell interconnects. *Solid State Ionics* — 2004, Volume 171, Issue 1-2, pp. 1-15. DOI: 10.1016/j.ssi.2004.04.010
- [17] Khandkar, A.C.; Milliken, C.E.; Elangovan, S.; Hartvigsen, J.J. Doped lanthanum chromite material for bipolar interconnects for solid oxide fuel cells. United States Patent number 5958304. September 28th, 1999. <https://patents.google.com/patent/US5958304>
- [18] Gupta, S.; Singh, P. Nickel and titanium doubly doped lanthanum strontium chromite for high temperature electrochemical devices. *Journal of Power Sources* — 2016, Volume 306, pp. 801-811. DOI: 10.1016/j.jpowsour.2015.11.111
- [19] Sarno, C.; Luisetto, I.; Zurlo, F.; Licocchia, S.; Di Bartolomeo, E. Lanthanum chromite based composite anodes for dry reforming of methane. *International Journal of Hydrogen Energy* — 2018, Volume 43, Issue 31, pp. 14742-14750. DOI: 10.1016/j.ijhydene.2018.06.021
- [20] Tanasescu, S.; Orasanu, A.; Berger, D.; Jitaru, I.; Schoonman, J. Electrical conductivity and thermodynamic properties of some alkaline earth-doped

- lanthanum chromites. *International Journal of Thermophysics* — 2005, Volume 26, Issue 2, pp. 543-557. DOI: 10.1007/s10765-005-4516-7
- [21] Orikasa, Y.; Crumlin, E.J.; Sako, S.; Amezawa, K.; Uruga, T.; Biegalski, M.D.; Christen, H.M.; Uchimoto, Y.; Yang, S.H. Surface strontium segregation of solid oxide fuel cell cathodes proved by in situ depth-resolved x-ray absorption spectroscopy. *ECS Electrochemistry Letters* — 2014, Volume 3, Issue 4, pp. F23-F26. DOI: 10.1149/2.006404eel
- [22] Yasuda, I.; Hishinuma, M. Electrical-conductivity and chemical diffusion-coefficient of Sr-doped lanthanum chromites. *Solid State Ionics* — 1995, Volume 80, Issue 1-2, pp. 141-150. DOI: 10.1016/0167-2738(95)00136-T
- [23] Pirou, S.; Bermudez, J.M.; Tak Na, B.; Ovtar, S.; Yu, J.H.; Hendriksen, P.V.; Kaiser, A.; Ramirez Reina, T.; Millan, M.; Kiebach, R. Performance and stability of $(\text{ZrO}_2)_{0.89}(\text{Y}_2\text{O}_3)_{0.01}(\text{Sc}_2\text{O}_3)_{0.10}\text{-LaCr}_{0.85}\text{Cu}_{0.10}\text{Ni}_{0.05}\text{O}_{3-\delta}$ oxygen transport membranes under conditions relevant for oxy-fuel combustion. *Journal of Membrane Science* — 2018, Volume 552, pp. 115-123. DOI: 10.1016/j.memsci.2018.01.067
- [24] Haugen, A.B.; Martinez Aguilera, L.; Kwok, K.; Molla, T.; Andersen, K.B.; Pirou, S.; Kaiser, A.; Hendriksen, P.V.; Kiebach, R. Exploring the Processing of Tubular Chromite- and Zirconia-Based Oxygen Transport Membranes. *Ceramics* — 2018, Volume 1, Issue 2, pp. 229-245. DOI: 10.3390/ceramics1020019
- [25] Suvorov, S.A.; Shevchik, A.P. Chemical equilibria involving lanthanum chromite. *Refractories and Industrial Ceramics* — 2004, Volume 45, Issue 2, pp. 94-99. DOI: 10.1023/b:refr.0000029615.98571.67
- [26] Kothanda Ramachandran, D.; Kwok, K.; Søgaaard, M.; Clemens, F.; Glasscock, J.; Kaiser, A. The role of sacrificial fugitives in thermoplastic extrusion feedstocks on properties of MgO supports for oxygen transport membranes. *Journal of the European Ceramic Society* — 2015, Volume 35, Issue 5, pp. 1527-1537. DOI: 10.1016/j.jeurceramsoc.2014.11.014
- [27] Kothanda Ramachandran, D.; Clemens, F.; Glasscock, J.; Søgaaard, M.; Kaiser, A. Tailoring the microstructure of porous MgO supports for asymmetric oxygen separation membranes: Optimization of thermoplastic

- feedstock systems. *Ceramics International* — 2014, Volume 40, Issue 7, pp. 10465-10473. DOI: 10.1016/j.ceramint.2014.03.017
- [28] Kothanda Ramachandran, D.; Søggaard, M.; Clemens, F.; Gurauskis, J.; Kaiser, A. Fabrication and performance of a tubular ceria based oxygen transport membrane on a low cost MgO support. *Separation and Purification Technology* — 2015, Volume 147, pp. 422-430. DOI: 10.1016/j.seppur.2015.02.037
- [29] Kwok, K.; Kiesel, L.; Frandsen, H.L.; Søggaard, M.; Hendriksen, P.V. Strength characterization of tubular ceramic materials by flexure of semi-cylindrical specimens. *Journal of the European Ceramic Society* — 2014, Volume 34, Issue 5, pp. 1423-1432. DOI: 10.1016/j.jeurceramsoc.2013.12.005
- [30] Haugen A.B.; Geffroy A.; Kaiser A.; Gil V. MgO as a non-pyrolyzable pore former in porous membrane supports. *Journal of the European Ceramic Society* — 2018, Volume 38, Issue 9, pp. 3279-3285. DOI: 10.1016/j.jeurceramsoc.2018.02.039
- [31] Bernabé, Y. Permeability and pore structure of rocks under pressure. Doctoral diss. Massachusetts Institute of Technology, Dept. of Earth, Atmospheric, and Planetary Sciences, 1986.
- [32] Ovtar, S.; Gurauskis, Jonas.; Haugen, A.B.; Chatzichristodoulou, C.; Kaiser, A.; Hendriksen, P.V. Oxygen transport properties of tubular Ce_{0.9}Gd_{0.1}O_{1.95}-La_{0.6}Sr_{0.4}FeO_{3-d} composite asymmetric oxygen permeation membranes supported on magnesium oxide. *Journal of Membrane Science* — 2017, Volume 523, pp. 576-587. DOI: 10.1016/j.memsci.2016.09.060
- [33] Wagman, D.D.; Kilpatrick, J.E.; Taylor, W.J.; Pitzer, K.S.; Rossini, F.D. Heats, free energies, and equilibrium constants of some reactions involving O₂, H₂, H₂O, C CO, CO₂, and CH₄. United States Bureau of Standards -- *Journal of Research* — 1945, Volume 34, Issue 2, pp. 143-161.
- [34] Povoden, E.; Chen, M.; Grundy, A.N.; Ivas, T.; Gauckler, L.J. Thermodynamic Assessment of the La-Cr-O System. *Journal of Phase*

- Equilibria and Diffusion — 2009, Volume 30, Issue 1, pp. 12-27. DOI: 10.1007/s11669-008-9463-0
- [35] Fleming, P.; Farrell, R.A.; Holmes, J.D.; Morris, M.A. The rapid formation of $\text{La}(\text{OH})_3$ from La_2O_3 powders on exposure to water vapor. *Journal of the American Ceramic Society* — 2010, Volume 93, Issue 4, pp. 1187-1194. DOI: 10.1111/j.1551-2916.2009.03564.x
- [36] Nagao, M.; Hamano, H.; Hirata, K.; Kumashiro, R.; Kuroda, Y. Hydration Process of Rare-Earth Sesquioxides Having Different crystal Structures. *Langmuir* — 2003, Volume 19, Issue 22, pp. 9201-9209. DOI: 10.1021/la020954y
- [37] Molin, S.; Gazda, M.; Jasinski, P. Interaction of yttria stabilized zirconia electrolyte with Fe_2O_3 and Cr_2O_3 . *Journal of Power Sources* — 2009, Volume 194, Issue 1, pp. 20-24. DOI: 10.1016/j.jpowsour.2009.01.031
- [38] Opila, E.J.; Myers, D.L.; Jacobson, N.S.; Nielsen, I.M.B.; Johnson, D.F.; Olminky, J.K.; Allendorf, M.D. Theoretical and Experimental Investigation of the Thermochemistry of $\text{CrO}_2(\text{OH})_2(\text{g})$. *Cheminform* — 2007, Volume 38, Issue 23. DOI: 10.1021/jp0647380
- [39] Sfeir, J. LaCrO_3 -based anodes: stability considerations. *Journal of Power Sources* — 2003, Volume 118, Issue 1-2, pp. 276-285. DOI: 10.1016/S0378-7753(03)00099-5
- [40] Carter, J.D.; Appel, C.C.; Mogensen, M.B. Reactions at the calcium doped lanthanum chromite-yttria stabilized zirconia interface. *Journal of Solid State Chemistry* — 1996, Volume 122, Issue 2, pp. 407-415. DOI: 10.1006/jssc.1996.0134
- [41] Jarligo, M.O.D.; Kang, Y.S.; Kawasaki, A. Thermal evolution of single phase lanthanum zirconate. *Key Engineering Materials* — 2006, Volume 317-318, pp. 31-35. DOI: 10.4028/www.scientific.net/KEM.317-318.31
- [42] Chiodelli, G; Scagliotti, M. Electrical characterization of lanthanum zirconate reaction layers by impedance spectroscopy. *Solid State Ionics* — 1994, Volume 73, Issue 3-4, pp. 265-271. DOI: 10.1016/0167-2738(94)90043-4

- [43] Chen, A.; Bourne, G.; Siebein, K.; Dehoff, R.; Wachsman, E.; Jones, K. Characterization of lanthanum zirconate formation at the a-site-deficient strontium-doped lanthanum manganite cathode/yttrium-stabilized zirconia electrolyte interface of solid oxide fuel cells. *Journal of the American Ceramic Society* — 2008, Volume 91, Issue 8, pp. 2670-2675. DOI: 10.1111/j.1551-2916.2008.02524.x
- [44] Flegler, A.J.; Burye, T.E.; Yang, Q.; Nicholas, J.D. Cubic yttria stabilized zirconia sintering additive impacts: A comparative study. *Ceramics International* — 2014, Volume 40, Issue 10, pp. 16323-16335. DOI: 10.1016/j.ceramint.2014.07.071
- [45] Guo, F.; Xiao, P. Effect of Fe₂O₃ doping on sintering of yttria-stabilized zirconia. *Journal of the European Ceramic Society* — 2012, Volume 32, Issue 16, pp. 4157-4164. DOI: 10.1016/j.jeurceramsoc.2012.07.035
- [46] Tadesse Molla, T. (2014). Modeling Macroscopic Shape Distortions during Sintering of Multi-layers. (Doctoral dissertation) Technical University of Denmark, Denmark.
https://backend.orbit.dtu.dk/ws/files/102421296/Modeling_Macroscopic_Shape_Distortions.pdf
- [47] Hayashi, H.; Saitou, T.; Maruyama, N.; Inaba, H.; Kawamura, K.; Mori, M. Thermal expansion coefficient of yttria stabilized zirconia for various yttria contents. *Solid State Ionics* — 2005, Volume 176, Issue 5-6, pp. 613-619. DOI: 10.1016/j.ssi.2004.08.021
- [48] Fan, W.; Wang, Z.Z.; Bai, Y.; Che, J.W.; Wang, R.J.; Ma, F.; Tao, W.Z.; Liang, G.Y. Improved properties of scandia and yttria co-doped zirconia as a potential thermal barrier material for high temperature applications. *Journal of the European Ceramic Society* — 2018, Volume 38, Issue 13, pp. 4502-4511. DOI: 10.1016/j.jeurceramsoc.2018.06.002
- [49] Fu, Y.P.; Wang, H.C. Structure, electrical, and thermal expansion properties of (La_{0.8}Ca_{0.2})(Cr_{0.9-x}Co_{0.1}Ni_x)O_{3-d} interconnect materials for intermediate temperature solid oxide fuel cells. *Journal of Materials Research* — 2009, Volume 24, Issue 5, pp. 1748-1755. DOI: 10.1557/jmr.2009.0207

- [50] Schmidt, C.G.; Kammer Hansen, K.; Andersen, K.B.; Fu, Z.; Roosen, A.; Kaiser, A. Effect of pore formers on properties of tape cast porous sheets for electrochemical flue gas purification. *Journal of the European Ceramic Society* — 2016, Volume 36, Issue 3, pp. 645-653. DOI: 10.1016/j.jeurceramsoc.2015.09.030
- [51] Bohnke, O.; Gunes, V.; Kravchyk, K.V.; Belous, A.G.; Yanchevskii, O.Z. V'Yunov, O.I. Ionic and electronic conductivity of 3 mol% Fe₂O₃ 3-substituted cubic yttria-stabilized ZrO₂ (YSZ) and scandia-stabilized ZrO₂ (ScSZ). *Solid State Ionics* — 2014, Volume 262, pp. 517-521. DOI: 10.1016/j.ssi.2013.11.003
- [52] Barbashov, V.I.; Belousov, N.N. Conductivity of Fe₂O₃-doped YSZ. *Ionics* — 2014, Volume 20, Issue 8, pp. 1051-1053. DOI: 10.1007/s11581-013-1052-5
- [53] Chan, Y.H.; Lai, H.Y.; Chen, C.K. Enhancing oxygen ion conductivity of 8YSZ electrolytes in SOFC by doping with Fe₂O₃. *Computational Materials Science* — 2018, Volume 147, pp. 1-6. DOI: 10.1016/j.commatsci.2018.01.057
- [54] Johar, B.; Zaili, N.A. Fe-doped 8YSZ at different composition for solid electrolyte in solid oxide fuel cell. *Matec Web of Conferences* — 2016, Volume 78, pp. 01102. DOI: 10.1051/mateconf/20167801102
- [55] Huang, X.J.; Weppner, W. Electrical Properties of Modified TZP(+TiO₂,FeO_x). *Ionics* — 1995, Volume 1, Issue 3, pp. 220-227. DOI: 10.1007/BF02426021
- [56] Lybye, D.; Mogensen, M. Effect of transition metal ions on the conductivity and stability of stabilised zirconia. *Ceramic Engineering and Science Proceedings* — 2007, Volume 27, Issue 4, pp. 67-78.
- [57] Van Hassel, B.; Burggraaf, A. Effect of ion-implantation doping on electrical-properties of yttria-stabilized zirconia thin-films. *Solid State Ionics* — 1992, Volume 57, Issue 3-4, pp. 193-201. DOI: 10.1016/0167-2738(92)90148-I
- [58] Lee, S.H.; Messing, G.L.; Twinn, E.R.; Mohanram, A.; Randall, C.A.; Green, D.J. Co-sintering of multilayer ceramics. *Key Engineering Materials*

- 2002, Volume 206-2, Issue 1, pp. 257-260. DOI: 10.4028/www.scientific.net/kem.206-213.257
- [59] Heidarpour, A.; Choi, G.M.; Abbasi, M.H.; Saidi, A. A novel approach to co-sintering of doped lanthanum chromite interconnect on Ni-YSZ anode substrate for SOFC applications. *Journal of Alloys and Compounds* — 2012, Volume 512, Issue 1, pp. 156-159. DOI: 10.1016/j.jallcom.2011.09.055
- [60] Liang, B.; Suzuki, T.; Hamamoto, K.; Yamaguchi, T.; Fujishiro, Y.; Awano, M.; Ingram, B.J.; Carter, J.D. Anode-supported tubular SOFC at low temperature using Ni, Fe, GDC, and YSZ based anode support. *ECS Transactions* — 2011, Volume 35, Issue 1, pp. 705-711. DOI: 10.1149/1.3570049
- [61] Zyryanov, V.V.; Nemudry, A.P.; Sadykov, V.A. Nanostructured Perovskites for the Fabrication of Thin Ceramic Membranes and Related Phenomena. *Membranes for Membrane Reactors: Preparation, Optimization and Selection* — 2011, pp. 201-225. DOI: 10.1002/9780470977569.ch6
- [62] Suzuki, T.; Funahashi, Y.; Yamaguchi, T.; Fujishiro, Y.; Awano, M. Development of Fabrication/Integration Technology for Micro Tubular SOFCs. *Micro Fuel Cells* — 2009, pp. 141-177. DOI: 10.1016/B978-0-12-374713-6.00004-4
- [63] Mikhailov, A.V.; Gribchenkova, N.A.; Kolosov, E.N.; Kaul, A.R.; Alikhanyan, A.S. Mass spectrometric investigation of vaporization in the Bi₂O₃-Fe₂O₃ system. *Russian Journal of Physical Chemistry a* — 2011, Volume 85, Issue 1, pp. 26-30. DOI: 10.1134/s0036024411010183
- [64] Hartmanova, M.; Poulsen, F.W.; Hanic, F.; Putyera, K.; Tunega, D.; Urusovakaya, A.A.; Oreshnikova, T.V. Influence of copper- and iron-doping on cubic yttria-stabilized zirconia. *Journal of Materials Science* — 1994, Volume 29, Issue 8, pp. 2152-8. DOI: 10.1007/BF01154694
- [65] Kusnezoff, M. Fuel Cells – Solid Oxide Fuel Cells – Membranes. *Encyclopedia of Electrochemical Power Sources*. 2009, Pages 34-50. DOI: 10.1016/B978-044452745-5.00257-4

- [66] Yokokawa, H. Phase diagrams and thermodynamic properties of zirconia based ceramics. *Key Engineering Materials* — 1998, Volume 153-154, Issue 153-154, pp. 37-74. 10.4028/www.scientific.net/kem.153-154.37
- [67] Pineau, A.; Kanari, N.; Gaballah, I. Kinetics of reduction of iron oxides by H₂. Part I: Low temperature reduction of hematite. *Thermochimica Acta* — 2006, Volume 447, Issue 1, pp. 89-100.

5.6 Development of thermoplastic extrusion for the fabrication of single-phase ion-conducting ceramic capillaries

This section contains the manuscript “Development and fabrication of flexible ion-conductor ceramic capillaries via thermoplastic extrusion”, where the fabrication dense capillary tubes using thermoplastic extrusion is described. This section shows the methodology to fabricate archetypes of 3.5 mm diameter dense capillaries of $\text{Ce}_{0.9}\text{Gd}_{0.1}\text{O}_{2-\delta}$ and $(\text{Sc}_2\text{O}_3)_{0.10}(\text{Y}_2\text{O}_3)_{0.01}(\text{ZrO}_2)_{0.89}$, using thermoplastic extrusion as shaping technique.

Although only $\text{Ce}_{0.9}\text{Gd}_{0.1}\text{O}_{2-\delta}$ and $(\text{Sc}_2\text{O}_3)_{0.10}(\text{Y}_2\text{O}_3)_{0.01}(\text{ZrO}_2)_{0.89}$ archetypes capillaries were developed in this study, the proof of concept broadens the possibilities to shape other materials.

By using capillaries made of mixed iononic-electronic conductors or dual-phase composites, it could be possible to fabricate self-supported oxygen transport membranes without the intrinsic risks of thermal expansion coefficients mismatch or side-reactions of multilayer systems.

Development of thermoplastic extrusion for the fabrication of single-phase ion-conducting ceramic capillaries

Lev Martinez Aguilera, Astri Bjørnetun Haugen, Ragnar Kiebach *

Department of Energy Conversion and Storage, Technical University of Denmark, 2800 Kgs. Lyngby, Denmark.

** Corresponding author: woki@dtu.dk*

Abstract

Archetypes dense capillaries of $\text{Ce}_{0.9}\text{Gd}_{0.1}\text{O}_{2-\delta}$ – CGO and $(\text{Sc}_2\text{O}_3)_{0.10}(\text{Y}_2\text{O}_3)_{0.01}(\text{ZrO}_2)_{0.89}$ – ScYSZ with a diameter of 3.5 mm and wall thickness of 0.4 mm have been fabricated by thermoplastic extrusion. For the thermoplastic extrusion, thermoplastic feedstocks of CGO and ScYSZ have been developed which resulted in flexible capillaries that have been shaped in the green state to more complex architectures, such as U-turns, before sintering. Scanning electron microscopy (SEM) revealed a homogeneous and dense microstructure (>98%) of the capillary tubes. The use of thermoplastic extrusion of capillaries could be extended to the fabrication of mixed ionic-electronic conductors or dual-phase composite materials, as a promising alternative to asymmetric mixed conducting oxygen transport membranes.

Introduction

Oxygen transport membranes (OTMs) are a promising technology for oxygen separation with 100% selectivity. [1] Most of the studies and development regarding OTMs have been based on asymmetric architectures, where thin layers of materials with different compositions are deposited on a porous support structure to achieve sufficiently high oxygen fluxes. [2-4] The fabrication of tubular asymmetric multilayer OTMs brings several challenges due to a sophisticated fabrication process, which requires the application of a thin-film dense membrane layer and porous catalytic layers in several coating and co-firing steps [2,5]. During the processing of multilayer tubes, chemical compatibility issues between different materials and matching of densification rates and thermal expansion coefficient of the different layers need to be addressed carefully [6]. By using capillaries of mixed ionic-electronic conducting materials or dual-phase

composites, the manufacturing of the OTMs would be simplified, since only one composition and one thermal treatment would be required.

Ceramic capillaries with diameters between 0.5 mm – 5 mm have been widely used for applications in electronic industry, fiber optics, liquids filtration and aerospace applications. [7-9] Their main limitation are the large pressure drop along the longitudinal axis and the mechanical challenges when working with long samples. Thus, the length of the capillaries for practical applications is limited. However, larger surface area per volume unit than asymmetric tubular systems, typically increased by a factor of two, could compensate these limitations. [10-12]

In the case of oxygen separation applications, the main disadvantage in capillaries is the low oxygen flux per area caused by the thickness of the active layer (ca. 500 μm in capillaries vs. ca. 20 μm in thin asymmetric membranes). However, it is expected that the high packing density could compensate the oxygen production per volume unit. Dense $\text{Ba}_{0.5}\text{Sr}_{0.5}\text{Co}_{0.8}\text{Fe}_{0.2}\text{O}_{3-\delta}$ capillaries for oxygen separation have been manufactured by hot isostatic pressing, phase inversion and cold extrusion, which demonstrates the feasibility and interests of this concept. [13-15] Liu, et al. [16] developed $\text{Zr}_{0.84}\text{Y}_{0.16}\text{O}_{2-\delta}$ – $\text{La}_{0.8}\text{Sr}_{0.2}\text{Cr}_{0.5}\text{Fe}_{0.5}\text{O}_{3-\delta}$ capillaries of 2.6 mm external diameter and 270 μm wall-thickness by phase inversion. They obtained oxygen fluxes of 0.32 $\text{Nml}\cdot\text{s}^{-1}\cdot\text{cm}^{-2}$ and 4.53 $\text{Nml}\cdot\text{s}^{-1}\cdot\text{cm}^{-2}$ in Air/He and Air/CO gradients, respectively at 950 $^{\circ}\text{C}$.

The study paves the way towards manufacturing capillaries to be used as oxygen transport membranes. It describes a methodology to manufacture 3.5 mm diameter with 0.4 mm wall-thickness dense CGO and ScYSZ archetypes capillaries by thermoplastic extrusion.

Experimental

The dense capillary tubes of 3 mm diameter were prepared via thermoplastic extrusion using two different extrusion feedstocks, $\text{Ce}_{0.9}\text{Gd}_{0.1}\text{O}_{2-\delta}$ – CGO and $(\text{Sc}_2\text{O}_3)_{0.10}(\text{Y}_2\text{O}_3)_{0.01}(\text{ZrO}_2)_{0.89}$ – ScYSZ. The CGO and ScYSZ powders were coated with 2.5% stearic acid prior to the mixing process with ethylene-vinyl acetate copolymer (DuPont, USA) and paraffin wax (Sigma-Aldrich, USA). Compositions of the feedstocks are shown in Table 1. Formulations were adjusted according to the surface area of the ceramic powders. The feedstocks were homogenised at 100 $^{\circ}\text{C}$ using a W50 EHT

kneading unit attached to a driving unit Plastograph KE19 (Brabender, Germany). The extrusion of capillaries was using a single screw extruder 19/20DN attached to the same driving unit and using a 5 mm outer diameter and 4 mm inner diameter die. Temperatures at the feeding, compression and the die zones of the extruder were set at 100 °C, 95 °C and 80 °C for the CGO feedstock and 80 °C, 75 °C and 60 °C for the ScYSZ feedstock.

Table 1. Composition of the used thermoplastic extrusion feedstocks for capillary fabrication.

Component	CGO Feedstock [wt.%]	ScYSZ Feedstock [wt.%]
Ceramic powder + stearic acid	93.3	82.1
Ethylene-vinyl acetate	4.5	12.7
Paraffin wax	2.2	5.3

U-tubes, which could be used as open flow OTM, were prepared by setting the capillaries on a preheated alumina tube at 60 °C with the required diameter for the U-turn. In order to increase the flexibility of the green capillaries, warming up of the shaping areas was done using a heating gun providing an air flow at 80 °C. End-capping of the tubes was done by warming the edge of the tube at 80 °C and then pressing it with a piece of steel at room temperature.

Binder burnout and sintering of the capillary tubes were done by setting them directly on alumina plates in horizontal position and heating them up in air using a slow ramp of 15 °C·h⁻¹ in order to avoid excessive generation of gases and possible deformation of the tubes during the organic-phase decomposition. Three dwells of 2 hours each were set at 250 °C, 400 °C and 650 °C to allow gradual burning of the organic-phase fraction. After the last dwell at 650 °C, heating ramp of 30 °C·h⁻¹ was used up to sintering temperature of 1325 °C for ScYSZ and CGO, and 1400 °C and 1575 °C for CGO. A dwell of 5h was kept at the sintering temperature before cooling with ramp of 100 °C·h⁻¹.

Microstructural analysis of the capillaries was performed using an optical microscope and SEM Hitachi TM3000 working with secondary electron detector at 15 kV.

Results

Fig. 1 shows different stages of the manufactured capillaries, from green-state to sintered at different temperatures. It was observed that although green-tubes show high straightness just after extrusion, after full cooling the capillaries tended to bend. This was

attributed to two possible reasons: 1) Variations of thickness of the capillaries due to settings on the die, which could be easily fixed by a good control of the die's adjustment screws and, 2) the cooling rate of the capillaries is different at the bottom (in contact with a metal holder) and the top (exposed to air).

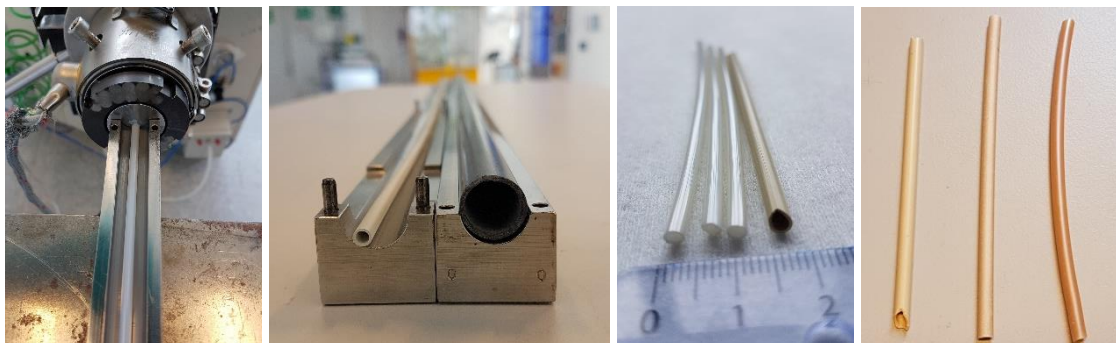


Fig. 1. Different stages of the manufactured capillaries: a) Extrusion process of the ScYSZ capillary, b) comparison of 1 m long 5 mm green-state CGO capillary with a 14 mm green-state YSZ-based porous support, c) sintered ScYSZ and a CGO capillaries, d) CGO capillaries sintered at 1325, 1400 and 1575 °C.

These could cause stresses leading to the bending of the capillaries during the cooling after leaving the extrusion die. Similar behavior was observed in the thermoplastic extrusion of 14 mm YSZ-based tubes. [2] This problem could be solve equalizing the cooling rate along the tube by using metal casts, as the one observed in Fig. 1b.

SEM microstructure of the ScYSZ and CGO capillaries after sintering is shown in Fig. 2. In the case of the CGO capillaries, three sintering temperatures were tested: 1325 °C, 1400 °C and 1575 °C, which resulted in 95 %, 97 % and 99 % densification of the capillaries, respectively. In the case of the ScYSZ, a densification of 98% was obtained at 1325 °C.

As observed in Fig. 2a – Fig. 2g, a “porosity ring” is observed in the middle section of the capillary. Although this porous ring did not cause delamination, it could cause structural problems, as well as increasing the bulk resistance by reducing the ion-conducting paths across the capillary's wall. Although additional analysis is needed to determine the source of this flaw, it might have been caused due to tensile stresses and difference in the flow behaviour of the feedstock trough the die. Despite the observed minor porosity, all the samples were gas-tight.

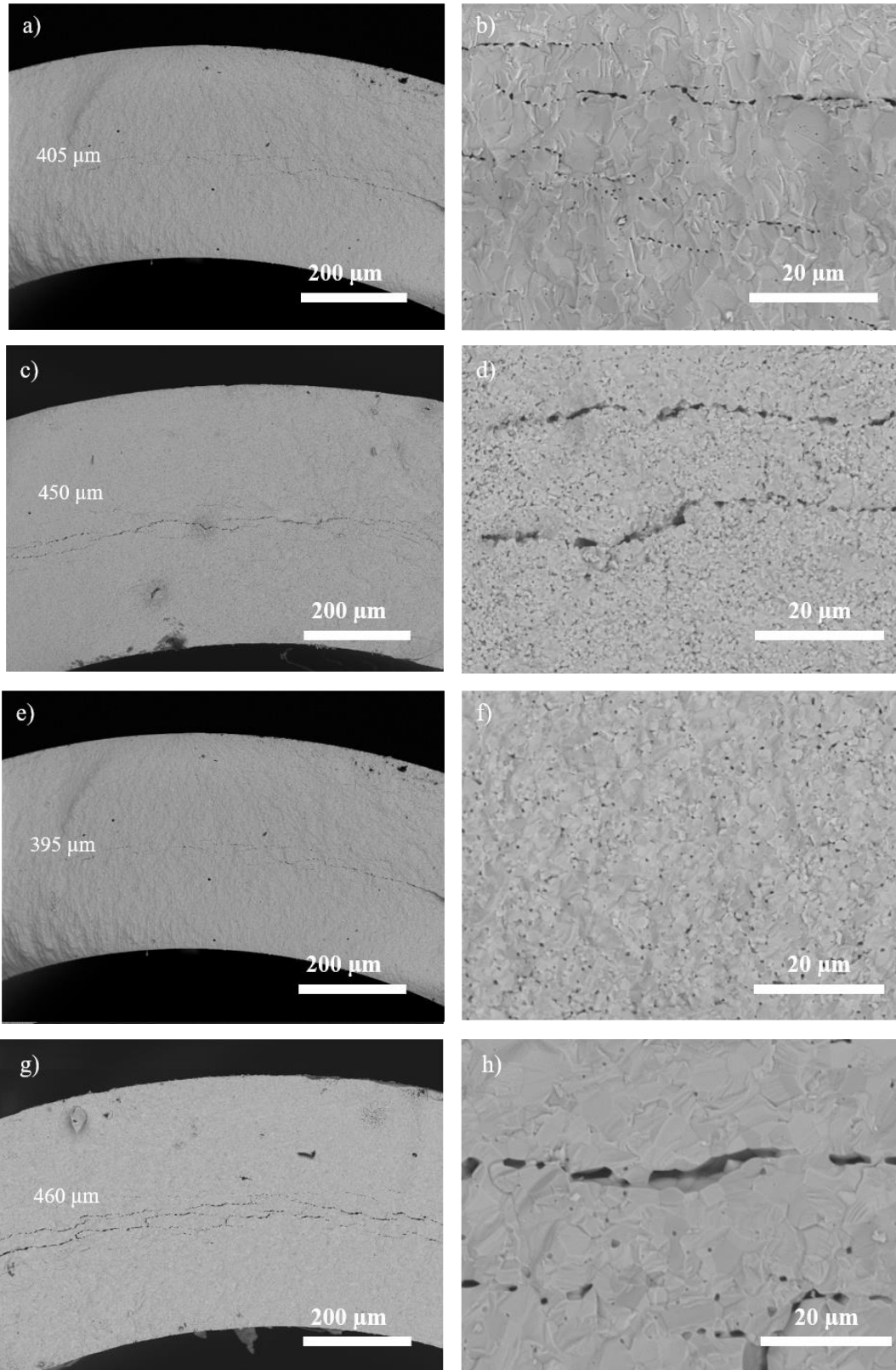


Fig. 2. Fractured cross section SEM micrographs of: a/b) ScYSZ sintered at 1325 °C, c/d) CGO sintered at 1325 °C, e/f) CGO sintered at 1400 °C, g/h) CGO sintered at 1575 °C.

After extrusion and cooling, the green-state capillaries show high flexibility, allowing an easy handling and storage. By re-heating the green tubes with warm air (80 °C), it was possible to increase the flexibility of the capillary tubes to the point where it is possible to modify their shape. U-shapes of the capillaries were prepared and sintered, as seen in Fig. 3. After the thermal treatment, the shape was kept.

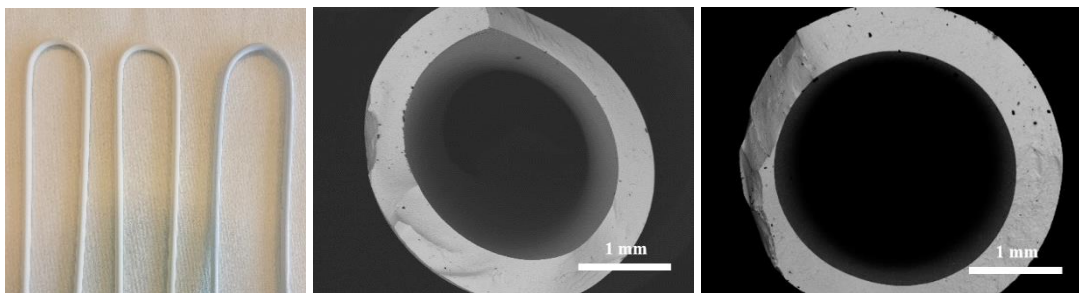


Fig. 3. Tests of U-turn in capillaries a) U-shape in CGO and ScYSZ green capillaries, b) SEM cross section of CGO capillary sintered at 1400 °C, c) SEM cross section of the U-turn in CGO capillary sintered at 1400 °C.

As expected, during the U-turn bending, the circular section of the capillaries was slightly deformed, reducing the section area by ca. 30%. However, blocking of the capillary was not observed. This was confirmed by flowing compressed air through the sintered U-turns. Deformation of the circular cross section might lead to structural weakening.

Capping of the capillaries was tested by following a similar procedure to increase the flexibility of the capillaries. A flat metal piece at room temperature was manually used to press the heated edges of the capillaries in green-state. After sintering, leak tests were made by flowing compressed air into the capillaries. No leaks were identified when the caps had lengths larger than 3 mm. samples with shorter caps showed leaks for both, ScYSZ and CGO capillaries.



Fig. 4. End-capping of capillaries. a) Capping tests of ScYSZ and CGO capillaries, b) optical microscope view of the capping in ScYSZ capillary, c) optical microscope view of the capping in CGO capillary.

Conclusions

Dense $\text{Ce}_{0.9}\text{Gd}_{0.1}\text{O}_{2-\delta}$ and $(\text{Sc}_2\text{O}_3)_{0.10}(\text{Y}_2\text{O}_3)_{0.01}(\text{ZrO}_2)_{0.89}$ archetypes capillaries of 3.5 mm diameter and 0.5 mm thickness were successfully manufactured by using thermoplastic extrusion. The green-state capillaries are easy to handle and show high flexibility, allowing subsequent shaping. Capping and U-turs were shaped in the capillaries by using simple heating methods to make specific areas flexible enough to modify the shape without affecting adjacent areas. Although SEM analysis showed slight deformation on the inner section of the capillary tubes during the U-turns, no structural damage on the walls was observed. Densification of 98% was obtained after sintering. This study demonstrates the potential of thermoplastic extrusion for manufacturing dense oxygen transport membranes capillaries if mixed ionic-electronic conductors or dual-phase composites are used.

Acknowledgments.

Authors acknowledge financial support from “Highly Flexible Energy Production by Oxy-Fired Biomass Gasification (HighFlex)” EUDP grant No.: 64018-0028 –before 12403– , "Highly Flexible Energy Production by Oxy-Fired Biomass Gasification (HighFlex)"

References

- [1] Julbe, A.; Farrusseng, D.; Guizard, C. Limitations and potentials of oxygen transport dense and porous ceramic membranes for oxidation reactions. IN *Catalysis Today* — 2005, Volume 104, Issue 2-4, pp. 102-113. DOI: 10.1016/j.cattod.2005.03.075
- [2] Haugen, A.B.; Martinez Aguilera, L.; Kwok, K.; Molla, T.; Andersen, K.B.; Pirou, S.; Kaiser, A.; Hendriksen, P.V.; Kiebach, R. Exploring the Processing of Tubular Chromite- and Zirconia-Based Oxygen Transport Membranes. *Ceramics* — 2018, Volume 1, Issue 2, pp. 229-245. DOI: 10.3390/ceramics1020019

- [3] Kothanda R., Dhavanesan¹; Sjøgaard, M.; Clemens, F.; Gurauskis, J.; Kaiser, A. Fabrication and performance of a tubular ceria based oxygen transport membrane on a low cost MgO support. *Separation and Purification Technology* — 2015, Volume 147, pp. 422-430. DOI: 10.1016/j.seppur.2015.02.037
- [4] Christie, G.M.; Lane, J.A. Composite oxygen transport membrane. United States Patent number 5958304. September 28th, 1999. US20130156978
- [5] Kothanda Ramachandran, D.; Clemens, F.; Glasscock, J.; Sjøgaard, M.; Kaiser, A. Tailoring the microstructure of porous MgO supports for asymmetric oxygen separation membranes: Optimization of thermoplastic feedstock systems. *Ceramics International* — 2014, Volume 40, Issue 7, pp. 10465-10473. DOI: 10.1016/j.ceramint.2014.03.017
- [6] Tadesse Molla, T.; Kothanda Ramachandran, D.; Ni, D.W.; Esposito, V.; Teocoli, F.; Olevsky, E.A.; Bjørk, R.; Pryds, N.; Kaiser, A.; Frandsen, H.L. Modeling constrained sintering of bi-layered tubular structures. *Journal of the European Ceramic Society* — 2015, Volume 35, Issue 3, pp. 941-950. DOI: 10.1016/j.jeurceramsoc.2014.10.010
- [7] Jiang, D.; Bu, X.; Sun, Bing; Lin, G.; Zhao, H.; Cai, Y.; Fang, L. Experimental study on ceramic membrane technology for onboard oxygen generation. *Chinese Journal of Aeronautics* — 2016, Volume 29, Issue 4, pp. 863-873. DOI: 10.1016/j.cja.2016.06.003
- [8] Kim, I.J.; Kim, H.S.; Seo, M.Y.; Gauckler, L.J. Advanced ceramics in wire bonding capillaries for semiconductor package technology. *Materials Science and Engineering a* — 2008, Volume 498, Issue 1-2, pp. 129-134. DOI: 10.1016/j.msea.2007.10.130
- [9] Corke, M.1 Kopera, P.M.1 Margolin, M.; Sweeney, K.L.; Clairardin, X. Low cost components for fibre optic systems. *Efoc/lan 86 Proceedings. Papers Presented At: the Fourth Annual European Fibre Optic Communications and Local Area Networks Exposition* — 1986, pp. 255-60.

- [10] Meulenberg, W.A.; Schulze-Kupfers, F.; Deibert, W.; Van Gestel, T.; Baumann, S. Ceramic Membranes: Materials – Components – Potential Applications. *Chembioeng Reviews* — 2019, Volume 6, Issue 6, pp. 198-208. DOI: 10.1002/cben.201900022
- [11] Amin, S.K.; Abdallah, H.A.M.; Roushdy, M.H.; El-Sherbiny, S.A. An overview of production and development of ceramic membranes. *International Journal of Applied Engineering Research* — 2016, Volume 11, Issue 12, pp. 7708-7721. DOI: 10.1063/1.5064344
- [12] Gaspar, I.; Koris, A.; Bertalan, Z.; Vatai, G. Comparison of ceramic capillary membrane and ceramic tubular membrane with inserted static mixer. *Chemical Papers* — 2011, Volume 65, Issue 5, pp. 596-602. DOI: 10.2478/s11696-011-0045-y
- [13] Schulz, M.; Pippardt, U.; Kiesel, L.; Ritter, K.; Kriegel, R. Oxygen permeation of various archetypes of oxygen membranes based on BSCF. *Aiche Journal* — 2012, Volume 58, Issue 10, pp. 3195-3202. DOI: 10.1002/aic.13843
- [14] Buysse, C.; Kovalevsky, A.; Snijkers, F.; Buekenhoudt, A.; Mullens, S.; Luyten, J.; Kretzschmar, J.; Lenaerts, S. Development, performance and stability of sulfur-free, macrovoid-free BSCF capillaries for high temperature oxygen separation from air. *Journal of Membrane Science* — 2011, Volume 372, Issue 1-2, pp. 239-248. DOI: 10.1016/j.memsci.2011.02.011
- [15] Weiß, M.; Maurath, J.; Willenbacher, N.; Koos,. Shrinkage and dimensional accuracy of porous ceramics derived from capillary suspensions. *Journal of the European Ceramic Society* — 2019, Volume 39, Issue 5, pp. 1887-1892. DOI: 10.1016/j.jeurceramsoc.2019.01.011
- [16] Liu, T.; Wang, Y.; Yuan, R.; Gao, J.; Chen, C.; Bouwmeester, H.J.M. Enhancing the oxygen permeation rate of $Zr_{0.84}Y_{0.16}O_{1.92}-La_{0.8}Sr_{0.2}Cr_{0.5}Fe_{0.5}O_{3-\delta}$ dual-phase hollow fiber membrane by coating with $Ce_{0.8}Sm_{0.2}O_{1.9}$ nanoparticles. *ACS Applied Materials and Interfaces* — 2013, Volume 5, Issue 19, pp. 9454-9460

Chapter 6. Summary and future work

The development of multilayer asymmetric tubular oxygen transport membranes (OTMs) for integration in gasification systems using thermoplastic extrusion and dip-coating as main shaping techniques was studied. This thesis work dealt with 1) the selection and investigation of dual-phase composite materials for the active membrane and functional layers to overcome stability limitations of single-phase mixed ionic-electronic conductors under syngas conditions, 2) definition of a manufacturing method, including fabrication of tubular supports, maximum thickness of functional layers, and sintering profiles, and 3) testing of the OTMs in lab-scale and in real biomass gasification conditions.

1) Integration in gasification systems – proof of concept.

Membranes based on $\text{Ce}_{0.9}\text{Gd}_{0.1}\text{O}_{1.95} - \text{La}_{0.6}\text{Sr}_{0.4}\text{FeO}_{3-\delta}$ (CGO-LSF) composite supported on MgO supports were tested in both controlled lab-scale and pilot-plant gasification conditions. An in-house built unit working at 850 °C, adjacent to a fluidized bed (LT-CFB) gasifier was used for partial oxidation of tars of a producer gas stream. Oxygen fluxes of $0.5 \text{ Nml}\cdot\text{cm}^{-2}\cdot\text{min}^{-1}$ and $1.5 \text{ Nml}\cdot\text{cm}^{-2}\cdot\text{min}^{-1}$ were obtained when operating the unit with producer gas/Air and H_2 /Air gradients using a 10 cm long membrane, respectively. In lab-scale, the same kind of membrane provided an oxygen flux of $4.4 \text{ Nml}\cdot\text{cm}^{-2}\cdot\text{min}^{-1}$ when using an H_2 /Air gradient and a 3 cm long membrane. The lower oxygen flux of the membranes in the partial oxidation unit might be due to the reduction of the driving force of the oxygen permeation along the membrane, an effect of the membrane under compression because of the design of the rig or due to lower accuracy related to the setup and equipment being used.

A crosscheck analysis of the gas and tar composition at the inlet/output of the membrane and the oxygen fluxes demonstrated that tar decomposition is driven by the combination of heat and oxygen provided by the membrane. However, 65% less tertiary tars and additional 50% and 20% more H_2 and CH_4 were obtained when comparing with the conversion related to thermal processes. This indicates that the membrane contributes to the decomposition of the tars, rising the quality of the produced gas. Decrement on the membrane performance was observed, which is attributable to carbon and sulphur-based compounds deposits and de-activation of the LaCoO_3 used as infiltrated catalyst.

Although the CGO-LSF membranes did not stand thermal cycling, the proof of concept for the integration of OTMs in gasification systems was demonstrated. Nevertheless, the use of stable and resistant membranes towards syngas conditions, as well as thermal cycling need to be further developed.

Beside the use of adequate OTMs and catalysts for syngas applications, some modifications to the tars partial oxidation unit could be done to increase the accuracy of the experimental setup. Some of these modifications could be the replacement of flowmeters with adequate flow ranges and modification of the tars sampling points to ensure having representative samples without risking the mechanical integrity of the membrane.

2) $(Sc_2O_3)_{0.10}(Y_2O_3)_{0.01}(ZrO_2)_{0.89} - LaCr_{0.85}Cu_{0.10}Ni_{0.05}O_{3-\delta}$, membranes.

Dual-phase membranes based on $(Sc_2O_3)_{0.10}(Y_2O_3)_{0.01}(ZrO_2)_{0.89} - LaCr_{0.85}Cu_{0.10}Ni_{0.05}O_{3-\delta}$, (ScYSZ-LCCN) in volumetric ratio 70:30, using $(Y_2O_3)_{0.03}(ZrO_2)_{0.97} - 3YSZ$ porous tubes were fabricated and investigated. A sintering temperature of 1450 °C was required to densify the active ScYSZ-LCCN membrane. This caused Cr vaporization from the LCCN, promoting the formation of $La(OH)_3$, and leading to longitudinal fractures of the membranes. The thermal properties mismatch between the membrane and the porous support led to transversal cracks. Thin membranes of 4 μm showed mechanical integrity, but $La_2Zr_2O_7$ was formed on the surface of the membrane and a lack of gas tightness was identified.

To reduce high processing temperatures, 1 mol% and 3mol% Fe_2O_3 was used as sintering aid in the formulations of the porous support and the functional layers. The sintering temperature to reach densification of the membranes was lowered to 1250 °C, which decreased the Cr vaporization from the perovskite and avoided the formation of secondary phases. The addition of Fe_2O_3 also reduced the thermal expansion and sintering onsets mismatch between the functional layers and the porous support. The addition of 3 mol% Fe_2O_3 to the 3YSZ supports allowed obtaining flexural strengths larger than 138 MPa and a gas permeability of $2.2 \times 10^{-14} \text{ m}^{-2}$, fulfilling the minimum requirements for tubular supports (flexural strength $\geq 50 \text{ MPa}$, gas permeability $\geq 2.2 \times 10^{-14} \text{ m}^{-2}$). It was found that the 26% total shrinkage of the porous support was the main driver for the densification of the membranes, due to a 2D compression given by the tubular geometry of the membranes.

On the other hand, the systems showed high sensitivity to manufacturing conditions, as well as to changes in composition and thickness of the functional layers. A heating ramp of $60\text{ }^{\circ}\text{C}\cdot\text{min}^{-1}$ led to cracks, which were probably caused by the sintering onset mismatch between the membrane and the supports. By increasing the heating rate to $200\text{ }^{\circ}\text{C}\cdot\text{min}^{-1}$, the stresses caused by this mismatch were minimized and dense membranes were obtained. It was also found that the total thickness of the functional layers must not exceed $15\text{ }\mu\text{m}$, otherwise they would show crack formation. The densification of the membrane is highly dependent on the quantity of the electronic-conductor phase in the ScYSZ-LCCN inner porous layer. If the YCCC phase is higher than 20 vol%, the active membrane will not densify; however, if only ScYSZ, the porous layer collapses forming dense structures. LCCN also creates porosity in the inner porous layers and allow the formation of triple phase boundaries in the interface with the active membrane. It was also found that ScYSZ-LCCN active membranes with a volumetric ratio of 60:40 hinder the densification of the membrane, which suggests that the Cr vaporization is strongly related to the low densification of the composite. It was possible to manufacture gas-tight membranes by combining 3YSZ+3 mol% Fe_2O_3 porous supports, ScYSZ-LCCN 90:10+3 mol% Fe_2O_3 inner porous layer, ScYSZ-LCCN 70:30 dense active membranes and ScYSZ-LCCN 70:30+3 mol% Fe_2O_3 outer porous layer. Though Fe_2O_3 was not used in the active membrane, Fe was found in both ionic and electronic phases of the membrane due to diffusion of Fe from the adjacent layers and porous support during the sintering process.

The obtained tubular membranes show outstanding mechanical and thermal stability. An oxygen flux of $0.28\text{ ml}\cdot\text{min}^{-1}\cdot\text{cm}^{-2}$ was obtained in an Air/ N_2 gradient at $950\text{ }^{\circ}\text{C}$ for the fabricated $8\text{ }\mu\text{m}$ thick membranes, which is one order of magnitude lower than the expected oxygen flux. The low oxygen flows might be attributed to the possible interaction of the Fe_2O_3 in the ionic conductivity of the oxygen-ion conducting phase, to the formation of $\text{La}_2\text{Zr}_2\text{O}_7$ insulating phase or to the lack of percolation of the electronic-conducting phase. However, it is important to point out that the outstanding stability of the membrane after exposing it to different gradients, including Air/ H_2 , makes it subject of future studies.

Different analysis techniques could be used to complement the results obtained for the ScYSZ-LCCN system to define the mechanisms that limit the oxygen flux. It is also

necessary to perform additional oxygen flux measurements to corroborate the obtained results, as well as to identify the main limitations of the oxygen flux. Although literature suggests that Fe does not affect the ion-conductivity of ZrO₂-based components, it would be advisable to carry out electric conductivity tests of the ScYSZ-LCCN 70:30 + 3 mol% composite in oxidizing and reducing conditions and in a range of relevant temperatures. An extensive XRD analysis would allow identifying the changes in the crystal structure of the composites caused by Fe₂O₃ doping. Fe could modify the crystal structure of the ScYSZ, decreasing its ion-conductivity; it could also substitute the B-site of the LCCN perovskite, disrupting the electronic conductivity. 30 vol% of electronic conducting phase in the composite is in the lower limit to ensure percolation of the phase. The use of 3D SEM analysis, supported by statistical 2D SEM, would show if percolation of the electronic-conducting phase is limiting the oxygen transport reactions.

3) *Ce_{0.9}Gd_{0.1}O_{1.95} – Y_{0.8}Ca_{0.2}Cr_{0.8}Co_{0.2}O_{3-δ}, as OTM membrane materials.*

Ce_{0.9}Gd_{0.1}O_{1.95} – Y_{0.8}Ca_{0.2}Cr_{0.8}Co_{0.2}O_{3-δ}, (CGO-YCCC) composite was investigated as OTM material after compatibility tests between the electronic conducting phase, YCCC, with CGO, ScYSZ and (Y₂O₃)_{0.08}(ZrO₂)_{0.92}. The CGO-YCCC showed easy densification at 1250 °C, which was attributed to the interaction of a Co liquid phase that acted as sintering aid for the CGO. The composite show oxygen fluxes of 0.3 ml·min⁻¹·cm⁻² and 0.25 ml·min⁻¹·cm⁻² in Air/Ar and Air/CO₂ gradients, respectively, at 900 °C when using a 1.3 mm thick membrane. The composite shows high stability over a period of 30 h in Air/CO₂ at 900 °C. In pO₂ ~10⁻²⁰, cracks are developed along the CGO grains, which might be associated to the chemical expansion of the CGO.

Attempts to develop thin CGO-YCCC membranes supported on 3YSZ-based supports were carried out. However, the large TEC and the sintering temperature onsets mismatch between the membrane composite and the porous supports were the main limitation of a successful fabrication. Cracks and delamination were observed in all the studied cases, although delamination was decreased by integrating a CGO + 1 mol% Co₃O₄ inner porous layers. The chemical stability of the active membrane was kept after processing.

In order to use this composite as a thin-layer on tubular supports, it is necessary to use compatible materials with similar thermal expansion coefficients, such as CGO-Co porous supports. However, other options, such as self-supported oxygen membranes could be considered.

An alternative to overcome the challenging process of a multilayer system was investigated by the development of flexible archetype capillaries of 4 mm diameter fabricated by thermoplastic extrusion. Although only dense CGO and ScYSZ capillaries were fabricated as proof of concept, this broadens the options to use dual-phase composites, such as CGO-LSF and CGO-YCCC to fabricate oxygen membranes. Although bulk limitations and high-pressure drops can be factors to consider by using capillaries, larger surface area per volume unit, typically increased by a factor of two, could compensate them. A larger analysis in the development of thermoplastic extruded capillaries, such as optimization of the feedstock according to the final design of the capillaries is needed. The development of a testing setup would be required to tests capillary systems.